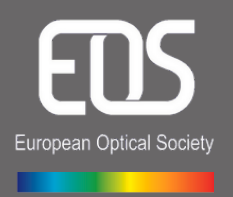
Journal of the European Optical Society

Rapid Publications





Topical Issue EOSAM 2023

Editorial: European Optical Society Annual Meeting (EOSAM) 2023

Patricia Segonds ¹, Guy Millot ² and Bertrand Kibler ^{2*}

The European Optical Society Annual Meeting, EOSAM, covers all aspects of optics and photonics within several topical meetings and sessions. The 11th EOSAM was organized by EOS and SFO onsite in Dijon, France, at the Dijon Exhibition and Convention Center, 11–15 September 2023. It was attended by over 500 researchers, key leaders, students, and industry experts from over 34 different countries all over the world. The event provided a comprehensive overview of cutting-edge research in optics and photonics, from fundamental to applied, and of industrial developments through more than 420 presentations in 10 thematic sessions highlighting the most innovative and emerging research, including: silicon photonics and integrated optics, adaptive and freeform optics, biophotonics, nanophotonics, optical materials, nonlinear and quantum optics, optical frequency combs, ultrafast optics, optoelectronic nanotechnologies and microsystems, and optics applications. Four focused sessions completed the panorama: specialty optical fibers, structured light, chiroptical phenomena, machine-learning for optics and photonic computing for Artificial Intelligence (AI). This annual international congress highlighted the richness and vigor of all the optics sectors in France, Europe and the rest of the world. An industrial session dedicated to technological innovations was complemented by an exhibition area for the photonics industry at the heart of the conference. A round table discussion was organized with the European Photonics Industry Consortium (EPIC), the world's leading industry association promoting the sustainable development of photonics organizations in Europe. The symposium demonstrated that research and technological advances in optics and photonics are formidable drivers of economic growth and cultural vitality, while respecting the environment.

Following the 11th EOSAM, the current special issue of Journal of the European Optical Society — Rapid Publications (JEOS-RP) gathers thirteen papers devoted to distinct topics of the conference, such as optical materials, nanophotonics, nonlinear optics, optical frequency combs, structured light, machine learning for optics, and various optical applications. This collection of eleven original research papers, one short communication and one review article is presented below, highlighting some of the latest advances in the studies presented at the conference.

Optical materials are essential for a wide range of current and future industrial applications, and generate important research with major scientific and technological challenges. The correlation between the optical characteristics of the material and its structure and composition is of great importance. With regard to this topic, Bravo et al. present a 3D diffusion modeling of photopolymers as a recording media for complex diffractive optical elements [1]. In another paper, Mohand Ousaid et al. report a more accurate Sellmeier equation derived from quasi-phase matching curves obtained from the investigation of optical parametric generation in 1-D periodically poled LiTaO3 crystals with varying periods [2]. The design of nanostructures is of crucial importance to enhance light-matter interactions and to control field distributions at subwavelength scales. In this topic, Shelling Neto et al. introduce a new bispectral optical cavity concept for which they design twin pairs of highly reflective, ultra-low noise metamirrors [3].

¹ Univ. Grenoble Alpes, CNRS, Grenoble INP, Institut Néel, F-38000 Grenoble, France

² Laboratoire Interdisciplinaire Carnot de Bourgogne (ICB), UMR 6303 CNRS-Université Bourgogne Franche-Comté, Dijon, France.

^{*} Corresponding author: bertrand.kibler@u-bourgogne.fr

Light structuring has emerged as a powerful tool for controlling the propagation dynamics of pulsed beams. The ability to manipulate and generate spatiotemporal light distributions has been enhanced in recent years, enabling us to envisage applications across the entire spectrum of optics. Nabadda et al. present a complete Mueller matrix imaging polarimeter that uses three liquid-crystal retarders and a pixelated polarization camera. This device is then tested experimentally by analyzing well-known samples for structured light applications [4]. In another paper, Klingmann et al. demonstrate the parallel generation of arbitrary arrays of Gaussian and Laguerre-Gaussian laser foci suitable for super-resolution microscopy by means of acousto-optic spatial light modulation [5]. As in most of scientific areas, Al techniques have opened up new horizons for photonics research in recent years. Numerical modeling using AI can achieve high efficiency and accuracy for photonics systems. In this topical issue, by using deep neural networks into digital holographic microscopy, Cuenat et al. propose a hybrid approach utilizing an adapted version of the GedankenNet model, coupled with a UNet-like model, for the purpose of accessing microobjects 3D pose measurements [6]. Nonlinear effects in optical systems are playing a prominent role in many fundamental physics discoveries as well as emerging technologies. Here, Guezennec et al. demonstrate the generation of broadband tunable and synchronized pulses exceeding the micro-joule level using the new concept of fiber optical parametric chirped-pulse oscillation [7]. In another paper, Deroh et al. report the generation of multi-wavelength light sources in the 1.55 µm telecommunication C band and then in the 2-µm waveband, through enhanced four wave-mixing processes, by using a straightforward and adaptable dual-frequency Brillouin fiber laser [8].

The fields of optics and photonics are now considered as key enabling technologies across many different industries. Applications-centered research in optics/photonics encompass any demonstration and application of optical technologies and instrumentation to address problems in various fields. To this regard, López-Bautista et al. build an optical setup with a hexagonal design that allowed a large number of Drosophila melanogaster cultures to be irradiated homogeneously with blue light simultaneously, thus opening potentially their investigation at genetic, behavioral and neuronal levels [9]. Bouquet et al. develop a real-time optical measurement system based on a customized microscope and an automatic system for non-contact measurement of airborne fungal spores in protected crops such as strawberries, tomatoes, and cucumbers [10]. In another paper, Bernabeu et al. investigate the role of absorption mechanism on the optimization of processing commercial polymers under high repetition rate femtosecond laser irradiation [11]. Next, Sirvent-Verdú et al. analyze the viability of a novel recording geometry to produce reflection holographic couplers in photopolymers without prisms [12]. Finally, Fritzsche et al. propose a design approach for an advanced multi-channel pyrometer for bulk oven processes [13].

In conclusion, this topical issue on EOSAM 2023 contains thirteen articles devoted to the multifaceted development of ongoing studies in the broad areas of optics and photonics. We strongly hope that this issue will lead to research inspiration and significant advances, which will be benefiting a wide range of theoretical and applied scientists.

Acknowledgments

The editors thank all of our contributing authors for their dedication to EOSAM 2023 and the reviewers for their constructive comments and suggestions.

References

1.	Bravo J.C., Sirvent-Verdú J.J., García-Vázquez J.C., Pérez-Bernabeu A., Colomina-Martínez J., Fernández R., Márquez A., Gallego S. (2024) Analysis of the recording of Fibonacci lenses on photopolymers with 3-D diffusion model, <i>J. Eur. Opt. Society-Rapid Publ.</i> 20 , 32. https://doi.org/10.1051/jeos/2024026
2.	Mohand Ousaid S., Chang KH., Peng LH., Boudrioua A. (2024) Temperature dependence of LiTaO3 refractive index corrections of Sellmeier equation, <i>J. Eur. Opt. Society-Rapid Publ.</i> 20 , 41. https://doi.org/10.1051/jeos/2024034
3.	Shelling Neto L., Dickmann J., Sauer S., Kroker S. (2024) Bispectral optical cavity based on twin metamirrors, <i>J. Eur. Opt. Society-Rapid Publ.</i> 20 , 3. https://doi.org/10.1051/jeos/2024002
4.	Nabadda E., Sánchez-López M.M., Vargas A., Lizana A., Campos J., Moreno I. (2024) Mueller matrix imaging polarimeter with polarization camera self-calibration applied to structured light components, <i>J. Eur. Opt. Society-Rapid Publ.</i> 20 , 5. https://doi.org/10.1051/jeos/2024003
5.	Klingmann F., Toledo-García N., Martín-Badosa E., Montes-Usategui M., Tiana-Alsina J. (2024) Parallel illumination for depletion microscopy through acousto-optic spatial light modulation, <i>J. Eur. Opt. Society-Rapid Publ.</i> 20 , 30. https://doi.org/10.1051/jeos/2024031
6.	Cuenat S., Brito Carcañoa J.E., Ahmad B., Sandoz P., Couturier R., Laurent G.J., Jacquot M. (2024) Digital holographic microscopy applied to 3D computer micro-vision by using deep neural networks, <i>J. Eur. Opt. Society-Rapid Publ.</i> 20 , 31. https://doi.org/10.1051/jeos/2024032
7.	Guezennec T., Idlahcen S., Cervera A., Hanzard PH., Landais D., Provino L., Haboucha A., Godin T., Hideur A. (2024) µJ-level normal-dispersion fiber optical chirped-pulse parametric oscillator, <i>J. Eur. Opt. Society-Rapid Publ.</i> 20 , 7. https://doi.org/10.1051/jeos/2024006
8.	Deroh M., Xu G., Lucas E., Beugnot JC., Maillotte H., Sylvestre T., Kibler B. (2024) Towards 2-µm comb light source based on multiple four-wave mixing in a dual-frequency Brillouin fiber laser, <i>J. Eur. Opt. Society-Rapid Publ.</i> 20 , 19. https://doi.org/10.1051/jeos/2024017
9.	López-Bautista M., Mejía-Sánchez J.E., Ornelas-Rodríguez F.J., Mesa-Cornejo V.M. (2024) Design of an optical system equipped with blue LEDs for the irradiation of <i>Drosophila melanogaster</i> cultures, <i>J. Eur. Opt. Society-Rapid Publ.</i> 20 , 24. https://doi.org/10.1051/jeos/2024022
10.	Bouquet G., Kaspersen K., Haugholt K.H. (2024) Optical measurement instrument for detection of powdery mildew and grey mould in protected crops, <i>J. Eur. Opt. Society-Rapid Publ.</i> 20 , 25. https://doi.org/10.1051/jeos/2024024
11.	Bernabeu A.P., Nájar G., Ruiz A., Bravo J.C., Ramirez M.G., Gallego S., Márquez A., Puerto D. (2024) The role of absorption mechanism on the optimization of processing commercial polymers under high repetition rate femtosecond laser irradiation, J. Eur. Opt. Society-Rapid Publ. 20, 27. https://doi.org/10.1051/jeos/2024021
12.	Sirvent-Verdú J.J., Bravo J.C., Colomina-Martínez J., Nájar G., Neipp C., Francés J., Gallego S., Beléndez A. (2024). Manufacturing reflection holographic couplers for see-through applications recorded in photopolymers without prisms: An experimental validation, <i>J. Eur. Opt. Society-Rapid Publ.</i> 20 , 29. https://doi.org/10.1051/jeos/2024029
13.	Fritzsche R., Kaiser C.F., Herdrich G. (2024) Design approach for an advanced multi-channel pyrometer for bulk oven processes, <i>J. Eur. Opt. Society-Rapid Publ.</i> 20 , 34. https://doi.org/10.1051/jeos/2024035

J. Eur. Opt. Society-Rapid Publ. 2024, $\bf 20,\ 32$ © The Author(s), published by EDP Sciences, 2024

https://doi.org/10.1051/jeos/2024026

Available online at: https://jeos.edpsciences.org

EOSAM 2023

Guest editors: Patricia Segonds, Guy Millot and Bertrand Kibler

REVIEW ARTICLE OPEN 3 ACCESS

Analysis of the recording of Fibonacci lenses on photopolymers with 3-D diffusion model

J. C. Bravo 1,2,* , J. J. Sirvent-Verdù 1,2 , J. C. García-Vázquez 1,2 , A. Pérez-Bernabeu 1,2 , J. Colomina-Martínez 1 , R. Fernández 1,2 , A. Márquez 1,2 , and S. Gallego 1,2

Received 13 November 2023 / Accepted 13 May 2024

Abstract. In this work a three-dimensional diffusion model is used to model photopolymers as a recording media. This model allows us to predict the properties of the Diffractive Optical Elements (DOEs) once we recorded into the photopolymer. This model had never been tested with more complex elements, such as multifocal diffractive lenses, as presented in the following in this work. In addition, the model includes; the estimation of the refractive index modulation, the low-pass filtering effect due to the experimental optical setup, and the evolution of the transverse intensity distribution. In this way, the selection of the appropriate material characteristics depending on the intended DOE application is made possible. Specifically, an acrylamide-based PVA/AA photopolymer is simulated using the proposed model. Moreover, coverplating and index matching systems are considered together to avoid the effects of thickness variation. Furthermore, in order to compare their properties using the proposed model, we focus on Fibonacci lenses (FL), a type of bifocal lenses. This allows us to evaluate the dependence of the focii intensity on the polymerisation rate, the diffusivity parameter, low-pass filtering effect and the use of the index matching system for these lenses. This enables us to know the recording parameters in order to produce this type of multifocal diffractive lenses with higher quality and precision.

Keywords: Diffractive optical elements, Photopolymers, Diffractive lenses, Diffusion model, Spatial light modulator, 4F system, PVA/AA, Intraocular lenses, Ophthalmology application, Low-pass filtering.

1 Introduction

Diffractive Optical Elements (DOEs) [1] have a wide range of practical applications in fields such as diffractive micro-optics [2], medical laser treatments [3], and solar energy concentrators [4], among others. Due to their unique properties and versatility, DOEs are commonly employed to manipulate light and obtain desired light patterns.

Photopolymeric materials offer an ideal platform for recording DOEs due to to their favorable phase modulation characteristics, as we have recently successfully modeled [5, 6]. This model reproduce the 3D phase image formation in the photopolymer [7, 8], considering factors like non-local polymerisation, depth-dependent light attenuation, diffusion process and variations in polymerisation rates, as addressed in [9]. Furthermore, it includes low-pass filtering to account for the recording optical configuration. The model presented also describes photopolymerisation in

three dimensions, showing a more complex and realistic diffusion process, as it is shown in [10]. It also introduce coverplating together with index matching techniques to avoid surface variation effects and to simulate the experimental results. The present work is divided in two main parts: experimental and numerical results. The numerical aspect can be further subdivided into three distinct stages. Firstly, we simulate the intensity pattern of a complex DOE, specifically focusing on Fibonacci Lenses (FL) [11–14]. This type of lens exhibit bifocal behaviour and present the capacity to achieve two distinct and reduced focal lengths by either increasing the lens order or decreasing the radius [15]. Secondly, we calculate the refractive index modulation resulting from the polymerisation process using our numerical diffusion model, thereby obtaining monomer and polymer concentration profiles over time. Finally, we use Fresnel propagation to illustrate the effects on the evolution of axial transverse intensity distribution generated by a zone plate composed of Fibonacci lens. Following the acquisition of numerical results, we establish an experimental setup for the production and subsequent recording of

¹ Instituto Universitario de Física Aplicada a las Ciencias y las Tecnologías, Universidad de Alicante, Apartado 99, Alicante E03080, Spain

² Departamento de Física, Ingeniería de Sistemas y Teoría de la Señal, Universidad de Alicante, Apartado 99, Alicante E03080, Spain

^{*} Corresponding author: juanc.bravo@ua.es

polyvinyl alcohol-acrylamide (PVA/AA) based photopolymer samples. This photopolymer recently was demonstrated its capability to be used as DOE recording media and present better behavior at low spatial frequency than other photopolymers like HPDLC or NPC [16, 17]. Firstly blazed gratings were recorded, then some DOEs such as axicon, fork and blaze gratings, were recorded and fabricated [9]. The next step is to record and optimizing more complex DOEs. To achieve this, we use a Liquid Crystal on Silicon (LCoS) Spatial Light Modulator (SLM) [18, 19] to obtain the desired amplitude recording intensity of these Fibonacci Lenses and a 4F system to record the DOE, which will enable us to mass fabrication. Notably, our setup allows real-time adjustments of the dimensions and magnification of the final recorded lens through the SLM and optical 4F system. This capability facilitates real-time monitoring during the recording process, underscoring the predictive capabilities of our diffusion model in relation to the experimental results.

Once these stages are shown, we present numerical results relating to various parameters. These results include insights into the nonlinear response of the polymerisation rate concerning the recording intensity, the influence of different diffusivity values in PVA/AA solution samples, and the utilization of coverplating techniques. Consequently, this work allow us to explore the influence of the material properties in the recording of Fibonacci lenses. These lenses represent the fusion between the mathematical Fibonacci sequence and the practical functionality of bifocal diffractive lenses, thus forming a novel intersection within the field of optics. This unique combination not only redefines the visual experience by optimizing near and far vision correction but also opens doors to innovative applications in fields such as ophthalmology, including intraocular lenses.

2 Theory

2.1 Theoretical Diffusion Model

In general, DOEs formation in photopolymers depends on several factors; the monomer and polymer concentration, M and P respectively, the polymerisation rate, F_R , the molecules diffusion inside the recording media, D, due to Fick's Law and the creation of holes during the polymerisation process H. The holes are the primary origin of the thickness variation. We assumed that the fast swelling of the illuminated areas (initially there is rapid shrinkage in the illuminated areas), is due to the mass transport through the surface, clearly faster than the diffusion in the bulk of the material, and the surface tension forces [20]. Therefore, the equations that govern this model are:

$$\frac{\partial M(x,y,z,t)}{\partial t} = D(t)\nabla^2 M(x,y,z,t) - F_R(x,y,z,t)M(x,y,z,t)$$
(1)

$$\frac{\partial P(x, y, z, t)}{\partial t} = F_R(x, y, z, t) M(x, y, z, t)$$
 (2)

(3)

$$\frac{\partial H(x,y,z,t)}{\partial t} = D_h(t) \nabla^2 H(x,y,z,t) - K_h(x,y,z,t) M(x,y,z,t)$$

In this work, both the monomer and holes diffusivity in the polymerisation process are consider as constants, D_m , D_h respectively. On the other hand, K_h represents the holes rate generation, which is assumed proportional to F_R , the polymerisation rate, which also depends on the reaction rate and the recording intensity. This dependence is given by:

$$F_R(x, y, z, t) = k_R(t)I(x, y, z)^{\gamma} = k_R(t)[I(x, y)e^{-\beta(t)z}]^{\gamma}$$

$$k_R(t) = k_{R0}e^{-\alpha_T t}$$
 (4)

where I(x, y) is the recording intensity, k_{R0} is the rate constant, γ is the relationship between intensity and polymerisation rate, $\beta(t)$ is the intensity depth attenuation coefficient due to light absorption and α_T is the attenuation of the polymerisation due to the Trommsdorff's effect [10]. To solve these differential equations we use Finite-Differences Method (FDM). Thus, in our formulation these equations can be written as:

$$\begin{split} M_{i,j,k}^{l} &= \frac{\Delta_{t}}{\Delta x^{2}} D_{m} \left[M_{i+1,j,k}^{l-1} - 2M_{i,j,k}^{l-1} + M_{i-1,j,k}^{l-1} \right] \\ &+ \frac{\Delta_{t}}{\Delta y^{2}} D_{m} \left[M_{i,j+1,k}^{l-1} - 2M_{i,j,k}^{l-1} + M_{i,j-1,k}^{l-1} \right] + \\ &+ \frac{\Delta_{t}}{\Delta z^{2}} D_{m} \left[M_{i,j,k+1}^{l-1} - 2M_{i,j,k}^{l-1} + M_{i,j,k-1}^{l-1} \right] \\ &- \Delta t F_{Ri,j,k}^{l-1} M_{i,j,k}^{l-1} + M_{i,j,k}^{l-1} \end{split}$$

$$(5)$$

$$P_{i,j,k}^{l} = P_{i,j,k}^{l-1} + \Delta t F_{Ri,j,k}^{l-1} M_{i,j,k}^{l-1}$$
 (6)

$$\begin{split} H_{i,j,k}^{l} &= \frac{\Delta t}{\Delta x^{2}} D_{h} \Big[H_{i+1,j,k}^{l-1} - 2H_{i,j,k}^{l-1} + H_{i-1,j,k}^{l-1} \Big] \\ &+ \frac{\Delta t}{\Delta y^{2}} D_{h} \Big[H_{i,j+1,k}^{l-1} - 2H_{i,j,k}^{l-1} + H_{i,j-1,k}^{l-1} \Big] + \\ &+ \frac{\Delta t}{\Delta z^{2}} D_{h} \Big[H_{i,j,k+1}^{l-1} - 2H_{i,j,k}^{l-1} + H_{i,j,k-1}^{l-1} \Big] \\ &- \Delta t F_{Ri,j,k}^{l-1} M_{i,j,k}^{l-1} + H_{i,j,k}^{l-1}, \end{split}$$
(7)

where the superscript l represent the temporal step, while the spatial steps in coordinate x, y, z are denoted by the subscripts i, j, k, respectively. In the other hand, due to the use of a numerical method, the Courant-Friedrichs-Lewy condition or stability criterion must be satisfied:

$$\Delta t < \frac{1}{2D_m} \left(\frac{(\Delta x \Delta y \Delta z)^2}{(\Delta y \Delta z)^2 + (\Delta x \Delta z)^2 + (\Delta x \Delta y)^2} \right)$$
(8)

To obtain the refractive index modulation during the recording process, it is necessary to calculate monomer and polymer concentrations during the exposure time. Therefore, average refractive index can be measured using Lorentz-Lorenz equation as follows:

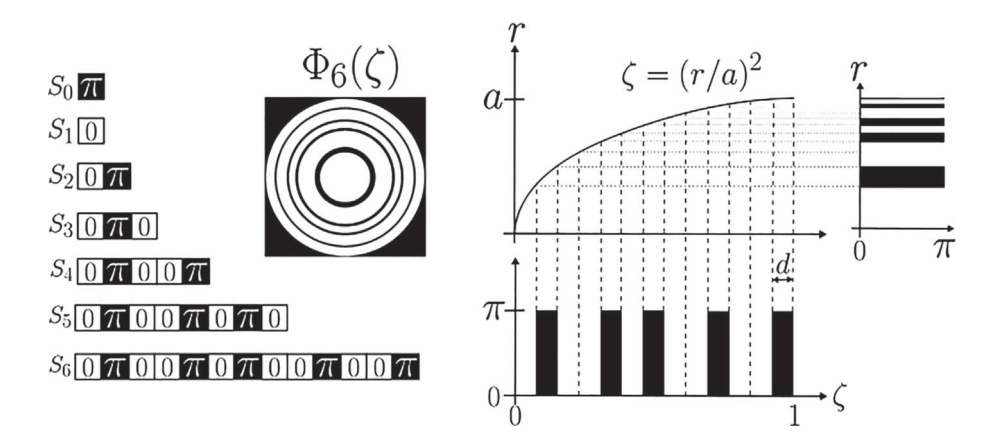


Fig. 1. Generation of 6-order Fibonacci Lens. In the left side, set construction is presented, and in the right side, axial mapping function is shown.

$$\frac{n^2 - 1}{n^2 + 2} = \frac{n_m^2 - 1}{n_m^2 + 2} M + \frac{n_p^2 - 1}{n_p^2 + 2} P + \frac{n_h^2 - 1}{n_h^2 + 2} H + \frac{n_b^2 - 1}{n_b^2 + 2} (1 - M_0)$$
(9)

In this context, the subscripts m, p, h and b denote the refractive indices of the monomer, polymer, holes and binder, respectively. On the other hand, the refractive index of interest is denoted as n, representing the average refractive index of the photopolymer. This average refractive index depends on the concentrations of monomer and polymer, as well as the initial monomer concentration, denoted as M_0 . Hence, n is influenced by both spatial and temporal variations in these concentrations.

On the other hand, local thickness variation in x and y are determined by the volume fraction of the holes:

$$d(x,y) = d_0(x,y) - d_h(x,y), \tag{10}$$

where d is the thickness of the sample layer, d_0 is the intrinsic thickness (that can change due the monomer diffusion), and d_h is the shrinkage due to the holes. In order to avoid this thickness variation due to the holes creation and the relief effects we used a non soluble paraffin liquid with refractive index of 1.4679 that fits perfectly the PVA/AA sample. So the phase change $\Delta \varphi$ depends on:

$$\Delta\varphi(x,y) = \frac{2\pi}{\lambda} \{ n(x,y)d(x,y) + d_h(x,y)n_h \}$$
 (11)

and the holes refractive index, n_h , is 1 when index-matching system is not used, and 1.4679 when we use the paraffin, which is liquid at room temperature.

2.2 Fibonacci Lenses

The Fibonacci sequence is a recursive set of numbers that obeys:

$$F_{n+1} = F_n + F_{n-1} \lim_{n \to \infty} \frac{F_{n+1}}{F_n} = \frac{1 + \sqrt{5}}{2} \equiv \varphi,$$
 (12)

where φ is the golden ratio. In [11] is presented a binary generating function, $\Phi_n(\zeta)$ for a π -phase of the FL as follows:

$$\Phi_n(\zeta) = \begin{cases}
0 & \text{if } (\lfloor l\varphi \rfloor) - 1) d \le \zeta < (\lfloor l\varphi \rfloor) d \\
\pi & \text{othercase}
\end{cases}$$
(13)

where $l = 1, 2, 3, ..., F_n$ and $\zeta = (r/a)^2$ is the normalized radial coordinate, with a the radius of the lens and $\forall \zeta \in [0,1]$, plus this interval is segmented into F_{n+1} subintervals of length $d = 1/F_{n+1}$. $\lfloor x \rfloor$, denotes the floor function of x, which yields the largest integer less than or equal to x as its output. In Figure 1, the generation of a binary Fibonacci function is presented. This function obeys the recurring set $S_{n+1} = \{S_n S_{n-1}\}$. Then, a binary $(0, \pi)$ Fibonacci phase function $\Phi_n(\zeta)$ is constructed. Finally, the radial profile is generated by mapping the axial reduced coordinate with the lens radius, a. To achieve this, we first establish two seed or starter sets, $S_0 = [\pi]$ and $S_1 = [0]$. Subsequently, following the recurrence law, set S_2 is constructed. The construction proceeds to the desired order, as depicted in Figure 1, which is illustrated up to the 6th order. Once the final set, S_6 , is constructed, we normalize its length to unity and establish the correspondence between the radial normalized coordinate ζ and the lens radius a.

3 Experimental Setup

3.1 Photopolymeric solution

The photopolymeric media is a Polyvinilal cohol-Acrylamide (PVA/AA) solution based on water. PVA is used as support polymer or binder, triethanolamine (TEA) as electron donor, acrylamide (AA) as monomer, Yellow Eosine (YE) as a dye and N,N' methyl-bisacrylamide (BMA) as a crosslinker. In Figure 2, a photochemistry scheme of the photopolymerization reaction is shown to facilitate comprehension of the role played by each compound.

On the other hand, in Table 1, the different compounds and their proportions are presented.

This photopolymeric solution is sensitive to green light ($\lambda = 533$ nm) and transparent for red light ($\lambda = 632$ nm)

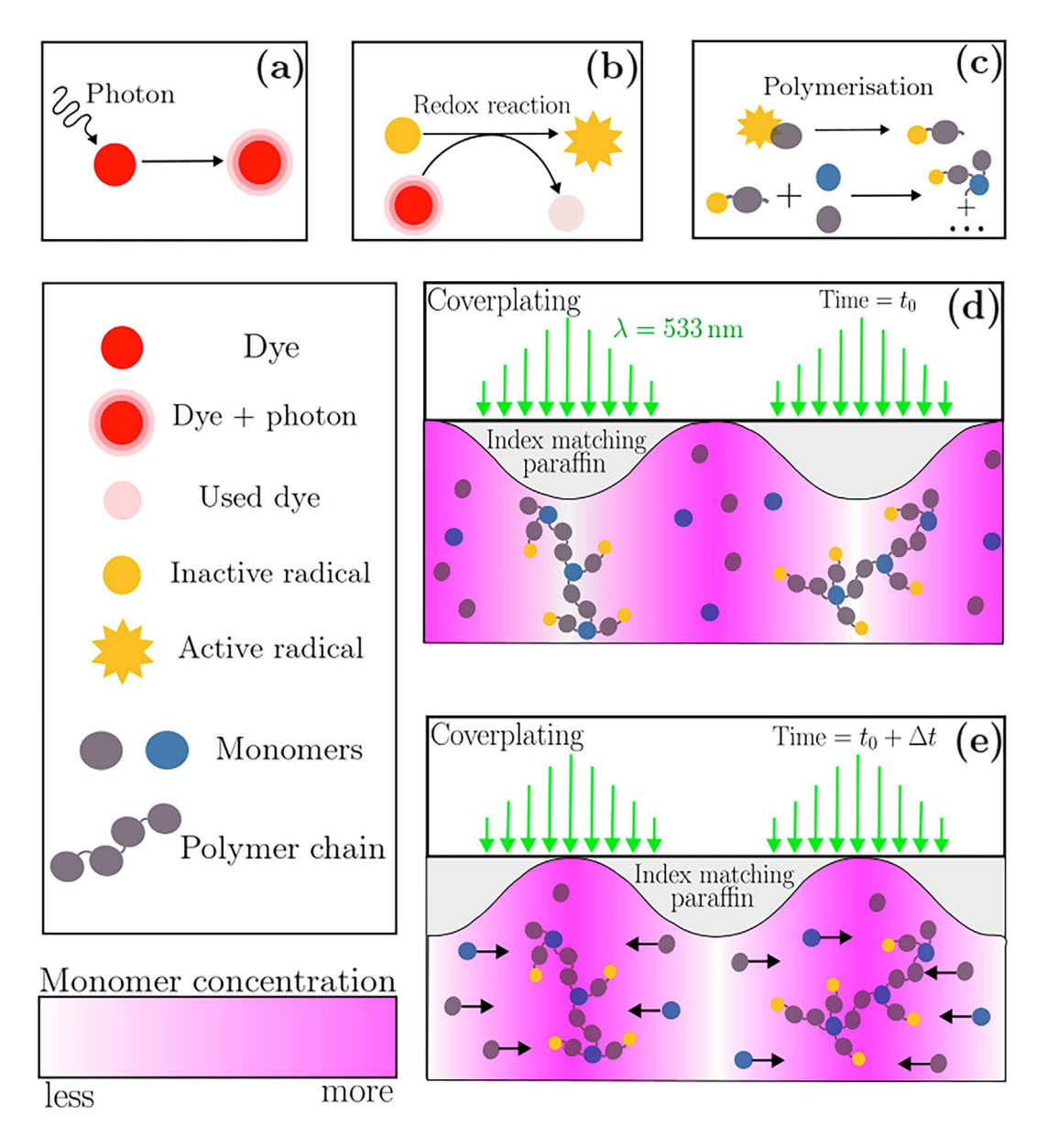


Fig. 2. Schematic of photochemistry of photopolymerisation reaction. (a) The dye absorbs a photon from the incident light with wavelength $\lambda = 533\,\mathrm{nm}$. (b) Through a redox reaction the dye transfers its energy to the initiator, thereby activating it. (c) The photopolymerisation is initiated when the activated radical generator binds to a monomer. The generation of radicals is propagated along the chain to form a polymer chain [21]. (d) At t_0 the photopolymerisation reaction forms a dense mesh in the illuminated areas causing shrinkage. A monomer gradient forms. (e) After a certain exposure time, $t_0 + \Delta t$, diffusion of monomers cause the illuminated areas to swell, as it is presented in [22]. An index matching liquid evens out the surface relief.

due to the addition of Yellowish Eosine (YE). Subsequently, the next step involves depositing the PVA/AA solution onto glass substrates of $6.5 \times 2.6~\rm cm^2$, typically employing a volume of 1500 µl to achieve a thickness ranging from 100 to 130 µm. The drying process typically requires an operational window with a temperature of 24°C and a humidity of 60%. It is necessary to ensure that this deposition is conducted on a flat levelled surface to minimize thickness variations across the sample. Furthermore, it is essential to allow water vapor dissipation from the sample, avoiding complete enclosure during the drying process. Regarding the polymerisation reaction, there are two

distinct mechanisms to induce phase modulation within the photopolymer. These mechanisms involve either alterations in surface height (thickness) or modulation of refractive indices. To minimize thickness variation an "index matching system" is implemented. A brief scheme of this system is presented in Figure 3. This system entails the utilization of a liquid paraffin with a refractive index of $n_h = 1.4679$, closely matching that of the compounds present in the PVA/AA photopolymer solution. Additionally, a coverplate is employed to physically restricting the surface. This system affords us the capability to maintain a consistent photopolymer thickness, and preserve the

Table 1. Formula used for elaborating the photopolymeric solution to recording DOEs.

Composition of the liquid solution of PVA/AA based photopolymer					
Compounds	pure TEA	PVA (8% w/v)	YE (0.8% w/v)	BMA	TEA & AA
Proportion	200 μl	10 ml	280 µl	100 mg	1400 μl

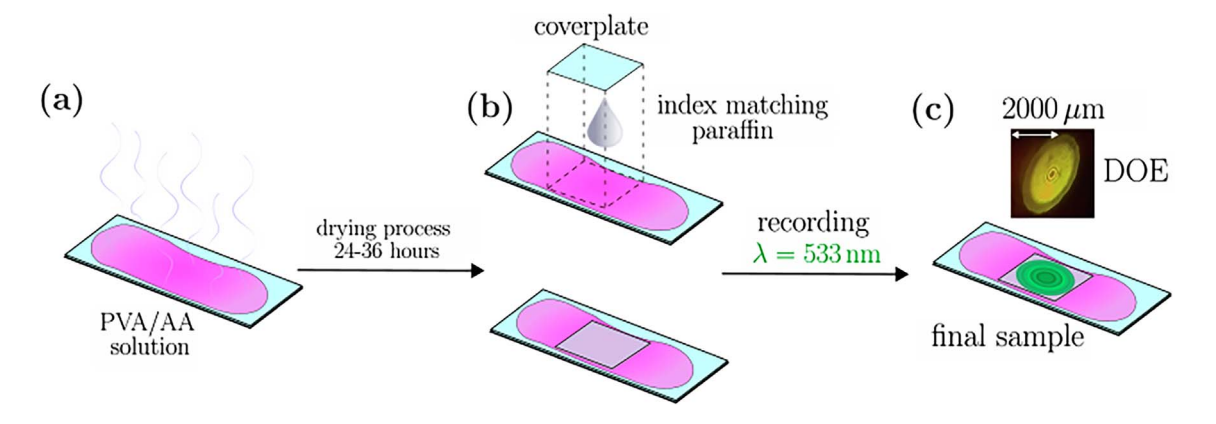


Fig. 3. Schematic of index-matching system. (a) after 24 hours of drying, paraffin and coverplate glass are put over the PVA/AA sample. (b) The final sample is ready to be placed into the experimental setup presented in Figure 4. (c) Fibonacci lens about 2000 μ m of radius is recorded into the sample.

recorded DOE, while ensuring that phase modulation is contingent solely upon refractive index modulation.

3.2 Set-up used for recording FL

Figure 4 represents the scheme of the set-up used, which includes a spatial light modulator (SLM) based on liquid crystal on silicon (LCoS) to generate FL patterns working in amplitude mode. In this set-up, we can distinguish two distinct arms. The recording arm is formed by the green beam provided by a 533 nm laser. This recording light is directed towards the SLM based on LCoS which has a resolution of 1920×1080 px² and a 8 µm pixel pitch. Two Linear Polarizers (LP) are used in $+45^{\circ}$ and -45° to linearly polarize the green beam since the SLM operates in amplitude-only mode. After modulating the recording beam, a 4F system is used to reproduce the image in the PVA/AA sample. This enable us to adjust the final magnification of the recorded lenses. This takes importance in the diffraction efficiency, since the resolution of the white and black rings are crucial for the correct formation of the multifocal phase lens. In our work, we employed a 2:3 image scale by using lenses L4 and L3. Thus, reducing the size of the image enables the recording of higher spatial frequencies. Therefore, lenses with shorter focal lengths can be recorded compared to previous works [8]. The other arm utilizes a laser with a wavelength of 632 nm for the readout process. Thanks to a red filter (RF), only the light from the reading can reaches the CCD camera positioned on an axial scanning platform, which is used to locate the two focal points of a FL. The use of a CCD camera enables us to acquire detailed information about the diffraction pattern at each step along the axial platform with high resolution. On the other hand, the use of diaphragm D3 enables us to filter high frequencies and speckles. The final resolution of the lens depends on the diameter of the diaphragm, the alignment of the recording and read-out beams, and the lens aperture. Regarding the diaphragm size, diameters smaller than 0.6 cm adversely affect the final diffraction pattern recorded by the lens.

4 Results and discussion

We choose Fibonacci lenses for their complexity and practical applications to test the model's accuracy. We simulated the recording of a FL profile after 150 s of exposure time and a material with a thickness of $d=100~\mu m$. As it is shown in [11], FL produce two focal points. To validate this, an analysis will be conducted on the variation of axial intensity distribution, considering the influence of the factor γ from equation (4).

4.1 Comparison between experimental and numerical results

Once the FL intensity pattern, shown in Figure 1, is projected onto the photopolymeric material, the diffusion process begins. This leads to a modulation of the refractive index during the exposure time in the sample section (Figure 5a). The use of a 4F system for forming images of these lenses in the material plane implies a non-ideal formation. The resolution of the optical system is affected by the use of a diaphragm between the lenses, as well as the size

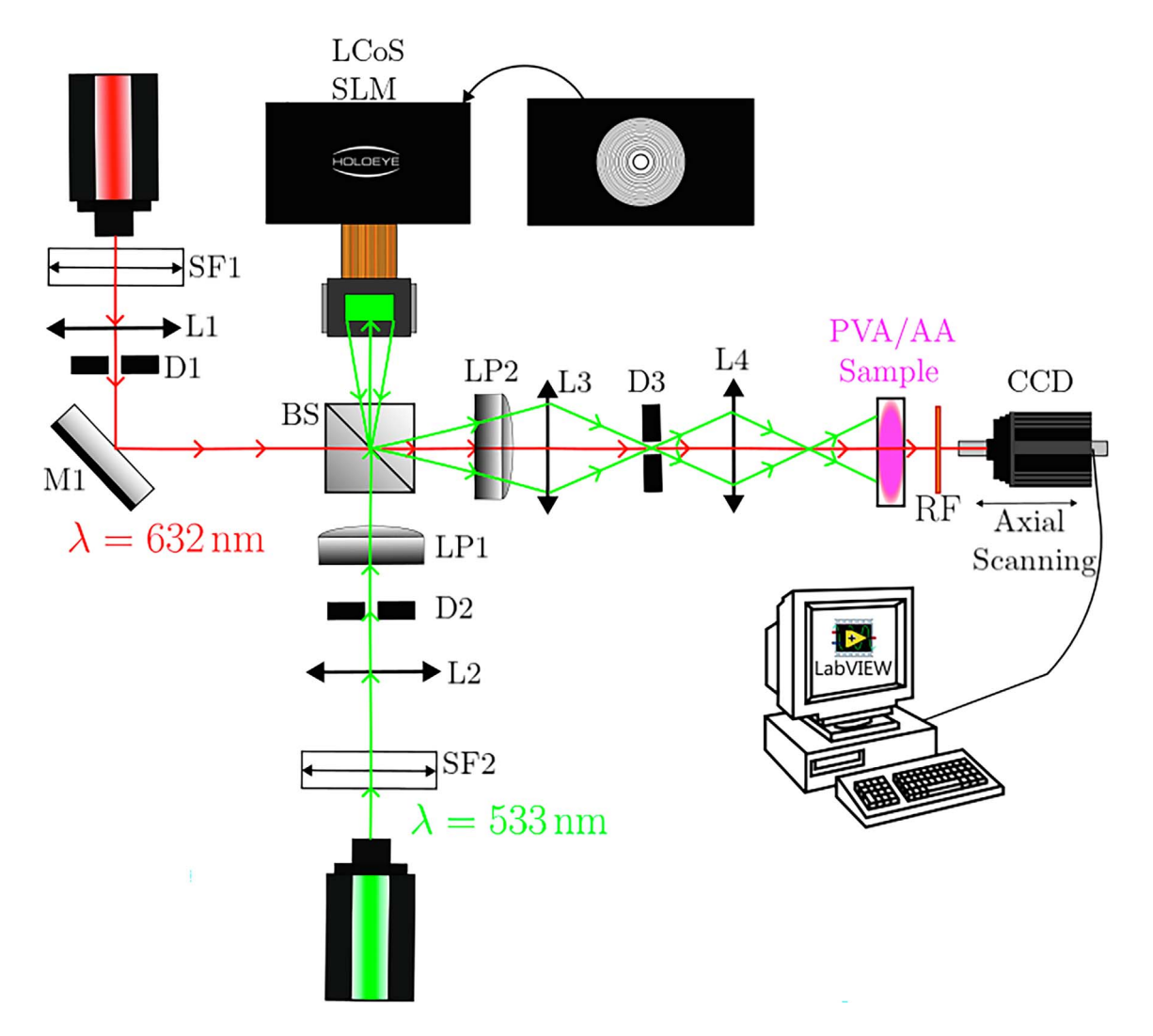


Fig. 4. Set-up used to record FL and to analyze in real time the formation and the different focal points. Where D is a diaphragm, L denotes a lens, SF is a spatial filter, BS is a beam splitter, M is a mirror, LP is a linear polarizer, and RF is a red filter.

and numerical aperture of the lenses themselves. These optical components act as a low-pass filter, eliminating the higher spatial frequencies. This has a direct result on the modulation of the refractive index of the lens, as shown in Figure 5b). Therefore, the refractive index modulation profile is smoothed in the areas where more gradient exists.

Once the refractive index modulation, $n(\zeta)$, has been obtained, a plane wave is propagated through the material to simulate its reconstruction. The axial irradiance distribution produced by an FL and its associated Fresnel Zone Plate (FZP) can be calculated with the Fresnel-Kirchhoff integral:

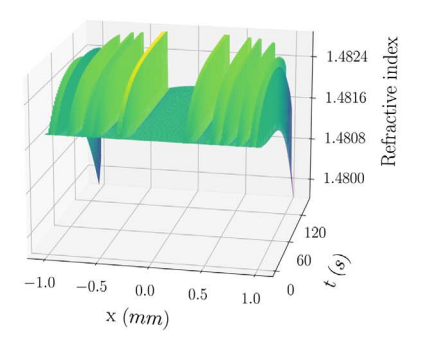
$$I(u) = 4\pi^2 u^2 \left| \int_0^1 \exp\left(-i2\pi u\zeta\right) \exp\left(\frac{i2\pi n(\zeta)d}{\lambda}\right) d\zeta \right|^2$$
(14)

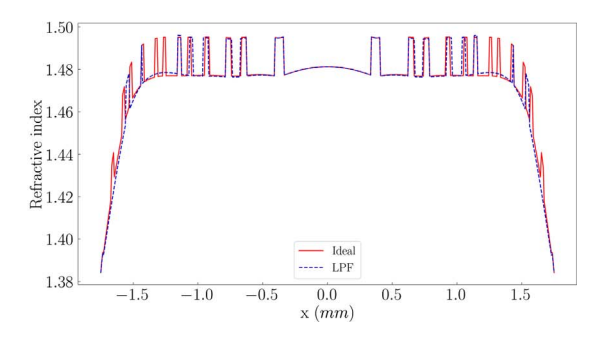
Where $u=a^2/2\lambda z$ is the axial reduced coordinate, $\lambda=632$ nm, $2\pi n(\zeta)d/\lambda$ is equal to the phase change $\Delta \varphi$ in equation (11), z the axial distance from the material and ζ is the input plane spatial coordinate. Figure 6 presents a heat map representing the intensity distribution for a transverse

cross section of the area close to the Fibonacci lens. The relationship between the two focal points is given by $f_1/f_2 = F_n/F_{n-1} \approx \varphi$. Therefore, foci approaches the axial positions $f_1 = a^2/2\lambda F_8 = 11.52$ cm and $f_2 = a^2/2\lambda F_9 = 7.11$ cm. Moreover, the farther focal point is broader than the close one, as predicted in [11]. In addition to this, the broadening relation shows that the far focil lobe, in f_1 , is φ^2 times broader than the second lobe in f_2 .

This result is also obtained using the diffusion model, and the main difference between the curves lies in the decrease of the intensity of the shortest focal point f_2 . This decrease is due to the low-pass filtering of the 4F configuration. The higher spatial frequencies disappear and affect the intensity and energy of the lowest focal point, f_2 . Furthermore, it is important to note that the proposed diffusion model aims to accurately simulate the real photopolymerization process, thus revealing the fundamental properties of a Fibonacci lens.

The experimental data, presented in Figure 6, were obtained using a 12.3-megapixel color camera with a CMOS sensor. We were able to observe the formation of the focal





(a) Refractive index modulation of an ideal FL. (b) Low-pass filtering effect on refractive index modulation.

Fig. 5. In (a), the refractive index modulation due to the diffusion process during the recording of the FL phase into the photopolymer is represented. Therefore, in (b), a refractive index modulation slice is represented for the ideal lens and low-pass filtering. Red and blue curves represent the ideal refractive index modulation and low-pass effect, respectively.

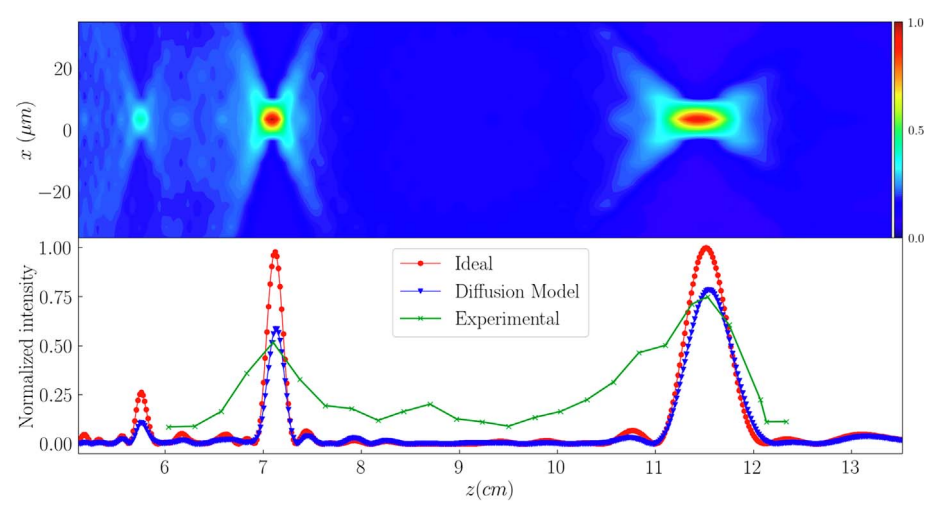


Fig. 6. Evolution of the axial and transverse intensity distribution for a $\Phi_9(\zeta)$ Fibonacci Lens with a radius of a = 1.75 mm and the result obtained using the proposed diffusion model and the experimental results. Heat map plot corresponds to the intensity distribution of an ideal FL.

points in real-time while recording the lens. At each time step, corresponding to each spatial step of the linear stage on which the camera is positioned, we computed the average intensity of diffracted light at the center of the lens. However, experimentally the intensity maximums are not as sharp as the numerical results due to the small relative transverse width of the foci. This transverse width is around 10 microns in diameter, see heat map in Figure 6, which affects the average intensity calculation. Nevertheless, both focal points can be located. The blue line, labeled as Diffusion Model, in Figure 6 is the result obtained in equation (14) after numerically determining the average refractive index. The red dotted line, labeled as *Ideal*, corresponds to the diffraction pattern with Fresnel-Kirchhoff integral but using the Fibonacci phase function (13) instead of the phase change due to refractive index modulation from equation (11).

We observed that both experimental focal points fall within the range predicted by the diffusion model and the ideal result. Furthermore, the ratio of the width of the longer focal point, f_1 , and the shorter focal point, f_2 , corresponds to the relationship $f_1/f_2 \approx \varphi$.

4.2 Influence of the parameter γ Lg

The parameter γ represents the non-linearity of the polymerization rate with the incident light into the material [23]. This factor relates diffusion with photopolymerization process, showing the saturation possibility of the phase modulation rate. Figure 7 shows the numerical influence of non-linearity on diffraction efficiency at each focal point for various exposure times. In Figure 8, we present the numerical results for each γ value. The focal points are clearly visible, showing for $\gamma=0.5$, the diffraction efficiency is higher than that for a linear relationship, such as $\gamma=1$. This result demonstrates that the photopolymer phase modulation depends on the exposure, which, in turn, relies on irradiance and time. The intensity of the green laser beam (532 nm) used for the recording process was 1.5 mW/cm^2 , with a diffusivity value of $D_m=2\cdot 10^{-2} \text{ }\mu\text{m}^2/\text{s}$.

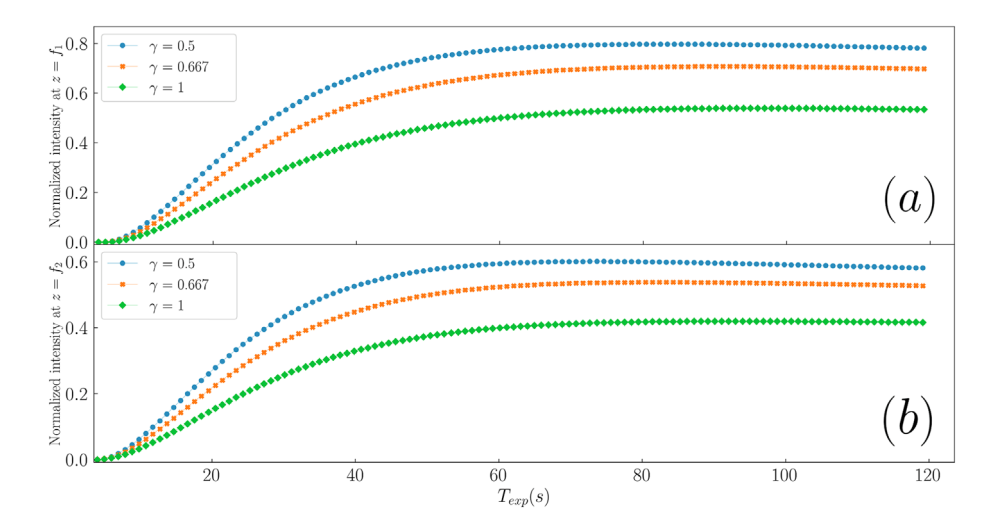


Fig. 7. Diffraction efficiency at each focal point for different values of exposure times and γ . Results obtained by the numerical diffusion model including low-pass filtering.

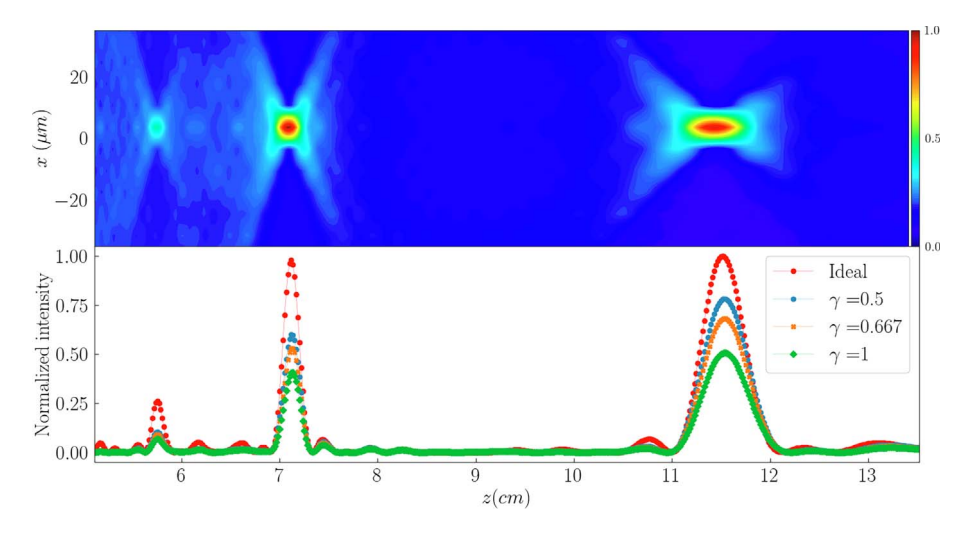


Fig. 8. Numerical simulation of the evolution of the axial and transverse numerical intensity distribution after 60 seconds of recording produced by a $\Phi_9(a=1.75 \text{ mm})$ FL for different values of γ obtained by the diffusion model and the ideal result (represented in red dotted line). The heat-map above corresponds to the simulation for $\gamma = 0.5$ for an ideal lens.

4.3 Influence of the diffusivity parameter D_m Lg

The diffusivity value of the PVA/AA photopolymer depends on several factors, including the proportions of the compounds, environmental temperature, and humidity, as studied in [24]. The mean diffusivity values fall within the range of $D_m \in [10^{-2}, 10^2]~\mu\text{m}^2/\text{s}$. Therefore, we can calculate how the diffraction efficiency of FL is affected by changes in diffusivity using the proposed model. In Figure 9, the simulated normalized intensity in each focal point is represented for different exposure times and for different values of mean photopolymer diffusivity. As it is shown, for higher values of the mean diffusivity parameter, the numerical results reach higher diffraction efficiency values

for lower exposure times. Despite this, for lower values such as $0.02~\mu\text{m}^2/\text{s}$, there are less perturbations due to there are less phase profile changes than for higher values of D_m . This distribution is due to the liquid behavior of the photopolymer [25]. When the recording media is more liquid (higher mean diffusivity), the photopolymerization process takes less time to achieve the estimated diffraction efficiency. Hence, for lower values of mean diffusivity, the axial irradiance distribution decreases in general terms because the diffusion process has not yet completed. So, these numerical simulations allow us to fit the exposure time of recording this lenses for achieving higher diffraction efficiency. Showing that only 60 seconds of recording for an irradiance of $I_0 = 1.5~\text{mW/cm}^2$ is enough to obtain higher diffraction

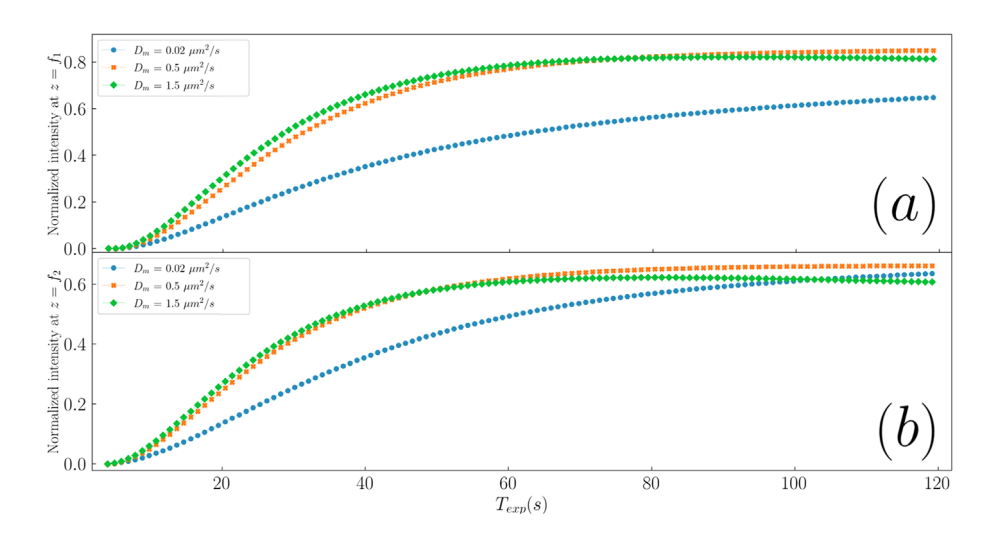


Fig. 9. Numerical simulation of the intensity distribution at each focal point produced by a FL for different exposure times and for different values of D_m with low-pass filtering. The intensity pattern of the FL used was $\Phi_9(a = 1.75 \text{ mm})$.

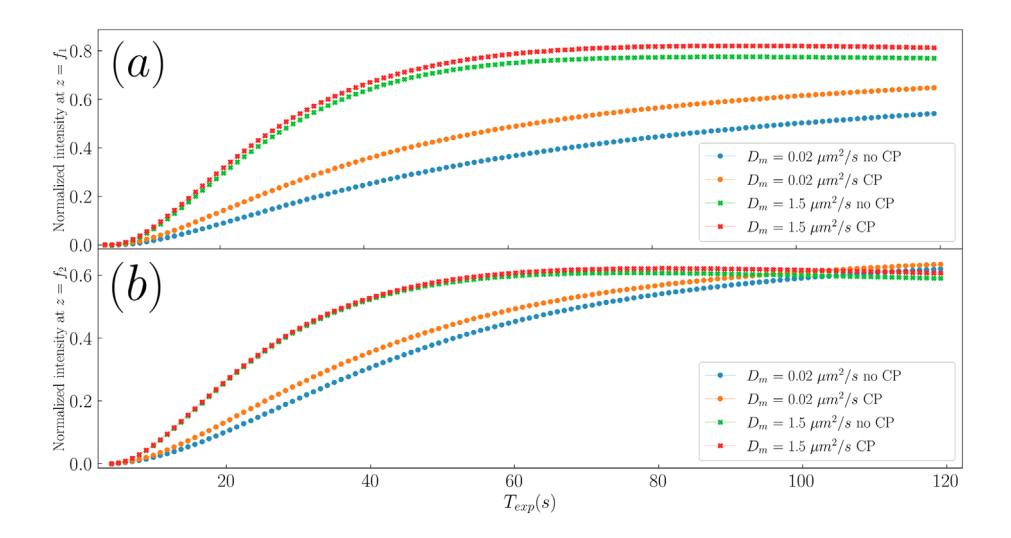


Fig. 10. Evolution of the diffracted intensity at each focal point for a FL with $\Phi_9(a=1.75\,\mathrm{mm})$. Each curve corresponds to a different value of mean diffusivity, D_m , with low-pass filtering, and with or without coverplating. The label "no CP" in the green and blue dotted curves indicate the cases where coverplating technique was not used.

efficiencies for higher diffusivities; around 80% for the large focal lenght, f_1 , (9(a)). Approximately 60% diffraction efficiency is achieved for the shorter, f_2 , as depicted in Figure 9(b). It is important to mention the impact of low-pass filtering, which directly influences the diffraction efficiency of the focal points. For the shorter focal point, f_2 , the diffraction efficiency is lower than the longer focal point f_1 regardless of the diffusivity. This is due to the elimination of the higher spatial frequencies with low-pass filtering. On the other hand, extending lens recording for a prolonged period of time, the diffraction efficiency reaches its maximum level for lower values of mean diffusivity, which may be slightly higher than for higher mean diffusivities. Thus, if the mean diffusivity is small and the exposure time

is long enough, the lens image can be formed more accurately and reaching higher diffraction efficiencies while avoiding overmodulation.

4.4 Influence of the coverplate

The application of coverplating and index matching techniques enables precise control over the thickness of photopolymeric material. In Figure 10, we present the numerical normalized intensity of each focal point, for f_1 (a) and for f_2 (b) as a function of exposure time, comparing results with and without the implementation of the coverplating technique. The numerical data shows that, for the same exposure time, higher diffraction efficiency can be

achieved when using lower values of the mean diffusivity parameter, D_m . This is particularly significant when using the coverplate. Consequently, these techniques take into account that, when the photopolymer's diffusivity is low, the effects of thickness variation and refractive index modulation are negligible. Furthermore, Figure 10 underscores the significance of exposure time in the case where coverplating is not employed. In general terms, the use of the index-matching technique allows us to achieve higher diffraction efficiencies with shorter exposure times in every focii. The energy distribution behavior across the exposure time is similar in both cases; however, the main difference lies in the higher diffraction efficiency achieved with the cover plating application, along with a higher mean diffusivity parameter. This behaviour can be understood through the physics of the index-matching and coverplating system. Avoiding thickness variation permits only modulation in the refractive index of the photopolymer when the incident light is recorded. Nevertheless, index-matching reduces the measured monomer diffusion by more than a factor of 10 [20]. This result is coherent when considering the rapid rates of surface recovery and monomer diffusion through the surface.

5 Conclusions

Fibonacci lenses have been recorded in PVA/AA based photopolymers. Upon obtaining theoretical results using a 3D diffusion model with low-pass filtering of the amplitude image of these lenses, a value for γ can be proposed. This value is established by relating the recording intensity to the polymerisation rate. Accordingly, lower values of γ yield higher diffraction efficiencies, which explains the correlation between exposure and phase modulation. On the other hand, it is crucial to emphasize the significance of employing index matching and coverplating techniques. Particularly, for lower mean diffusivity values, these techniques carry great importance to achieve higher diffraction efficiency within reduced exposure times. Nevertheless, when considering longer exposure times in the absence of coverplating, variations in thickness become more significant. Furthermore, the experimental setup and index-matching system proposed enable us to efficiently mass-produce and preserve these types of lenses. Consequently, the diffusion model has the capability to fit parameters such as exposure time, diffusivity, and recording light intensity, thus yielding results similar to experimental findings. Another conclusion drawn from this work is the predictive capability of the model when studying the diffraction efficiency of the focal points. Incorporating the low-pass filtering intrinsic to the experimental optical system into the model allows us to obtain significantly more realistic results. The elimination of higher spatial frequencies has a direct effect on the energy distribution of the diffracted light. Thus, distributing more energy to the longest focal point than to the shortest one, in line with what was obtained experimentally for a Fibonacci lens.

To sump up, the experimental results obtained clearly show the bifocal behaviour of these lenses in spite of the narrow diffracted light spot. It should be noted that the 3D model does not simulate perfect illumination. This is

due to the consideration of a low-pass filtering in the amplitude image to replicate the effect of the experimental setup. Therefore, resulting in the observed intensity distributions of the two focal points in both experimental and simulated data.

This study represents an ongoing experimental investigation with a significant potential. Bifocal diffractive lenses have a broad spectrum of applications in various fields, such as ophthalmology and X-ray microscopy. For example, in the field of ophthalmology, Fibonacci lenses can be used as intraocular progressive lenses to effectively manage presbyopia in patients.

Funding

Funded by the "Generalitat Valenciana" (Spain) (IDIFEDER/2021/014, cofunded by EU through FEDER Programme; PRO-METEO/2021/006 and INVEST/2022/419 financed by Next Generation EU), "Ministerio de Ciencia e Innovación" (Spain) (PID2021-123124OB-I00 and PID2019-106601RB-I00).

Conflicts of interest

The authors declare that they have no known competing financial interests or personal relationships that could have appeared to influence the work reported in this paper.

Data availability statement

The data that support the findings of this study are available from the corresponding author upon reasonable request.

Author contribution statement

Following the taxonomy of CRediT, the contributions of each author are as follows:

- J. C. Bravo contributed to the conceptualization, formal analysis, investigation, methodology, resources, software development, data curation, visualization, and writing of the original draft as well as the review and editing of the manuscript.
- J. J. Sirvent-Verdù participated in the conceptualization, formal analysis, investigation, and visualization.
- ${\bf J}.$ C. García-Vázquez was responsible for data curation and visualization.
- A. Pérez-Bernabeu also handled data curation and visualization.
- J. Colomina-Martínez contributed to the conceptualization, formal analysis, software development, and visualization.
- R. Fernández was involved in project administration, conceptualization, investigation, resources, supervision, validation, and visualization.
- A. Márquez focused on funding acquisition, investigation, resources, supervision, validation, and visualization.
- S. Gallego was responsible for funding acquisition, project administration, conceptualization, investigation, methodology, resources, supervision, validation, and visualization.

References

- 1 Kazanskiv N. (2018) Opt. Tec. Tel. 10774, 206.
- 2 Rossi M., Kunz R., Herzig H.P. (1995) Appl. Opt. 34, 5996.
- 3 Kim H., Hwang J.K., Jung M., Choi J., Kang H.W. (2020) Biomed. Opt. Exp. 11, 7286.

- 4 Huang Q., Wang J., Quan B., Zhang Q., Zhang D., Li D., Meng Q., Pan L., Wang Y., Yang G. (2013) Appl. Opt. 52, 2312.
- 5 Lawrence J., O'Neill F. (2001) J. Sheridan. Optik. 112, 449.
- 6 Fernández R., Gallego S., Márquez A., Navarro-Fuster V., Beléndez A. (2016) Materials. 9, 195.
- 7 Bowley C., Crawford G. (2000) Appl. Phys. Lett. **76**, 2235.
- 8 R. Fernández, S. Gallego Rico, A. Márquez, J. Francés, C. Neipp, D. Puerto, E.M. Calzado, I. Pascual Villalobos, A. Beléndez. Proc. SPIE. 11367: 113671E (49) (2020).
- 9 Fernández R., Gallego S., Márquez A., Neipp C., Calzado E., Francés J., Morales-Vidal M., Beléndez A. (2019) *Polymers*. 11, 1920.
- 10 Kelly J.V., O'Neill F.T., Sheridan J.T., Neipp C., Gallego S., Ortuño M. (2005) J. Opt. Soc. Am. B 22, 407.
- 11 Monsoriu J.A., Calatayud A., Remon L., Furlan W.D., Saavedra G., Andrés P. (2013) IEEE Photonics J. 5, 3400106.
- 12 Ferrando V., Calatayud A., Andrés P., Torroba R., Furlan W.D., Monsoriu J.A. (2014) *IEEE Photonics J.* **6**, 1.
- 13 Calatayud A., Ferrando V., Remón L., Furlan W.D., J.A. (2013) Monsoriu, Opt. Exp. 21, 10234.
- 14 Cheng S., Liu M., Xia T., Tao S. (2018) Laser Phys. 28.
- 15 Ke J., Zhang J. (2016) Opt. Commun. 368, 34.

- 16 Fernández R., Gallego S., Márquez A., Francés J., Martínez F., Pascual I., Beléndez A. (2018) Opt. Mater. 76, 295.
- 17 Infusino M., De Luca A., Barna V., Caputo R., Umeton C. (2012) Opt. Exp. 20, 23138.
- 18 G. Lazarev, P.J. Chen, J. Strauss, N. Fontaine, A. Forbes, Opt. Exp. (2019).
- 19 Yzuel M.J., Campos J., Márquez A., Escalera J.C., Davis J. A., Iemmi C., Ledesma S. (2000) Appl. Opt. 39, 6034.
- 20 Gallego S., Fernández R., Márquez A., Ortuño M., Neipp C., Gleeson M.R., Sheridan J.T., Beléndez A. (2015) Opt. Lett. 40, 3221.
- 21 Weiser M., Bruder F., Fäcke T., Hönel D., Jurbergs D., Rölle T. (2010) Macromol. Symposia 296, 133.
- 22 Wu D., Huang Y., Zhang Q., Wang P., Pei Y., Zhao Z., Fang D. (2022) Journal of the Mechanics and Phys, *Solids* 162.
- 23 Gallego S., Márquez A., Guardiola F.J., Riquelme M., Fernández R., Pascual I., Beléndez A. (2013) Opt. Exp. 21, 10995.
- 24 Gallego S., Márquez A., Ortuño M., Francés J., Marini S., Beléndez A., Pascual I. (2011) Opt. Exp. 19, 10896.
- 25 Close C.E., Gleeson M., Mooney D.A., Sheridan J.T. (2011) JOSA B. 28, 842.

J. Eur. Opt. Society-Rapid Publ. 2024, $\bf 20,\,41$ © The Author(s), published by EDP Sciences, 2024

 $\rm https://doi.org/10.1051/jeos/2024034$

Available online at: https://jeos.edpsciences.org

EOSAM 2023

Guest editors: Patricia Segonds, Guy Millot and Bertrand Kibler

RESEARCH ARTICLE OPEN 3 ACCESS

Temperature dependence of LiTaO₃ refractive index: Corrections of Sellmeier equation

Safia Mohand Ousaid^{1,*}, Kai H. Chang^{1,2}, Lung H. Peng², and Azzedine Boudrioua¹

Received 31 January 2024 / Accepted 22 July 2024

Abstract. We report a new and more precise Sellmeier equation obtained by using the analysis of quasi-phase-matching curves of the optical parametric generation (OPG) in 1D periodically poled LiTaO₃ (1D-PPLT) of different grating periods.

Keywords: Sellmeier equation, Lithium tantalate, Nonlinear photonic crystals, Nonlinear optics.

1 Introduction

Lithium tantalate (LiTaO₃) possesses unique electro- optical, pyroelectric and piezoelectric properties combined with good mechanical and chemical stability, a high optical damage threshold [1], high resistance to photo-refractive effects, high non-linear coefficients [2], and a broad transparency range spanning from 280 to 5500 nm allowing for frequency conversion ranging from UV to infrared [3, 4]. These characteristics render it highly suitable for numerous applications, particularly in the field of nonlinear optics, makes it a very interesting material for the realization of non-linear periodically polarized components [5] including electro-optical modulators, pyroelectric detectors, optical waveguides and SAW substrates, piezoelectric transducers, etc. [6, 7].

LiTaO₃ is a nonlinear positive uniaxial crystal with low birefringence and belongs to the 3 m (C_{3V}) trigonal crystal-lographic group [8]. The elements of its second-order tensor $\chi^{(2)}$ allow for three more types of nonlinear interactions: o-oo (d_{22} , d_{21} , d_{16}), e-oo (d_{31} , d_{32}), and o-eo (d_{24} , d_{15}) [8]. Because of the highest nonlinear susceptibility tensor element $d_{33} \sim 16$ pm/V, the most commonly used nonlinear interaction is e-ee, where an extraordinary wave generates two other extraordinary waves. In addition, for these interactions, only the extraordinary index is needed [9].

Accurate knowledge of the dispersion of the extraordinary refractive index is crucial for designing frequency conversion devices as well as interpreting experimental results of nonlinear interactions. Typically, an accuracy exceeding 10^{-4} of the refractive index is needed to correctly predict phase matching terms of frequency conversion processes [8].

Various techniques are employed to measure refractive index variations [10]: spectrophotometry, ellipsometry, mlines, and minimum deviation can yield measurements with accuracies ranging from ± 0.05 to $\pm 10^{-3}$.

Besides, directly deducing the Sellmeier equation from experimental phase matching curves [11] offer an accuracy greater than 10^{-4} and makes this technique highly effective.

Different processes are reported such as the sphere method developed by Boulanger $et\ al.\ [11].$

Another method is to deduce the Sellmeier equation from the curves of the quasi-phase matching obtained by characterizing samples of several periods by varying the pump wavelength [12] or varying the temperature [13–15]. Indeed, a simultaneous interpolation of all the quasi-phase matching curves measured, allows to fit all the coefficients of the Sellmeier equation and thus, to find out a very precise index dispersion of the crystal studied [5, 11]. It should be noted that LiTaO₃ exists under different types: stoichiometric (SLT), congruent (CLT), and doped stoichiometric. Several investigations have reported the Sellmeier equation for the various lithium tantalate types. However, as far as our knowledge extends, only three versions of the Sellmeier equation have been reported in the literature specifically for the CLT type [13–15]. In 1996, Abedin et al. [13] defined the Sellmeier equation of LiTaO₃-CLT using the experimental measurement. Then, Mayen et al. [14] and Bruner et al. [15] derived this equation from the phase matching curves.

While the existing studies [13-15] concern the entire transparency range of LiTaO₃ and cover a sufficient temperature interval, we recently showed a significant discrepancy between these different Sellmeier equations and theoretical and experimental measurements, as well. Moreover, when encountering several nonlinear phenomena

¹ Laboratoire de Physique des Lasers, CNRS UMR 7538, Université Sorbonne Paris Nord, 99 avenue JB Clément, 93430 Villetaneuse, France

² Graduate Institute of Photonics and Optoelectronics, GIPO, National Taiwan University, No. 1 Sec 4 Roosevelt Rd., Taipei 106, Taiwan

^{*} Corresponding author: safia.mohandousaid@univ-paris13.fr

in the same sample, especially at high power pumping, the interpretation using these established Sellmeier equations proved challenging [16].

In this work, we propose a novel and more accurate Sellmeier equation derived from quasi-phase-matching curves obtained from the investigation of optical parametric generation (OPG) in 1D periodically poled $LiTaO_3$ (1D-PPLT) crystals with varying periods.

Sellmeier equation which contains the dependence of the refractive index on temperature is essential to consider thermos-optics effect when developing functional optical systems, particularly in applications where stability and control of optical properties are crucial, such as frequency generation devices, sensors, and stabilized lasers.

2 Experimental procedure and method

In order to study the optical parametric generation (OPG) process in PPLT crystals, we used the experimental setup, which its simplified scheme is depicted in Figure 1.

We used the one dimension periodically poled LiTaO₃ (1D-PPLT) nonlinear photonic crystals fabricated by the electric poling technique [17]. The investigated grating periods Λ include 8.08 µm, 8.29 µm, 8.43 µm, 8.52 µm and 12 µm. The filling ratio is 50%, chosen to obtain the most efficient frequency conversion [18]. The samples were made on z-cut congruent-grown LiTaO₃ with dimensions of 1.5 (W) × 2 (L) × 0.5 (thickness) cm³.

The samples are pumped by a Q-switch doubled Nd: YAG pump laser frequency doubled at 532 nm with a pulse duration of 0.5 ns. The pulse repetition rate can be adjusted from 10 Hz to 1 kHz. A half-wave plate is used to control the polarization of the pump beam, which is aligned with the PPLT z-axis in order to take advantage of the crystal largest nonlinear coefficient d_{33} . The samples are placed on a temperature controller, allowing the crystal temperature to be adjusted within a range of 40 °C to 200 °C with an accuracy of ± 0.1 °C. The optical parametric generated (OPG) beam is coupled to a 50 µm optical fiber using an optical lens followed by microscope objective. The optical fiber is connected to an optical Spectrum Analyzer (OSA, ANDO AQ6315A), which can take measurement with a spectral coverage from 350 nm to 1750 nm with a resolution between 0.05 nm and 10 nm. A 532 nm stop-band filter was used to absorb the residual output pump beam.

For each sample, we measured the corresponding OPG spectra with a resolution of 0.5 nm. The measurements were performed over a temperature range from 40 °C to 200 °C, with increments of 2 °C, and a pump energy of 15 μ J.

Subsequently, we developed a specific Matlab code capable of simultaneously fitting all the measured OPG spectral data corresponding to a temperature ranging from 40 °C to 200 °C for a give QPM period in the PPLT samples. This code is employed to derive the Sellmeier equation which, together with the grating period of the PPLT sample, fulfils the conservation of momentum for the pump, the signal, and the idler wavelength in the basic quasi phase matching (QPM)- OPG conditions as follows.

For fulfilling the law of energy conservation, the wavelengths of the pump, the signal, and the idler of λ_p , λ_s , λ_i obeys:

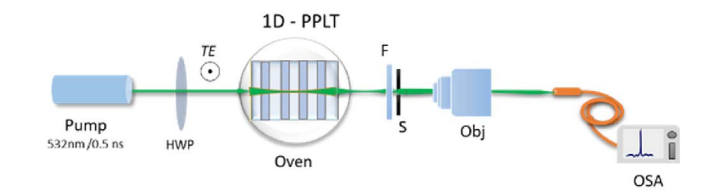


Figure 1. Scheme of the experimental setup utilized for the optical characterization of nonlinear photonic crystals.

$$\frac{1}{\lambda_n} = \frac{1}{\lambda_s} + \frac{1}{\lambda_i} \tag{1}$$

The conservation of momentum expressed by the QPM-OPG condition for a given PPLT periodicity of Λ is:

$$\frac{n_{ep}(\lambda_p, T)}{\lambda_p} - \frac{n_{es}(\lambda_s, T)}{\lambda_s} - \frac{n_{ei}(\lambda_i, T)}{\lambda_i} - \frac{m}{\Lambda(T)} = 0$$
 (2)

Where $\lambda_{p,s,i}$ denote the wavelengths of the pump, signal and idler. $n_{e,p,s,i}$ represent the extraordinary refractive indices corresponding to the pump, signal and idler, respectively. m is an integer that defines the order of the quasi-phase matching, and Λ signifies the period of the lattice.

Additionally, we consider the thermal expansion effect of the lithium tantalate lattice, as described by Y.S. Kim *et al.* [19].

$$\Lambda(T) = \Lambda(20^{\circ}\text{C})[1 + 1.6 \times 10^{-5}(T - 20^{\circ}\text{C}) + 7 \times 10^{-9}(T - 20^{\circ}\text{C})^{2}]$$
(3)

The used Sellmeier equation model is based on the formulation reported by [7, 8]:

$$n_e^2(\lambda, T) = A + \frac{B + b(T)}{\lambda^2 - (C + c(T)^2)} + \frac{E}{\lambda^2 - F^2} + D\lambda^2$$
 (4)

 $A,\ B,\ C,\ D,\ E$ and F are constant parameters, b and c are coefficients that vary with temperature. The wavelength λ is expressed in micrometers.

For determining the latter formulation, we consider the OPG-(signal, idler) wavelength data obtained from the five sets of PPLT samples of QPM periodicity Λ in 8.08 µm, 8.29 µm, 8.43 µm, 8.52 µm and 12 µm, respectively, over a temperature range from 40 to 200 °C. We, then, apply equation (4) to retrieve the corresponding coefficients from A to F for the temperature dependent Sellmeier Eq. with our Matlab coding subject to the least square method. In writing the Matlab codes to solve the Sellmeier equation, we have taken into account the QPM-OPG processes and considered the lattice thermal expansion effect [19].

3 Results and discussions

As an example, the OPG spectra, recorded at T=110 °C and a pump energy of 15 μ J for 1D-PPLT with a period $\Lambda=8.29~\mu m$ shown in Figure 2(a), reveal two peak wavelengths at (851, 1418) nm which corresponds to the signal and idler, respectively. The mapping of signal and idler

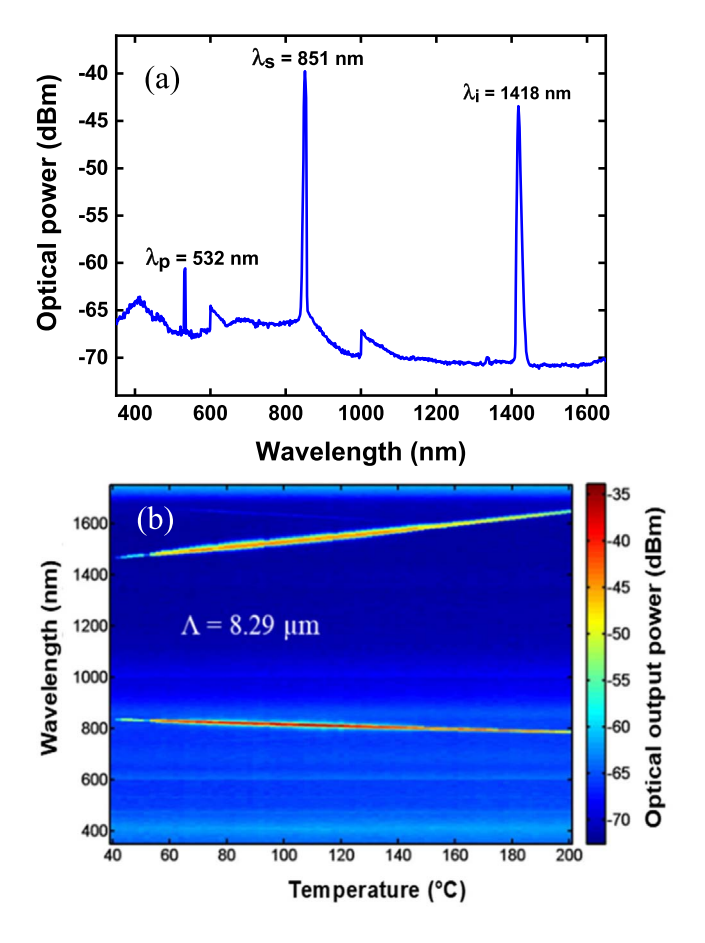


Figure 2. (a) Spectrum of the signal (851 nm) and idler (1418 nm) measured at 110 °C. (b) OPG map from 40 °C to 200 °C generated from 1D-PPLT of $\Lambda=8.29~\mu m$ at 15 μJ .

wavelengths generated by the OPG process as a function of temperature ranging from 40 °C to 200 °C are represented in Figure 2(b).

Note that for the 12 μm period PPLT sample, the spectral detection limits of the OSA prevent to record the idler waves in the mid-infrared (3 $\mu m)$ spectral regime. Thus, the corresponding idler wavelengths, between 3.355 μm and 3.67 μm , are calculated from the measured signal waves.

For instance, Figure 3. displays the variation of the signal wavelength as a function of temperature for 1D-PPLT samples of $\Lambda=8.52~\mu m$ and $\Lambda=12~\mu m$, respectively.

Our experimental data are compared to those calculated by using the three Sellmeier models already reported [13–15]. It is worth noting that similar results have been obtained in the case of the idler.

It is evident that the experimental signal wavelengths differ from those calculated by the existing formulae of Sellmeier equations cited in references [13–15]. This discrepancy is more pronounced when using the equation proposed by Abedin et al. [13], where the wavelength of OPG-signal/idler deviates significantly with the temperature increase. This variation can be attributed to the optical reflection measurement technique used to retrieve the raw refractive index data cited in [13] to define the Sellmeier equation. The divergence is less pronounced with the predictions

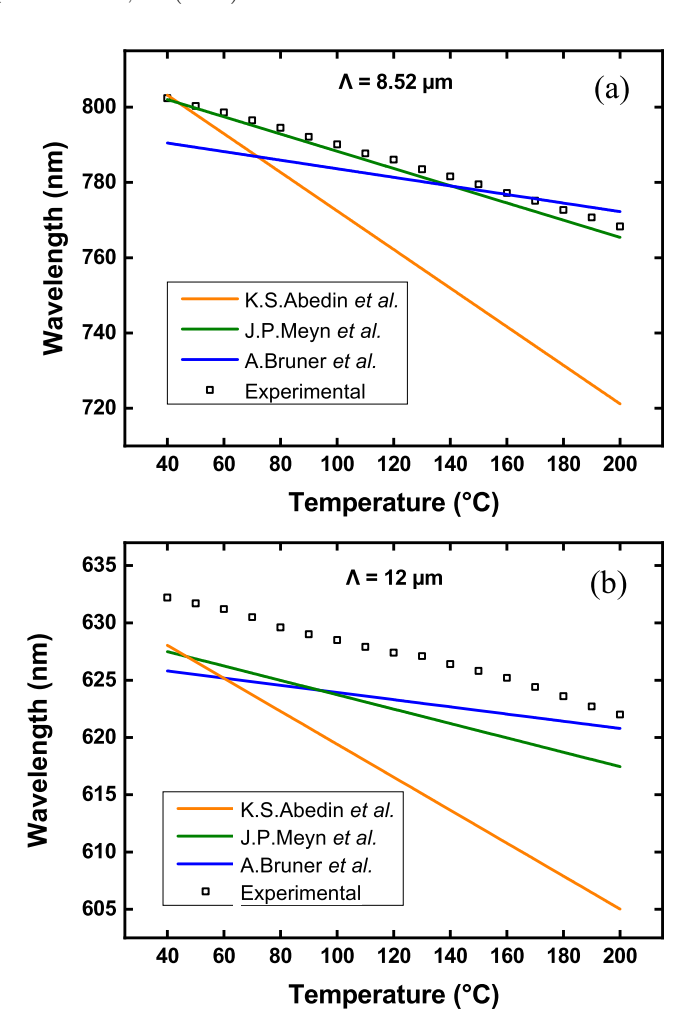


Figure 3. Signal wavelengths vs. temperature for 1D-PPLT of (a) $\Lambda=8.52~\mu m$ and (b) $\Lambda=12~\mu m$.

made by the other two variants of Sellmeier Eq. in [14] and [15].

Although the discrepancies between theoretical and experimental results may be attributed to various sources of errors, such as pump and temperature fluctuations, possible irregularities in the periodic lattice, equipment precision, and measurement errors, the observed divergences are significant and increase with the rise in temperature and period. For instance, using the equation provided by Meyn $et\ al.$, a variation of the period ranging from 0.004 μm to 0.03 μm is observed when the temperature varies from 40 °C to 200 °C for the sample of a period of 8.52 μm . A substantial deviation (0.2 μm at 200 °C) is noted for the sample with a period of 12 μm .

Again, these results emphasize the importance of precisely determining the Sellmeier coefficients.

Finally, we analyzed the results obtained from the study of the five sets of 1D-PPLT samples of QPM periodicity Λ in 8.08 μ m, 8.29 μ m, 8.43 μ m, 8.52 μ m and 12 μ m, as reported on Figure 4. for the signal (note that similar work was performed in the case of the idler, as well).

The experimental data were fitted using the same Sellmeier equation, allowing us to determine the best results

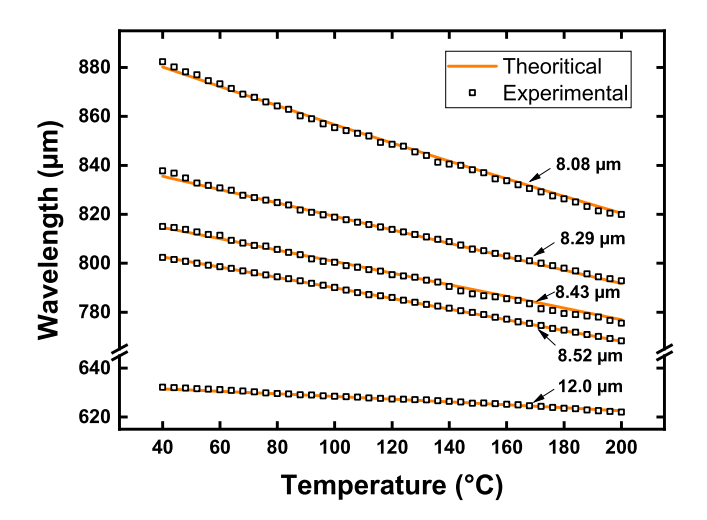


Figure 4. Theoretical (red line) and experimental Signal wavelengths (squares) as a function of the temperature for 1D-PPLT $\Lambda=8.08~\mu m,~8.29~\mu m,~8.43~\mu m,~8.52~\mu m$ and 12 $\mu m.$

Table 1. Sellmeier equation parameters verifying the QPM wavelengths over the range $0.6\text{--}3.6~\mu m$ and $40\text{--}200~^{\circ}\text{C}$.

A	4.5281
В	0.00724542
C	0.2439
D	-0.02172
E	0.07858
F	0.1835
b(t)	$2.5488 \times 10^{-8} \mathrm{T}^2$
c(t)	$1.6225 \times 10^{-8} \mathrm{T}^2$

obtained giving the new coefficients of the Sellmeier equation are as reported in Table 1.

Note that the fitting process involves both the signal and the idler. The resulting equation is valid for wavelengths between 0.6 μm and 3.6 μm and for a temperature range between 40 and 200 °C.

It is important to indicate that the above parameters have different influences. For example, unlike parameter A, a small variation in parameter B results in a significant change in n.

To confirm these results, we first conducted a comparative study between the experimental results and theoretical simulations using the new equation.

To illustrate the validity of the proposed equation, we compared the effective periods of the studied samples with those obtained from the different Sellmeier equations. Because the period is a physical property given by the fabrication procedure, we used the different equations to calculate the periods of the 5 1D-PPLT gratings studied, from the OPG measurements. The results obtained show significant divergences as indicated in Figure 5. In fact, this figure reports the difference between the calculated values and those given by the fabrication technique (named period error). However, this difference is negligible when using

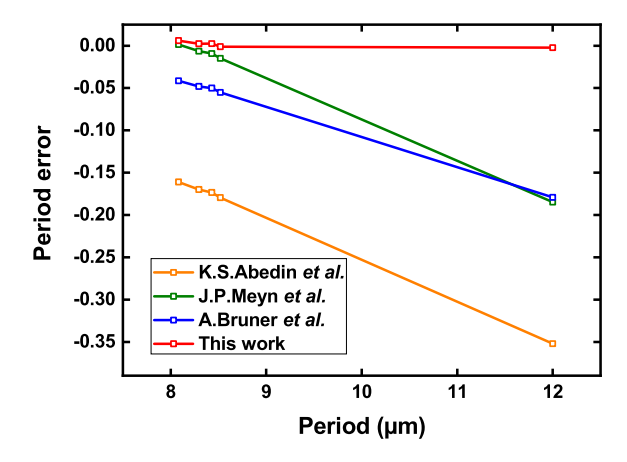


Figure 5. The period error at T = 110 °C.

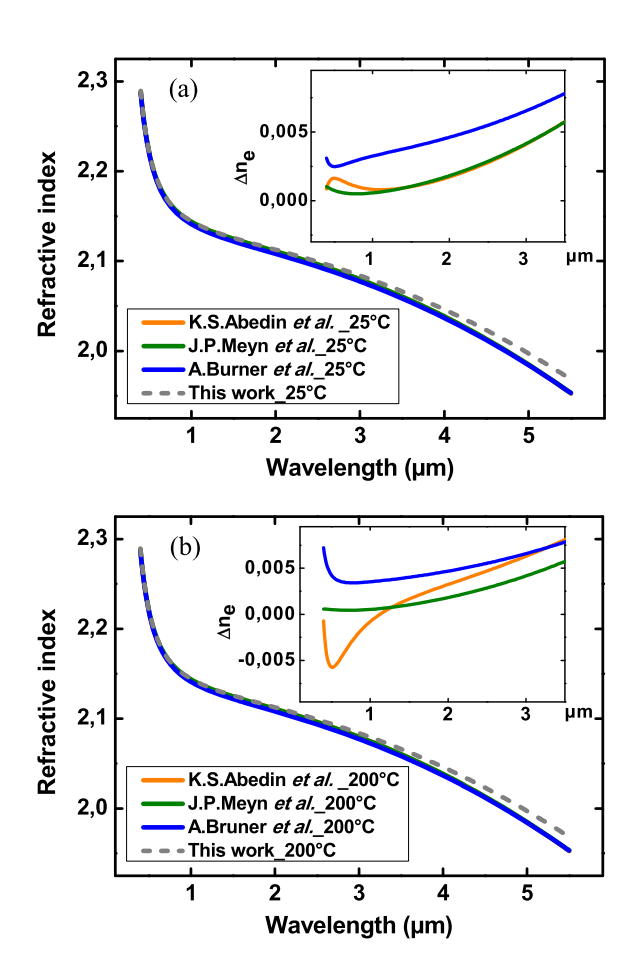


Figure 6. Comparison of the extraordinary refractive index dispersion n_e as a function of wavelength obtained using the previous Sellmeier equations and the new proposed equation. (a) $T=25~^{\circ}\mathrm{C}$ and (b) $T=200~^{\circ}\mathrm{C}$. The zooms represent the difference of refractive index values obtained with the new equation and the previous ones.

the equation that we propose in this work. This further confirms the validity of this new equation.

To go further in the analysis of the validity of our new corrected sellmeier equation related to already published ones, we present in Figure 6 the plot of dispersion curve for $n_{\rm e}$ with wavelength at room temperature and 200 °C, respectively.

Considerable deviations are observed between the refractive indices plotted using different Sellmeier equations compared to the one proposed in this work. The most significant differences are obtained with the refractive index calculated from the equation given by Bruner et al. [15], and this holds across the entire wavelength range for both $T=25~{\rm ^{\circ}C}$ and 200 ${\rm ^{\circ}C}$. At low temperatures, the difference increases with the increase of wavelength, especially for wavelengths close to the infrared region. The calculated error of the extraordinary refractive index ranges between -6.10^{-3} and 7.10^{-3} . These discrepancies are substantial enough to introduce errors in the design of optical devices.

4 Conclusion

Our exploration of optical parametric generation with respect to temperature variations in PPLT-1D crystals with various periods has enabled us to identify and present a more precise Sellmeier equation. The chosen criterion was associated with the temperature-dependent evolution of the grating periods in the samples. The refined equation provides a more accurate extraordinary refractive index for congruent lithium tantalate.

Funding

This work was supported by the Labex SEAM and the Federative Structure of Researche NAP MOAIC of the University USPN.

Conflicts of interest

We declare that we have no conflicts of interest to report.

Data availability statement

All the data used in this paper are available upon request.

Author contribution statement

Safia Mohand Ousaid performed the experimental work and the analysis of the obtained results as this is a part of her PhD project.

Kai H. Chang worked in close connection with Safia Mohand Ousaid, specially for the analysis of the results obtained.

Professors Lung Han Peng and Azzedine Boudrioua as the PhD supersivors, provided their expertise in conducting the work reported in this paper as well as in the preparation of the paper and the corrections.

References

- 1 Tangonan G.L., Barnoski M.K., Lotspeich J.F., Lee A. (1977) High optical power capabilities of Ti-diffused LiTaO₃ waveguide modulator structures, *Appl. Phys. Lett.* **30**, 238–239. https://doi.org/10.1063/1.89348.
- 2 Zhu S.N., Zhu Y.Y., Wang H.F., Zhang Z.Y., Ming N.B., Shen W.Z., Chang Y., Shen X.C. (1995) J. Phys. D Appl. Phys. 28, 2389–2391.

- 3 Chiang A.C., Huang Y.C., Fang Y.W., Chen Y.H. (2001) Compact, 220-ps visible laser employing single-pass, cascaded frequency conversion in monolithic periodically poled lithium niobate, *Opt. Lett.* **26**, 66–68. https://doi.org/10.1364/OL.26.000066.
- 4 Izumi S., Sato M., Suzuki J., Taniuchi T., Ito H. (1998) Jpn. J. Appl. Phys. Part 2 37, L1383.
- 5 Hatanaka T., Nakamura K., Taniuchi T., Ito H., Furukawa Y., Kitamura K. (2000) Quasi-phase-matched optical parametric oscillation with periodically poled stoichiometric LiTaO₃, Opt. Lett. 25, 651–653. https://doi.org/10.1364/OL.25.000651.
- 6 Hang W., Zhou L., Shimizu J., Yuan J., Yamamoton T. (2013) Study on the mechanical properties of lithium tantalate and the influence on its machinability, *Int. J. Autom. Technol.* 7, 644–653.
- 7 Eason R.W., Barry I.E., Ross G.W., Smith P.G.R., Gawith C.B.E. (2000) Proc. SPIE 4075, 124.
- 8 Boyd R.W. (2008) Nonlinear optics, 3rd ed., Academic Press, USA.
- 9 Dolev I., Ganany-Padowicz A., Gayer O., Arie A., Mangin J., Gadret G. (2009) Linear and nonlinear optical properties of MgO: LiTaO₃, *Appl. Phys. B* **96**, 423–432. https://doi.org/10.1007/s00340-009-3502-3.
- 10 Bréhault A. (2015) Ph.D. thesis, University of Rennes-France.
- 11 Segonds P., Boulanger B., Menaert B., Zaccaro J. (2008) State of the art of the sphere method, a unique characterization technique for non-linear crystals, Res. Chem. Intermed. 34, 217–228. https://doi.org/10.1163/ 156856708783623519.
- 12 Nakamura M., Higuchi S., Takekawa S., Terabe K., Furukawa Y., Kitamura K. (2002) Refractive indices in undoped and MgO-doped near-stoichiometric LiTaO₃ crystals, *Jpn. J. Appl. Phys.* **41_2**, 465–467. https://doi.org/10.1143/JJAP.41.L465.
- 13 Abedin K.S., Ito H. (1996) Temperature-dependent dispersion relation of ferroelectric lithium tantalate, J. Appl. Phys. 80, 6561–6563. https://doi.org/10.1063/1.363679.
- 14 Meyn J.-P., Fejer M.M. (1997) Tunable ultraviolet radiation by second-harmonic generation in periodically poled lithium tantalate, *Opt. Lett.* **22**, 1214–1216. https://doi.org/10.1364/OL.22.001214.
- 15 Bruner A., Eger D., Oron M.B., Blau P., Katz M., Ruschin S. (2003) Temperature-dependent Sellmeier equation for the refractive index of stoichiometric lithium tantalatehium tantalate, Opt. Lett. 28, 194–196. https://doi.org/10.1364/ol.28.000194.
- 16 Mohand Ousaid S., Chang K.-H., Chakaroun M., Billeton T., Peng L.-H., Boudrioua A. (2021) Multi-resonant forward optical parametric oscillations without external mirrors based on nonlinear photonic crystals of LiTaO₃, J. Opt. 23, 115501. https://doi.org/10.1088/2040-8986/ac2167.
- 17 Peng L.-H., Tseng Y.-P., Lin K.-L., Huang X.-Z., Huang C.-T., Kung A.-H. (2008) Depolarization field mitigated domain engineering in nickel diffused lithium tentalate, Appl. Phys. Lett. 92, 092903. https://doi.org/10.1063/1.2890728.
- 18 Arie A., Voloch N. (2010) Periodic, quasi-periodic, and random quadratic nonlinear photonic crystals, *Laser Photon. Rev.* 4, 3, 355–373. https://doi.org/10.1002/lpor.200910006.
- 19 Kim Y.S., Smith R.T. (1969) Thermal expansion of lithium tantalate and lithium niobate single crystals, *J. Appl. Phys.* **40**, 4637–4641. https://doi.org/10.1063/1.1657244.

J. Eur. Opt. Society-Rapid Publ. 2024, **20**, 3 © The Author(s), published by EDP Sciences, 2024

https://doi.org/10.1051/jeos/2024002

Available online at: https://jeos.edpsciences.org

 $EOSAM\ 2023$

Guest editors: Patricia Segonds, Guy Millot and Bertrand Kibler

RESEARCH ARTICLE OPEN 3 ACCESS

Bispectral optical cavity based on twin metamirrors

Liam Shelling Neto^{1,2,3,*}, Johannes Dickmann^{1,2,3}, Steffen Sauer^{1,2,3,4}, and Stefanie Kroker^{1,3,4}

Received 12 December 2023 / Accepted 18 January 2024

Abstract. In this work, we introduce a new bispectral optical cavity concept for which we design twin pairs of highly reflective, ultra-low noise metamirrors. Metasurfaces, artificial structures composed of periodic or quasi-periodic arrays of nanostructures, offer unprecedented control over light properties, paving the way for new applications in areas from high-precision optical metrology to quantum science. Custom phase and an ultra-high reflection coefficient make these metasurfaces an ideal candidate to surpass traditional multilayer mirrors as metamirrors in precision interferometry, particularly by also minimizing thermal noise. The focusing metamirrors designed in this study expect to reflect 99.95% and 99.96% of the incoming light at both, 1064 nm and 1550 nm wavelength. Their planar counterparts even reach theoretical reflectivities of 99.9999% (1064 nm) and 99.9995% (1550 nm). These specialized metamirrors enable bispectral low-noise optical cavities, which would reduce the number of cavities in optical experiments or could be used as a versatile transfer cavity for frequency locking.

Keywords: Metasurface, Metamirror, Optical Cavity, High-Precision Optical Metrology.

1 Introduction

High-precision optical metrology hinges on the unparalleled frequency stability provided by ultra-stable laser systems. This ability to provide minimal frequency fluctuations over time has enabled research of the most fundamental laws of nature, such as variations of the fine structure constant [1] and validation tests of special relativity [2], among others. In addition, the search for gravitational waves is intrinsically linked to the use of ultra-stable lasers in interferometry [3, 4]. Nevertheless, the bottleneck of these laser systems is the thermal noise emanating from the cavities' mirror coatings [5].

Metasurfaces, i.e. micro-structured surfaces, offer a low-noise alternative to traditional Bragg mirrors by leveraging photonic resonances as the driving mechanism to achieve unprecedented reflectivities [6–9]. Essentially, the right choice of period Λ and duty cycle f can limit the number of propagating Bloch modes to two. By then carefully changing the geometric parameters, the modes interfere constructively in reflection and destructively in transmission [10]. Such metamirrors not only shape the amplitude of incident light but also control its polarization and phase to focus light from a flat surface [11]. The latter attribute is crucial,

as stable optical cavities necessitate at least one focusing mirror [12]. Otherwise, divergence would cause the light to eventually leave the cavity after a few round-trips. It is important to note that the mirror's focal length does not restrict the cavity's length. In fact, typical ultra-stable cavities are constructed with lengths spanning several tens of centimeters [5, 13]. Our objective is to achieve longer focal lengths, which will expand the optical mode diameter, thereby reducing thermal noise [14]. Metaatoms, which constitute the metasurface, are central to these advanced functionalities [15–19].

In our prior work [11], we demonstrated the potential of a tandem neural network for the inverse design of metaatoms. Although effective, the present work proposes an alternative design methodology by utilizing a pathfinding algorithm. Pathfinding algorithms in metaatom design offer distinct advantages over deep learning, including enhanced interpretability due to their deterministic nature, and greater computational efficiency as they require less resources and no extensive training. Their simpler algorithmic structure allows for faster solution generation and easier integration of specific design constraints, e.g. reflectivity thresholds, making them particularly suitable for applications where speed, clarity, and simplicity are critical.

¹ Technical University of Braunschweig, Institute for Semiconductor Technology, Hans-Sommer-Str. 66, Braunschweig, Germany

²CAVITY technologies UG (haftungsbeschraenkt), Wilhelmsgarten 3, Braunschweig, Germany

³ Laboratory for Emerging Nanometrology (LENA), Langer Kamp 6a/b, Braunschweig, Germany

⁴ Physikalisch-Technische Bundesanstalt, Bundesallee 100, Braunschweig, Germany

^{*} Corresponding author: liam.shelling-neto@tu-braunschweig.de

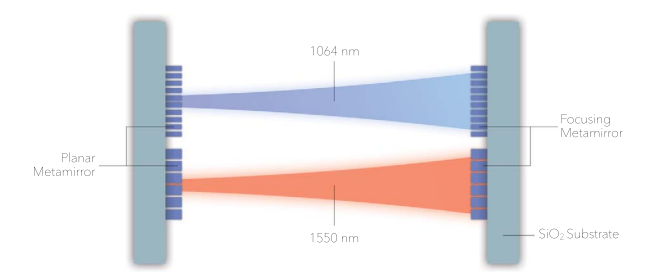


Fig. 1. Schematic of bispectral twin cavity configuration featuring two hemispherical cavities for 1064 nm and 1550 nm by utilizing dielectric metasurfaces as low-noise mirrors.

For our relatively simple metaatom designs, the utilization of pathfinding or even more rudimentary design approaches remains feasible and effective, whereas the intricacies of more complex metaatom structures necessitate the advanced capabilities of deep learning methodologies.

The main issue addressed in this work concerns the footprint of optical cavity setups. Recently, significant effort has been directed towards making optical cavities smaller and more robust [20–29]. This is aimed at reducing the footprint of experiments that require multiple optical cavities [30, 31] for enhancing their suitability for space applications [32–34] or quantum computers [35]. For instance, in the case of the latter application, a variety of laser wavelengths are crucial for qubit operations. Furthermore, the concept of a bispectral optical cavity offers the potential to transfer stability between two cavities operating at different wavelengths [31]. We begin by identifying critical parameters for each metamirror within a twin cavity configuration, as illustrated in Figure 1. Subsequently, we employ a pathfinder design strategy to create highly reflective metamirrors that focus light at the wavelengths 1064 nm and 1550 nm, suitable for bispectral optical cavities. These wavelengths are particularly suitable for bispectral optical cavities and are frequently utilized in high-precision optical metrology, such as in gravitational wave detectors [3, 36]. In the final section, we examine selected metaatoms through FEM simulations of their electric fields.

2 Setting fixed parameters

We commence by employing an amorphous Silicon (a–Si) metaatom with a cross-shape geometry with perfect periodicity atop a silicon dioxide (SiO₂) substrate, as depicted in Figure 2. The refractive indices of both materials are assumed to be $n_{\text{a-Si-1064}} = 3.536$, $n_{\text{a-Si-1550}} = 3.441$, $n_{\text{SiO2-1064}} = 1.450$, and $n_{\text{SiO2-1550}} = 1.444$ for both 1064 nm and 1550 nm, respectively. This configuration is characterized by four key parameters: L_x , L_y , h, and P. The parameters L_x and L_y are reserved for subsequent phase and amplitude modulation, while h and P are constants for both mirrors. Given that both metamirrors will share the same substrate and material composition, the structural height h is chosen to be uniform for the two target wavelengths. However, while the period P may vary between the designs of the two metamirrors, it must remain constant within each



Fig. 2. Schematic of the cross-shaped metaatom with variable lateral height h, period P, and parameters L_x and L_y . The material system is chosen to be amorphous silicon (a–Si) on Fused Silica (SiO₂).

mirror to enable the integration of various metaatoms. These individual metaatoms, each producing distinct optical responses, are assembled to create the final metamirror structure.

We utilize a Python-based Rigorous Coupled Wave Analysis (RCWA) package [37] to evaluate metaatom configurations at 1064 nm and 1550 nm with regard to their phase ϕ and reflectivity R. While a global optimization algorithm could theoretically identify suitable parameters, it poses the risk of converging to highly sensitive, narrowband solutions that tend to be vulnerable to fabrication errors. Hence, a computationally manageable parametric sweep is performed of the three parameters $h \in [0.3,0.5]$ µm, $P_{1064} \in [0.45,0.6]$ µm, and $P_{1550} \in [0.75,0.95]$ µm while keeping the metaatom shape constant. These boundaries for the period are determined following equation [38]:

$$\frac{\lambda_i}{n_{\text{sub,i}} + \sin \theta_{\text{target}}} < P_i < \frac{\lambda_i}{n_{\text{sub,i}}}, \quad i \in \{1064, 1550\}, \quad (1)$$

for the wavelength λ_i , the refractive index of the substrate $n_{\rm sub}$, and the propagation angle of the first diffraction order $\phi_{\rm target}$, i.e. 90°. Value ranges for the structure height are dictated by the effective wavelength inside the coating material:

$$\lambda_{\text{eff}, i} = \frac{\lambda_i}{n_{\text{coating, i}}}, \quad i \in \{1064, 1550\}.$$
 (2)

Here, $n_{\rm coating}$ refers to the refractive index of the mirror coating. These results are visualized in Figure 3 (top). To pinpoint the parameter zones achieving high reflectivity at both wavelengths, we impose a reflectivity threshold of 99.9%. Figure 3 (bottom) reveals a distinct zone meeting these criteria, from which we select h=395 nm, $P_{1064}=555$ nm, and $P_{1550}=893$ nm.

3 Navigating the design space

We proceed to simulate combinations of L_x , $L_y \in [0.1, 0.9]$ (normalized to P) to form a design-response dataset (see Fig. 4b), wherein each pair embodies a metaatom with respective reflectivity and phase values based on L_x and L_y . To this end, we first identify a suitable flat-phase

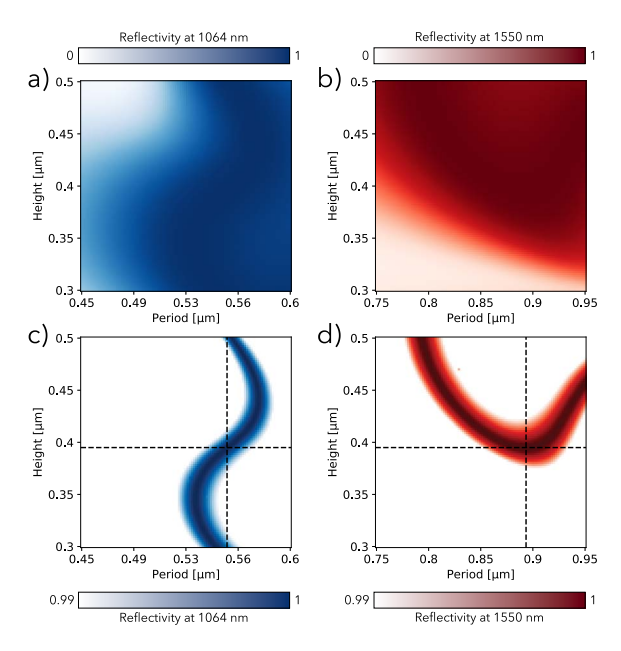


Fig. 3. RCWA simulated reflectivity for 1064 nm (left) and 1550 nm (right) of the parametric sweep of the three parameters $h \in [0.3, 0.5] \, \mu m$, $P_{1064} \in [0.45, 0.6] \, \mu m$, and $P_{1550} \in [0.75, 0.95] \, \mu m$ with a fixed metaatom cross. Top. Raw Data, Bottom. Reflectivity threshold of 99.9% applied to the data.

metaatom by focusing solely on reflectivity values at both $1064~\rm nm$ and $1550~\rm nm$, attaining theoretical reflectivities of 99.9999% for $1064~\rm nm$ and 99.9995% for $1550~\rm nm$, respectively. These two metaatom species uniformly cover the two planar metamirrors for each wavelength.

While the straightforward tactic for achieving the desired phase profile would be to cherry-pick metaatoms that fit best the target phase, this could cause abrupt changes in structural parameters, thereby breaching the periodic boundary conditions assumed during simulation. In this study, we adopt a pathfinding strategy to mitigate these neighbor coupling effects [39, 40]. The pathfinding algorithm requires suitable start- and end-points, hence, we first filter the dataset with a reflectivity threshold of 99.9%, as shown in Fig. 4a), ensuring that high-reflectivity zones are retained. Utilizing Python's scikit-image package [41], we label diagonally connected areas (see Figs. 4c, 4d) to subsequently identify the region offering the largest phase variance.

This region aids the pathfinding algorithm in optimizing phase flexibility across the metasurface, avoiding the abrupt transitions typical of a cherry-picking approach. Figure 5 shows the optimal path found by the pathfinding algorithm that will act as the ground truth data to render the whole metamirror later on.

Additionally, we implemented a metric M to quantify relative changes in the design parameters L_x and L_y of a metaatom at position i along the radial axis of the metamirror:

$$M_i = \left| \frac{L_{x_{i+1}} - L_{x_i}}{L_{x_i}} \times 100 \right| + \left| \frac{L_{y_{i+1}} - L_{y_i}}{L_{y_i}} \times 100 \right|.$$
 (3)

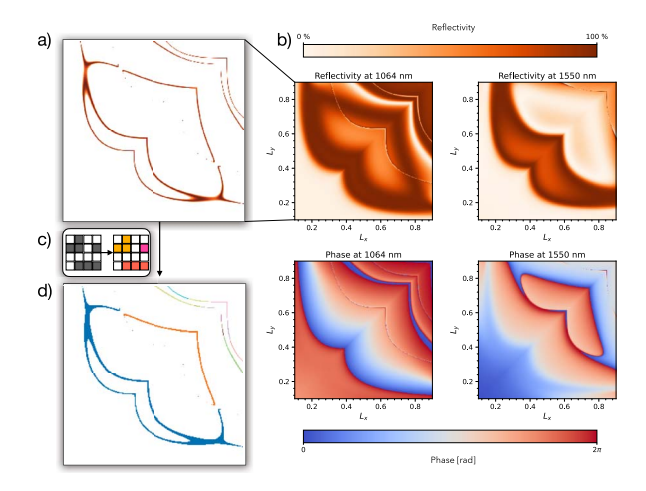


Fig. 4. a) A reflectivity threshold of 99.9% applied to the dataset. b) RCWA simulated phase and reflectivity maps for (left) 1064 nm and (right) 1550 nm. c) Scheme for labeling horizontally and diagonally connected areas. d) Color-coded high-reflectivity areas are shown for 1064 nm.

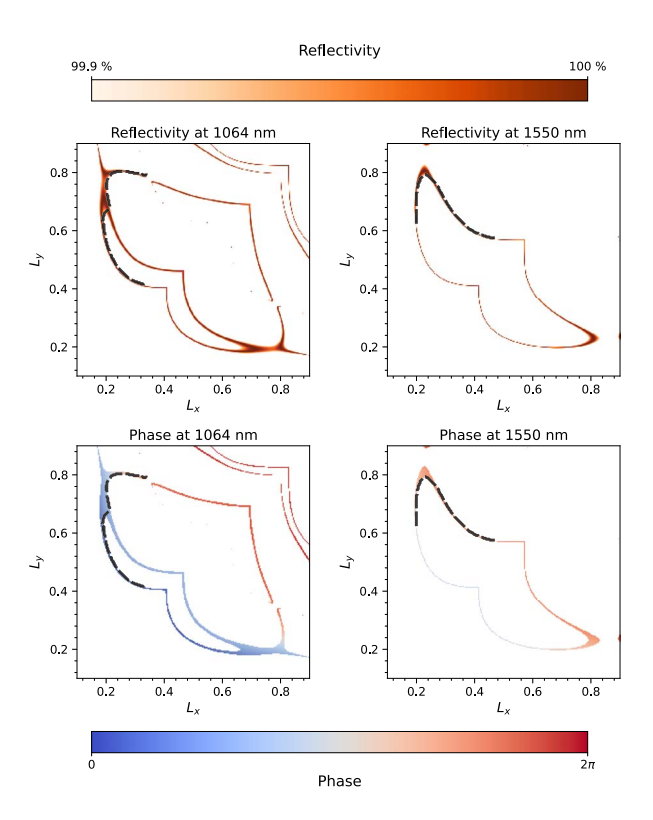


Fig. 5. Calculated phase and reflectivity maps with a threshold of 99.9% applied to the dataset. The black dotted line represents the optimal path found by the pathfinding algorithm.

Figure 6 validates the superiority of pathfinding over cherry-picking in minimizing M and therefore possible neighboring coupling effects. The phase gradient along the metamirror's diagonal is illustrated in Figure 7, emulating

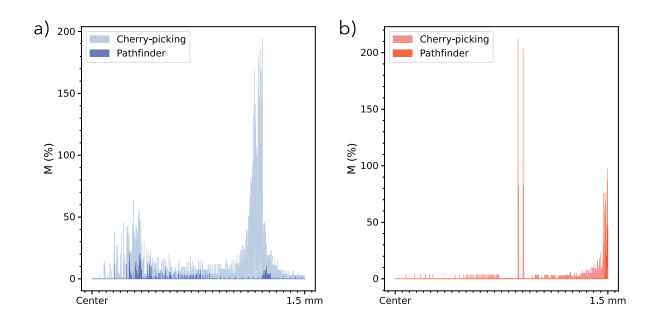


Fig. 6. Using the metric M from eq. (3) to quantify the net change in the parameters L_x and L_y for (a) 1064 nm and (b) 1550 nm.

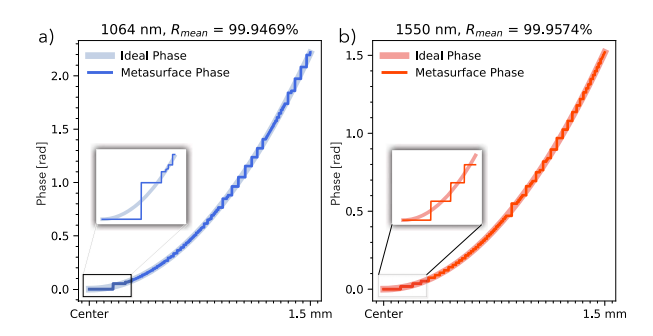


Fig. 7. Radial phase profile of the metamirror pair for a) 1064 nm and b) 1550 nm. Both mirrors yield theoretical reflectivities of > 99.9% at a size of 3×3 mm and a focal length of 6 m. The inset shows the step-wise phase profile caused by the discrete metaatoms.

a parabolic mirror of dimensions $3 \times 3 \text{ mm}^2$ and a focal length of 6 m. Despite small deviations from the optimum, the phase profile fits the ideal case of a conventional parabolic mirror. The inset shows the discrete nature of the metamirror caused by individual metaatoms and how the pathfinder chose different step-widths throughout the surface. This underscores the advantage of metamirrors: they enable the design of large focal lengths without the need for intricate polishing, as traditional mirrors do. It is important to note that the precise fabrication of nanostructures on curved surfaces introduces its own set of unique challenges. The designed focusing metamirrors exhibit mean reflectivities of 99.95% and 99.96% for 1064 nm and 1550 nm, respectively. That is, assuming equal illumination across the entire metamirror. In a more detailed and realistic scenario, the reflectivity of each metaatom should be considered in conjunction with the intensity of light at its specific location. For instance, with a Gaussian illumination profile featuring a beam waist of 800 µm, we observe an intensity-weighted mean reflectivity increase to 99.96% and 99.97% for wavelengths of 1064 nm and 1550 nm, respectively. These values are calculated by considering the spatial variation in illumination across the metamirror surface. Combining these focusing metamirrors with

their planar counterparts allows for the calculation of the expected finesse \mathcal{F} , as described by [42]:

$$\mathcal{F} = \frac{\pi\sqrt{R}}{1-R} \tag{4}$$

where $R = \sqrt{R_1 * R_2}$ represents the geometric mean of the reflectivities of the individual mirrors. Applying equation (4) results in a calculated finesse of 15,526 for 1064 nm and 20,911 for 1550 nm. These values theoretically exceed the previous record measurements [9]. However, in [9], the metamirror was designed for a reflectivity of nearly 100%, vet the measurement revealed a reflectivity of only 99.95%. It is essential to note that current fabrication limitations likely impede achieving such high-performance metamirrors. Future advancements in manufacturing precision are necessary to realize metamirrors capable of reflecting 99.997% of light, not only theoretically but also practically, and to achieve a finesse surpassing 100,000, as per equation (4). The implications of reaching such high finesse values could be significant, potentially opening new avenues in photonic applications and research in high-precision optical metrology.

4 Electric field distribution within the metaatoms

To gain a deeper understanding of the physics underlying the highly reflective metaatoms developed in the previous section, we now shift our focus to an in-depth analysis of individual metaatoms. Considering the dimensions of the metamirrors and the period of their respective metaatoms, we can determine that the metamirror designed for a wavelength of 1064 nm comprises 2703×2703 metaatoms, while the one for 1550 nm consists of 1680×1680 metaatoms. Across the diagonal of each metamirror (from the center to the edge, leveraging symmetry), we select a linearly spaced sample of nine metaatom designs. These designs are presented side-by-side in Figure 8, facilitating initial observations of their topology. Firstly, the metaatoms for 1064 nm exhibit more pronounced variations than those for 1550 nm, as corroborated by Figure 6. Secondly, it is observed that the metaatoms for 1064 nm transition from square shapes at the center to cross-like shapes towards the edge of the metamirror, whereas the reverse trend is observed for 1550 nm. Furthermore, we select three distinctive metaatom designs for each wavelength for simulation in COMSOL Multiphysics [43]. The aim is to obtain detailed electric field distributions. These electric field distributions for all three spatial planes are depicted in Figure 8, positioned beneath their corresponding metaatom visualizations. The observed mode shapes appear relatively simplistic and thus more robust. This can be attributed to the low height of the structures, which impedes the development of higher-order modes. It is noted that the majority of the light fields are concentrated within the metaatom structures. Nevertheless, the fields are not entirely confined to these structures; significant field excitations are also

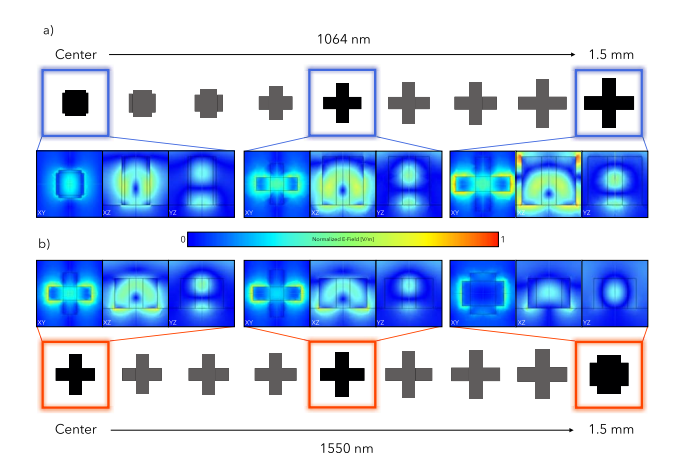


Fig. 8. Electric field distributions of a selection of metaatoms simulated with COMSOL Multiphysics. For both metamirror designs of Figure 7, we visualized 9 linearly spaced metaatoms along the diagonal from the center to the edge of the metamirror, i.e. at 1.5 mm distance. For three, the electric field distributions for all three spacial planes are shown for both (a) 1064 nm and (b) 1550 nm. The field distributions have been normalized across all 18 plots.

observed at the interfaces with the substrate (Silica) and the superstrate (air). In practical experiments, this could result in scattering due to side-wall roughness, potentially diminishing the efficiency of each metaatom. Despite these observations, it is evident that the straight-forward topology of the metaatoms is conducive to the generation of highly reflective optical modes within the structures. The developed framework is inherently adaptable, allowing for future enhancements to include additional elements such as fabrication tolerances and noise contributions [6], thus broadening its applicability and robustness.

5 Conclusion

In this work, we showcased a novel concept of a compact, bispectral optical cavity utilizing twin pairs of low-noise metamirrors. We began by optimizing fixed structural parameters for both metamirrors, disregarding their phase profiles. Subsequent simulations enabled us to identify ideal parameter combinations for flat-phase metamirrors, boasting theoretical reflectivities of 99.9999% at 1064 nm and 99.995% at 1550 nm. We could then utilize a pathfinding algorithm to render two focusing metamirrors with focal lengths of 6 m and theoretical mean reflectivities of 99.95% at 1064 nm and 99.96% at 1550 nm. Finally, we had an in-depth analysis of the electric fields of a selection of metaatoms, aiming to help understand the underlying physics. Despite its simplicity, our methodology can be readily adapted for multi-wavelength scenarios, offering a versatile platform for creating low-noise, portable optical cavities across various wavelengths.

Acknowledgments

L.S.N. would like to extend his heartfelt thanks to his friends from the "St. Juergens am Strande" club for their support and encouragement.

Funding

The authors gratefully acknowledge the support by the Deutsche Forschungsgemeinschaft (DFG, German Research Foundation) under Germany's Excellence Strategy – EXC-2123 QuantumFrontiers – 390837967. J.D. and S.K also acknowledge partial support by European Association of National Metrology Institutes. This project (20FUN08 NEXTLASERS) has received funding from the EMPIR programme co-financed by the Participating States and from the European Union's Horizon 2020 research and innovation programme.

Conflict of interest

The authors declare no conflicts of interest related to the research presented in this paper. While some of the authors are affiliated with *CAVITY technologies*, there is no direct connection or financial arrangement between the startup and the research conducted at *Technical University of Braunschweig* or *Physikalisch-Technische Bundesanstalt* presented in this work. The startup's activities are unrelated to the specific focus of this paper.

Data Availability Statement

Data underlying the results presented in this paper are not publicly available at this time but may be obtained from the authors upon reasonable request.

Author Contribution Statement

All authors made significant contributions to this work.

References

- 1 Roberts B.M., Delva P., Al-Masoudi A., Amy-Klein A., Bærentsen C., Baynham C.F.A., Benkler E., Bilicki S., Bize S., Bowden W. (2020) New J. Phys. 22, 093010.
- 2 Delva P., Lodewyck J., Bilicki S., Bookjans E., Vallet G., Le Targat R., Pottie P.E., Guerlin C., Meynadier F., Le Poncin-Lafitte C., et al. (2017) Phys. Rev. Lett. 118, 221102.
- 3 Abbott B.P. (2009) Rep. Prog. Phys. 72, 076901.
- 4 Weiss R. (2018) Rev. Mod. Phys. 90, 040501.
- 5 Matei D.G., Legero T., Häfner S., Grebing C., Weyrich R., Zhang W., Sonderhouse L., Robinson J.M., Ye J., Riehle F., et al. (2017) Phys. Rev. Lett. 118, 263202.
- 6 Kroker S., Dickmann J., Rojas Hurtado C.B., Heinert D., Nawrodt R., Levin Y., Vyatchanin S.P. (2017) *Phys. Rev. D* **96**, 022002
- 7 Dickmann J., Kroker S. (2018) Phys. Rev. D 98, 082003.
- 8 Dickmann J., Hurtado C.R., Nawrodt R., Kroker S. (2018) Phys. Lett. A 382, 2275.
- 9 Dickmann J., Sauer S., Meyer J., Gaedtke M., Siefke T., Bruckner U., Plentz J., Kroker S. (2023) Commun. Phys. 6, 16.
- 10 Kroker S., Kasebier T., Kley E.B., Tünnermann A. (2013) Opt. Lett. 38, 3336.
- 11 Shelling Neto L., Dickmann J., Kroker S. (2022) Opt. Express 30, 986.
- 12 Boyd J.A., Lahaye T. (2024) Am. J. Phys. 92, 50.
- 13 Kessler S., Hagemann C., Grebing C., Legero T., Sterr S., Riehle F., Martin M.J., Chen L., Ye J. (2012) Nature Photon. 6, 687.
- 14 Levin Y. (1998) Phys. Rev. D 57, 659-663.
- 15 Kruk S., Kivshar Y. (2017) ACS Photon. 4, 2638.
- 16 Balli F., Sultan M., Lami S.K., Hastings J.T. (2020) Nature Commun. 11, 3892.
- 17 Shi X., Liang Z., Hou E., Yang F., Dong Y., Xin W., Dai R., Jia Y., Xu H. (2023) Opt. Express 31, 41105.
- 18 Zheng X., Lin J., Wang Z., Zhou H., He Q., Zhou L. (2023) PhotoniX 4, 3.
- 19 Richards C.A., Ocier C.R., Xie D., Gao H., Robertson T., Goddard L. L., Christiansen R.E., Cahill D.G., Braun P.V. (2023) Nature Commun. 14, 3119.
- 20 Barbiero M., Calonico D., Levi F., Tarallo M.G. (2022) IEEE Trans. Instrum. Measure. 71, 1.

- 21 Dawel F., Wilzewski A., Herbers S., Pelzer L., Kramer J., Hild M.B., Dietze K., Krinner L., Spethmann N.C.H., Schmidt P.O. (2023) 2311.11610.
- 22 Grotti J., Koller S., Vogt S., Häfner S., Sterr U., Lisdat C., Denker H., Voigt C., Timmen L., Rolland A., et al. (2018) Nat. Phys. 14, 437.
- 23 Hill I.R., Hobson R., Bowden W., Bridge E.M., Donnellan E.A. Curtis, Gill P. (2016) J Phys. Conf. Ser. 723, 012019.
- 24 Takamoto M., Ushijima I., Ohmae N., Yahagi T., Kokado K., Shinkai H., Katori H. (2020) Nat. Photon. 14, 411.
- 25 Gellesch M., Jones J., Barron R., Singh A., Sun Q., Bongs K., Singh Y. (2020) Adv. Opt. Technol. 9, 313.
- 26 Zhao W., Wu H., Fu Y., Ge J., Yang H., Zhang S. (2023) Front. Phys. 10.
- 27 Davila-Rodriguez J., Baynes F.N., Ludlow A.D., Fortier T.M., Leopardi H., Diddams S.A., Quinlan F. (2017) Opt. Lett. 42, 1277.
- 28 McLemore C.A., Jin N., Kelleher M.L., Hendrie J.P., Mason D., Luo Y., Lee D., Rakich P., Diddams S.A., Quinlan F. (2022) Phys. Rev. Appl. 18, 054054.
- 29 Kelleher M.L., McLemore C.A., Lee D., Davila-Rodriguez J., Diddams S.A., Quinlan F. (2023) Opt. Express 31, 11954.
- 30 Milani G., Rauf B., Barbieri P., Bregolin F., Pizzocaro M., Thoumany P., Levi F., Calonico D. (2017) Opt. Lett. 42, 1970.
- 31 Leopold T., Schmöger L., Feuchtenbeiner S., Grebin C., Miche P., Scharnhorst N., Leroux I., Crespo Lopez-Urrutia J., Schmidt P. (2016) Appl. Phys. B 122.

- 32 Cacciapuoti L., Salomon C. (2009) The European Physical Journal Special Topics 172, 57.
- 33 Kuschewski F., Wüst J., Oswald M., Blomberg T., Gohlke M., Bischof J., Boac A., Alam T., Bußmeier A., Abich K., et al. (2023) *GPS Solu.* **28**, 10.
- 34 Świerad D., Häfner S., Vogt S., Venon B., Holleville D., Bize S., Kulosa A., Bode S., Singh Y., Bongs K., et al. (2016) Scientific Rep. 6, 33973.
- 35 Bruzewicz C.D., Chiaverini J., McConnell R., Sage J.M. (2019) Appl. Phys. Rev. 6, 021314.
- 36 E.S. Team (2020), Einstein gravitational wave Telescope conceptual design study, https://doi.org/10.5281/zenodo. 3911261.
- 37 Jin W., Li W., Orenstein M., Fan S. (2020) ACS Photon. 7, 2350.
- 38 Steiner S., Kroker S., Käsebier T., Kley E.B., Tünnermann A. (2012) Opt. Express 20, 22555.
- 39 An S., Zheng B., Shalaginov M.Y., Tang H., Li H., Zhou L., Dong Y., Haerinia M., Agarwal A.M., Rivero-Baleine C., et al. (2022) Adv. Opt. Mater. 10.
- 40 Johnson S.G., Bienstman P., Skorobogatiy M.A., Ibanescu M., Lidorikis E., Joannopoulos J.D. (2002) Phys. Rev. E 66, 066608.
- 41 van der Walt S., Schönberger J.L., Nunez-Iglesias J., Boulogne F., Warner J.D., Yager N., Gouillart E., Yu T. (2014) the Scikit-image contributors, *PeerJ* 2, e453.
- 42 Ismail N., Kores C.C., Geskus D., Pollnau M. (2016) Opt. Express 24, 16366
- 43 COMSOL AB (2023) COMSOL Multiphysics® v. 5.4, www. comsol.com.

J. Eur. Opt. Society-Rapid Publ. 2024, 20, 5
© The Author(s), published by EDP Sciences, 2024

 $\rm https://doi.org/10.1051/jeos/2024003$

Available online at: https://jeos.edpsciences.org

EOSAM 2023

Guest editors: Patricia Segonds, Guy Millot and Bertrand Kibler

RESEARCH ARTICLE OPEN 3 ACCESS

Mueller matrix imaging polarimeter with polarization camera self-calibration applied to structured light components

Esther Nabadda¹, María del Mar Sánchez-López^{1,2,*}, Asticio Vargas³, Angel Lizana⁴, Juan Campos⁴, and Ignacio Moreno^{1,5}

- ¹ Instituto de Bioingeniería, Universidad Miguel Hernández de Elche, 03202 Elche, Spain
- ² Departamento de Física Aplicada, Universidad Miguel Hernández de Elche, 03202 Elche, Spain
- ³ Departamento de Ciencias Físicas, Universidad de La Frontera, Temuco, Chile
- ⁴ Departament de Física, Universitat Autònoma de Barcelona, 08193 Bellaterra, Barcelona, Spain
- ⁵ Departamento de Ciencia de Materiales, Óptica y Tecnología Electrónica, Universidad Miguel Hernández de Elche, 03202 Elche, Spain

Received 8 August 2023 / Accepted 25 January 2024

Abstract. This work presents a complete Mueller matrix imaging polarimeter that uses three liquid-crystal retarders and a pixelated polarization camera. The polarimeter is characterized and optimized with a standard correction procedure here adapted to be performed fully in-situ, without any additional element, based on considering the polarization camera as the reference. The accuracy limit caused by the extinction ratio in the camera micro-polarizers is analyzed. Finally, the imaging polarimeter is tested experimentally by analyzing well-known samples for structured light applications such as patterned retarders, a patterned polarizer, and a liquid-crystal depolarizer. The work is presented in a tutorial style useful to reproduce the procedure by non-experts in polarimetry.

Keywords: Polarimetry, Liquid-Crystals Retarders, Structured Light, Polarization Camera.

1 Introduction

Among the different properties of light, polarization has been demonstrated to provide extremely useful information [1]. This is becoming especially relevant in bioimaging, where several techniques harnessing biological and clinical research are based on the vectorial properties of light [2, 3]. In the last decades, important technological advances related to the generation and measurement of polarized light have been produced, that provide tools and devices like liquid-crystal variable retarders, spatial light modulators (SLM) or polarization cameras that have become common in optics laboratories, leading to the development of precise imaging polarimeters [4, 5].

Another field developed in parallel is the generation and detection of structured light. This denomination was introduced to describe light beams with a spatial and temporal control of their amplitude, phase and state of polarization [6]. Light beams with non-uniform polarization, known as vector beams, are prompting important advances in areas such as microscopy, materials processing, metrology, or optical communications [7, 8]. Structured light is typically

produced with patterned polarization elements [9, 10]. SLM devices show the advantage of being reconfigurable, although requiring bulk optical systems [11, 12]. Alternatively, flat patterned polarization components can be fabricated with metamaterials [13] or with liquid-crystal (LC) geometric-phase elements [14, 15]. Patterned polarizers with arbitrary spatial distributions of the transmission axis are of great interest especially for developing micropolarizers in polarization cameras [16].

Research in patterned polarization elements and research in polarimetric imaging are closely related [17]. While patterned polarization elements are providing new tools for advanced polarization imaging [18, 19], polarimetric imaging relying on the Mueller matrix has proven very worthy to evaluate the quality of the fabricated components [20, 21]. Although Mueller matrix imaging polarimetry has been employed for almost three decades [22], it is a technique in constant evolution, where multiple variants have been introduced over the years [23, 24]. In this context, this work presents the realization of a complete Mueller matrix (MM) imaging polarimeter whose performance is tested on polarization elements commonly applied to generate structured light. This polarimeter is based on our previous system [21], but here we provide the following

^{*} Corresponding author: ${\tt mar.sanchez@umh.es}$

improvements: (1) the use of a multiwavelength LED light source to avoid interference and speckle noise, (2) the realization of a setup on a rotatable breadboard to easily change the polarimeter from a transmission to a back-reflection configuration, (3) the use of spectrally calibrated liquid-crystal retarders (LCR), both in the polarization state generator (PSG) and in the polarization state analyzer (PSA), and (4) the application of a well-stablished sequential polarimeter calibration and optimization method [25], here adapted to consider the polarization camera as the reference for polarization measurements (self-calibration). This way, the method can be applied without any additional elements simply by properly tuning the LCR devices in the system. These improvements allow us to present a multifunctional complete MM imaging polarimeter that can be applied to a variety of samples.

The paper is organized as follows: after this introduction, Section 2 describes the polarimeter components. Then, Section 3 presents the calibration steps required to correctly operate the system, including the correct tuning of the LCR devices and the calibration and compensation procedure of the PSG and the PSA systems. Finally, in Section 4 we discuss the results obtained to evaluate different elements used in structured light like spatially patterned retarders and polarizers, and a liquid-crystal depolarizer.

2 Description of the imaging polarimeter

The developed imaging polarimeter system is shown in Figure 1. As mentioned, it represents an upgraded version of our previous system [21] with larger potential for sample imaging and quality control applications. The light source is a multiwavelength RGB LED (Thorlabs LED4D067) with controllable intensity level. A light guide (Thorlabs LLG05-4H) directs the light to the polarimeter entrance. A 50 mm photographic objective lens is used to image the lightguide output onto the sample. A diffuser (Edmund Holo 30 deg) is added to improve the intensity uniformity on the sample plane. The PSG is composed by a vertically oriented linear polarizer, and two liquid-crystal variable retarders (LCR1 and LCR2) from ARCOptix. LCR1 is oriented at 45° while LCR2 is oriented vertically, such that upon adjusting their retardances, an arbitrary fullypolarized state of polarization (SOP) can be generated.

The polarized light illuminates the sample and after light-matter interaction the output is analyzed with a PSA. A circular iris diaphragm of variable diameter is placed just in front of the sample plane and kept in the calibration procedure. The PSA is an imaging detector that comprises a polarization camera and another variable retarder (LCR3), also from ARCOptix. The sample and the PSA are positioned on a rotating breadboard (Thorlabs RBB300A/M), so the detection system can be rotated an angle θ , changing from a transmission configuration (Fig. 1e) to a reflection configuration (Fig. 1f). The transmission configuration is used in the calibration process, and it is useful for analyzing highly transparent samples. The reflection configuration is suitable for samples with high scattering and for reflective devices.

The polarization camera (Thorlabs CS505MUP Kiralux) is a monochrome sensor with 12 bit resolution (4096 intensity digital levels) and with 2448 \times 2048 square pixels of 3.45 μm side. The sensor includes an integrated micro-polarizer array attached to the pixel detectors. Thus, images for horizontal (H), vertical (V), diagonal (D) and antidiagonal (A) linear analyzers can be captured in a single shot (Fig. 1c). An objective macro zoom lens (Computar MLH 10X) is attached to the polarization camera; thus, the sample can be imaged with relatively large magnification at distances around 20 cm. If larger magnification is required, an extension tube is added.

The three RGB LEDs of the light source have central wavelengths at 660 nm (red light), 565 nm (green light) and 470 nm (blue light) respectively. Figure 1d shows the spectra of the three LEDs, measured with a spectrometer (Stellar-Net, STN-BLK-C-SR) in the spectral range from 400 to 700 nm, with 2 nm resolution). A spectral filter (SF) filters each of these LED spectra, resulting in filtered spectra with full width at half maximum (FWHM) of about 10 nm, as the measured narrow RGB bands shown in Figure 1d. The SF is useful to reduce depolarization values that might have been artificially added to the final measurements due to the LCRs wavelength retardance dependence.

3 Calibration procedure

This section presents the calibration procedures required to accurately operate the MM imaging polarimeter. First, we review the method for calibrating the LCR devices. Then, the following subsection describes the calibration and optimization of the polarimeter.

3.1 Calibration of the LCR devices

The first step to properly operate the polarimeter is to calibrate the retardance of the LCR devices that will be used to provide the required SOPs, both in the PSG and in the PSA. For that purpose, we follow a simple yet accurate enough procedure that consists in placing the LCR device between crossed/parallel polarizers, oriented at 45° with respect to the LC director axis [26, 27]. The normalized transmission for crossed polarizers is given by

$$T_{\perp}(\lambda, V) = \cos^2\left[\frac{1}{2}\varphi(\lambda, V)\right],$$
 (1)

where the LC retardance $\varphi(\lambda, V) = (2\pi/\lambda) \cdot \Delta n \cdot t$ depends on the thickness of the LC layer (t), $\Delta n(V)$ is the voltage-dependent birefringence, λ is the wavelength and V is the applied voltage. This relation shows the expected oscillatory behavior of T_{\perp} (λ, V) both as a function of λ and V.

We measured the LCRs retardance versus the applied voltage for the three wavelength bands. As an example, Figure 2 shows the results obtained for LCR1. Figure 2a illustrates the normalized transmission curves T_{\perp} (V) for the three wavelength bands centered at $\lambda_{\rm R}=660$ nm,

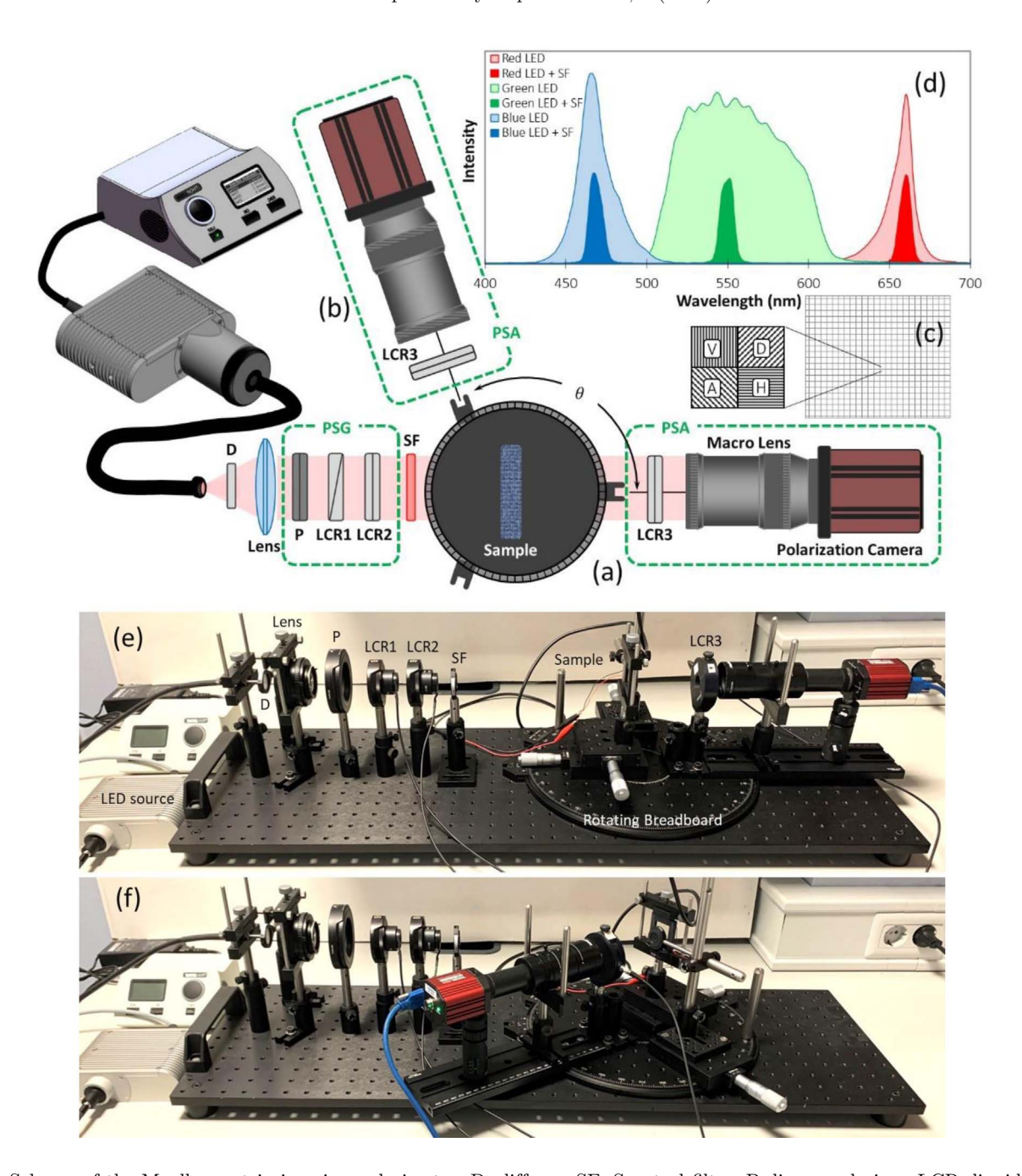


Fig. 1. Scheme of the Mueller matrix imaging polarimeter. D: diffuser. SF: Spectral filter. P: linear polarizer. LCR: liquid-crystal retarders. (a) Transmission geometry. (b) Reflection geometry. (c) Scheme of the micro-polarizers pattern on a macro-pixel of the polarization camera. (d) Spectra of the three LED sources with central wavelengths of 470 nm, 565 nm and 660 nm, and after being filtered by the corresponding spectral filter (SF). Pictures of the system in (e) the transmission configuration and (f) the reflection configuration.

 $\lambda_{\rm G}=565$ nm and $\lambda_{\rm B}=470$ nm. The curves feature the typical oscillatory behavior, with more oscillations for the shortest blue wavelength. Figure 2b shows the retrieved retardance function $\varphi(V)$ for the three wavelengths. For the longer wavelength $\lambda_{\rm R}=660$ nm the retardance variation is slightly greater than 2π , while it almost reaches 3π and 3.5π for the green and blue bands respectively.

3.2 Calibration of the PSG

We operate the polarimeter to generate and detect the well-known polarimetric basis consisting of six standard SOP: namely horizontal (H), vertical (V), diagonal (D) and antidiagonal (A) linear states, and right (R) and left (L) circular states. These six SOP define an octahedron in the

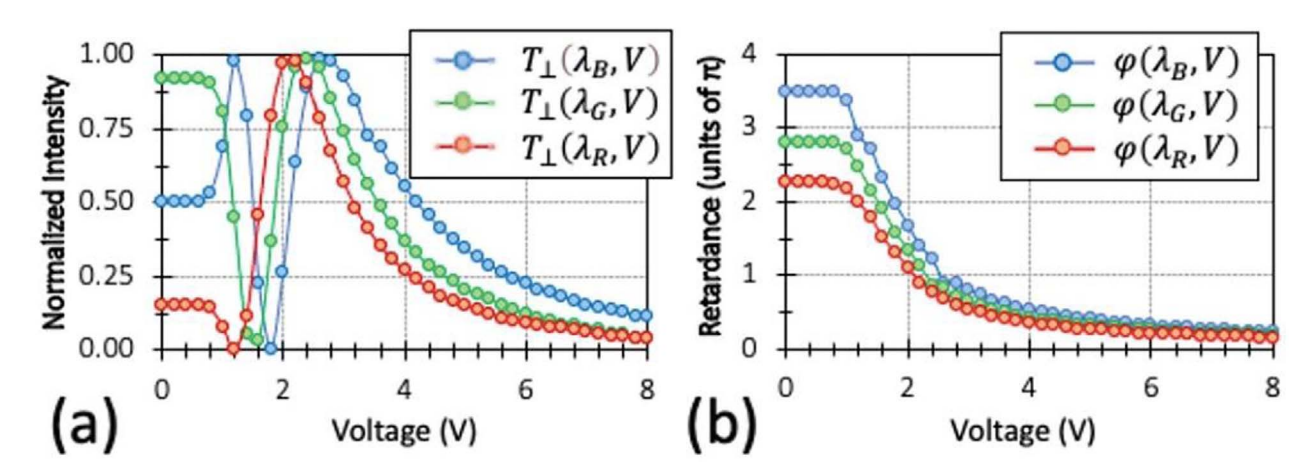


Fig. 2. Example of calibration of an LCR device in the MM imaging polarimeter. (a) Transmission $T_{\perp}(V)$ between crossed polarizers oriented at 45° with respect to the LC director. (b) LCR retardance $\varphi(V)$. Both graphs show the results for the three bands, with central wavelengths 470 nm (B), 565 nm (G) and 660 nm (R).

Table 1. Retardances required on LCR1 and LCR2 to provide SOP in the PSG.

SOP generated with PSG	Н	V	D	A	R	L
LCR1 Retardance	$_{ m HW}$	FW	QW	QW	QW	3QW
LCR2 Retardance	FW	FW	QW	3QW	FW	FW

QW: quarter-wave; HW: half-wave; 3QW: three quarter-wave; FW: full-wave.

Poincaré sphere and provide the polarimeter ideal conditional number (CN = 1.732) [25], thus ensuring an optimal performance in terms of noise amplification minimization from intensity measurements to polarimetric measurements. The LCR calibration provides the required voltages; typically, the quarter-wave retardance, the half-wave retardance or the full-wave retardance. Considering that the PSG polarizer (P) is oriented vertically, LCR1 is at 45° and LCR2 is vertical, Table 1 provides the retardances required to achieve the input SOPs.

However, variable LCRs feature effects that might introduce inaccuracy in the polarimeter, being the most relevant the non-uniform retardance on the clear aperture [26], the retardance temperature dependance, and multiple reflection interference effects that cause intensity variations coupled to the retardance modulation [28]. These effects must be compensated to achieve accurate polarimetric values. Among the different methods [29–31], here we propose and apply a modification of a well-stablished sequential calibration and optimization method [32, 33]. In the typical procedure, a calibrated polarimeter serves as the reference to measure the SOP of the PSG states, and the results are compared to those measured with the developed polarimeter. Here the technique is adapted to consider the polarization camera as the reference. This way, a self-reference procedure is applied that does not require any additional external element. Of course, the accuracy of this self-calibration depends on the quality of the micro-polarizers in the polarization camera. To this goal Appendix A includes an analysis of the limits of this procedure considering the extinction ratio of the micro-polarizers in the camera. We measured extinction ratios over 120:1. Although other sources of error have been identified [34] (such as spatial variations of the extinction ratio or misalignments in the orientation of the micro-polarizers), here we assume this simplified model with a limited but uniform extinction ratio. According to the approach described in the Appendix, the self-calibration procedure leads to an error in the measured MM elements below 1.7%.

Figure 3 shows the intensity captured for the circular iris diaphragm under red light illumination. The polarization camera provides a four-quadrant image where quadrants i, ii, iii and iv correspond to the detection of the V, D, A and H linear states. The input intensity is adjusted to ensure the non-saturation of the camera and it is maintained in the sample characterization. Each picture in Figure 3 corresponds to one of the six standard input SOP generated with the PSG (H, V, D, A, R, L). In each case, the voltage values derived from the LCR1 and LCR2 calibrations are taken as the starting point, but a fine adjustment must be then performed to provide images like those in Figure 3. The successful generation of the linear states H, V, A and D is verified when the following conditions are simultaneously fulfilled: the image quadrant of the orthogonal detector becomes the darkest, the image quadrant corresponding to the given input state is the brightest, and the other two quadrants feature the same intensity. On the contrary, the generation of the circular R and L states is verified when the four quadrants appear with equal weight. The information provided by the LCR calibration in Figure 2 allows differentiating

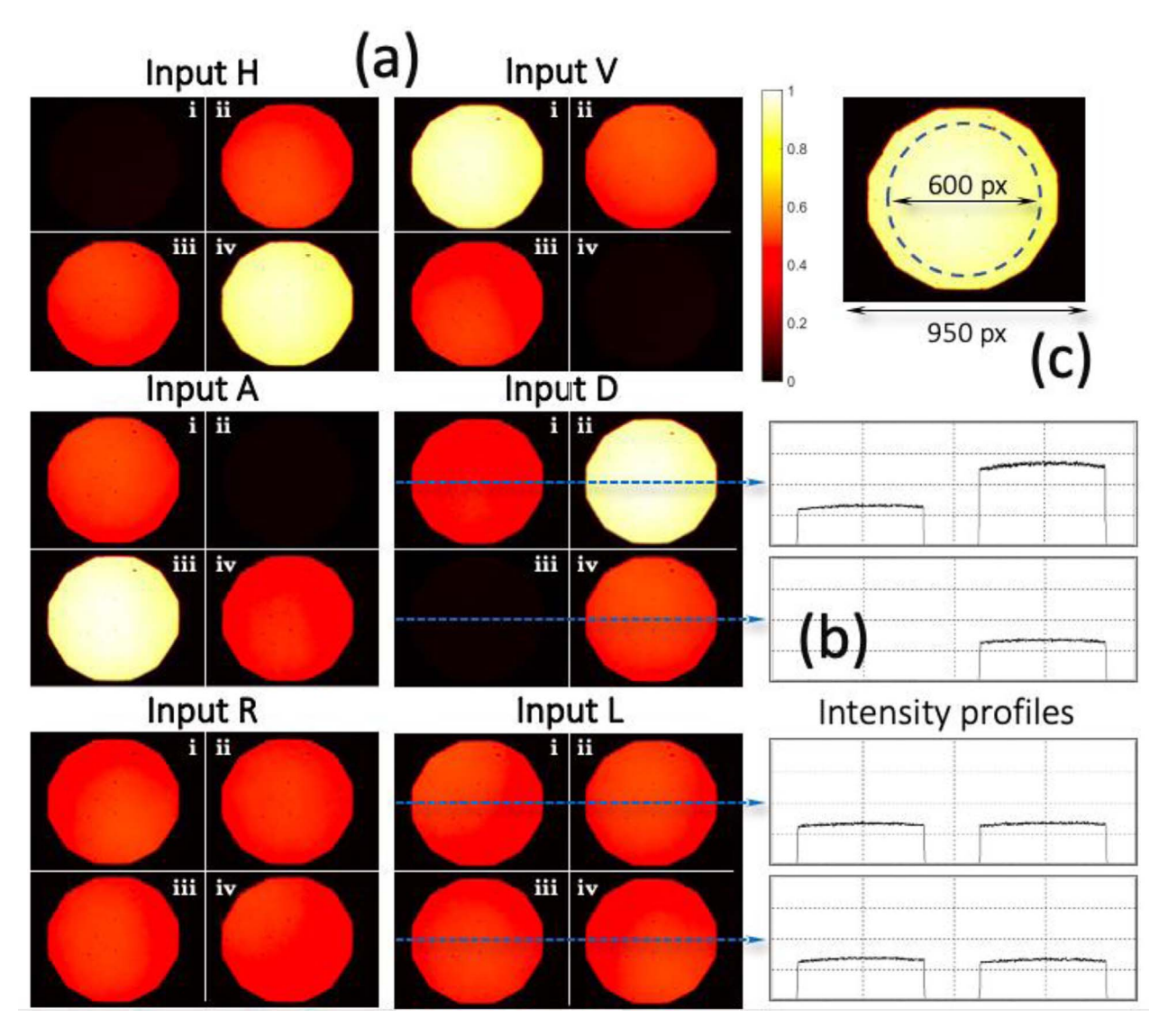


Fig. 3. (a) Calibration of the PSG system: experimental four-quadrant images captured by the polarization camera under the red channel illumination for input SOPs as linear horizontal (H), vertical (V), antidiagonal (A), diagonal (D), circular left (R) and circular right (L). (b) The intensity profiles for inputs D and L. (c) Calculations of average values are performed in the central circle with diameter of 600 pixels.

R and L states. On the right, the intensity profiles of the four quadrants for inputs D and L are shown.

The polarization camera is an incomplete polarimeter, since only the linear polarization components are measured. The first three Stokes parameters S_0 , S_1 , S_2 can be retrieved from the intensity images $I_i(x, y)$, $I_{ii}(x, y)$, $I_{ii}(x, y)$, and $I_{iv}(x, y)$ captured in quadrants i, ii, iii, and iv as

$$S_0(x,y) = \frac{1}{2} [I_i(x,y) + I_{ii}(x,y) + I_{iii}(x,y) + I_{iv}(x,y)], (2a)$$

$$S_1(x, y) = I_{iv}(x, y) - I_i(x, y),$$
 (2b)

$$S_2(x, y) = I_{ii}(x, y) - I_{iii}(x, y).$$
 (2c)

To retrieve S_3 , a quarter-wave plate must be placed in front of the polarization camera, to measure the circular polarization components. However, since LCR2 is oriented vertical, a quarter-wave retardance can be added to this retarder to achieve an equivalent situation and make quadrants ii and iii behave as equivalent R and L circular analyzers. Therefore, the PSG calibration can be completed with

$$S_3(x, y) = I'_{ii}(x, y) - I'_{iii}(x, y),$$
 (2d)

where now I' indicates that the additional quarter-wave retardance is added to LCR2. Note that LCR1 and LCR2 devices remain within the PSG system in all measurements, and they simply change voltage, so there are not differences due to reflection or absorption losses.

In	put H	Input	V
$\langle I_i \rangle = 0.014 \pm 0.002$	$\langle I_{ii} \rangle = 0.496 \pm 0.013$	$\langle I_i \rangle = 0.938 \pm 0.021$	$\langle I_{ii}\rangle = 0.498 \pm 0.013$
$\langle I_{iii}\rangle = 0.493 \pm 0.012$	$\langle I_{iv} \rangle = 0.923 \pm 0.021$	$\langle I_{iii}\rangle = 0.494 \pm 0.014$	$\langle I_{iv} \rangle = 0.017 \pm 0.002$
In	put A	Input	D
$\langle I_i \rangle = 0.497 \pm 0.012$	$\langle I_{ii}\rangle = 0.016 \pm 0.002$	$\langle I_i \rangle = 0.448 \pm 0.012$	$\langle I_{ii}\rangle = 0.954 \pm 0.021$
$\langle I_{iii}\rangle = 0.957 \pm 0.021$	$\langle I_{iv} \rangle = 0.490 \pm 0.013$	$\langle I_{iii}\rangle = 0.018 \pm 0.002$	$\langle I_{iv} \rangle = 0.504 \pm 0.013$
In	put R	Input	L
$\langle I_i \rangle = 0.501 \pm 0.024$	$\langle I_{ii}\rangle = 0.501 \pm 0.017$	$\langle I_i \rangle = 0.497 \pm 0.020$	$\langle I_{ii}\rangle = 0.511 \pm 0.014$
$\langle I_{iii}\rangle = 0.495 \pm 0.015$	$\langle I_{iv} \rangle = 0.496 \pm 0.022$	$\langle I_{iii}\rangle = 0.508 \pm 0.014$	$\langle I_{iv} \rangle = 0.523 \pm 0.023$

Table 2. Average intensity values and standard deviation of the images shown in Figure 3.

Table 2 presents the average value of the intensity measured for each of the 6×4 images shown in Figure 3. The error is given by the standard deviation. These values are calculated in a circle centered on the image and with diameter 600 pixels, as indicated in Figure 3c. These error values are also affected by noise in the detector. The camera was calibrated following a standard procedure [35] and it was operated in the regime limited by shot noise. The impact of this noise can be reduced by averaging several captures of each image, at the cost of increasing the time required for acquisition. Since we are using relatively high levels of intensity and samples with high transmission, we take single captures.

The measurement of the Stokes parameters for each PSG input state defines the **S** matrix, whose columns are given by images S_{ig} where index $i=0,\ 1,\ 2,\ 3$ indicates the Stokes parameter, and index g denotes the state generated by the PSG (in our case. $g=\mathrm{H,V,D,A,R,L}$). Thus, **S** is a 4×6 matrix defined as:

$$\mathbf{S} = egin{pmatrix} S_{0H} & S_{0V} & S_{0D} & S_{0A} & S_{0R} & S_{0L} \ S_{1H} & S_{1V} & S_{1D} & S_{1A} & S_{1R} & S_{1L} \ S_{2H} & S_{2V} & S_{2D} & S_{2A} & S_{2R} & S_{2L} \ S_{3H} & S_{3V} & S_{3D} & S_{3A} & S_{3R} & S_{3L} \end{pmatrix}$$

$$= \begin{pmatrix} 1 & 1 & 1 & 1 & 1 & 1 \\ 1 & -1 & 0 & 0 & 0 & 0 \\ 0 & 0 & 1 & -1 & 0 & 0 \\ 0 & 0 & 0 & 0 & 1 & -1 \end{pmatrix}, \tag{3}$$

where the second part of equation (3) denotes the ideal values. Since **S** is not a square matrix, its pseudo-inverse matrix is a 6×4 matrix given by:

$$\mathbf{S}^{-1} = \mathbf{S}^{T} \begin{bmatrix} \mathbf{S} \cdot \mathbf{S}^{T} \end{bmatrix}^{-1} = \begin{pmatrix} 1/6 & 1/2 & 0 & 0\\ 1/6 & -1/2 & 0 & 0\\ 1/6 & 0 & 1/2 & 0\\ 1/6 & 0 & -1/2 & 0\\ 1/6 & 0 & 0 & 1/2\\ 1/6 & 0 & 0 & -1/2 \end{pmatrix},$$

$$(4)$$

where superindex T indicates the transposed matrix and where the matrix on the right corresponds again to the ideal values. This expression of the pseudo-inverse matrix is valid when it is considered to multiply a matrix on the right.

Figure 4 shows matrices S(x,y) and $S^{-1}(x,y)$ retrieved from the data in Figure 3. We use a color map to represent values from +1 to -1. To avoid presenting calculations in pixels where the input light is blocked by the iris diaphragm, we calculated the average $I_{\text{mean}}(x, y)$ of the 24 images in Figure 3a and searched for its maximum value $M = \max[I_{\text{mean}}(x, y)]$. Then, polarimetric matrices and parameters are calculated at pixels (x, y) where $I_{\text{mean}}(x, y) > 0.2M$, while pixels not fulfilling this threshold are represented in black. The value 0.2 was tested to provide a visualization of the polarimetric parameters within the iris aperture, while the outside region, which otherwise would appear with random values, appears pitch black. The average values of each element in matrices $\mathbf{S}(x, y)$ and $\mathbf{S}^{-1}(x, y)$ were also calculated, together with its corresponding standard deviation, again within the circle defined in Figure 3c, leading to the results indicated in Table 3. These numerical results agree well with the expected theoretical values in equations (3) and (4).

3.3 Calibration of the PSA

Once the PSG has been calibrated, the polarimeter calibration is completed by adding the variable retarder LCR3 to the PSA and measuring again for each input SOP generated with the PSG. LCR3 is set with its axes oriented at 45°. LCR3 retardance is switched between zero or full-wave retardance, where the polarization camera measures H, V, D and A states, and a quarter-wave retardance, where circular R and L states can be measured at the micropixels with vertical and horizontal polarizers. This way, the PSA operates within an octahedron and it thus corresponds to the optimal solution named "T" in [36].

Setting the PSA to detect different SOPs yields the intensity matrix \mathbf{I} defined by the images $I_{ag}(x, y)$, where a denotes the analyzer in the PSA and g denotes the input state at the PSG. We also select the six standard SOP for the PSA. Hence, \mathbf{I} is a 6×6 matrix where each element I_{ag} is the intensity measured for each input state $g = \mathbf{H}$, \mathbf{V} , \mathbf{D} , \mathbf{A} , \mathbf{R} , \mathbf{L} when being detected through analyzer $a = \mathbf{H}$, \mathbf{V} , \mathbf{D} , \mathbf{A} , \mathbf{R} , \mathbf{L} , i.e.:

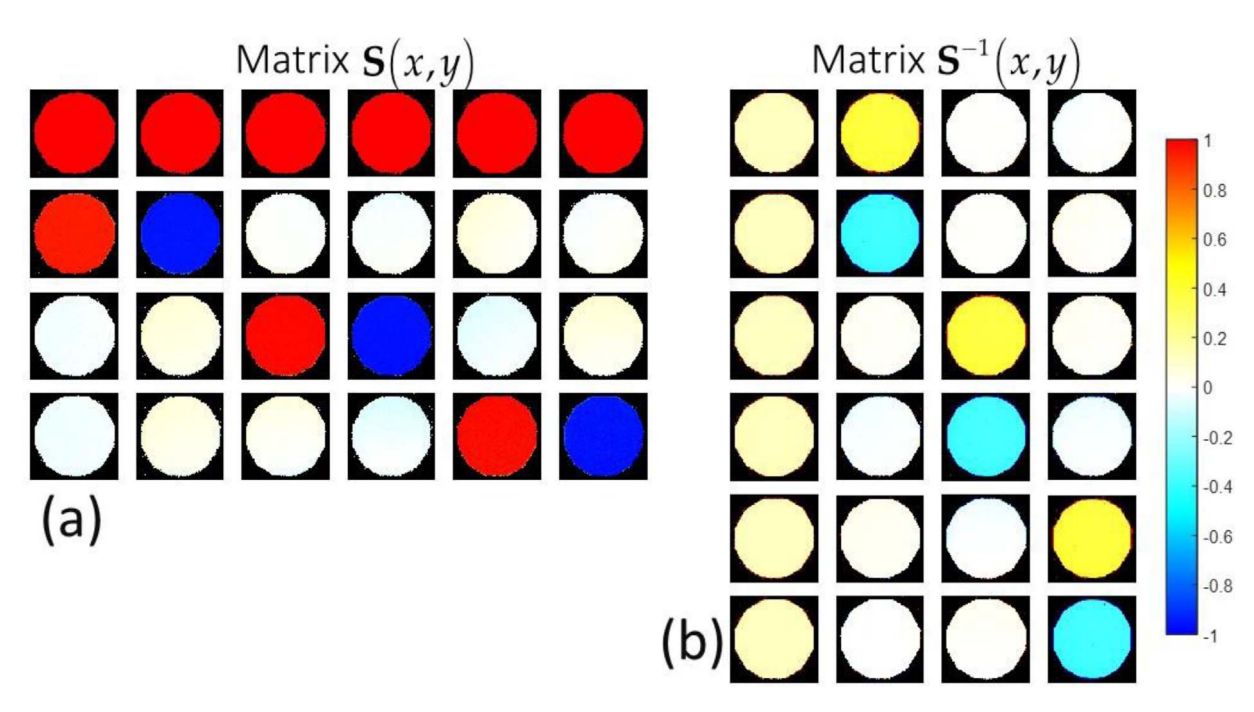


Fig. 4. Experimental images for the PSG polarimeter calibration under the red channel illumination. (a) $\mathbf{S}(x, y)$ matrix and (b) its pseudo-inverse matrix $\mathbf{S}^{-1}(x, y)$.

Table 3a. Average values of the matrix $\langle \mathbf{S}(x, y) \rangle_{\text{exp.}}$

1	1	1	1	1	1
$+0.948\pm0.010$	-0.960 ± 0.010	-0.005 ± 0.014	-0.015 ± 0.014	$+0.038\pm0.018$	$+0.006\pm0.016$
-0.023 ± 0.014	$+0.034 {\pm} 0.016$	$+0.996{\pm}0.010$	-0.965 ± 0.010	-0.061 ± 0.017	$+0.075 \pm 0.020$
$+0.030{\pm}0.014$	$+0.025{\pm}0.017$	$+0.044{\pm}0.020$	-0.057 ± 0.022	$+0.978 \pm 0.017$	-0.962 ± 0.017

$$\mathbf{I} = \begin{pmatrix} I_{HH} & I_{HV} & I_{HD} & I_{HA} & I_{HL} \\ I_{VH} & I_{VV} & I_{VD} & I_{VA} & I_{VL} \\ I_{DH} & I_{DV} & I_{DD} & I_{VA} & I_{DL} \\ I_{AH} & I_{AV} & I_{AD} & I_{AA} & I_{AL} \\ I_{RH} & I_{RV} & I_{RD} & I_{RA} & I_{RL} \\ I_{LH} & I_{LV} & I_{LD} & I_{LA} & I_{LL} \end{pmatrix}$$

$$= \begin{pmatrix} 1 & 0 & 1/2 & 1/2 & 1/2 & 1/2 \\ 0 & 1 & 1/2 & 1/2 & 1/2 & 1/2 \\ 1/2 & 1/2 & 1 & 0 & 1/2 & 1/2 \\ 1/2 & 1/2 & 0 & 1 & 1/2 & 1/2 \\ 1/2 & 1/2 & 1/2 & 1/2 & 1 & 0 \\ 1/2 & 1/2 & 1/2 & 1/2 & 0 & 1 \end{pmatrix}, (5)$$

where again the matrix values on the right stand for the ideal case.

Let us emphasize that matrix **I** is formed by images so each element $I_{ag}(x, y)$ depends on the pixel location. Also, note that the polarization camera only requires two shots to capture the six images per input SOP. Thus the

36 images required in matrix I are acquired after only 12 shots corresponding to 6 PSG configurations by 2 PSA configurations. Figure 5a shows the experimental result obtained for I(x, y) under the red channel illumination. For each input SOP, the images were normalized to the image where the analyzer matches the input polarization. The results bear good agreement with the ideal values in equation (6) despite slight variations along the diaphragm aperture. These variations are due to lighting non-uniformities (as shown in the intensity profiles in Fig. 3b), but also to the insertion of the LCR3 device in the PSA. Again, we calculated the average values and standard deviation of the intensity images in Figure 5a characterizing the intensity matrix. The result given in Table 4, although approximates reasonably well the expected values indicated in equation (5), shows significant differences that suggest the necessity of performing the compensation procedure to achieve accurate results.

Matrices **I** in equation (5) and **S** in equation (3) are related as $\mathbf{I} = \mathbf{A} \cdot \mathbf{S}$, where for simplicity we omit the pixel dependence. Here **A** is the detector matrix that characterizes the PSA. For the selected SOP, **A** is a 6 × 4 matrix that can be calculated as:

Table 3b. Average values of the matrix $\langle \mathbf{S}^{-1}(x, y) \rangle_{\text{exp.}}$

$+0.159\pm0.004$	$+0.497\pm0.009$	-0.004 ± 0.006	-0.009 ± 0.007
$+0.159\pm0.004$	-0.504 ± 0.009	0.000 ± 0.006	$+0.008\pm0.007$
$+0.156\pm0.004$	$+0.012\pm0.006$	$+0.487\pm0.009$	$+0.031\pm0.007$
$+0.164\pm0.004$	-0.020 ± 0.007	-0.484 ± 0.009	-0.036 ± 0.008
$+0.160\pm0.004$	$+0.026\pm0.007$	-0.026 ± 0.008	$+0.495\pm0.009$
$+0.158\pm0.004$	0.000 ± 0.007	$+0.024\pm0.008$	-0.487 ± 0.009

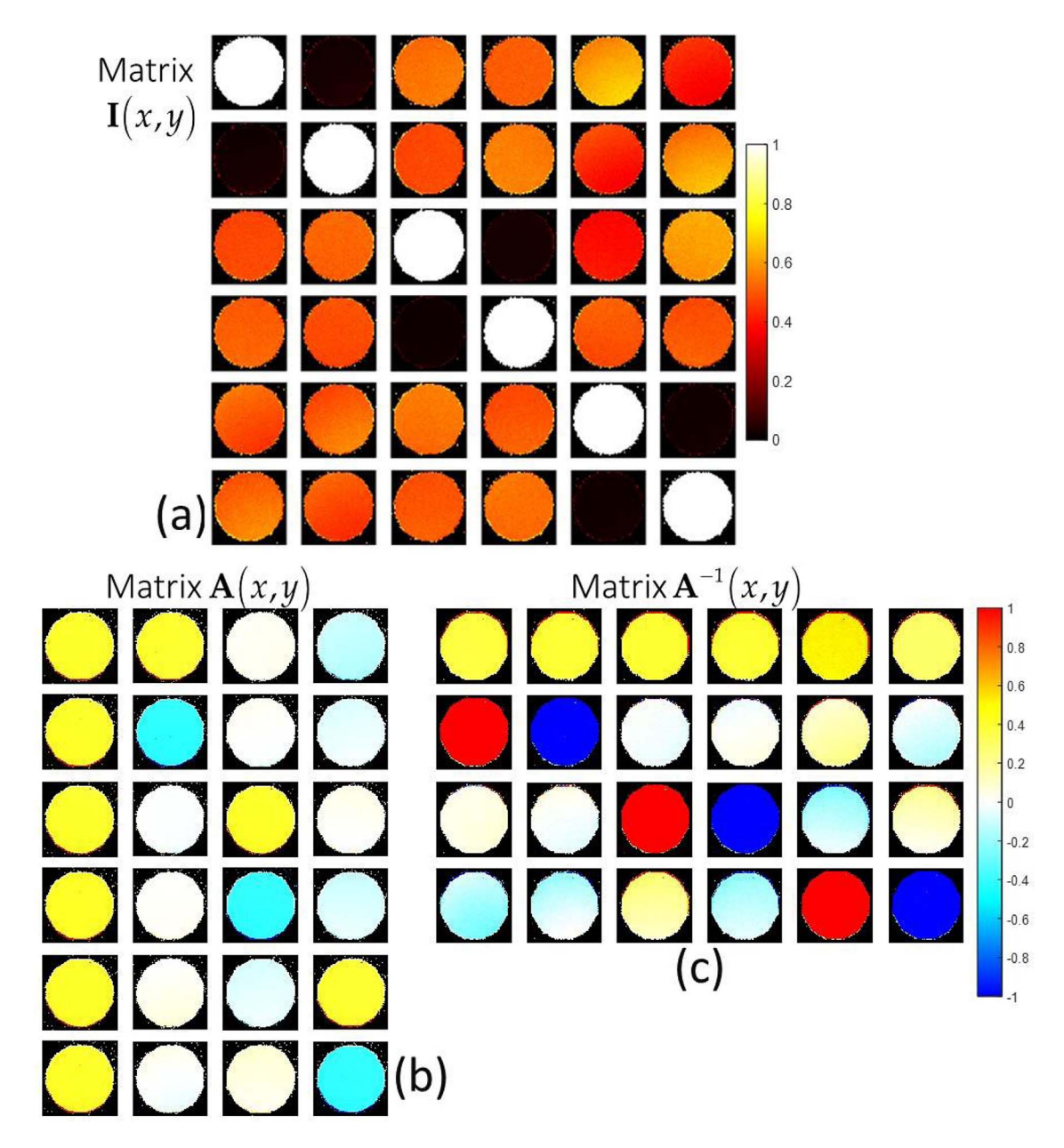


Fig. 5. Experimental images for the polarimeter PSA calibration under the red channel illumination. (a) Intensity matrix $\mathbf{I}(x, y)$. (b) Detector matrix $\mathbf{A}(x, y)$. (c) Pseudo-inverse detector matrix $\mathbf{A}^{-1}(x, y)$.

Table 4. Average values of the matrix $\langle \mathbf{I}(x, y) \rangle_{\text{exp.}}$

1	0.023 ± 0.004	0.544 ± 0.015	0.499 ± 0.014	0.395 ± 0.018	0.628 ± 0.025
0.035 ± 0.006	1	0.512 ± 0.017	0.537 ± 0.014	0.410 ± 0.020	0.617 ± 0.025
0.461 ± 0.012	0.527 ± 0.014	1	0.018 ± 0.002	0.498 ± 0.018	0.490 ± 0.017
0.532 ± 0.014	0.475 ± 0.013	0.029 ± 0.003	1	0.426 ± 0.016	0.581 ± 0.018
0.497 ± 0.022	0.525 ± 0.023	0.464 ± 0.014	0.579 ± 0.016	1	0.023 ± 0.002
0.541 ± 0.024	0.473 ± 0.023	0.580 ± 0.017	0.456 ± 0.014	0.023 ± 0.002	1

Table 5a. Average values of the matrix $\langle \mathbf{A}(x, y) \rangle_{\text{exp}}$.

$+0.393\pm0.008$	$+0.393\pm0.010$	$+0.019\pm0.008$	-0.096 ± 0.012
$+0.398\pm0.009$	-0.389 ± 0.012	-0.005 ± 0.011	-0.075 ± 0.013
$+0.395\pm0.009$	-0.011 ± 0.008	$+0.398\pm0.011$	$+0.032\pm0.015$
$+0.403\pm0.008$	$+0.013\pm0.008$	-0.387 ± 0.011	-0.090 ± 0.015
$+0.398\pm0.008$	0.001 ± 0.016	-0.066 ± 0.012	$+0.384\pm0.010$
$+0.398\pm0.008$	$+0.022\pm0.016$	$+0.068\pm0.014$	-0.387 ± 0.011

Table 5b. Average values of the matrix $\langle \mathbf{A}^{-1}(x, y) \rangle_{\text{exp.}}$

$+0.39\pm0.02$	-0.41 ± 0.02	$+0.43\pm0.02$	$+0.42\pm0.02$	$+0.55\pm0.02$	$+0.310\pm0.013$
$+0.96\pm0.03$	-0.99 ± 0.03	-0.04 ± 0.02	$+0.02\pm0.03$	$+0.07\pm0.04$	0.00 ± 0.04
$+0.04\pm0.02$	-0.02 ± 0.03	$+0.94\pm0.03$	-0.93 ± 0.03	-0.20 ± 0.05	$+0.19\pm0.05$
-0.11 ± 0.05	-0.19 ± 0.05	$+0.24\pm0.04$	-0.18 ± 0.04	$+0.95\pm0.03$	-0.91 ± 0.03

$$\mathbf{A} = \mathbf{I} \cdot \mathbf{S}^{-1} = \begin{pmatrix} 1/2 & 1/2 & 0 & 0\\ 1/2 & -1/2 & 0 & 0\\ 1/2 & 0 & 1/2 & 0\\ 1/2 & 0 & -1/2 & 0\\ 1/2 & 0 & 0 & 1/2\\ 1/2 & 0 & 0 & -1/2 \end{pmatrix}, \quad (6)$$

where the pseudo-inverse matrix S^{-1} in equation (4) was applied. The corresponding pseudo-inverse matrix A^{-1} is a 4×6 matrix given by

$$\mathbf{A}^{-1} = \begin{bmatrix} \mathbf{A}^{T} \cdot \mathbf{A} \end{bmatrix} \cdot \mathbf{A}^{T}$$

$$= \begin{pmatrix} 1/3 & 1/3 & 1/3 & 1/3 & 1/3 & 1/3 \\ 1 & -1 & 0 & 0 & 0 & 0 \\ 0 & 0 & 1 & -1 & 0 & 0 \\ 0 & 0 & 0 & 0 & 1 & -1 \end{pmatrix}, (7)$$

where the matrices on the right in equations (6) and (7) correspond to the ideal values. This expression in equation (7) is valid when it is considered to multiply a matrix on the left.

Figures 5b and 5c show the experimental images of $\mathbf{A}(x, y)$ and $\mathbf{A}^{-1}(x, y)$, which again bear a good agreement with the expected values in equations (6) and (7). However, note some elements of \mathbf{A}^{-1} in Figure 5c appreciably differ from the ideal zero value in equation (7), indicating the correction that the PSA experimental matrix requires. Let us remark that these matrices are calculated at every

pixel, thus providing a PSA calibration at pixel level. Again, for each element on these matrices, we calculated the average value and its standard deviation on the circle defined in Figure 3c. The results are given in Table 5. These values differ appreciably from the ideal values in equations (6) and (7) since they account for the non-ideal behaviour of the components involved in the PSG and the PSA.

4 Mueller matrix imaging

Once the PSG and PSA matrices, $\mathbf{S}(x, y)$ and $\mathbf{A}(x, y)$, have been determined, the sample can be introduced in the polarimeter. For each input SOP generated by the PSG, the images given by the PSA are captured. As a result, a new set of 36 images are obtained that define a new intensity matrix $\mathbf{I}_{\mathbf{S}}(x, y)$, like in equation (5), now related to the sample Mueller matrix $\mathbf{M}_{\mathbf{S}}(x, y)$ as

$$\mathbf{I}_{S}(x,y) = \mathbf{A}(x,y) \cdot \mathbf{M}_{S}(x,y) \cdot \mathbf{S}(x,y). \tag{8}$$

 $\mathbf{M}_{\mathrm{S}}(x, y)$ is then obtained with the aid of the pseudo-inverse matrices \mathbf{A}^{-1} and \mathbf{S}^{-1} as:

$$\mathbf{M}_{S}(x,y) = \mathbf{A}^{-1} \cdot \mathbf{I}_{S} \cdot \mathbf{S}^{-1}$$

$$= \left\{ \left[\mathbf{A}^{T} \cdot \mathbf{A} \right]^{-1} \cdot \mathbf{A}^{T} \right\} \cdot \mathbf{I}_{S} \cdot \left\{ \mathbf{S}^{T} \cdot \left[\mathbf{S} \cdot \mathbf{S}^{T} \right]^{-1} \right\}. \tag{9}$$

We illustrate the procedure by considering different polarization devices that modify the input SOP by three distinct physical mechanisms: a pure retarder, a pure diattenuator,

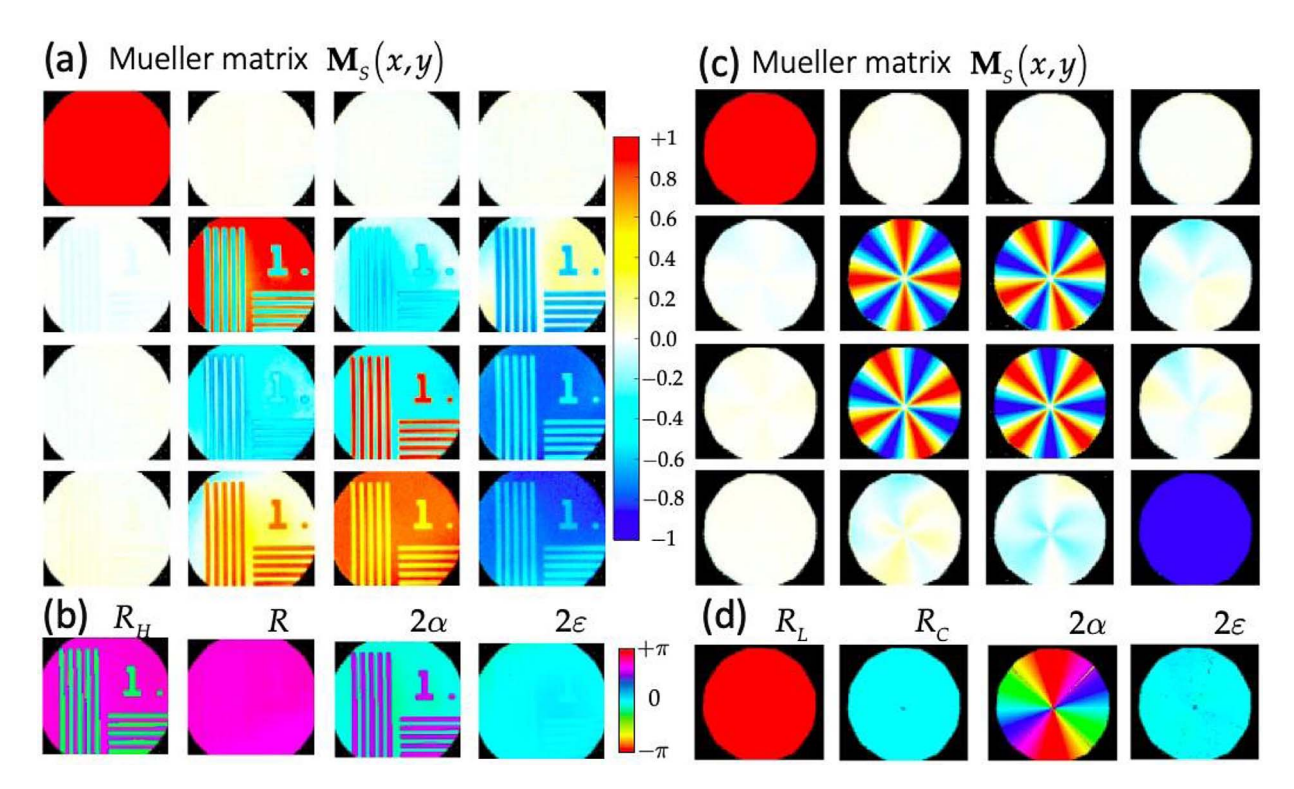


Fig. 6. (a) Experimental MM of the birefringent resolution test under red light channel illumination. (b) Retrieved horizontal linear retardance (R_L) and total retardance (R), and azimuth (α) and ellipticity (ε) of fast eigenstates. (c) and (d) show equivalent results for the q-plate element under red channel illumination.

and a pure depolarizer. These samples of well-defined properties thus serve as validation tests to probe the accuracy of the imaging polarimeter. For each sample, the experimental MM was retrieved following equation (9) and the Lu–Chipman decomposition $\mathbf{M}_{\mathrm{S}} = \mathbf{M}_{\Delta} \cdot \mathbf{M}_{\mathrm{R}} \cdot \mathbf{M}_{\mathrm{D}}$ [37] was applied to calculate relevant polarimetric parameters using standard formulas [21]. We applied the very well-known Lu–Chipman decomposition because these samples, each of distinct physical mechanism, imply relatively simple Mueller matrices. Note that more complex Mueller matrices, simultaneously dealing with retardance, depolarization and diattenuation responses could require other decompositions, like for instance the inverse decomposition, the arrow form decomposition or the symmetric decomposition, among others [38].

As a first example, Figure 6 shows the results for two patterned retarders: a birefringent NBS 1963A resolution test (Thorlabs R2L2S1B), and a q-plate device (Thorlabs WPV10-633), both under the red channel illumination. Figures 6a and 6c show the retrieved MM normalized to m_{00} . They show the expected result for a retarder, where $m_{0j} = m_{j0} \approx 0$, for j=1,2,3, indicating null polarizance and null diattenuation. The retarder information is contained in the 3×3 bottom right submatrix. The retardance vector [21, 37] is calculated and some representative parameters of the retarder are shown in each case.

Figures 6a and 6b show the results for the birefringent resolution test. This is a linear retarder designed to have a

uniform retardance but a different orientation in the patterns compared to the background. The total retardance $\,$ R(x, y) appears uniform all over the image, with average value $\langle R \rangle = 131^{\circ} \pm 1^{\circ}$ (the value is obtained by averaging over the significant pixels and the error is given by its standard deviation, where again, the significant pixels are those comprised within a circle as defined in Fig. 3c). However, the horizontal component of the retardance vector $R_H(x, y)$ clearly shows a difference between the patterns and the background. The azimuth $\alpha(x, y)$ of the fast eigenstate confirms the two regions, with the background oriented approximately horizontal, $\langle \alpha_b \rangle =$ $-8.5^{\circ} \pm 0.5^{\circ}$, and the resolution test pattern oriented at $\langle \alpha_t \rangle = -55.8^{\circ} \pm 1.0^{\circ}$. The ellipticity image $\varepsilon(x, y)$ of the fast eigenstate remains uniform over the entire image, with a very small value, $\langle \varepsilon \rangle = 2.6^{\circ} \pm 1.2^{\circ}$ as expected for a linear retarder.

Figures 6c and 6d show equivalent results for the q-plate component, a patterned retarder widely used to generate orbital angular momentum (OAM) beams and vector beams [39]. This is a linear retarder with fixed retardance and whose axes orientation changes azimuthally. This q-plate was designed as a half-wave retarder for the 633 nm wavelength and with value q=1, so the retarder axes make a complete azimuthal rotation. In this case, since the retarder is very close to the half-wave condition, the most relevant information in the MM is in the m_{11} , m_{12} , m_{21} , and m_{22} elements, which show an azimuthal variation in the complete range from -1 to +1, and in the m_{33} element, which

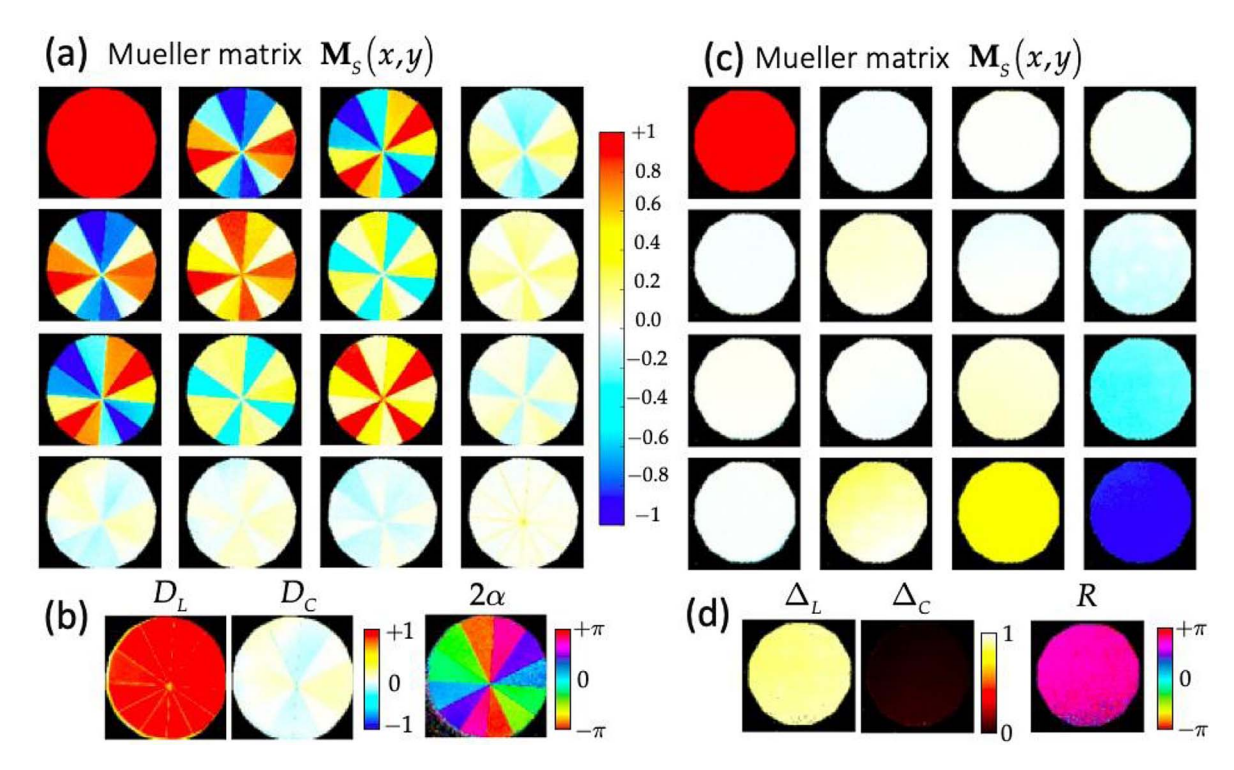


Fig. 7. (a) Experimental MM of a radial polarizer under red channel illumination. (b) Linear diattenuation (D_L) , circular diattenuation (D_C) , and azimuth (α) of the transmission axis. (c) Experimental MM for a depolarizing FLC modulator under the green channel illumination. (d) Linear depolarizance (Δ_L) , circular depolarizance (Δ_C) , and total effective retardance (R).

appears uniform with a value around -1. In this case Figure 6d illustrates the linear R_L and circular R_C components of the retardance vector, which confirm the linear retarder condition of this component. The total retardance is uniform with an average value $\langle R \rangle = 178^{\circ} \pm 1.1^{\circ}$ in agreement with the half-wave retardance design of this q-plate for red light. The azimuth of the fast eigenstate orientation $\alpha(x,y)$ shows a continuous azimuthal variation, as corresponding to a q-plate with q=1 and the eigenstate ellipticity $\varepsilon(x,y)$ shows a null constant value with an average value $\langle \varepsilon \rangle = 1^{\circ} \pm 3^{\circ}$, as expected for a linear retarder.

The second type of structured polarization sample is a pure diattenuator: a radial polarizer from the company Codixx (ColorPol VIS500 BC3), consisting of 12 segments where the transmission axis is aligned radially, thus being shifted 30° between adjacent segments. Figure 7a shows the corresponding MM, again using the red channel. In this case the last row and column become null, $m_{3j} = m_{j3} \approx 0$ with j = 0, 1, 2. The other MM elements clearly show the segmentation of the polarizer. Figure 7b shows as parameters of interest the linear and circular components of the diattenuation, $D_L(x, y)$ and $D_C(x, y)$. The average total diattenuation is $\langle D \rangle = 0.85 \pm 0.13$, where again the value is averaged over the significant pixels and the error is given by its standard deviation. We also calculate the polarizer transmission angle $\alpha(x, y)$, which confirms the expected rotation.

Finally, as a pure depolarizing sample we consider a ferroelectric liquid–crystal (FLC) modulator. This type of modulator behaves as a linear retarder whose director

axis switches between two stable orientations within the modulator plane [40]. When operated at a high frequency compared to the detector integration time, FLC modulators have proven to be useful to generate an effective depolarization [41]. In this work, we use a FLC modulator (CRL Opto LCS2-G) showing a switching angle of 45° and a retardance of 180° for green light [40]. We operate the device at a switching frequency of 500 Hz, much higher than the frame rate of the polarization camera. Therefore, each measurement with the camera corresponds to the incoherent superposition of the two states emerging from the FLC [42]. The measured MM can be regarded as the average of $\mathbf{M}_{\rm A}$ and $\mathbf{M}_{\rm B}$ the two matrices corresponding to the two stable states of the modulator.

The MM of a retarder with retardance φ and orientation α , corresponding to the first FLC stable position is given by [1]:

$$\mathbf{M}_{\mathbf{A}} = \begin{pmatrix} 1 & 0 & 0 & 0 \\ 0 & c_{2\alpha}^2 + c_{\varphi} s_{2\alpha}^2 & (1 - c_{\varphi}) s_{2\alpha} c_{2\alpha} & -s_{\varphi} s_{2\alpha} \\ 0 & (1 - c_{\varphi}) s_{2\alpha} c_{2\alpha} & s_{2\alpha}^2 + c_{\varphi} c_{2\alpha}^2 & s_{\varphi} c_{2\alpha} \\ 0 & s_{\varphi} s_{2\alpha} & -s_{\varphi} c_{2\alpha} & c_{\varphi} \end{pmatrix},$$

$$(10)$$

where $c_x = \cos(x)$ and $s_x = \sin(x)$. The second FLC stable position is given by $\mathbf{M}_B = (-45^\circ) \cdot \mathbf{M}_A \cdot \mathbf{R} (+45^\circ)$ where \mathbf{R} stands for the Mueller rotation matrix. Then, the average MM given by $\langle \mathbf{M}_{FLC} \rangle = \frac{1}{2} (\mathbf{M}_A + \mathbf{M}_B)$ results in

$$\langle \mathbf{M}_{\text{FLC}} \rangle = \begin{bmatrix} 1 & 0 & 0 & 0 \\ 0 & c_{2\varphi}^2 & 0 & -\frac{1}{2} s_{\varphi} (c_{2\alpha} + s_{2\alpha}) \\ 0 & 0 & c_{2\varphi}^2 & \frac{1}{2} s_{\varphi} (c_{2\alpha} + s_{2\alpha}) \\ 0 & \frac{1}{2} s_{\varphi} (c_{2\alpha} + s_{2\alpha}) & -\frac{1}{2} s_{\varphi} (c_{2\alpha} + s_{2\alpha}) & c_{\varphi} \end{bmatrix}.$$
(11)

In the case of a half-wave retardance, $\phi=180^\circ$, this average matrix $\langle \mathbf{M}_{\rm FLC} \rangle$ becomes:

This result can be regarded as a perfect depolarizer for input linear polarizations, whereas circular polarizations retain the full degree of polarization but change handedness.

Figure 7c shows the experimental MM results obtained with the polarimeter. In this case we use the green channel where the FLC layer behaves closely to the half-wave retardance condition [40]. Now the experimental MM elements are uniform images since the FLC modulator is a singlepixel element. The retrieved MM matches quite well the expected ideal result in equation (12). All the elements are close to zero, except $m_{00} \approx 1$ and $m_{33} \approx -1$. Elements m_{32} and m_{23} slightly differ from zero, due to the nonperfect half-wave retardance of the FLC layer. Figure 7d shows images of the depolarization and retardance parameters are calculated. The linear depolarizance $\Delta_L(x, y)$ shows high values, with an average value $\langle \Delta_L \rangle = 0.88 \pm 0.03$, while the circular depolarization $\Delta_{\mathcal{C}}(x, y)$ has very low values, with $\langle \Delta_C \rangle = 0.04 \pm 0.03$. This confirms the ability of the FLC modulator to depolarize linearly polarized input light. Finally, the effective retardance R(x, y) shows an average value $\langle R \rangle = 158^{\circ} \pm 3^{\circ}$, not far but non-perfect half-wave retardance. Again, the error given in these average values is calculated as the standard deviation of the values in all pixels in the aperture.

5 Conclusion

In summary, this work presents an imaging complete MM polarimeter comprised of a polarization camera and three LCRs. The use of polarization cameras in imaging systems is quite recent and it is arising high interest in a wide range of applications. The presented polarimeter is an improved version of our previous system [21] with significant advances. First, a multiwavelength LED light source replaced the laser source, thus avoiding interference and speckle derived from the coherent source. A rotatable breadboard is added to allow changing from the transmission configuration to a configuration useful for reflective or back-scattering samples. The system incorporates two LCRs in the PSG and another one in the PSA, to allow

fully automated measurements without any moving element. All LCR devices were calibrated for the three spectral bands of the LED source.

The polarimeter was calibrated and compensated by modifying the time sequential method [25, 32]. The procedure has been illustrated step by step. The novelty here is that the polarization camera included in the polarimeter is itself the calibration reference. This way no additional external elements are required and the polarimeter can be fully optimized in situ. Furthermore, the procedure is applied at pixel level, therefore compensating the residual non-uniformities in the illumination and in the PSA system, because of the pixelwise calculation of the normalized Mueller matrix.

This approach of course relies on the quality of the polarization camera. To this aim, the Appendix incorporates a calculation of the error in the measurement of the MM elements caused by the limited extinction ratio (ER) of the micro-polarizers, which shows an error lower than 1.7% for the minimum value of ER = 120 measured in our camera. The calibration and compensation procedure has been illustrated step by step by displaying the $\mathbf{S}(x, y)$ and $\mathbf{A}(x, y)$ images that define the PSG and the PSA. They are compared with the theoretical expected values, showing a very good agreement in all cases.

Finally, three different samples used in structured light applications with well-known polarization properties were evaluated to verify the accuracy of the polarimeter: (1) two patterned pure retarders with constant retardance but different orientation of the optical axis (a birefringent resolution test and a q-plate), (2) a radial linear polarizer, and 3) a linear depolarizer based on a fast-switching FLC modulator with 45° switching angle. The retrieved experimental MM agree very well with the expected results and, after performing the Lu–Chipman decomposition, the polarization parameters of interest (retardance, diattenuation and depolarization) were derived in each case.

Funding

This work was financed by Ministerio de Ciencia e Innovación, Spain (refs.: PID2021-126509OB-C22, -C21 and PDC2022-133332-C22) and Generalitat Valenciana (ref. CIAICO/2021/276). EN acknowledges Generalitat Valenciana (ref. GRISOLIAP/2020/004). AV acknowledges Fondecyt $\rm N^\circ$ 1191811.

Conflicts of Interest

This work has no financial or non-financial competing interests.

Data availability statement

Data will be made available on request.

Author contribution statement

All coauthors contributed to the paper. EN and AV contributed with the realization of the experiments. EN and IM contributed with the computer calculations. MMSL, AL, JC and IM contributed to the conceptualization, design of the experiments, and analysis of the results. MMSL contributed to writing the manuscript, and all authors contributed to the revision of the manuscript.

References

- 1 Goldstein D.H. (2010) Polarized Light, Marcel Dekker, New York, NY, USA.
- 2 Ramella-Roman J.C., Saytashev I., Piccini M. (2020) A review of polarization-based imaging technologies for clinical and preclinical applications, J. Opt. 22, 123001. https://doi.org/10.1088/2040-8986/abbf8a.
- 3 He C., He H., Chang J., Chen B., Ma H., Booth M.J. (2021) Polarisation optics for biomedical and clinical applications: a review, *Light: Sci Appl* 10, 194. https://doi.org/10.1038/s41377-021-00639-x.
- 4 Gottlieb D., Arteaga O. (2021) Mueller matrix imaging with a polarization camera: application to microscopy, *Opt. Express* **29**, 21, 34723–34374. https://doi.org/10.1364/OE.439529.
- 5 Van Eeckhout A., Garcia-Caurel E., Garnatje T., Escalera J.C., Durfort M., Vidal J., Gil J.J., Campos J., Lizana A. (2021) Polarimetric imaging microscopy for advanced inspection of vegetal tissues, *Sci. Rep.* 11, 3913. https://doi.org/10.1038/s41598-021-83421-8.
- 6 Rubinsztein-Dunlop H., Forbes A., Berry M.V., Dennis M.R., Andrews D.L., Mansuripur M., Denz C., Alpmann C., Banzer P., Bauer T., Karimi E., Marrucci L., Padgett M., Ritsch-Marte M., Litchinitser N.M., Bigelow N.P., Rosales-Guzmán C., Belmonte A., Torres J.P., Neely T.W., Baker M., Gordon R., Stilgoe A.B., Romero J., White A.G., Fickler R., Willner A.E., Xie G., McMorran B., Weiner A.M. (2017) Roadmap on structured light, J. Opt. 19, 013001. https://doi.org/10.1088/2040-8978/19/1/013001.
- 7 Piquero G., Martínez-Herrero R., de Sande J.C.G., Santarsiero M. (2020) Synthesis and characterization of non-uniformly totally polarized light beams: tutorial, *J. Opt. Soc. Am. A* 37, 4, 591. https://doi.org/10.1364/JOSAA.379439.
- 8 Rosales-Guzmán C., Ndagano B., Forbes A. (2018) A review of complex vector light fields and their applications, J. Opt. 20, 123001. https://doi.org/10.1088/2040-8986/aaeb7d.
- 9 Devrinkas R., Kazansky P.G. (2017) High-performance geometric phase elements in silica glass, APL Photon. 2, 066104. https://doi. org/10.1063/1.4984066.
- 10 Liu G.-G., Lee Y.-H., Huang Y., Zhu Z., Tan G., Cai M.-Q., Li P.-P., Wang D., Li Y., Pang S., Tu C., Wu S.-T., Wang H.-T. (2017) Dielectric broadband meta-vector-polarizers based on nematic liquid crystal, APL Photon. 2, 066104. https://doi.org/10.1063/1.5006016.
- 11 Davis J.A., McNamara D.E., Cottrell D.M., Sonehara T. (2000) Two-dimensional polarization encoding with a phase-only liquid-crystal spatial light modulator, Appl. Opt. 39, 10, 1549–1554. https://doi.org/10.1364/AO.39.001549.
- 12 Kenny F., Lara D., Rodríguez-Herrera O.G., Dainty C. (2012) Complete polarization and phase control for focus-shaping in high-NA microscopy, *Opt. Exp.* **20**, 13, 14015–14029. https://doi.org/10.1364/OE.20.014015.
- 13 Wen D., Croizier K.B. (2021) Metasurfaces 2.0: Laser-integrated and with vector field control, APL Photon. 6, 080902. https://doi.org/ 10.1063/5.0057904.
- 14 De Sio L., Roberts D.E., Liao Z., Nersisyan S., Uskova O., Wickboldt L., Tabiryan N., Steeves D.M., Kimball B.R. (2016) Digital polarization holography advancing geometrical phase optics, Opt. Exp. 24, 16, 18297–18306. https://doi.org/10.1364/OE.24.018297.
- 15 Curcio V., Alemán-Castañeda L.A., Brown T.G., Brasselet S., Alonso M.A. (2020) Birefringent Fourier filtering for single molecule coordinate and height super-resolution imaging with dithering and orientation, *Nature Commun.* 11, 5307. https://doi.org/10.1038/s41467-020-19064-6.

- 16 Zhang Z., Dong F., Cheng T., Qiu K., Zhang Q., Chu W., Wu X. (2014) Nano-fabricated pixelated micropolarizer array for visible imaging polarimetry, Rev. Sci. Instrum. 85, 105002. https://doi.org/10.1063/1.4897270.
- 17 Singh K., Tabebordbar N., Forbes A., Dudley A. (2020) Digital Stokes polarimetry and its application to structured light: tutorial, *J. Opt. Soc. Am. A* **37**, C33–C44. https://doi.org/10.1364/JOSAA. 397912.
- 18 Angelo J.P., Germer T.A., Litorja M. (2019) Structured illumination Mueller matrix imaging, *Biomed. Opt. Exp.* 10, 6, 2861–2868. https://doi.org/10.1364/BOE.10.002861.
- 19 Rubin N.A., D'Aversa G., Chevalier P., Shi Z., Chen W.T., Capasso F. (2019) Matrix Fourier optics enables a compact full-Stokes polarization camera, *Science* 365, eaax1839. https://doi.org/10.1126/science.aax18.
- 20 Arteaga O., Bendada H. (2020) Geometrical phase optical components: Measuring geometric phase without interferometry, Crystals 10, 880. https://doi.org/10.3390/cryst10100880.
- 21 López-Morales G., Sánchez-López M.M., Lizana A., Moreno I., Campos J. (2020) Mueller matrix polarimetric imaging analysis of optical components for the generation of cylindrical vector beams, Crystals 10, 1155. https://doi.org/10.3390/cryst10121155.
- 22 Pezzaniti J.L., Chipman R.A. (1995) Mueller matrix imaging polarimetry, Opt. Eng. 34, 6, 1558–1568. https://doi.org/10.1117/ 12.206161.
- 23 Kudenov M.W., Escuti M.J., Hagen N., Dereniak E.L., Oka K. (2012) Snapshot imaging Mueller matrix polarimeter using polarization gratings, Opt. Lett. 37, 8, 1367–1369. https://doi.org/10.1364/ OL.37.001367.
- 24 Carnicer A., Bosch S., Javidi B. (2019) Mueller matrix polarimetry with 3D integral imaging, *Opt. Exp.* 27, 8, 11525–11536. https://doi. org/10.1364/OE.27.011525.
- 25 Garcia-Caurel E., Ossikovski R., Foldyna M., Pierangelo A., Drévillon B., De Martino A. (2013) Advanced Mueller ellipsometry instrumentation and data analysis (Chapter 2), in *Ellipsometry at the* nanoscale, M. Losurdo, K. Hingerl (eds.), Springer Verlag, Berlin.
- 26 Vargas A., Donoso R., Ramírez M., Carrión J., Sánchez-López M.M., Moreno I. (2013) Liquid crystal retarder spectral retardance characterization based on a Cauchy dispersion relation and a voltage transfer function, Opt. Rev. 20, 5, 378–384. https://doi.org/10.1007/ s10043-013-0068-4.
- 27 Messaadi A., Sánchez-López M.M., García-Martínez P., Vargas A., Moreno I. (2016) Optical system for measuring the spectral retardance function in an extended range, J. Eur. Opt. Soc. – Rapid Pub. 12, 12, 21. https://doi.org/10.1186/s41476-016-0023-7.
- 28 Vargas A., Sánchez-López M.M., García-Martínez P., Arias J., Moreno I. (2014) Highly accurate spectral retardance characterization of a liquid crystal retarder including Fabry-Perot interference effects, J. Appl. Phys. 115, 3, 033101. https://doi.org/10.1063/ 1.4861635.
- 29 Chipman R.A. (1995) Polarimetry, in *Handbook of Optics*, 2nd edn., McGraw-Hill, New York.
- 30 Twietmeyer K.M., Chipman R.A. (2008) Optimization of Mueller matrix polarimeters in the presence of error sources, Opt. Exp. 16, 15, 11589–11603. https://doi.org/10.1364/OE.16.011589.
- 31 Peña-Gutiérrez S., Royo S. (2023) Polarization calibration assessment for a broadband imaging polarimeter based on a division of aperture architecture, *Opt. Exp.* **31**, 3, 3839–3856. https://doi.org/10.1364/OE.472070.
- 32 Peinado A., Lizana A., Vidal J., Iemmi C., Campos J. (2010) Optimization and performance criteria of a Stokes polarimeter based on two variable retarders, *Opt. Exp.* **18**, 8, 9815. https://doi.org/10.1364/OE.18.009815.
- 33 Cofré A., Vargas A., Torres-Ruiz F.A., Campos J., Lizana A., Sánchez-López M.M., Moreno I. (2017) Quantitative performance of a polarization diffraction grating polarimeter encoded onto two liquid-crystal-on-silicon displays, Opt. Laser Technol. 96, 219–226. https://doi.org/10.1016/j.optlastec.2017.05.027.
- 34 Roussel S., Boffety M., Goudail F. (2018) Polarimetric precision of micropolarizer grid-based camera in the presence of additive and

Poisson shot noise, *Opt. Exp.* **26**, 23, 29968–29982. https://doi.org/10.1364/OE.26.029968.

- 35 Janesick J. (1997) CCD transfer method standard for absolute performance of CCDs and digital CCD camera systems, *Proc. SPIE* **3019**, 70–102. https://doi.org/10.1117/12.275190.
- 36 Roussel S., Boffety M., Goudail F. (2019) On the optimal ways to perform full Stokes measurements with a linear division-of-focal plane polarimetric imager and a retarder, *Opt. Lett.* **44**, 11, 2927–2930. https://doi.org/10.1364/OL.44.002927.
- 37 Lu S.-Y., Chipman R.A. (1996) Interpretation of Mueller matrices based on polar decomposition, *J. Opt. Soc. Am. A* 13, 5, 1106–1113. https://doi.org/10.1364/JOSAA.13.001106.
- 38 Gil J.J., Ossikovski R. (2022) Polarized light and the mueller matrix approach, CRC Press, New York. https://doi.org/10.1201/9780367815578.
- 39 Rubano A., Cardano F., Piccirillo B., Marrucci L. (2019) Q-plate technology: A progress review, J. Opt. Soc. Am. B 36, 5, D70–D87. https://doi.org/10.1364/JOSAB.36.000D70.
- 40 Martínez A., Beaudoin N., Moreno I., Sánchez-López M.M., Velásquez P. (2006) Optimization of the contrast ratio of a ferroelectric liquid crystal optical modulator, J. Opt. A: Pure Appl. Opt. 8, 11, 1013–1018. https://doi.org/10.1088/1464-4258/8/11/013.
- 41 Lizana A., Estévez I., Torres-Ruiz F.A., Peinado A., Ramirez C., Campos J. (2015) Arbitrary state of polarization with customized degree of polarization generator, *Opt. Lett.* 40, 16, 3790–3793. https://doi.org/10.1364/OL.40.003790.
- 42 Marco D., López-Morales G., Sánchez-López M.M., Lizana A., Moreno I., Campos J. (2021) Customized depolarization spatial patterns with dynamic retardance functions, Sci. Rep. 11, 9415. https://doi.org/10.1038/s41598-021-88515-x.

Appendix

A1 Evaluation of the micro-polarizers limited extinction ratio

The polarization camera has wire-grid micro-polarizers attached to the pixels of the CMOS detector. In this appendix we evaluate the accuracy of the polarimeter selfcalibration procedure in terms of their extinction ratio. Since the polarization camera is used as the reference, the accuracy of the polarimeter calibration is dictated by the quality of its polarizers. Although other sources of errors have been identified (such as the spatial variation of the extinction ratio, or spatial variations in the orientation angle of the micro-polarizers transmission axes) [34], here we assume a simplified model where we consider the micro-polarizers perfectly oriented (horizontal, vertical, diagonal and antidiagonal), but having a limited and spatially uniform extinction ratio $\mathrm{ER} = T_{||}/T_{\perp}$ where $T_{||}$ and T_{\perp} are the transmission for parallel and crossed polarizers respectively. Information about this main source of error in the polarization camera is provided by the supplier, indicating in our case values ER > 120:1 in the three colour

bands. To take this into account, the MM of these four linear polarizers with limited ER is calculated analytically. The MM of a polarizer aligned horizontal and with limited extinction ratio is given by [1]:

$$\mathbf{P}_{0} = \frac{T_{\parallel}}{2} \begin{pmatrix} 1+e & 1-e & 0 & 0\\ 1-e & 1+e & 0 & 0\\ 0 & 0 & 2\sqrt{e} & 0\\ 0 & 0 & 0 & 2\sqrt{e} \end{pmatrix}, \tag{A1a}$$

where $e \equiv 1/\text{ER} = T_{\perp}/T_{\parallel}$. The limit $e \to 0$ leads to the ideal polarizer with normalized MM:

We measured values ER > 120:1 for our camera polarizers in the three spectral bands, in agreement with the manufacturer data. The MM of the micro-polarizers oriented vertical and at $\pm 45^{\circ}$ are simply obtained by applying the corresponding rotation transformation [1].

Assuming ideal input states (ideal values in the S matrix in Eq. (3)), and that the circular components R and L are measured using an ideal QWP in front of the camera, the intensity measured for each input state when being analyzed with these limited linear micro-polarizers can be calculated analytically, leading to an intensity matrix as in equation (5) which now takes the following form:

See the equation (A2) bottom of the page

where the ideal matrix in equation (5) is recovered for the limit $e \to 0$ and $T_{\parallel} \to 1$. Hence, equation (A2) is the intensity matrix of the polarimeter calibration, which contains the errors induced by the limited ER of the micro-polarizers. The analytical expression of the calibrated PSA matrix that compensates the limited ER is thus obtained as $\mathbf{A}(e) = \mathbf{I}_{\text{air}}(e) \cdot \mathbf{S}^{-1}$) using equation (A2) and the ideal \mathbf{S}^{-1} matrix in equation (4). Its pseudo-inverse is given by:

$$\mathbf{A}^{-1}(e) = \frac{1}{T_{\parallel}} \begin{pmatrix} \frac{1}{3(1+e)} & \frac{1}{3(1+e)} & \frac{1}{3(1+e)} & \frac{1}{3(1+e)} & \frac{1}{3(1+e)} \\ \frac{1}{1-e} & \frac{1}{1-e} & 0 & 0 & 0 & 0 \\ 0 & 0 & \frac{1}{1-e} & \frac{1}{1-e} & 0 & 0 \\ 0 & 0 & 0 & \frac{1}{1-e} & \frac{1}{1-e} & \frac{1}{1-e} \end{pmatrix}.$$
(A3)

$$\mathbf{I}_{air}(e) = T_{\parallel} \begin{pmatrix} 1 & e & \frac{1}{2}(1+e) & \frac{1}{2}(1+e) & \frac{1}{2}(1+e) & \frac{1}{2}(1+e) \\ e & 1 & \frac{1}{2}(1+e) & \frac{1}{2}(1+e) & \frac{1}{2}(1+e) & \frac{1}{2}(1+e) \\ \frac{1}{2}(1+e) & \frac{1}{2}(1+e) & 1 & e & \frac{1}{2}(1+e) & \frac{1}{2}(1+e) \\ \frac{1}{2}(1+e) & \frac{1}{2}(1+e) & e & 1 & \frac{1}{2}(1+e) & \frac{1}{2}(1+e) \\ \frac{1}{2}(1+e) & \frac{1}{2}(1+e) & \frac{1}{2}(1+e) & \frac{1}{2}(1+e) & 1 & e \\ \frac{1}{2}(1+e) & \frac{1}{2}(1+e) & \frac{1}{2}(1+e) & \frac{1}{2}(1+e) & e & 1 \end{pmatrix},$$
(A2)

This matrix recovers the ideal case in the right part of equation (7) in the limit when $e \to 0$ and $T_{\parallel} \to 1$.

To evaluate analytically the impact of the limited extinction ratio on the polarimeter measurement, we first consider as sample the air and apply equation (9), $\mathbf{M} = \mathbf{A}^{-1} \mathbf{I} \mathbf{S}^{-1}$, to obtain the MM of air. Here we use the non-ideal intensity matrix \mathbf{I}_{air} in equation (A2), but we consider the ideal values of the matrices \mathbf{S}^{-1} and \mathbf{A}^{-1} given in the right part of equation (4) and equation (7) respectively. This way we assume that the polarizers extinction ratio error is present in the experiment, but it is ignored in the polarimetric calculation. The analytical calculation leads to a MM matrix affected by the error e given by:

$$\mathbf{M}_{\text{air}}(e) = \mathbf{A}^{-1} \cdot \mathbf{I}_{\text{air}}(e) \cdot \mathbf{S}^{-1}$$

$$= T_{\parallel} \begin{pmatrix} 1 + e & 0 & 0 & 0 \\ 0 & 1 - e & 0 & 0 \\ 0 & 0 & 1 - e & 0 \\ 0 & 0 & 0 & 1 - e \end{pmatrix}, \quad (A4)$$

which recovers the expected identity matrix of air when $e\to 0$ and $T_{||}\to 1.$ The MM in equation (A4) can be rewritten as

$$\mathbf{M}_{air}(e) = T_{\parallel}(1+e) \begin{pmatrix} 1 & 0 & 0 & 0 \\ 0 & 1-\delta & 0 & 0 \\ 0 & 0 & 1-\delta & 0 \\ 0 & 0 & 0 & 1-\delta \end{pmatrix}, \quad (A5)$$

which shows that the MM normalized to m_{00} has diagonal elements $m_{11}=m_{22}=m_{33}=(1-e)/(1+e)\equiv 1-\delta$. This result reflects that the limited extinction ratio of the camera micro-polarizers induces an error δ in the diagonal elements of the normalized MM for air given by:

$$\delta = 1 - \frac{1 - e}{1 + e} = \frac{2e}{1 + e} = \frac{2}{1 + ER} \simeq \frac{2}{ER},\tag{A6}$$

where we used that e=1/ER and $ER\gg 1$ in the final approximation. Figure A1 shows the evolution of this error parameter as a function of the extinction ratio. Since ER > 120:1 in our polarization camera, the deviation expected from this problem is $\delta < 1.7\%$.

Obviously, the identity MM of air is also recovered when the PSA calibration compensates for the limited ER i.e., when using the PSA pseudo-inverse matrix $\mathbf{A}^{-1}(e)$ in equation (A3). Then equation (9) results directly on the identity matrix since $\mathbf{A}^{-1}(e) \cdot \mathbf{I}_{air}(e) \cdot \mathbf{S}^{-1} = \mathbf{A}^{-1}(e) \cdot \mathbf{A}(e)$.

We can now analytically show that, for any other sample, the procedure described in Section 4 compensates the limited ER of the micro-polarizers if the PSA pseudo-inverse matrix $\mathbf{A}^{-1}(e)$ in equation (A3) is the one employed to retrieve the Mueller matrix. To illustrate this, we consider as sample an ideal linear polarizer with horizontal transmission axis, whose MM is given by equation (A1b). The 6×6 elements of the intensity matrix $\mathbf{I}_{p}(e)$ of this polarizer sample are analytically obtained by calculating the intensity I_{ag} expected for each input state, g=H,V,D,A,R,L (assumed ideal), when being detected through analyzers a=H,V,D,A,R,L affected by a limited extinction ratio ($e\neq 0$). In this case, the obtained intensity matrix is:

See the equation (A7) bottom of the page

The MM of this polarizer sample is then obtained from equation (9). If the calculation is made ignoring the error in the micro-polarizers, i.e., using the ideal \mathbf{A}^{-1} matrix defined equation (7), the analytical expression of such non-compensated MM is:

Thus, the the normalized MM contains errors in the m_{10} and m_{11} elements. These errors are completely compensated by using the pseudo-inverse matrix $\mathbf{A}^{-1}(e)$ of equation (A3). A simple calculation shows that the matrix product $\mathbf{A}^{-1}(e) \mathbf{I}_p(e) \mathbf{S}^{-1}$ results in the expected MM in equation (A1b).

Finally, the same kind of calculation can be generalized to an arbitrary sample described by a generic MM:

$$\mathbf{M}_{s} = \begin{pmatrix} m_{00} & m_{01} & m_{02} & m_{03} \\ m_{10} & m_{11} & m_{12} & m_{13} \\ m_{20} & m_{21} & m_{22} & m_{23} \\ m_{30} & m_{31} & m_{32} & m_{33} \end{pmatrix}.$$
(A9)

We again evaluate analytically the intensity matrix $I_{\rm s}(e)$ when the sample is introduced in the polarimeter affected by the error e. We calculate the intensity $I_{\rm ag}$ expected for each input state $g={\rm H,V,D,A,R,L}$ (assumed ideal), when

$$I_{p}(e) = T_{\parallel} \begin{pmatrix} 1 & e & \frac{1}{2} & \frac{1}{2} & \frac{1}{2} & \frac{1}{2} \\ e & 1 & \frac{1}{2}e & \frac{1}{2}e & \frac{1}{2}e & \frac{1}{2}e \\ \frac{1}{2}(1+e) & 0 & \frac{1}{4}(1+e) & \frac{1}{4}(1+e) & \frac{1}{4}(1+e) & \frac{1}{4}(1+e) \\ \frac{1}{2}(1+e) & 0 & \frac{1}{4}(1+e) & \frac{1}{4}(1+e) & \frac{1}{4}(1+e) & \frac{1}{4}(1+e) \\ \frac{1}{2}(1+e) & 0 & \frac{1}{4}(1+e) & \frac{1}{4}(1+e) & \frac{1}{4}(1+e) \\ \frac{1}{2}(1+e) & 0 & \frac{1}{4}(1+e) & \frac{1}{4}(1+e) & \frac{1}{4}(1+e) \end{pmatrix}$$
(A7)

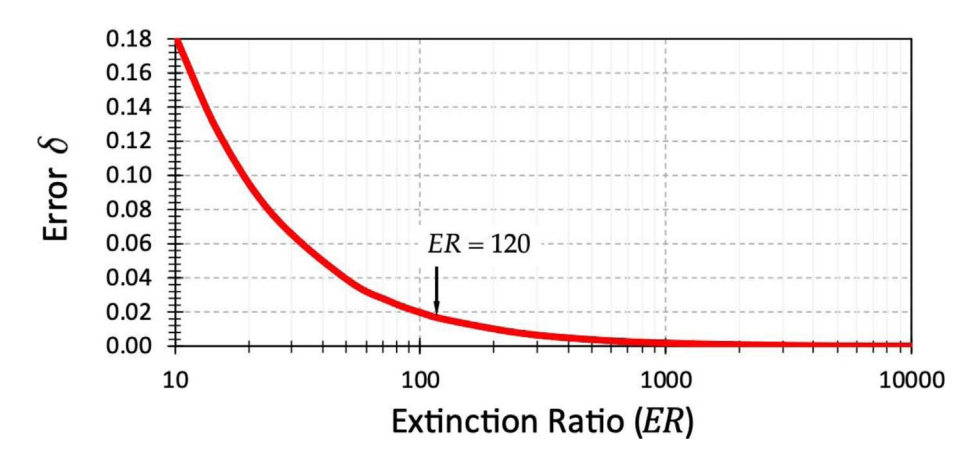


Fig. A1. Evolution of the error parameter δ as a function of the polarizers extinction ratio ER. The arrow indicates the limit value ER = 120 measured for our polarization camera.

$$M_{s}(e) = T_{\parallel}(1+e) \begin{pmatrix} m_{00} & m_{01} & m_{02} & m_{03} \\ m_{10}(1-\delta) & m_{11}(1-\delta) & m_{12}(1-\delta) & m_{13}(1-\delta) \\ m_{20}(1-\delta) & m_{21}(1-\delta) & m_{22}(1-\delta) & m_{23}(1-\delta) \\ m_{30}(1-\delta) & m_{31}(1-\delta) & m_{32}(1-\delta) & m_{33}(1-\delta) \end{pmatrix},$$
(A10)

being detected through analyzers a = H, V, D, A, R, L affected by a limited extinction ratio ($e \neq 0$). Again, the impact of the limited extinction ratio on the polarimeter measurement can be analytically evaluated by considering equation (9), $\mathbf{M}_{\mathbf{S}}(e) = \mathbf{A}^{-1} \cdot \mathbf{I}_{\mathbf{S}}(e) \cdot \mathbf{S}^{-1}$, where the ideal \mathbf{A}^{-1} is applied (thus ignoring the error in the micropolarizers). It is a long but straightforward calculation to obtain that the retrieved MM reads:

See the equation (A10) top of the page

which recovers the ideal matrix in equation (A9) in the limit $e \to 0$ ($\delta \to 0$) and $T_{\parallel} \to 1$. This shows that all elements

in the normalized MM except those in the first row are affected by the same factor $1 - \delta$.

However, it can also be demonstrated that the sample matrix in equation (A10) is recovered when using the PSA matrix in equation (A3) to calculate $\mathbf{A}^{-1}(e) \cdot \mathbf{I}_{\mathrm{s}}(e) \cdot \mathbf{S}^{-1} = \mathbf{M}_{\mathrm{s}}$, i.e., the ER error of the micro-polarizers is completely compensated.

Finally, let us note that we are applying this compensation method to a simplified model where only a uniform limited extinction ratio of the micro-polarizers is considered. The effect of spatial variations of the extinction ratio or errors in the orientation of the micro-polarizers can be considered as indicated in [34]. J. Eur. Opt. Society-Rapid Publ. 2024, $\bf 20,\ 30$ © The Author(s), published by EDP Sciences, 2024

https://doi.org/10.1051/jeos/2024031

 $Available\ online\ at:\ https://jeos.edpsciences.org$

EOSAM 2023

Guest editors: Patricia Segonds, Guy Millot and Bertrand Kibler

RESEARCH ARTICLE OPEN 3 ACCESS

Parallel illumination for depletion microscopy through acousto-optic spatial light modulation

Fabian Klingmann^{1,2}, Nick Toledo-García¹, Estela Martín-Badosa^{1,3}, Mario Montes-Usategui^{1,3}, and Jordi Tiana-Alsina^{1,3,*}

- Department de Física Aplicada, Facultat de Física, Universitat de Barcelona, Martí i Franquès 1, 08028 Barcelona, Spain
- ² Fraunhofer-Institut für Photonische Mikrosysteme (IPMS), Maria-Reiche-Str. 2, 01109 Dresden, Germany
- ³ Institut de Nanociència i Nanotecnologia (IN2UB), Diagonal 654, 08028 Barcelona, Spain

Received 31 January 2024 / Accepted 27 May 2024

Abstract. State-of-the-art super-resolution microscopy techniques, including Stimulated Emission Depletion (STED), Reversible Saturable Optical Fluorescence Transitions (RESOLFT), and Switching Laser Mode (SLAM) microscopies, implement Laguerre-Gaussian beams, also known as vortex or doughnut beams to capture fluorescence information within a sub-wavelength area of the observed sample, effectively surpassing the diffraction limit and significantly improving the quality of the image. However, these techniques typically operate at point by point basis, involving time-consuming scanning of the sample to construct a complete, meaningful image. Therefore, for real-time live cell imaging purposes, the parallelization of illumination is crucial. In this study, we demonstrate the parallel generation of arbitrary arrays of Gaussian and Laguerre-Gaussian laser foci suitable for super-resolution microscopy. We achieve rapid scanning through the sample using acousto-optic spatial light modulation, a technique we have previously pioneered across various fields. By employing parallelized illumination with both Gaussian and doughnut beams, we aim to capture super- resolution images.

Keywords: Parallel ilumination, Acousto-optical devices, Super-resolution microscopy, Subtraction microscopy.

1 Introduction

Resolution is one of the most significant constraints in fluorescence microscopy, even for the edge-cutting technology confocal microscopes that are the most prevalent for visualization in many applications in the Life Sciences. It is no wonder, then, that the emergence of optical superresolution, around the turn of the century [1, 2], has profoundly transformed the modern microscopy landscape. The emerging super-resolution techniques, Stimulated Emission Depletion (STED) and its variants (Ground State Depletion, GSD [3], Continuous Wave STED, CW-STED [4], Reversible Saturable Optical Fluorescence Transitions, RESOLFT [5, 6], and Minimum Emission Fluxes, MINFLUX [7]) are noteworthy for their exceptional resolution capabilities (reaching down to 1–2 nm for MINFLUX). Depletion microscopies like STED are based on the confinement of the fluorescent emission within a sub-wavelength region through the coordinated action of two lasers. The first laser beam presents a typical TEM00 Gaussian intensity profile, and it is used to excite (or activate, in RESOLFT) the fluorophores within the sample. A second

2 Acousto-optic deflectors (AODs) for parallel illumination

Despite the success of the implementation of highly parallel depletion microscopy setups, typically RESOLFT due to its

laser beam, characterized by a "doughnut" intensity profile (i.e., a Laguerre-Gaussian beam), suppresses the spontaneous fluorescence (or deactivates the fluorophores) around the central singularity, leaving the molecules near the dark core unaffected. Consequently, the resulting fluorescent emission comes from a reduced, sub-diffractive area of the sample. The subsequent image is constructed by scanning the sample. The collection of emitted photons yields an effective point spread function (PSF) that achieves superresolution within the range of 30–70 nm [1, 2]. While STED uses standard fluorophores, RESOLFT uses photoswitchable molecules, which drastically reduce the laser power needed for the depletion beam, thus inducing less photodamage, making prolonged observation of living cells more feasible [5]. Nevertheless, one of the several drawbacks associated with STED and its derivatives is the relatively slow operation due to the sequential composition of images.

^{*} Corresponding author: jordi.tiana@ub.edu

cell friendly properties, which significantly speed up the scanning process, as described in the literature [6, 8], these methods depend on the periodic minima of a standing wave illumination to confine fluorescence at multiple spots simultaneously. In this contribution, we present an alternative approach: the generation of extensive arrays of switchable Gaussian and Laguerre-Gaussian laser spots using acousto-optic holography. Acousto-optic deflectors (AODs) are TeO2 crystal based beam-steering devices, wherein the refractive index is modulated by an acoustic wave generated with an oscillating piezoelectric transducer driven by an electrical signal. Recent studies have demonstrated the versatility of AODs as general-purpose spatial light modulators. This is achieved by computing driving signals using digital holography techniques and feeding the transducer with these signals via a programmable radiofrequency generator [9–11]. Within the crystal, a specific refractive index variation emerges, enabling spatial control over a laser beam as it traverses the device. The details of how we compute such holographic driving signals have been reported elsewhere [9–11]; however, throughout the next sections we show that properly designed acousto-optic holograms can be used as the basis for parallelizing the paired excitation/de-excitation beams essential in STED-like super-resolution microscopy. Additionally, acousto-optic holography offers a convenient method for rapidly scanning the sample using these illumination arrays, thereby presenting a promising technology for the development of future live-cell, optical super-resolution microscopes capable of operating at video rates. Although there are previous studies of the behavior of Laguerre-Gaussian beams after deflection by AODs, which show that their shape remains largely unaffected, these studies do not specifically consider their suitability for super-resolution microscopy [12, 13].

3 Experimental setup

In this work we aim to produce, assess, and validate the optical quality of TEM01 Laguerre-Gaussian beams, also known as optical vortices or doughnut beams, after going through a pair of active acousto-optic cells with a view to parallelize STED-like super-resolution microscopy. To accomplish this goal, we will utilize the experimental setup depicted in Figure 1, which employs a two-path scheme illuminated with a TEM00 Gaussian beam. The illumination laser source is a $\lambda = 488$ nm laser (Integrated Optics, MatchBox 0488L-15A-NI-PT-NF). The setup offers flexibility in controlling the active light path by adjusting the input polarization using a half-wave plate placed on a rotation mount that allows for precise tuning at the entrance port of the polarizing beam splitter. In one of the paths, the TEM01 Laguerre-Gaussian mode is generated when a Gaussian beam passes through a vortex phase plate. A vortex phase plate or spiral phase plate consists of a dielectric coating plate whose thickness increases in a given number of steps, proportionally to the azimuth angle around a point in the center [14]. The Vortex-Photonics phase plate (V-488-10-1) possesses 64 steps, and is tuned to our working wavelength ($\lambda = 488 \text{ nm}$) with a topological charge m = 1.

On the other path, the input TEM00 Gaussian mode is freely propagated. A second half-wave retarder is placed after a polarizing beam-splitter that again merges the two optical trains. By always moving both $\lambda/2$ -plates by the same angle, the polarization at the AOD will not change. Two mirrors are then used to align the beam with the camera port of the microscope. Since metallic mirrors were used, it was necessary to place a linear polarizer after them, to filter out undesired polarization components. The image acquisition time of this setup is currently limited by the rotation time of the $\lambda/2$ -plates, which takes around 100 us to complete the 45° travel needed to change between input and output polarization states. Finally, either the Gaussian or the doughnut beam enters into our microscope (Nikon Eclipse TE2000) equipped with a high numerical aperture objective (Nikon CFI PlanApo λD, oil-immersion, 100×, NA = 1.45). As previously mentioned, in order to create a 2D spot array for illuminating the sample, two AODs are employed (Fig. 1, upper right inset). The scanning of the sample along the horizontal and vertical directions is achieved by shifting the illumination pattern through a linear phase ramp introduced into the hologram (since there is a Fourier transform relationship between the AODs and the objective focal plane). To image a sample with a field of view spanning $66 \times 66 \mu m$, we employed an illumination matrix consisting of 20×20 points, featuring Gaussian or doughnut beams, each spaced 3.3 µm apart. This illumination matrix scanned the sample in 20×20 steps. For each scanning step the sample was exposed for 10 ms for a resulting frame rate around 0.25 Hz (corresponding to the images shown in the manuscript). With the reported prototype, we could eventually achieve a frame rate of one image per second, by reducing the exposure time and compensating for with an increased illumination power.

Based on this scheme, we have designed and implemented, at a proof of concept level, a microscope capable of parallelizing the illumination. In what follows, we will provide results that demonstrate the capacity of this instrument for super-resolution microscopy, for which we will employ an algorithm based on the subtraction between the images obtained with Gaussian and doughnut illuminations.

4 Weighted subtraction microscopy approach

As described in [15, 16], subtraction microscopy is a technique that involves illumination with both a Gaussian and a doughnut beam, which leads to a super-resolution comparable to that provided by structured illumination microscopy. Subtraction microscopy is a cost-effective implementation of STED microscopy, a type of laser scanning microscopy where two fluorescent images are taken, one when illuminated by a standard Gaussian and one with a doughnut profile, as the excitation beams. The doughnut-illuminated image is then subtracted from the Gaussian-illuminated image with a weighting factor α :

$$I_{im}(x,y) = I_q(x,y) - \alpha \cdot I_d(x,y) \tag{1}$$

The choice of the α factor has a large influence on the image quality and resolution. A value that is too small will not

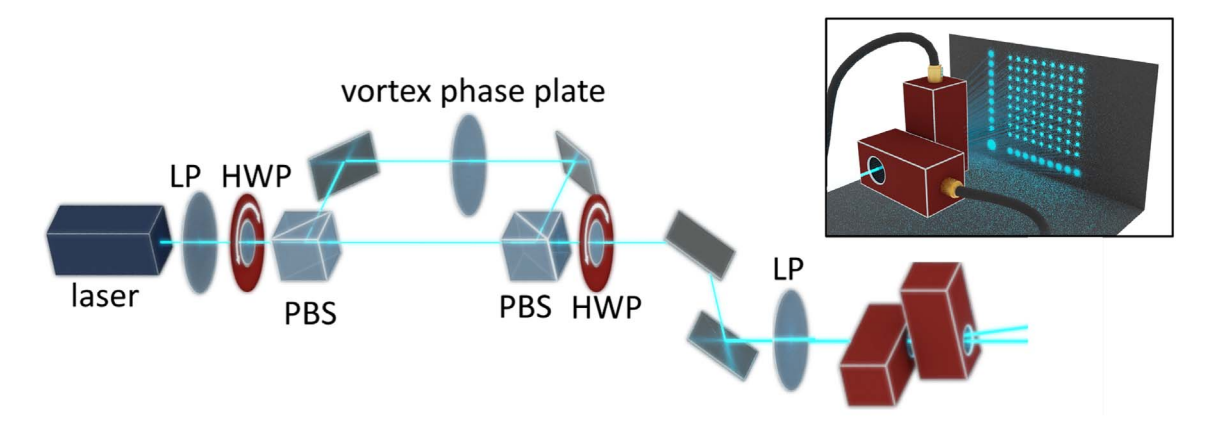


Figure 1. Experimental setup for the characterization of the doughnut beam. (LP) linear polarizers, (HWP) half-wave plates mounted in rotation mounts, (PBS) polarizing beam splitters. The upper right inset shows the two AOD configuration used to generate the 2D illumination spot array.

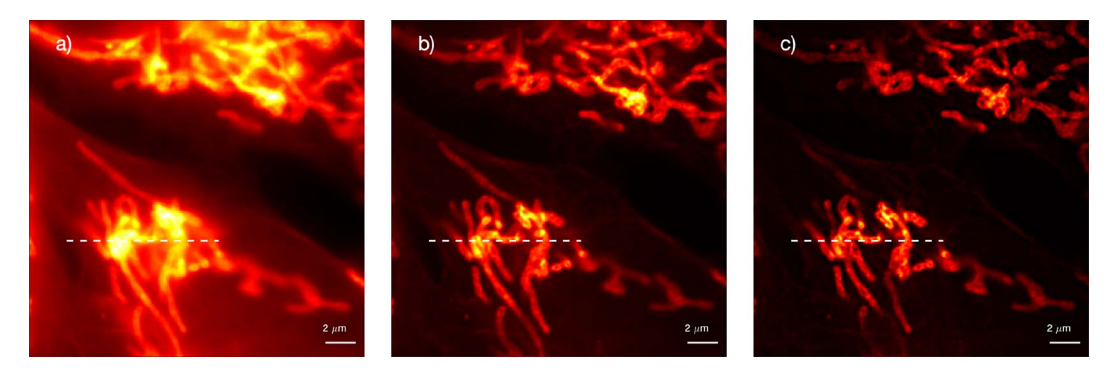


Figure 2. Images of mitochondria in huFIB cells synthesized with (a) epifluorescence, (b) virtual pinhole with Gaussian illumination and (c) virtual pinhole with subtraction algorithms. For the subtraction algorithm, a constant coefficient of $\alpha = 0.58$ was chosen.

lead to an increase in resolution, whereas too large a value will produce artifacts in the final image. We have found that a factor $\alpha=0.58$ leads to maximum resolution without visible artifacts in our case.

5 Results

We show in Figure 2 the reconstructed images of mitochondria in human fibroblasts labelled with Alexa Fluor 488 (Cells 4c, GATTAquant). In Figure 2(a) epifluorescence images are synthesized by assigning to each pixel the averaged value of that pixel in all images gathered under Gaussian illumination. As expected, under this reconstruction algorithm, the background from out-of-focus light is quite prominent.

In Figure 2(b) we used a virtual pinhole reconstruction algorithm, imitating the physical pinhole of confocal microscopy, where each point of the captured image is multiplied by a Gaussian mask with a size of the effective point spread function (PSF, in our case the size was chosen to be 195 nm). This method allows for the capture of optical sections of samples with improved resolution and

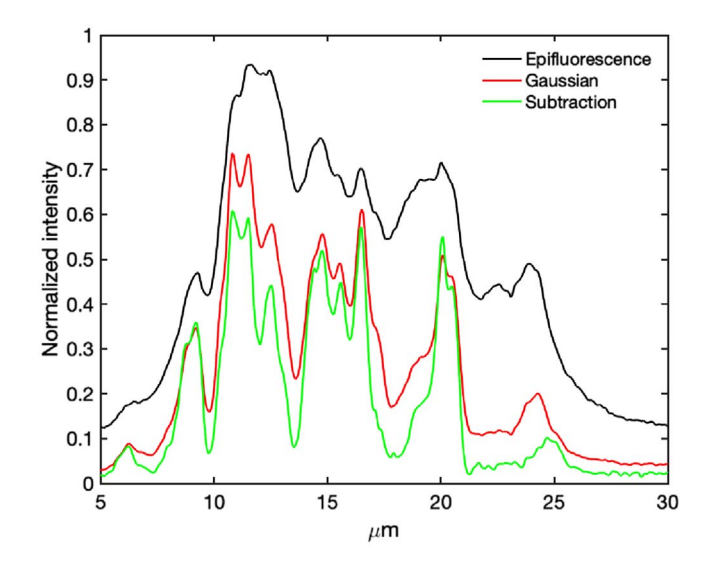


Figure 3. Intensity profiles extracted from dashed white lines in Figure 2 corresponding to epifluorescence (black line), virtual pinhole with Gaussian illumination (red line), and virtual pinhole with subtraction (green line) reconstructed images.

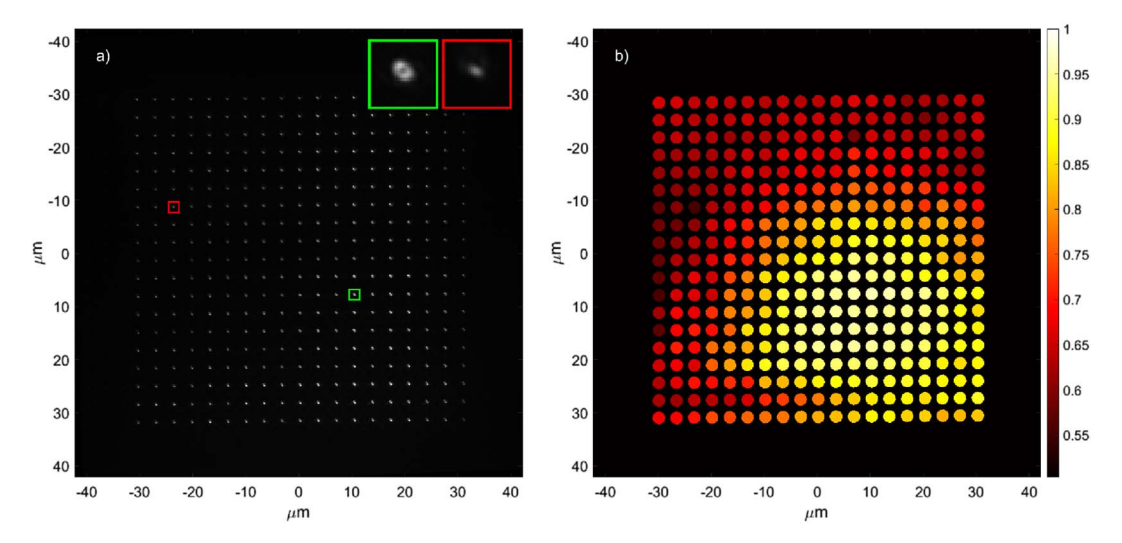


Figure 4. (a) Image of the doughnut illumination pattern using a mirror sample and (b) R^2 map to quantify the quality of doughnuts. The red and green squares represent the doughnut spots with the lowest and highest R^2 values within the array, respectively.

reduced background noise. Under this algorithm, a clear improvement in terms of out-of-focus light is observed, although the images still do not show super-resolution information.

Finally, in Figure 2(c) the reconstructed image using the subtraction algorithm in combination with the two illuminations (Gaussian/Laguerre-Gaussian) and virtual pinholing is presented. A clear improvement in both out-of-focus light and resolution can be appreciated.

In order to qualitatively assess the enhancement in resolution achieved by the three implemented algorithms in Figure 3, we present a horizontal cross-section (indicated by the dashed white line in Fig. 2). This figure demonstrates a noticeable improvement in both background intensity and resolution. Particularly with the subtraction algorithm, significantly finer intensity peaks are evident, characterized by a reduced full width at half maximum of the mitochondria membrane sections.

Furthermore, in order to quantitatively evaluate the resolution of these images, the ImageJ plugin presented in [17] is used. The resolution obtained is 230 nm, 200 nm and 136 nm for epifluorescence, Gaussian pinholing and subtraction with pinholing methods, respectively. With respect to the Abbe diffraction limit, $\Delta x = \frac{\lambda}{2NA} = 190$ nm for a wavelength of 488 nm and an effective numerical aperture of 1.33, we have achieved a $\sqrt{2}$ improvement factor.

Finally, in order to illustrate the quality of the doughnuts across the entire field of view, we examine their characteristics. As discussed in [18], doughnut beams are highly sensitive to off-axis deformations and very particularly to astigmatic aberrations. In Figure 4, it is evident that the quality of the doughnuts, characterized by the \mathbb{R}^2 factor obtained from the 2D fitting of the doughnut modes, deteriorates as we move radially away from the optical axis. It is worth noting that in our setup, the optical axis is slightly shifted to the bottom right corner of the image.

6 Conclusions

In this work we have presented a proof of concept microscope, based on AODs technology to parallelise both Gaussian and doughnut illumination, capable of obtaining super-resolution images with a subtraction-based algorithm. Even though we already obtained super-resolved images, we anticipate a better resolution in the future when addressing the correction of astigmatic aberrations in our setup.

Currently, the main time limitation comes from the rotational mounts that control the input and output polarization states (that switch from Gaussian to doughnut illumination), but in future implementations we expect to reduce it by using two lasers and triggering signals. Then the imaging time will mainly depend on the exposure time and the number of steps in the scanning process, but since the scanning is parallelized, a significant reduction compared to conventional laser scanning microscopes will be easily achieved.

Acknowledgments

We thank Raùl Bola for his previous development of a parallel confocal microscope, which significantly facilitated our own research and development efforts. Furthermore, we are grateful for his valuable insights and informal scientific discussions, which have greatly contributed to the advancement of our work.

Funding

This work was supported by grant PREP2022-000292, funded by MICIU/AEI/10.13039/501100011033 and ESF+, by grant PID2022-136796OB-I00, funded by MCIN/AEI/10.13039/501100011033/FEDER, UE, by Ministerio de Ciencia e Innovación (PDC2022-133351-I00 and PID2022-136796OB-I00), and Fundació Bosch i Gimpera (F2I-PdC-2023-008-600427).

Conflicts of interest

The authors declare no conflicts of interest.

Data availability statement

The data is available from the corresponding author under reasonable request.

Author contribution statement

Fabian Klingmann: Investigation (equal); Software (equal); Validation (equal); Formal analysis (equal); Visualization (equal); Writing – original draft (equal); Writing – review & editing (equal). Nick Toledo-García: Software (equal); Validation (equal); Formal analysis (equal); Writing – review & editing (equal). Estela Martín-Badosa: Conceptualization (equal); Visualization (equal); Writing – original draft (equal); Writing – review & editing (equal); Funding acquisition (equal). Mario Montes-Usategui: Conceptualization (equal); Visualization (equal); Writing – original draft (equal); Writing – review & editing (equal); Funding acquisition (equal). Jordi Tiana-Alsina: Conceptualization (equal); Investigation (equal); Visualization (equal); Writing – original draft (equal); Writing – review & editing (equal); Funding acquisition (equal).

References

- 1 Lakadamvali M. (2014) ChemPhysChem 15, 630.
- 2 Sahl S.J., Hell S.W. (2019) High-resolution 3D light microscopy with STED and RESOLFT, Springer International Publishing, Cham.
- 3 Hell S.W., Kroug M. (1995) Appl. Phys. B 60, 495.

- 4 Willig K.I., Harke B., Medda R., Hell S.W. (2007) Nat. Methods 4, 915.
- 5 Hofmann M., Eggeling C., Jakobs S., Hell S.W. (2005) Proc. Natl. Acad. Sci. 102, 17565.
- 6 Chmyrov A., Keller J., Grotjohann T., Ratz M., d'Este E., Jakobs S., Eggeling C., Hell S.W. (2013) Nat. Methods 10, 737.
- 7 Balzarotti F., Eilers Y., Gwosch K.C., Gynnå A.H., Westphal V., Stefani F.D., Elf J., Hell S.W. (2017) Science 355, 606.
- 8 Masullo L.A., Bodén A., Pennacchietti F., Coceano G., Ratz M., Testa I. (2018) *Nat. Commun.* **9**, 3281.
- 9 Treptow D., Bola R., Martín-Badosa E., Montes-Usategui M. (2021) Sci. Rep. 11, 21261.
- 10 Bola R., Treptow D., Marzoa A., Montes-Usategui M., Martín-Badosa E. (2020) Opt. Lett. 45, 2938.
- 11 Montes-Ustegui M., Bola R., Martín-Badosa E., Treptow D. (2019) Programmable multiple-point illuminator, confocal filter, confocal microscope and method to operate said confocal microscope, PCT/EP2019/067517.
- 12 Mur J., Kavčič B., Poberaj I. (2013) Appl. Opt. 52, 6506.
- 13 Martynyuk-Lototska I., Vasylkiv Y., Dudok T., Skab I., Vlokh R. (2018) Optik 155, 179.
- 14 Beijersbergen M.W., Coerwinkel R.P.C., Kristensen M., Woerdman J.P. (1994) Opt. Commun. 112, 321.
- 15 Korobchevskaya K., Peres C., Li Z., Antipov A., Sheppard C.J.R., Diaspro A., Bianchini P. (2016) Sci. Rep. 6, 25816.
- 16 Kuang C., Li S., Liu W., Hao X., Gu Z., Wang Y., Ge J., Li H., Liu X. (2013) Sci. Rep. 3, 1441.
- 17 Descloux A., Grußmayer K.S., Radenovic A. (2019) Nat. Methods 16, 918.
- 18 Ohland J.B., Eisenbarth U., Roth M., Bagnoud V. (2019) Appl. Phys. B 125, 202.

J. Eur. Opt. Society-Rapid Publ. 2024, $\bf 20,\,31$ © The Author(s), published by EDP Sciences, 2024

https://doi.org/10.1051/jeos/2024032

Available online at: https://jeos.edpsciences.org

EOSAM 2023

Guest editors: Patricia Segonds, Guy Millot and Bertrand Kibler

SHORT COMMUNICATION

OPEN 3 ACCESS

Digital holographic microscopy applied to 3D computer micro-vision by using deep neural networks

Stéphane Cuenat^a, Jesús E. Brito Carcaño^a, Belal Ahmad, Patrick Sandoz, Raphaël Couturier, Guillaume J. Laurent, and Maxime Jacquot^{*}

Université de Franche-Comté, SUPMICROTECH-ENSMM, CNRS, Institut FEMTO-ST, 25000 Besançon, France

Received 31 January 2024 / Accepted 13 June 2024

Abstract. Deep neural networks (DNNs) are increasingly employed across diverse fields of applied science, particularly in areas like computer vision and image processing, where they enhance the performance of instruments. Various advanced coherent imaging techniques, including digital holography, leverage different deep architectures like convolutional neural networks (CNN) or Vision Transformers (ViT). These architectures enable the extraction of diverse metrics such as autofocusing reconstruction distance or 3D position determination, facilitating applications in automated microscopy and phase image restitution. In this work, we propose a hybrid approach utilizing an adapted version of the GedankenNet model, coupled with a UNet-like model, for the purpose of accessing micro-objects 3D pose measurements. These networks are trained on simulated holographic datasets. Our approach achieves an accuracy of 98% in inferring the 3D poses. We show that a GedankenNet can be used as a regression tool and is faster than a Tiny-ViT (TViT) model. Overall, integrating deep neural networks into digital holographic microscopy and 3D computer micro-vision holds the promise of significantly enhancing the robustness and processing speed of holograms for precise 3D position inference and control, particularly in micro-robotics applications.

Keywords: Digital holography, Microscopy, Computer micro-vision, Deep neural networks.

1 Introduction

In computer vision and robotics, accurate 3D positioning and trajectory determination are crucial for a variety of applications, including industrial and clinical [1]. Neural networks, including convolutional neural networks (CNNs) or Vision Transformers (ViT) play a significant role in visual data processing [2]. Digital holography (DH) in microscopy enhances the analysis of object amplitude and phase in a single image with off-axis configuration, improving the accuracy of in-focus position detection without mechanical adjustments. Combining Deep Neural Networks (DNN), mixing version of the GedankenNet model [3] and a UNet-like model [4] with DH provides a promising solution for accurately controlling complex trajectories of micro-objects in automated microscopy in real-time constrains [5].

2 Theoretical background and context

2.1 Deep neural networks

DNNs inspired by biological neural networks, process, classify, and predict complex data through multi-layer structures. These networks employ non-linear transformations from input to output layers, enabling tasks like linearization in higher-dimensional spaces [4]. Optimization of DNN results involves a learning step, training the network with input-output data pairs. Adequate training data volume is crucial for optimal performance. DNNs, notably convolutional CNNs and ViT models, have demonstrated high effectiveness in tasks like image classification, computer vision, and solving complex problems such as autofocusing in DH [2, 3].

2.2 Digital holographic microscopy and computer micro-vision for micro-robotics

DH is an advanced imaging technique capturing both amplitude and phase of an object's entire wavefield using a CMOS imaging sensor. In Figure 1, we show typical experimental digital hologram a 2D pseudo-periodic pattern

^aJesús E. Brito Carcaño and Stéphane Cuenat contributed equally to this work as first authors.

^{*} Corresponding author: maxime.jacquot@univ-fcomte.fr

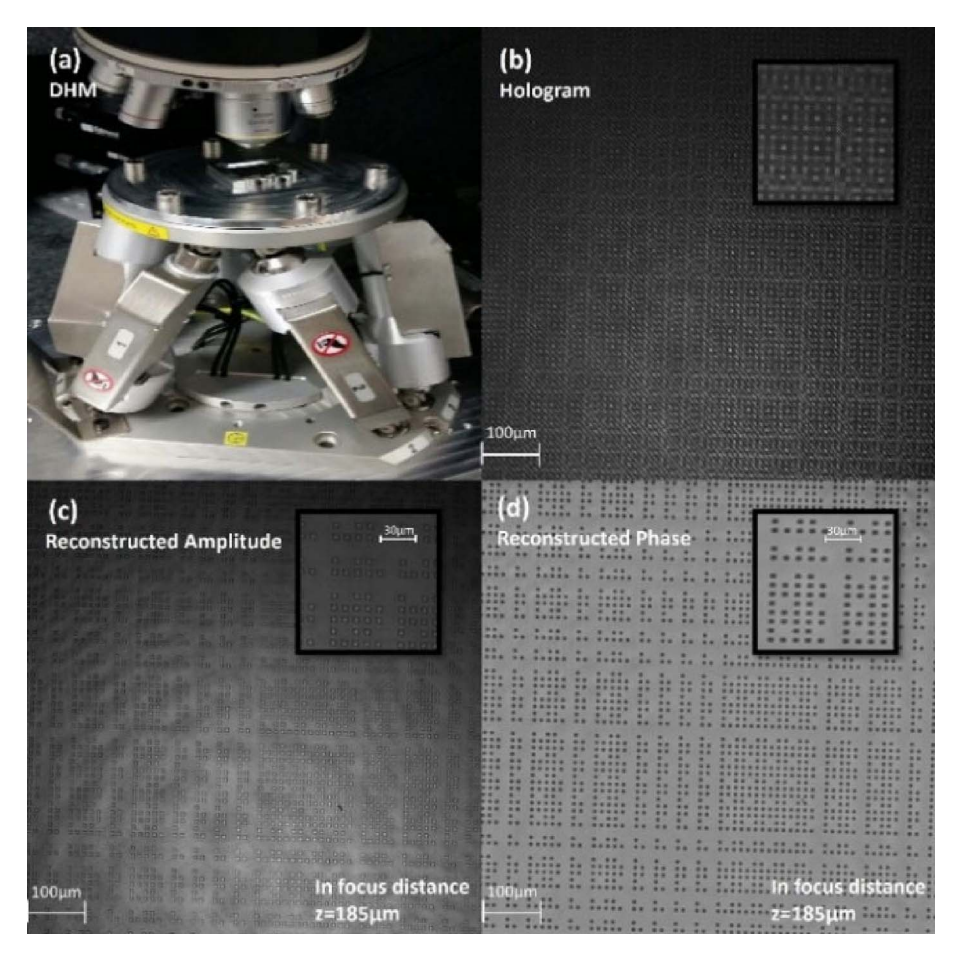


Figure 1. (a) Lyncee-tec DHM observing a micro-structured pattern moved by a hexapod stage. (b) A typical experimental hologram of a pseudo-periodic pattern that allow 3D pose measurement [2]. Image reconstruction (c) in amplitude and (d) in phase at a numerical in-focus distance of 185 μ m.

as phase object to perform 3D pose control in 3D through a microscope [2]. This study explores DH coupled with a computer micro-vision approach, employing phase correlation image processing techniques for sub-voxel sample pose measurements in micro-robotics [6, 7].

Digital hologram reconstruction relies on the Angular Spectrum Method [8], and a Lyncee-Tec Digital Holographic Microscope (DHM) equipped with 10× MO lens, adapts these principles to micro-objects, see reference [2] for experimental details. DHM works with digital autofocusing, enables automated microscopy and 3D pose control of micro-objects. Recent research highlights the use of DNN for faster auto-autofocusing in DHM through statistical image reconstruction, treating autofocusing as a classification or regression task [5]. The challenges include improving multiscale sensitivity for automated microscopy in 6 degrees of freedom (DoF) pose estimation while maintaining a broad field of view and depth of field [1]. A 2D pseudo-periodic pattern serves as a referencing sample (Fig. 1(c) and (d)). High-tech micro-assembly platforms in robotics demand translation and rotation stages (Fig. 1(a)), addressing increasingly complex tasks with nanoscale positioning resolution and large-scale movements beyond the centimetre range. This work addresses the challenge to target 3D inference and video-rate control of samples for complex micro-nano manipulation such as 3D MEMS micro-nano-assembly and alignment, 3D nanoprinting, visual servoing for 3D nanopositioning [1].

3 Positioning models (X, Y and Z)

In this work, we combine previous autofocusing with DHM accelerated with DNN [2] giving Z position and a new approach to determine in the same time X and Y coordinates. In Figure 2(a-c), the structure of the XY Model (consisting of a series of 2D Convolution Layers and Max Pooling Layers) based on the UNet architecture [4] is presented, specifically designed for 3D pose estimation. The model takes a Region of Interest (ROI) extracted from the input hologram, initially sized at 768×768 pixels within a hologram of 1024×1024 pixels. The resulting output from the model is a reconstructed thumbnail of 64 × 64-pixels, encapsulating the X and Y positional information [6]. Subsequently, Figure 2(d-f) outlines the arrangement of the Z Model, which is based on an adapted version of a GedankenNet model proposed in [3]. The primary distinctions from the original version are that it

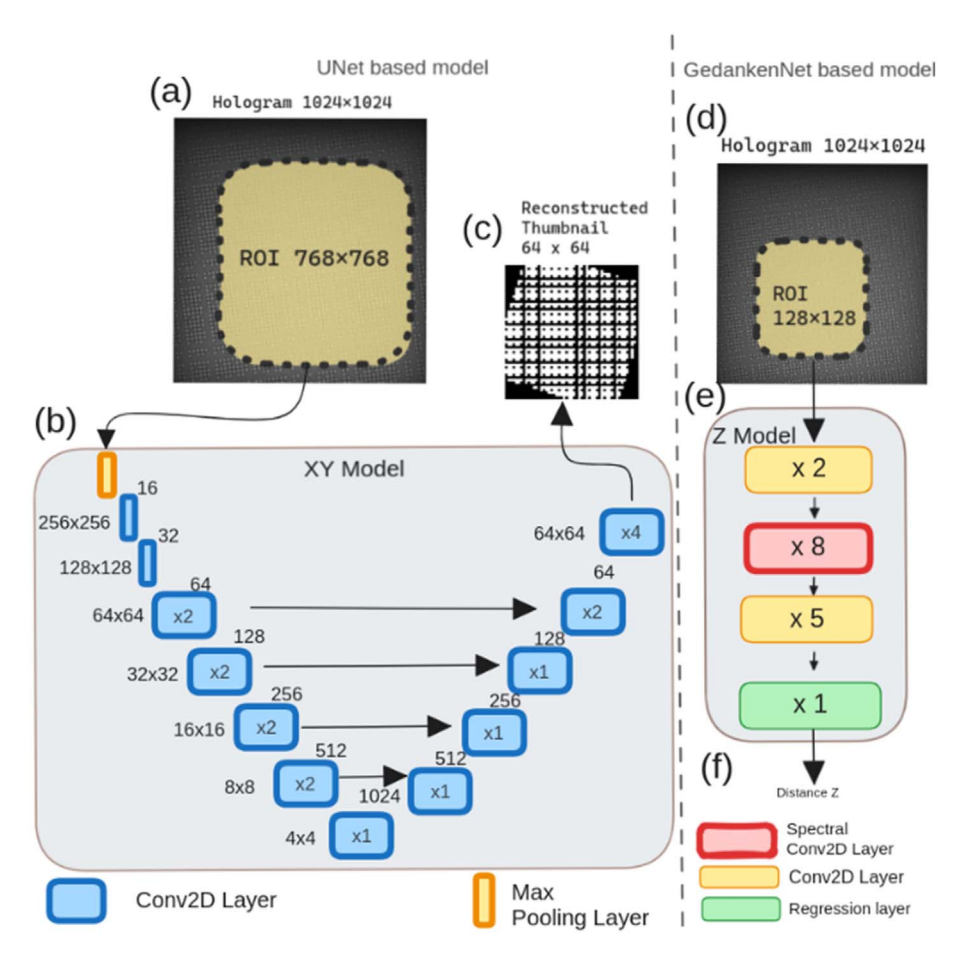


Figure 2. (a–c) Thumbnail reconstruction. (d–f) Assess the distance Z. (a) A ROI of 768×768 is cropped from the hologram at a fixed position. (b) XY Model (based on a UNet like model). (c) The reconstructed thumbnail of 64×64 pixels. (d) A ROI of 128×128 is randomly cropped from the hologram space. (e) Z model based on an adapted version of a GedankenNet model [3]. (f) The distance Z.

accepts a single image as input and the input size has been minimized to 128×128 pixels for faster computation of the Spectral Conv2D Layers (Fig. 2(f)). The XY Model's uniqueness lies in not reconstructing an image of the same size as the input (Fig. 2(b) depicts the initial Conv2D layers downsizing the input to 64×64).

4 Methodology

We address this issue by applying DNNs to micro-vision measurement of 3D trajectories with DH. Recently, we demonstrated the ability of new generation of deep neural networks such as ViT to predict the in-focus distance with a high accuracy [2]. In a previous work, we also showed the ability of 2D pseudo-periodic pattern combined to conventional imaging system, used as in-plane position encoder, has allowed a 108 range-to resolution ratio through robust phase-based decoding [7]. Here, we present DNNs dedicated to hybrid approach combining computer micro-vision and DHM, able to perform simultaneously in-plane and outplane measurements, at video-rate and without in focus full image reconstruction. The experimental setup is presented

in Figure 1. It consists in a DHM, a hexapod capable of precise motions along the 6DoF and a micro encoded pattern. We also show a typical hologram obtained and its reconstruction (Fig. 1(b)). The interferometric character of DH converts out-of-plane position of the sample in phase data that, combined with in-plane information retrieved from the micro-structured pattern, allows accurate measurement of 3D trajectories. DNNs speed up data processing and infer video-rate position detection.

DNNs require training to realize expected tasks and to reach the best performances. In our work, the training step is conducted from a dataset constituted by simulated holograms. Various experimental parameters have been considered in simulations such as spherical aberration introduced by objective microscope lens, and has been implemented in simulated hologram datasets, with the aim of being able to mimic real experimental conditions. To rigorously evaluate the effectiveness of the proposed methodology, which integrates DH with DNNs and video-rate micro-vision, we conducted a comprehensive validation through simulation. Our primary objective was to assess the DNNs capability to predict a simulated 3D trajectory under precisely controlled conditions. For this purpose, we selected a Lissajous' figure

(result of superposing two harmonic motions on the X-Y plane). This complex trajectory served as a challenging yet well-defined path for rigorously testing the capabilities of the DH-DNN system. We simulated a complete 3D trajectory of 2D pseudo-periodic pattern with period of 9 µm, displaced by the hexapod stage (Fig. 1(a)), along the two-dimensional Lissajous trajectory in the X-Y plane and generated corresponding sequence of digital holograms. This trajectory was then extended into the third dimension by introducing incremental steps along the Z-axis, simulating motion in depth. Each step in the Z-direction corresponds to a subsequent holographic reconstruction distance for the simulated hologram. Subsequently, the generated holographic datasets were used in DNNs for training step and infer the trajectory. The networks were tasked with accurately predicting the Lissajous' trajectory based on the holographic dataset inputs, essentially capturing and replicating the complex curve in their predictions. To analyse each hologram (inference mode), both models are used (Fig. 2), XY Model and Z Model to get the associated thumbnail and Z distance. A post-processing algorithm is applied on the reconstructed thumbnail to extract the binary vectors representing the positions (X and Y) (Fig. 2c). To convert the binary vectors into meaningful micron-scale coordinates, each vector within the complete sequence of bits is identified. Those indexes are used to compute the final X and Y coordinates as described in [6].

5 Results

We present the results obtained from the DH-DNN system methodology for predicting 3D trajectories. The models (XY Model and Z Model) have been trained using a total of 65000 simulated holograms. The XY Model is using binary cross entropy loss. The Z Model has been trained using a cross-validation method using the TanhExp loss function [9]. Both models are trained using the Adam optimizer. The models have been tested on a simulated trajectory of 1121 holograms. In Figure 3(a), the list of outliers (red points), the simulated (dashed blue line) and estimated (green line) trajectories are shown in 3D space. The accuracy exceeds 98% which demonstrates the system's ability to correctly estimate the 3D poses. Figure 3(b) provides a visual representation of the error along the Z axis and the deviation on the X-Y plane (L2-norm). This graphical depicts the precision of DNN predictions, revealing a max error of 25 µm on X-Y and less than 1 µm on Z. This X, Y level of performance must be compared with a maximum encoded area of $11 \times 11 \text{ cm}^2$. This allows video-rate monitoring of large displacements with a coarse but sufficient accuracy whereas eventual fine 3D pose is controlled by high accurate but much slower conventional processing.

Figure 4 shows the matching rate associated to each estimated 3D pose. This underscores that a rate level between 90 and 100 is adequate for accurately decoding the correct position. The precision along the Z axis is of the same magnitude as in [2]. These results emphasize the DH-DNN methodology's capability to provide highly accurate and detailed predictions of three-dimensional

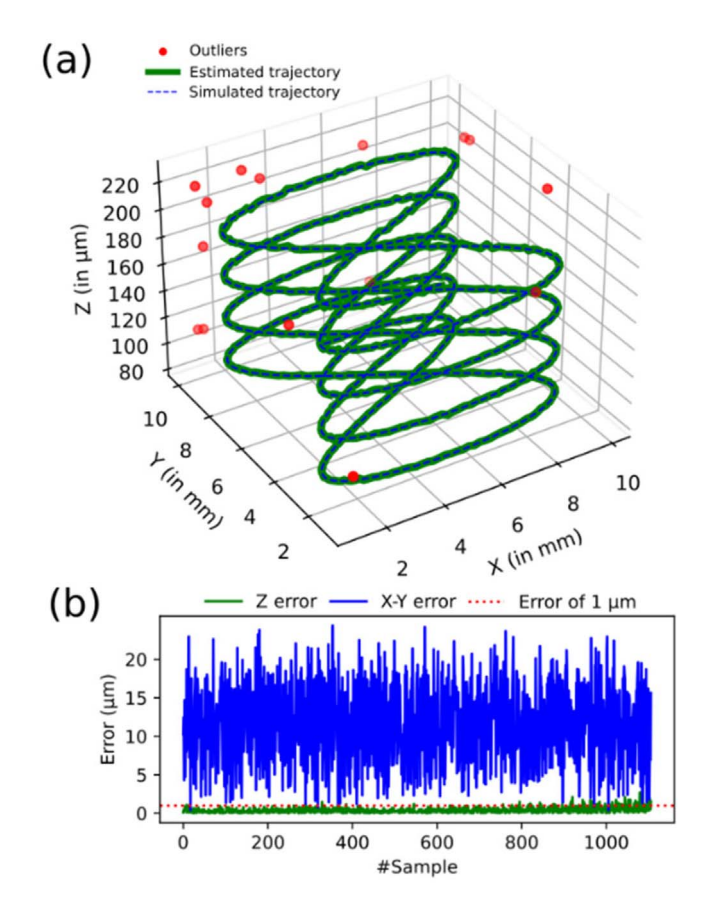


Figure 3. (a) Outliers (in red), simulated (in blue) and estimated (in green) trajectory in the 3D space. (b) Z and X-Y errors in μ m (absolute difference and L2-norm). The Z error is mostly below an error of 1 μ m (red dashed line).

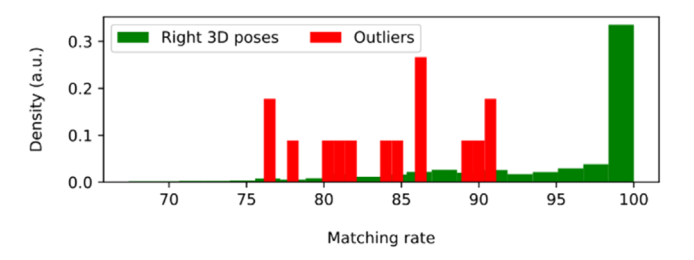


Figure 4. Matching rate associated to each 3D pose (red: outliers, green: right 3D poses).

trajectories. This highlights its practical utility in real-time micro-robotics and micro-vision applications. Moreover, the average inference speed is below 20 ms on a NVidia RTX 3090 32 GB mainly consumed by the data transfer of the images to the GPU (XY Model: 7.5 ms inference; Z Model: 2.5 ms inference; 10 ms for the data transfer).

6 Conclusions

We propose a method that enables the direct determination of 3D positions from hologram space with a mean error of $1~\mu m$ on Z and $12~\mu m$ on X-Y, effectively by passing the need for full holographic image reconstruction. These errors must be compared to the complete encoded area of $11\times11~{\rm cm}^2.$ Moreover, our study offers a thorough analysis of the matching rate levels attributed to each 3D pose. We believe it is the first time a Gedanken Net model is used as a regression tool. The modified Gedanken Net (Z Model) achieved an inference speed of 2.5 ms, contrasting with the over 20 ms required by a TViT [2].

Funding

This work was supported by Agence Nationale de la Recherche, HOLO-CONTROL project (Contract No. ANR-21-CE42-0009), by the French Investissements d'Avenir program, TIRREX project (Contract No. ANR-21-ESRE0015), SMARTLIGHT project (ANR-21-ESRE-0040) and by Cross-disciplinary Research (EIPHI) Graduate School (contract No. ANR-17-EURE-0002). This work was performed using HPC resources from GENCIIDRIS (Grant 20XX-AD011012913R2) and the Mésocentre de Franche-Comté.

Conflicts of interest

The authors declare that they have no competing interests to report.

Data availability statement

The data associated with this study is available upon request. Please contact the corresponding author to request access to the data.

Author contribution statement

PS, RC, GJL and MJ contributed to the conceptualization of the idea. The development of deep neural networks and datasets was performed by SC. The experiments and simulations of data were performed by BA and JBC. The development of digital hologram algorithms was performed by JBC. SC, JBC and MJ wrote the manuscript with feedback from RC, GJL and PS. All authors discussed the results and contributed to the final manuscript.

References

- 1 Yao S., Li H., Pang S., Zhu B., Zhang X., Fatikow S. (2021) *IEEE Trans. Instrum. Meas.* **70**, 1–28.
- 2 Cuenat S., Andréoli L., André A.N., Sandoz P., Laurent G.J., Couturier R., Jacquot M. (2022) Opt. Express 30, 14.
- 3 Huang L., Chen H., Liu T., et al. (2023) Self-supervised learning of hologram reconstruction using physics consistency, *Nat. Mach. Intell.* **5**, 895–907.
- 4 Ronneberger O., Fischer P., Brox T. (2015) arXiv. 1505.04597.
- 5 Zeng T., Zhu Y., Lam E.Y. (2021) Opt. Express 29, 24.
- 6 André A.N., Sandoz P., Mauzé B., Jacquot M., Laurent G.J. (2022) Int. J. Comput. Vis. 130, 6.
- 7 André A.N., Sandoz P., Mauzé B., Jacquot M., Laurent G.J. (2020) *EEE/ASME Trans. Mech.* **25**, 1193–1201.
- 8 Goodman J.W. (2005) Introduction to fourier optics, Roberts & Company Publishers, Englewood, pp. 55–61.
- 9 Liu X., Di X. (2020) arXiv. 2003.09855.

J. Eur. Opt. Society-Rapid Publ. 2024, **20**, 7 © The Author(s), published by EDP Sciences, 2024

https://doi.org/10.1051/jeos/2024006

Available online at: https://jeos.edpsciences.org

EOSAM 2023

Guest editors: Patricia Segonds, Guy Millot and Bertrand Kibler

RESEARCH ARTICLE OPEN 3 ACCESS

µJ-level normal-dispersion fiber optical chirped-pulse parametric oscillator

Tristan Guezennec^{1,2}, Saïd Idlahcen¹, Armand Cervera¹, Pierre-Henry Hanzard¹, David Landais^{2,a}, Laurent Provino², Adil Haboucha², Thomas Godin^{1,*}, and Ammar Hideur¹

Received 30 January 2024 / Accepted 16 February 2024

Abstract. We demonstrate the generation of broadband tunable and synchronized pulses exceeding the microjoule level using the new concept of Fiber Optical Parametric Chirped-Pulse Oscillation (FOPCPO). The oscillator is based on a collapsed-ends photonic crystal fiber pumped in the normal dispersion regime by an ytterbium fiber laser delivering highly-chirped pulses. The experimental results are compared with the results of numerical simulations and highlight that the feedback ratio appears as a key parameter for optimizing the system's efficiency and dynamics.

Keywords: Parametric Sources, Nonlinear Fibers, Fiber laser, Ultrafast laser, Parametric oscillator, FOPCPO.

1 Introduction

Optical parametric amplifiers and oscillators delivering ultrashort pulses are a well-established technology that has enabled considerable progresses in many research and industrial applications [1]. Multi-mJ energies and few cycles pulse durations are now reached using solid-state optical parametric sources but their complexity, cost, and alignment sensitivity hinder their use outside the laboratory environment. In the last years, significant advances have been made in their fiber-based counterparts which rely on Degenerate Four-Wave Mixing (DFWM - third-order nonlinearity of silica). Nonlinear wavelength conversion of ultrashort pulses has then been obtained with a variety of fiber systems. In particular, using the concept of Fiber Optical Parametric Chirped-Pulse Amplification (FOPCPA) [2–4] has allowed to overcome the saturation of the nonlinear process and the µJ level has been reached, by either using complex optical fiber designs or using Raman gain assistance. However, such systems operate in the anomalous group velocity dispersion of the fiber which restricts the parametric sidebands near the pump wavelength. FOPCPA pumped in the normal dispersion regime and delivering sub-picosecond pulse with wide wavelength separations have been reported but are still limited in terms of tunability as they require a seed source [5-7]. A way to circumvent this limitation is to use a resonant fiber optical parametric oscillator (FOPO) where the dispersion map can be tailored. High energy levels and ultrashort pulses – along with excellent signal-to-noise ratios – have then been obtained in FOPOs combining DFWM in Photonic Crystal Fibers (PCF) with pumping in the normal dispersion regime [8, 9]. Further energy scaling is however quite limited due to high peak powers and subsequent nonlinearities. To overcome this limitation, a natural idea is then to combine FOPCPAs capabilities in terms of energy scaling by using chirped pulses with FOPO's flexibility and wavelength tunability. Such a concept – termed FOPCPO – was first investigated numerically and showed significant potential for bandwidth control of parametric waves [10]. We then demonstrated experimentally the feasibility of this concept by generating broadly-tunable highly chirped pulses with energies exceeding 200 nJ in such a FOPCPO [11]. By combining highly-chirped pump pulses with a collapsed-ends photonic crystal fiber, we now confirm this idea and report on the generation of broadband signal and idler waves exceeding the µJ level at MHz-repetition rates from a FOPCPO pumped in the normal dispersion regime.

2 Experimental set-up

The experimental setup is depicted in Figure 1. The pump laser is a commercial ytterbium fiber laser (*Active Fiber Systems GmbH*), delivering highly-chirped pulses of 800 ps at 1032 nm (200 fs transform-limited) with 15 W average

¹ CORIA, UMR 6614 CNRS – INSA Rouen – Université de Rouen Normandie, 675 avenue de l'Université, 76801 Saint Etienne du Rouvray, France

² Photonics Bretagne, 4 rue Louis de Broglie, 22300 Lannion, France

^a Currently at Lumibird, Lannion, France

^{*} Corresponding author: thomas.godin@coria.fr

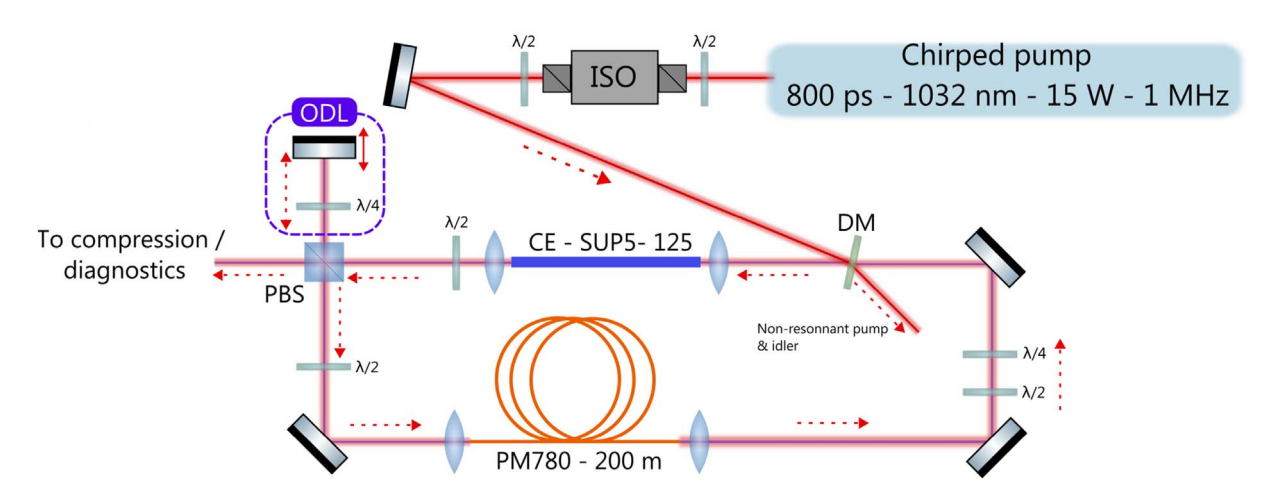


Figure 1. Experimental setup. ISO: Isolator, CE-SUP5-125: Collapsed-ends SUP5-125 fiber, DM: Dichroic mirror, PBS: Polarization beam splitter, ODL: Optical delay line.

power at 1 MHz repetition rate. The pump pulses are injected into the nonlinear fiber through a combination of a dichroic mirror and an aspheric lens (11 mm focal length).

The nonlinear fiber is an air-silica micro-structured 8 cm long SUP-5-125 (Product line Perfos®) fiber, developed and drawn at Photonics Bretagne facilities. It exhibits a nonlinear coefficient of 15 $\mathrm{W}^{-1}\cdot\mathrm{m}^{-1},$ a 5 $\mu\mathrm{m}$ mode field diameter, and a zero-dispersion wavelength of 1055 nm. Both ends of the fiber are collapsed in order to mitigate the laser induced damages due to the high peak power coming from the pump laser (up to 20 kW). The collapsed region is tailored to avoid beam diffraction on the fiber tip, resulting in an excellent output beam quality, as shown in Figure 2c on the beam profile taken at directly at the output of the fiber. As the phase-matching diagram depicted in Figure 2a suggest, such a fiber should generates a signal wave in the 800 nm band, along with an idler wave in the 1500 nm band.

The cavity is closed with a 200 m PM780 spool, so the signal wave propagates in the normal dispersion regime allalong the intracavity components, and match the repetition rate of the pump laser. In order to finely adjust the round-trip delay of the cavity, we also implemented an Optical Delay Line (ODL), which allows us to tune the emission wavelength using a dispersive filtering effect [12]. This indeed gives the possibility to overlap different spectral components of the pump pulses and the signal pulses, hence changing the phase-matching condition of the parametric process. The feedback ratio is controlled via an adjustable optical circulator before the ODL, and the polarization of the signal is controlled in the cavity in order to improve the parametric conversion and to mitigate any polarization-dependent phase mismatching in the nonlinear fiber.

3 Numerical simulations

3.1 Numerical FOPCPO model

In order to predict the FOPCPO performances, we developed a script for a typical cavity as depicted in Figure 3. The script propagates the complex optical envelop through

the different fibers and components, and reuse a fraction of the output field into the next cavity roundtrip. Numerical simulations along the fiber segments were performed using an in-house Generalized Nonlinear Schrödinger Equation (GNLSE) solver, with a Runge-Kutta 4 in Interaction Picture (RK4IP) method [13]. The main idea is to solve the following GNLSE:

$$\frac{\partial A(z,T)}{\partial z} = -\frac{\alpha(\omega)}{2} A(z,T) + \sum_{k\geq 2} \frac{i^{k+1}}{k!} \beta_k \frac{\partial^k A(z,T)}{\partial T^k} + \dots$$

$$\dots i\gamma \left(1 + \tau_{\text{shock}} \frac{\partial}{\partial T} \right) \times \left(A(z,T) \int_{-\infty}^{\infty} R(T') |A(z,T-T')|^2 dT' \right)$$

$$(1)$$

By applying the following transformation,

$$A_I(z, T) = e^{(z-z')\hat{L}}A(z, T)$$
 (2)

it is possible to solve equation (1) using standard Runge-Kutta 4 algorithm. The fibers parameters (*i.e.* the Taylor coefficients β_k and the nonlinear coefficient γ) were determined using an in-house developed fiber mode solver based on a finite- difference method, while the material loss α are approximated using the fused silica losses model presented in [14]. The pump pulses are modeled using:

$$A(t) = \sqrt{P_0} e^{-1/2 \left(\frac{t-t}{0}\right)^2} e^{i\left(\frac{C_2}{2}(\omega - \omega_0)^2\right) - i\omega_0 t}$$
 (3)

where C_2 is the 2nd order phase coefficient that control the quadratic phase (i.e. the chirp) of the pulse [15]. In order to initiate the parametric fluorescence in the nonlinear fiber, the pump pulses are injected with a noise of one photon per spectral mode.

The numerical parameters used in the simulations are detailed in Table 1.

The pump pulses are defined as linearly chirped gaussian pulse, with a Fourier-limited duration of 200 fs, energies of

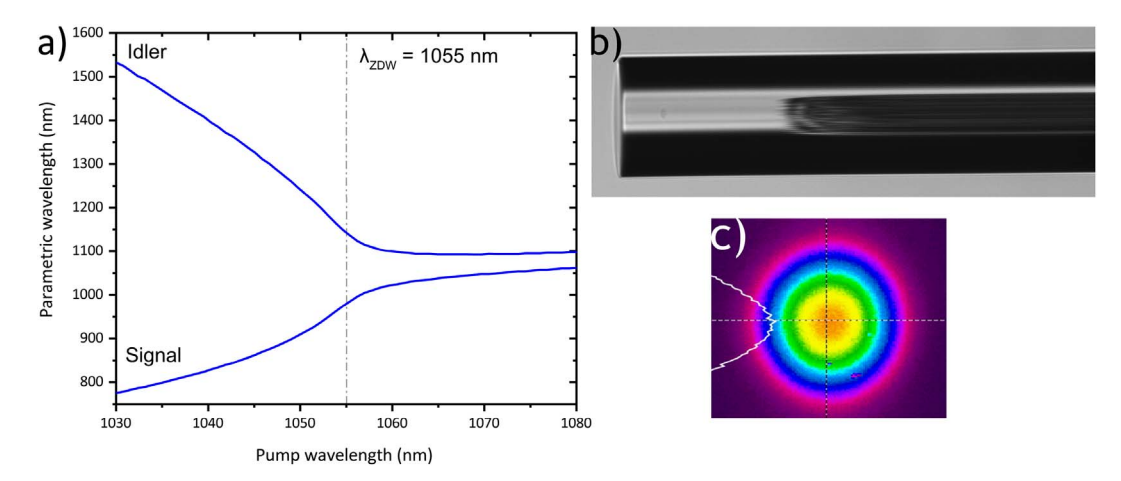


Figure 2. a) Phase matching diagram of the SUP5-125 fiber. b) Collapsed-end of the SUP5-125 fiber. c) Beam profile at the output of the SUP5-125 fiber

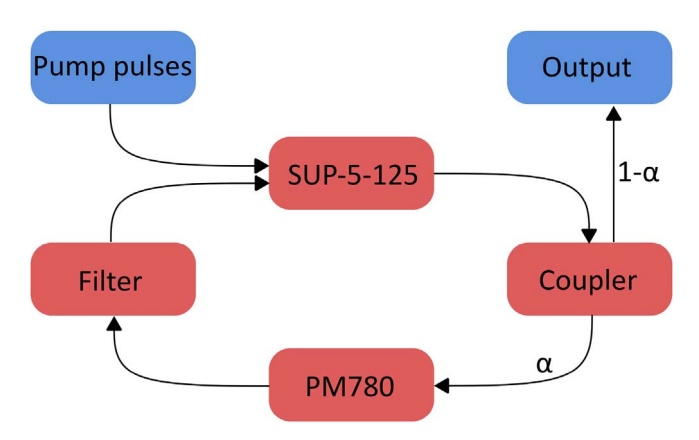


Figure 3. Outline of the cavity simulation.

10 μ J, and a 2nd order phase coefficient of $5.8 \cdot 10^{-23} \text{ s}^2$, leading to a pulse duration of 800 ps at 1032 nm.

3.2 Numerical results

Simulations were performed for 100 roundtrips in the cavity. As depicted in Figure 4, we extracted narrowband signal pulses of 1.2 μ J centered at 785 nm, along with broadband idler pulses of 650 nJ, exceeding our previous numerical predictions [11]. The FOPCPO is self-starting from noise and is stable after roughly 60 roundtrips. As predicted by Brinkmann et al. [10], all the pulses are linearly and positively chirped, allowing compression using standard grating-based compressors. By defining the compressor dispersion coefficients using the model given in [16], it is possible to compress the pulses below 950 fs for the idler and 3 ps for the signal. The feedback ratio given by the losses of the coupler was carefully adjusted in order to allow a stable operation with coherent output pulses.

4 Experimental results

The FOPCPO output measured at 10 μ J pump energy are summarized in Figure 5a. Using time-dispersion tuning, the FOPCPO output pulses can be widely tuned over the gain

bandwidth with a tunability of 30 nm for the signal (from 780 to 810 nm), and 70 nm for the idler (from 1440 to 1510 nm), with a maximum gain obtained at 800 nm and 1450 nm and a pulse duration of 260 ps has been measured using a fast detection system (25 GHz photodiode and 33 GHz oscilloscope). The output signal energy scales linearly with the pump energy and reaches 1.4 μ J, see Figure 5b.

It is worth noting that both idler and signal pulses are relatively broadband (from 5 to 10 nm), which is a major difference with the numerical simulations as narrower signal pulses were expected. The physical reason behind this discrepancy is still being investigated. However, it appears that several regimes are actually accessible by adjusting the feedback ratio. We identified two specific regimes, one with a low feedback ratio that appears slightly narrower than the one with a high feedback ratio, as depicted in Figure 6. In addition, the highest energies were obtained with the high-feedback regime.

As discussed by Zhang et al. [17], it appears that the output spectrum broadens as the feedback ratio increases, before reaching an unstable regime for a critical feedback ratio. Although this phenomenon is easy to detect in numerical simulations, it is no mean feat experimentally. Because of the spectrum analyser integration time, one should track the FOPCPO output dynamic pulse by pulse, by means for example of dispersive Fourier transform, however it needs a spool of normal dispersion optical fiber at the wavelength of interest. Pulse compression is an ongoing work, as it can be a challenging task for oscillators that exhibits several dynamic behaviors.

5 Outline and prospects

We demonstrate that using highly chirped pulses in combination with PCF ends functionalization to mitigate fiber tips damage, energy scaling of the FOPCPO scheme beyond the microjoule barrier is possible. This opens the path for the development of widely tunable parametric oscillators delivering high energy levels at high-repetition rates. These features would make FOPCPOs prominent sources for stimulated coherent Raman spectroscopy

Table 1. Simulation parameters of the FOPCPO.

Element	Length (m)	$\alpha \; (\mathrm{m}^{-1})$	$\gamma (W^{-1} \cdot m^{-1})$	$\beta^2 (s^2 \cdot m^{-1})$	$\beta^3 (s^3 \cdot m^{-1})$	$\beta^4 (s^4 \cdot m^{-1})$	$\lambda_{\mathrm{cut}} \; (\mathrm{nm})$
SUP-5-125	0.08	0.002	15	$2.17.10^{-27}$ @1040 nm	$6.36.10^{-41}$ @1040 nm	$-8.9.10^{-56}$ @1040 nm	
PM780	200	0.002	10	$4.31.10^{-26}$ @785 nm	$2.37.10^{-41}$ @785 nm	$-1.38.10^{-56}$ @785 nm	
Coupler		13					
Filter							980 nm shortpass filter

The gray shaded areas correspond to parameters that cannot be applied to the corresponding elements. For example, the length of the filter cannot be defined as it is not a fiber component.

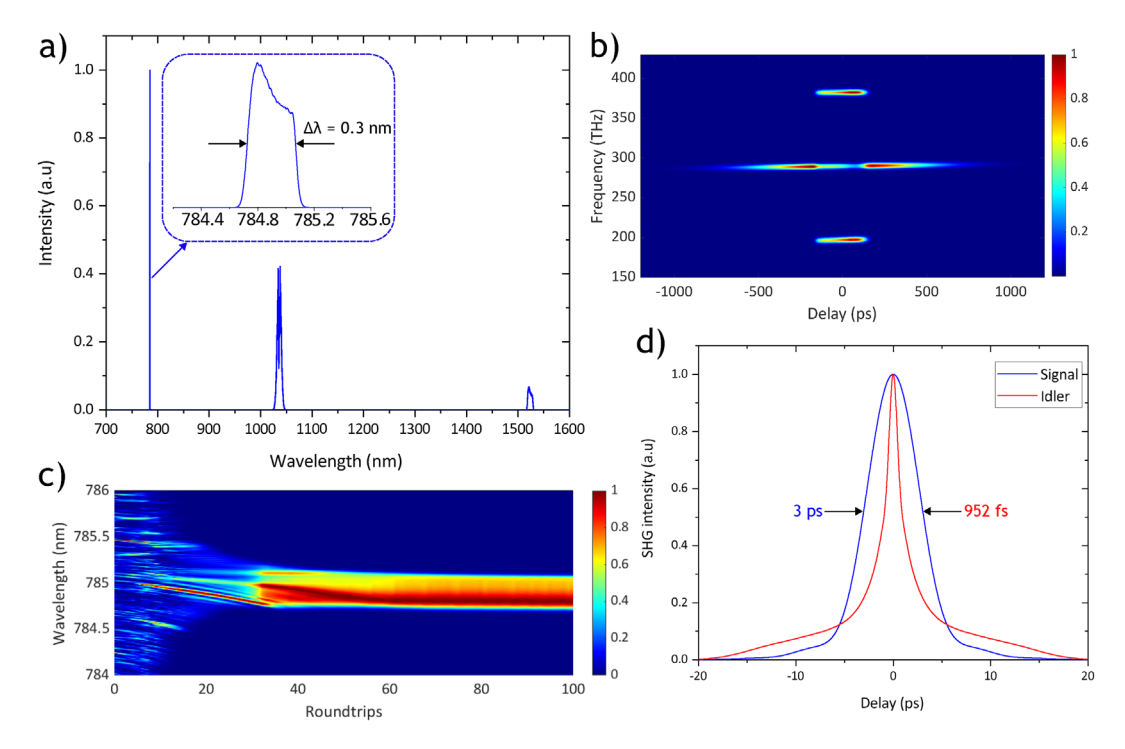


Figure 4. Numerical results. a) Output spectrum of the FOPCPO. b) Output spectrogram. c) Signal wave build-up. d) Autocorrelation traces of the dechirped signal and idler pulses.

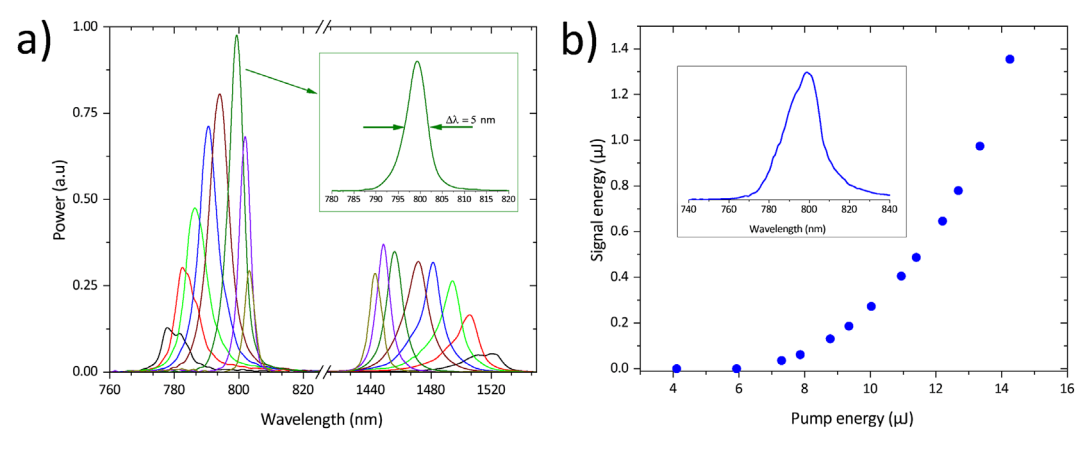


Figure 5. a) FOPCPO tunability for a pumping energy of 10 μ J. Power is normalized to the highest value obtained at 800 nm (see inset). b) FOPCPO energy scaling. Inset: Output spectrum at nominal power.

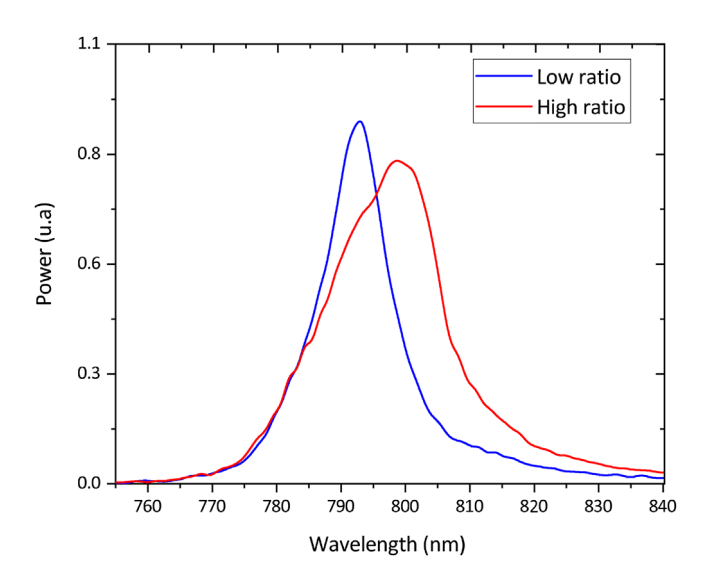


Figure 6. Impact of the feedback ratio on the output signal spectrum.

(SRS) [18], or multiphoton imaging [19]. Further experiments should now be done on pulse compression and the impact of the feedback ratio on the dynamics of the pulses. However, the chirp properties of such a system could also be used without compression in a spectral focusing based SRS setup [20, 21].

Funding

The authors acknowledge the support of the Conseil Régional de Normandie and the European Regional Development Fund, the Région Bretagne, the Département des Côtes d'Armor, Lannion-Trégor Communauté (LTC) and the Agence Nationale de la Recherche et de la Technologie (ANRT).

Conflicts of Interest

The authors declare no conflict of interests

Data availability statement

Data underlying the results presented in this paper are not publicly available at this time but may be obtained from the authors upon reasonable request.

Author contribution statement

All authors made significant contributions to this work.

References

- 1 Dubietis A., Matijošius A. (2023) Table-top optical parametric chirped pulse amplifiers: past and present, $Opto-Electron\ Adv.\ {\bf 6},\ 220046.$
- 2 Hanna M., Druon F., Georges P. (2006) Fiber optical parametric chirped-pulse amplification in the femtosecond regime, *Opt. Express* 14, 2783–2790.

- 3 Morin P., Dubertrand J., Beaure d'Augeres P., Quiquempois Y., Bouwmans G., Mussot A., Hugonnot E. (2018) μ J-level Raman-assisted fiber optical parametric chirped-pulse amplification, *Opt. Lett.* 43, 4683–4686.
- 4 Lafargue L., Scol F., Vanvincq O., Poeydebat E., Bouwmans G., Hugonnot E. (2022) All-polarization-maintaining and high-energy fiber optical parametric chirped-pulse amplification system using a solid core photonic hybrid fiber, Opt. Lett. 47, 4347–4350.
- 5 Fu W., Wise F.W. (2018) Normal-dispersion fiber optical parametric chirped-pulse amplification, Opt. Lett. 43, 5331–5334.
- 6 Qin Y., Batjargal O., Cromey B., Kieu K. (2020) All-fiber high-power 1700 nm femtosecond laser based on optical parametric chirped-pulse amplification, Opt. Express 28, 2317–2325.
- 7 Fu W., Herda R., Wise F.W. (2020) Design guidelines for normaldispersion fiber optical parametric chirped-pulse amplifiers, J. Opt. Soc. Am. B 37, 1790–1805.
- 8 Gottschall T., Meyer T., Schmitt M., Popp J., Limpert J., Tünnermann A. (2015) Four-wave-mixing-based optical parametric oscillator delivering energetic, tunable, chirped femtosecond pulses for non-linear biomedical applications, *Opt. Express* 23, 23968– 23977.
- 9 Gottschall T., Limpert J., Tünnermann A. (2017) Ultra-short pulse fiber optical parametric oscillator, Opt. Lett. 42, 3423–3426.
- 10 Brinkmann M., Hellwig T., Fallnich C. (2017) Optical parametric chirped pulse oscillation, Opt. Express 25, 12884–12895.
- 11 Becheker R., Touil M., Idlahcen S., Tang M., Haboucha A., Barviau B., Grisch F., Camy P., Godin T., Hideur A. (2020) High-energy normal-dispersion fiber optical parametric chirped-pulse oscillator, Opt. Lett. 45, 6398–6401.
- 12 Zhou Y., Cheung K.K.Y., Yang S., Chui P.C., Wong K.K.Y. (2009) A time-dispersion-tuned picosecond fiber-optical parametric oscillator, *IEEE Photonics Technol. Lett.* 21, 17, 1223–1225.
- 13 Balac S., Fernandez A., Mahé F., Méhats F., Texier-Picard R. (2016) The interaction picture method for solving the generalized nonlinear Schrödinger equation in optics, ESAIM: M2AN 50, 4, 945–964
- 14 Sørensen S.T. (2013) Deep-blue supercontinuum light sources based on tapered photonic crystal fibers, Technical University of Denmark.
- 15 Fork R.L., Brito Cruz C.H., Becker P.C., Shank C.V. (1987) Compression of optical pulses to six femtoseconds by using cubic phase compensation, Opt. Letters 12, 7, 483.
- 16 Hugonnot E. (2019) Chirped-pulse amplification, Techniques de l'ingénieur, TIP520WEB, e6515. Available at https://doi.org/ 10.51257/a-v1-e6515.
- 17 Zhang W.Q., Sharping J.E., White R.T., Monro T.M., Shahraam Afshar V. (2010) Design and optimization of fiber optical parametric oscillators for femtosecond pulse generation, *Opt. Express* 18, 17294– 17305.
- 18 Kong C., Pilger C., Hachmeister H., Wei X., Cheung T.H., Lai C.S.W., Lee N.P., Tsia K.K., Wong K.K.Y., Huser T. (2020) High-contrast, fast chemical imaging by coherent Raman scattering using a self-synchronized two-colour fiber laser, *Light Sci. Appl.* 9, 25.
- 19 Horton N., Wang K., Kobat D., Clark C.G., Wise F.W., Schaffer C. B., Xu C. (2013) In vivo three-photon microscopy of subcortical structures within an intact mouse brain, Nature Photon. 7, 205–209.
- 20 Chen K., Wu T., Chen T., Wei H., Yang H., Zhou T., Li Y. (2017) Spectral focusing dual-comb coherent anti-Stokes Raman spectroscopic imaging, Opt. Lett. 42, 3634–3637.
- 21 Qin Y., Cromey B., Batjargal O., Kieu K. (2021) All-fiber single-cavity dual-comb for coherent anti-Stokes Raman scattering spectroscopy based on spectral focusing, Opt. Lett. 46, 146–149.

J. Eur. Opt. Society-Rapid Publ. 2024, $\bf 20,\,19$ © The Author(s), published by EDP Sciences, 2024

 $\rm https://doi.org/10.1051/jeos/2024017$

Available online at: https://jeos.edpsciences.org

EOSAM 2023

Guest editors: Patricia Segonds, Guy Millot and Bertrand Kibler

RESEARCH ARTICLE OPEN 3 ACCESS

Towards 2-µm comb light source based on multiple four-wave mixing in a dual-frequency Brillouin fiber laser

Moise Deroh^{1,2,*}, Gang Xu^{1,3}, Erwan Lucas¹, Jean-Charles Beugnot², Hervé Maillotte², Thibaut Sylvestre², and Bertrand Kibler¹

Received 29 January 2024 / Accepted 5 April 2024

Abstract. In this study, we report the generation of multi-wavelength light sources through enhanced four-wave-mixing processes using a straightforward and adaptable dual-frequency Brillouin fiber laser. This passive optical and nonreciprocal cavity is first tested and analyzed with long fiber lengths up to 1 km in the 1.55 μ m telecommunication C band and then in the 2- μ m waveband. In the latter case, we demonstrate that our fiber cavity enables efficient multiple four-wave mixings, in the continuous-wave regime, which are commonly inaccessible in long silica-fibers due to increased losses. We also report on the tunable repetition rate from tens of GHz to hundreds of GHz, by simply changing the frequency spacing between the two continuous-wave pumps. The coherence limitations of our all-fiber system are discussed, along with the impact of the dispersion regime of the nonlinear fiber that forms the cavity.

Keywords: Stimulated Brillouin Scattering, Fiber cavities, Four-wave mixing, Frequency combs.

1 Introduction

Compact and coherent comb light sources in the 2-µm waveband are becoming attractive components for molecular spectroscopy, environmental monitoring, and nextgeneration high-speed optical communications [1–6]. Coherent comb light sources can be obtained in general through various optical configurations such as electro-optic modulation schemes and mode-locked pulsed lasers often assisted by additional nonlinear frequency conversion [7–11], and parametric oscillations from a continuous-wave (CW) laser in high quality factor microresonators [12, 13]. Mostly, developed systems focused on the telecommunication wavelength around 1.55 μ m, thus benefiting from the numerous high-quality optical components. In the specific 2-µm waveband, common approaches typically involve near-infrared to mid-infrared conversion techniques of frequency combs and mode-locked lasers [3, 14, 15]. Alternately, other systems may be implemented using thulium (Tm)-doped silica fiber lasers and components or semiconductor lasers [2]. It is also worth mentioning that multi-wavelength fiber lasers have been developed around 2 µm using distinct cavity arrangements based on Tm-doped fibers [16–20].

In general, direct generation of comb light sources in the 2-µm waveband remains challenging in a cavity-free configuration with CW pumping, for instance, due to the detrimental losses in the required long optical fiber lengths (typically, tens of dB/km). As a consequence, multiple fourwave mixing (MFWM) processes in the simultaneous propagation of two pump waves through an optical fiber cannot be simply applied as in the conventional telecommunication window [21], even if bi-chromatic pumping allows for FWM to be free of power threshold. However, another alternative for generating combs has recently emerged by combining Kerr and Brillouin effects with the aim of improving some nonlinear performances. Indeed, stimulated Brillouin Scattering (SBS) can manifest with several orders of magnitude stronger than the Raman or Kerr effect, and it is also tunable over a wide spectral range [22]. Then one can excite and enhance MFWM processes in a non-reciprocal fiber cavity platform featuring bi-chromatic Brillouin lasing [23]. Direct coherent pumping is replaced by lasing on specific cavity modes, offering easily adjustable repetition rates and enhanced coherence by Brillouin purification [24]. A similar approach can be applied for generating a Kerr comb in an optical microresonator, using the Brillouin laser generated in the same cavity [25]. Highly coherent combs were also demonstrated in short fiber cavities by finely controlling the bi-chromatic Brillouin lasing [24].

¹ Laboratoire Interdisciplinaire Carnot de Bourgogne, UMR 6303 CNRS, Université de Bourgogne, Dijon, France

² Institut FEMTO-ST, UMR 6174 CNRS, Université Franche-Comté, Besançon, France

³School of Optical and Electronic Information, Huazhong University of Science and Technology, Wuhan, PR China

^{*} Corresponding author: koffi.deroh@u-bourgogne.fr

Fiber cavity parameters	Cavity 1	Cavity 2	Units
Cavity length (L)	350	1000	m
Brillouin gain efficiency $(g_{ m B}/A_{ m eff})$	0.38	0.38	$\mathrm{m}^{-1} \cdot \mathrm{W}^{-1}$
Brillouin gain bandwidth $(\Delta v_{\rm B})$	55	55	MHz
Total roundtrip loss	1.5	2.2	dB
Zero dispersion wavelength (λ_0)	1575	1523	nm
Dispersion parameter (D)	-2.95	0.49	$ps \cdot nm^{-1} \cdot km^{-1}$
Group-velocity dispersion (β_2)	3.77	-0.62	$\mathrm{ps}^2\cdot\mathrm{km}^{-1}$
Nonlinear coefficient (γ)	12.5	10	$\mathrm{W}^{-1}\cdot\mathrm{km}^{-1}$
Free spectral range (FSR)	0.6	0.22	MHz
Cavity finesse	8.69	5.94	_

Table 1. Physical parameters at 1550 nm of the cavities study made of two distinct HNLFs in this work.

In this paper, we investigate two multi-line fiber laser sources centered at 1.55 µm (C-band) and 2-µm (thulium band) that exhibit a symmetrical spectral comb structure based on enhanced MFWM within a long passive fiber cavity platform, specifically designed for bi-chromatic Brillouin lasing. At 1.55 μm, we generate a multi-wavelength light source that operates in both dispersion regimes with distinct temporal and spectral features. Temporal characterization of the generated pulse train is provided by means of intensity autocorrelation measurements. Finally, at 2 µm, we demonstrate a multi-wavelength light source made of 22 comb lines operating in the anomalous dispersion regime with a frequency spacing up to 106 GHz. The stability and coherence of the multi-line sources and generated pulse trains are also discussed for the two pumping configurations.

2 Experimental setup

In our experiments, we analyzed two distinct cavities made of commercially available highly nonlinear fibers (HNLF) that exhibit a normal and anomalous dispersion. The main physical parameters of both cavities are summarized in Table 1. Figure 1 shows the experimental setup used for generating our multi-wavelength sources in both spectral bands, namely 1.55 and 2 µm. The bi-chromatic pumping configuration can be achieved by combining two wavelength-tunable CW lasers (external cavity laser diodes) or by means of electro-optical (intensity) modulation (EOM) of one laser, to vary the pump frequency spacing [24]. Here, we chose two CW lasers to investigate larger frequency spacings. The two pump lasers were amplified via an erbium or thulium-doped fiber amplifier (EDFA/TDFA) and then injected into the passive fiber cavity via an optical circulator (OC). The backscattered Brillouin signals coming back from the FUT, shifted at the Brillouin frequency around 9.6 GHz [24] and 7.5 GHz [26] at 1.55 and $2 \mu m$, respectively from our HNLF fibers, are then reinjected into the cavity ring via a fiber coupler (99:1). The output of the dual-frequency Brillouin fiber laser is extracted from a 1% fiber coupler while the remaining 99% is fed back into the ring cavity. An OC closes the ring cavity. This configuration system

allows free propagation of the Stokes waves, which perform multiple roundtrips in the counterclockwise direction (dual lasing occurs and initiates a cascade of FWM), while the pumps waves interact only over a single pass in the clockwise direction. We finally analyzed the output cavity spectrum using an optical spectrum analyzer (with 0.08 pm and 0.05 nm resolution, at 1.55 and 2 μm respectively) and a rapid scanning intensity autocorrelator. In order to maximize the efficiency of the cascaded FWM processes, polarization controllers are inserted between the pumping lasers and the couplers to ensure that the two pumps have the same polarization direction. Specific fiber components dedicated to the 1.55- or 2- μm spectral bands can be easily interchanged.

3 Experimental results at 1.55 μm

In the following, our experiments were first performed at 1.55 µm with the first cavity made of the normallydispersive HNLF. We first measured the output dualfrequency Brillouin laser power as a function of injected pump power, as shown in Figure 2a, and for a given frequency spacing of 25 GHz. A low lasing threshold of 7.5 mW was experimentally achieved. For a 25-GHz (0.2 nm) frequency spacing and 158-mW pump power, we specifically show the multi-line spectrum that was obtained in both open and closed cavity configurations as depicted in Figures 2a and 2c. Note that FWM processes occur and are analyzed in the clockwise direction in the particular opencavity configuration, since there is no Brillouin Stokes lasing. The enhanced efficiency of the cascaded FWM process in a closed cavity is evident when driven by the Brillouin Stokes. This results in a notable increase, transitioning from a limited number of comb lines to a substantial expansion, reaching dozens. Figure 2d shows the resulting spectral evolution by increasing the injected pump power from 80 to 316 mW in the closed cavity case. The number of comb lines increases significantly; however, the overall spectral shape exhibits an exponential decay when the pump power increases. This rapid decline in power per line can be attributed to both the strong normal cavity dispersion and also the multimode Brillouin lasing regime for such

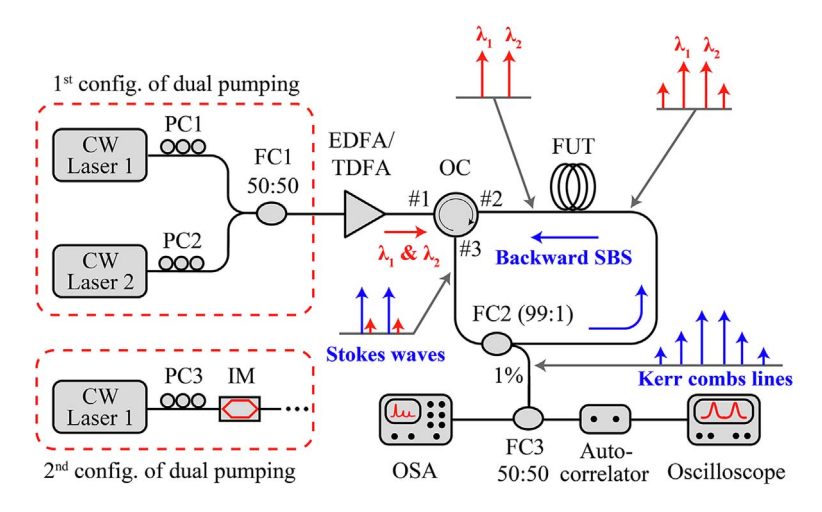


Fig. 1. Experimental setup for generating multi-wavelength light sources at both 1.55 μm and 2 μm by means of MFWM in a dual-frequency Brillouin fiber laser. CW: Continuous wave, PC: Polarization Controller, FC: Fiber Coupler, EDFA/TDFA: Erbium/Thulium Doped Fiber Amplifier, OC: Optical Circulator, FUT: Fiber Under Test, OSA: Optical Spectrum Analyzer.

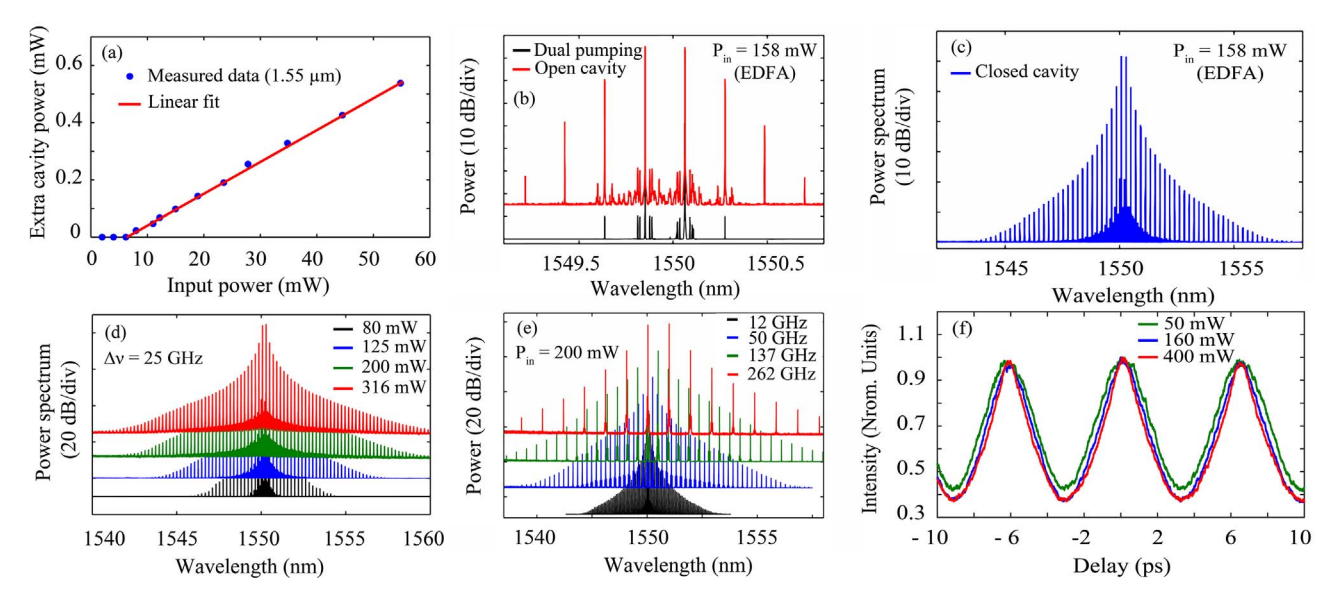


Fig. 2. Dual-frequency Brillouin laser and multi-wavelength light generation (cavity 1, normal dispersion regime). (a) Stokes lasing threshold measurement. (b) Experimental FWM results for bi-chromatic pumping (25-GHz frequency spacing) of the HNLF and cavity-free configuration for an input power of 158 mW. (c) Corresponding multi-wavelength generation in the closed cavity configuration. (d) Spectral broadening recorded (25-GHz frequency spacing) at increasing input pump powers from 80 to 316 mW. (e) Tunable frequency spacing of the multi-wavelength source for an input power of 200 mW. (f) Experimental autocorrelation traces of the generated pulse train with a period of 6.7 ps (repetition rate of 150 GHz) for distinct input powers of 50–400 mW.

long cavity length and high operating power [24]. Operating the Stokes laser in the multimode regime leads to a strong degradation in comb coherence as the Stokes pumps fluctuate across several cavity modes. Moreover, the thermal drift of our cavity relative to the pump lasers is not counterbalanced by any phase-lock loop, contrary to our previous work on a very short cavity [24]. As a result, our measurements only reflect a strong averaging of spectral broadening in the presence of pump power and cavity detuning fluctuations. Nevertheless, we show that the generated comb source can be tuned over a few hundreds of GHz by simply

modifying the initial frequency spacing of the two CW pumps. We measured the dependence of the output cavity spectrum as a function of the frequency spacing for a given input power of 200 mW in Figure 2e. More particularly, we increased the pump frequency spacing from 12.5 to 262 GHz (0.1–2.1 nm). The spectral bandwidth of the generated comb lines exhibits rapid expansion up to a saturation point, accompanied by a decrease in the number of lines. This behavior is attributed to the inherent dispersion of the fiber, which restricts the spectral broadening, or, in other words, the maximum steepening of the

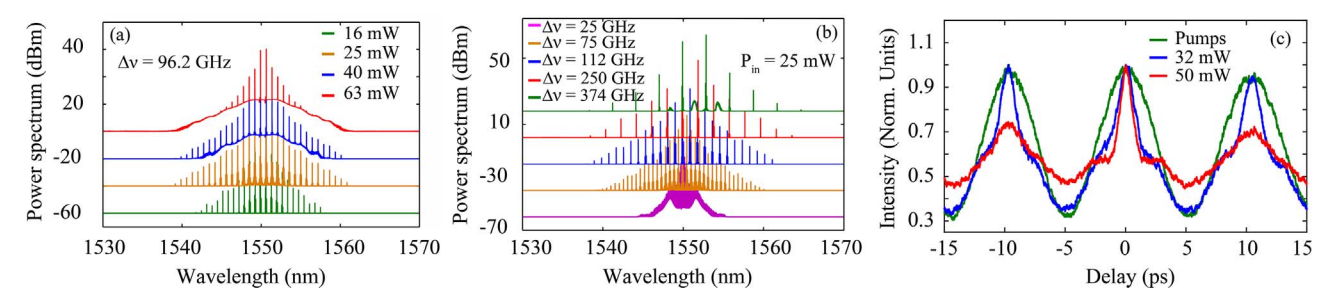


Fig. 3. Dual-frequency Brillouin laser and multi-wavelength light generation (cavity 2, anomalous dispersion regime). (a) Experimental FWM results for bi-chromatic pumping (96.2 GHz frequency spacing) of the HNLF and increasing input powers from 16 to 63 mW. (b) Tunable frequency spacing (from 25 GHz to 374 GHz) of the multi-wavelength source for an input power of 25 mW. (c) Experimental autocorrelation traces of the generated pulse train with a period of 10.4 ps (rep. rate of 96.2 GHz) for input powers of 32 to 50 mW.

temporal pulse fronts originating from the initial sinusoidal modulation induced by the two pumps [27]. Indeed, we characterized the temporal properties of the multi-wavelength spectrum with frequency spacing of 150 GHz for distinct pump powers, by means of a second-harmonic autocorrelator with a resolution of 10 fs (see Fig. 2f).

Under normal cavity dispersion, the initial sinusoidal temporal pattern resulting from the interference of the two Stokes fields in the cavity becomes a near-rectangular pulse train for increasing powers associated with larger spectral broadenings, as confirmed by the triangular waveform of the autocorrelation profile with a period of 6.7 ps.

Next, we carried out experiments with the second cavity made of the 1-km-long HNLF operating in the anomalous dispersion. We measured the spectral evolution of the output cavity for a given frequency spacing of 96.2 GHz (0.77 nm) and increased input powers from 16 to 63 mW (see Fig. 3a). In this dispersion regime, we once again observe the generation of a multi-wavelength light source; however, the spectral broadening experiences swift saturation at moderate powers, typically above 25 mW. Subsequently, a pronounced increase in the noise background becomes evident, creating a substantial pedestal beneath the comb lines. This distinct characteristic of the anomalous dispersion regime is closely related to the growth of modulation instability (MI) sidelobes. This adverse phenomenon, detrimental to coherence properties, was also observed in short fiber cavities [27]. However, it was successfully mitigated by employing suitable detuning conditions, resulting in the formation of a globally coherent comb. By contrast, the MI here prevents the growth of the combs lines in our long free-running cavity. In this case, it is important to avoid the MI effect. To this end, we restricted the input power to values below 25 mW. We then noticed that the MI emergence also depends on the frequency spacing between the two pumps. Figure 3b shows the output spectra obtained with different frequency spacings for an input power of 25 mW. We significantly increased the pump frequency spacing from 25 to 373.9 GHz (0.2–3.0 nm). We clearly confirm that the comb repetition rate can be easily tuned over a few hundreds of GHz. However, we note that MI sidelobes appear only for small or large frequency spacings (below 75 GHz or beyond 250 GHz). For a small frequency spacing, MI amplifies the noise under the overall MFWM spectrum, while MI sidelobes emerge between comb lines for a large frequency detuning. In between, when the pump frequency spacing is close to the MI offset frequency, the detrimental impact of MI remains negligible, at least for such a power. Indeed, in Figure 3c, we provide the temporal autocorrelation traces of the multi-wavelength source generated with 96.2-GHz frequency spacing (0.77 nm) for several pump powers.

We found that the initial sinusoidal pattern with a period of 10.4 ps evolves into a nearly triangular pattern with increasing powers (i.e., associated with larger spectra). However, for an input power of 32 mW, we clearly distinguish the formation of a localized short temporal structure within each period of the initial beating, in contrast with the normal dispersion regime. However, at input powers exceeding 50 mW, a noticeable decline in the intensity coherence of the temporal pattern is observed, directly attributed to the detrimental impact of MI, as depicted in Figure 3a. The reduced contrast between the central autocorrelation peak and the neighboring intercorrelation peaks in the signal exposes a pronounced jitter in the pulse train, related to coherence loss of the multi-line comb source.

4 Experimental results at 2 μm

Thanks to the simple architecture of our system, we extended this work to the 2-\mu m waveband by interchanging suitable fiber components and pump lasers. Due to the high linear losses of silica-based fibers in this spectral range, we used the shorter normally-dispersive HNLF (length equal to 350 m), which still exhibits normal dispersion ($\beta_2 \sim 1 \text{ ps}^2/\text{km}$) around 1.95–2.0 μ m. The nonlinear coefficient was estimated to be ${\sim}8~\mathrm{W^{-1}\,km^{-1}}.$ More details about the Brillouin properties at 2-µm pump wavelength of similar fibers can be found in Ref. [26]. We first measured the dual-frequency Brillouin lasing threshold by extracting only 1% of the optical cavity power as a function of the injected pump power. As shown in Figure 4a, an input power of 90 mW allowed us to reach the dual-frequency Stokes lasing in our ring cavity in the case of a frequency spacing of 106 GHz (0.85 nm) around 1.98 \textrm{\mu}m. In Figure 4b,

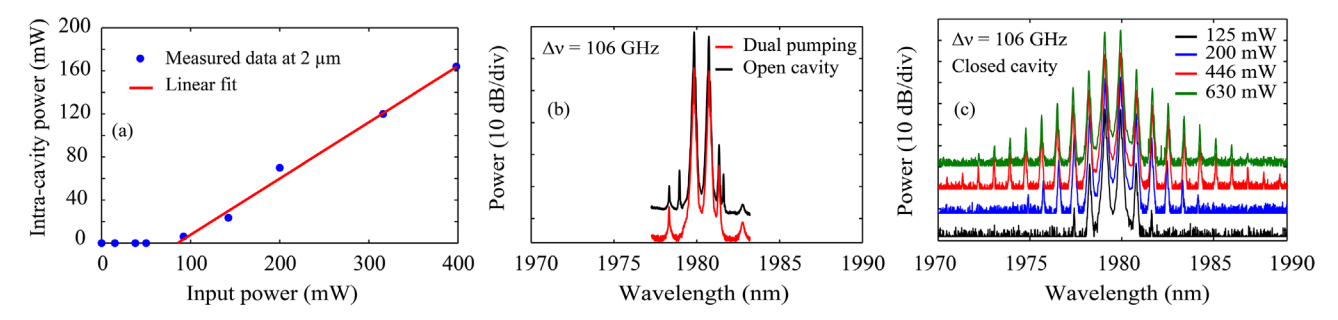


Fig. 4. Dual-frequency Brillouin lasing and multi-wavelength light generation in a multimode regime in the 2-μm waveband. (a) Stokes laser threshold measurement. (b) Experimental recording with 106 GHz frequency spacing of the dual pumping and cavity-free FWM configuration at 200 mW pomp power. (c) Experimental FWM results as a function of the injected power at fixed pumps frequency of 106 GHz in close cavity configuration.

the experimental spectrum of the initial dual-frequency pumping is illustrated alongside the corresponding output of the HNLF fiber (i.e., open cavity configuration) for an input power of 200 mW. Because of the higher fiber losses at such wavelengths (about 15 dB/km), the cascaded FWM process proves to be highly inefficient in this cavity-free configuration, failing to generate any new spectral lines. This outcome persists despite the judicious selection of this fiber due to its moderate losses compared to typical silica fibers. It becomes here obvious that our closed cavity configuration based on the dual-frequency Brillouin laser will provide an interesting solution for MFWM processes and the generation of a multi-wavelength light source. Figure 4c confirms this claim by showing the spectral broadening obtained in the cavity upon increasing input powers from 125 mW to 630 mW. As previously shown, the cavity operating in the normal dispersion does not present any saturation of MFWM due to MI. The number of comb lines increases rapidly to 22 lines when the input power reaches 446 mW. Furthermore, within this specific range of a few hundred milliwatts, we observe a spectral saturation, mirroring the behavior observed in the 1.55-um experiment. It is important to note that the generated comb lines are fewer in number compared to those at 1.55 µm, primarily due to the higher cavity losses, exhibiting an order of magnitude difference.

5 Conclusion

In conclusion, despite employing extended cavity lengths in the dual-frequency Brillouin fiber laser, resulting in multimodal laser operation, we have experimentally confirmed the effective generation of multiwavelength comb sources through cascaded four-wave mixing (FWM) processes at both 1.55 μm (C-band) and 2 μm (thulium band). We have shown that the number of comb lines undergoes rapid expansion with increasing input power, and their frequency spacing is adjustable by varying the initial pump wavelengths. Additionally, distinct characteristics related to the sign of net cavity dispersion were also evidenced. While this long-cavity configuration was previously examined at 1.55 μm in Ref. [23], it was limited to one dispersion

regime, without emphasizing the adverse effects of MI. Notably, we did not specifically optimize fiber cavity lengths for coherent comb generation in this study. For further insights into this aspect, we direct the reader to previous works conducted at $1.55 \, \mu m$ [24, 27].

Furthermore, we extended the approach to the 2- μ m waveband, where cascaded FWM in the continuous-wave regime is typically impeded by significant fiber losses. No asymmetric spectral broadenings were observed when initial power is equally distributed over the two pumps, since we were operating in a free-running configuration without a phase-locking loop scheme (in contrast with Ref. [24], where pump detuning is effectively controlled). Nevertheless, the enhanced performances of cascaded FWM in this simple architecture of the Brillouin fiber laser make it readily applicable at any wavelength where fiber components and CW lasers are available. A straightforward application in the future could extend in the mid-infrared region, leveraging fluoride glass fiber or chalcogenide fiber technology, but also in the high-demanding 1-µm waveband. However, to maintain the complete coherence properties of the generated combs, the implementation of a stabilization scheme is necessary, as recently demonstrated at 1 µm [28].

Funding

The authors acknowledge the support of the Agence Nationale de la Recherche (Grant Number: ANR-16-CE24-0010, ANR-17-EURE-0002, ANR-15-IDEX-0003), the Conseil Régional de Bourgogne Franche-Comté and the European Framework Programme (Grant 101135904).

Conflicts of interest

The authors declare no conflict of interests.

Data availability statement

Data underlying the results presented in this paper are not publicly available at this time but may be obtained from the authors upon reasonable request.

Author contribution statement

All authors made significant contributions to this work.

References

- 1 Cossel K.C., Waxman E.M., Finneran I.A., Blake G.A., Ye J., Newbury N.R. (2017) Gas-phase broadband spectroscopy using active sources: progress, status, and applications [Invited], J. Opt. Soc. Am. B 34, 1, 104–129.
- 2 Russell E., Corbett B., Gunning F.C.G. (2022) Gainswitched dual frequency comb at 2 μ m, *Opt. Express* **30**, 4, 5213–5221.
- 3 Parriaux A., Hammani K., Millot G. (2018) Two-micron all-fibered dual-comb spectrometer based on electro-optic modulators and wavelength conversion, *Commun. Phys.* 1, 1, 1–7.
- 4 Cao W., Hagan D., Thomson D.J., Nedeljkovic M., Littlejohns C.G., Knights A., Alam S.-U., Wang J., Gardes F., Zhang W., Liu S., Li K., Rouifed M.S., Xin G., Wang W., Wang H., Reed G.T., Mashanovich G.Z. (2018) High-speed silicon modulators for the 2 μm wavelength band, Optica 5, 9, 1055–1062.
- 5 Gunning F., Corbett B. (2019) Time to open the 2-μm window?, Opt. Photonics News 30, 3, 42–47.
- 6 Dada A.C., Kaniewski J., Gawith C., Lavery M., Hadfield R. H., Faccio D., Clerici M. (2021) Near-maximal two-photon entanglement for optical quantum communication at $2.1~\mu m$, *Phys. Rev. Appl.* **16**, 5, L051005.
- 7 Parriaux A., Hammani K., Millot G. (2020) Electro-optic frequency combs, *Adv. Opt. Photonics* **12**, 1, 223–287.
- 8 Kayes M.I., Rochette M. (2017) Optical frequency comb generation with ultra-narrow spectral lines, *Opt. Lett.* **42**, 14, 2718–2721.
- 9 Wu R., Supradeepa V.R., Long C.M., Leaird D.E., Weiner A.M. (2010) Generation of very flat optical frequency combs from continuous-wave lasers using cascaded intensity and phase modulators driven by tailored radio frequency waveforms, Opt. Lett. 35, 19, 3234–3236.
- 10 Washburn B.R., Diddams S.A., Newbury N.R., Nicholson J. W., Yan M.F., Jørgensen C.G. (2004) Phase-locked, erbium-fiber-laser-based frequency comb in the near infrared, *Opt. Lett.* 29, 3, 250–252.
- 11 Cundiff S.T., Ye J. (2003) Colloquium: Femtosecond optical frequency combs, *Rev. Mod. Phys.* **75**, 1, 325–342.
- 12 Del'Haye P., Schliesser A., Arcizet O., Wilken T., Holzwarth R., Kippenberg T.J. (2007) Optical frequency comb generation from a monolithic microresonator, *Nature* 450, 7173, 1214–1217.
- 13 Kippenberg T.J., Holzwarth R., Diddams S.A. (2011) Microresonator-based optical frequency combs, *Science* 332, 6029, 555–559.
- 14 Xing S., Kowligy A.S., Lesko D.M.B., Lind A.J., Diddams S. A. (2020) All-fiber frequency comb at 2 μm providing 1.4-cycle pulses, Opt. Lett. 45, 9, 2660–2663.
- 15 Wang X., Jia K., Chen M., Cheng S., Ni X., Guo J., Li Y., Liu H., Hao L., Ning J., Zhao G., Lv X., Huang S.-W., Xie Z.,

- Zhu S.-N. (2022) 2 μ m optical frequency comb generation via optical parametric oscillation from a lithium niobate optical superlattice box resonator, *Photonics Res.* **10**, 2, 509–515.
- 16 Hu K., Kabakova I.V., Lefrancois S., Hudson D.D., He S., Eggleton B.J. (2014) Hybrid Brillouin/thulium multiwavelength fiber laser with switchable single- and double-Brillouinfrequency spacing, *Opt. Express* 22, 26, 31884–31892.
- 17 Zhao S., Lu P., Liu D., Zhang J. (2013) Switchable multiwavelength thulium-doped fiber ring lasers, *Opt. Eng.* **52**, 8 086105.
- 18 Wang X., Zhu Y., Zhou P., Wang X., Xiao H., Si L. (2013) Tunable, multiwavelength Tm-doped fiber laser based on polarization rotation and four-wave-mixing effect, *Opt. Express* 21, 22, 25977–25984.
- 19 Peng W., Yan F., Li Q., Liu S., Feng T., Tan S. (2013) A 1.97 μm multiwavelength thulium-doped silica fiber laser based on a nonlinear amplifier loop mirror, *Laser Phys. Lett.* 10, 11 115102.
- 20 Jiang S., Guo C., Fu H., Che K., Xu H., Cai Z. (2020) Midinfrared Raman lasers and Kerr-frequency combs from an allsilica narrow-linewidth microresonator/fiber laser system, *Opt. Express* 28, 25, 38304–38316.
- 21 Fatome J., Pitois S., Fortier C., Kibler B., Finot C., Millot G., Courde C., Lintz M., Samain E. (2010) Multiple four-wave mixing in optical fibers: 1.5–3.4-THz femtosecond pulse sources and real-time monitoring of a 20-GHz picosecond source, Opt. Commun. 283, 11, 2425–2429.
- 22 Wolff C., Smith M.J.A., Stiller B., Poulton C.G. (2021) Brillouin scattering – theory and experiment: tutorial, *J. Opt. Soc. Am. B* **38**, 4, 1243–1269.
- 23 Li Q., Jia Z., Li Z., Yang Y., Xiao J., Chen S., Qin G., Huang Y., Qin W. (2017) Optical frequency combs generated by four-wave mixing in a dual wavelength Brillouin laser cavity, AIP Adv. 7, 7, 075215.
- 24 Lucas E., Deroh M., Kibler B. (2023) Dynamic interplay between Kerr combs and Brillouin lasing in fiber cavities, *Laser Photonics Rev.* 17, 12, 2300041.
- 25 Bai Y., Zhang M., Shi Q., Ding S., Qin Y., Xie Z., Jiang X., Xiao M. (2021) Brillouin-Kerr soliton frequency combs in an optical microresonator, *Phys. Rev. Lett.* 126, 6 063901.
- 26 Deroh M., Beugnot J.-C., Hammani K., Finot C., Fatome J., Smektala F., Maillotte H., Sylvestre T., Kibler B. (2020) Comparative analysis of stimulated Brillouin scattering at 2 μm in various infrared glass-based optical fibers, J. Opt. Soc. Am. B 37, 12, 3792–3800.
- 27 Deroh M., Lucas E., Kibler B. (2023) Dispersion engineering in a Brillouin fiber laser cavity for Kerr frequency comb formation, Opt. Lett. 48, 24, 6388–6391.
- 28 Deroh M., Lucas E., Hammani K., Millot G., Kibler B. (2023) Stabilized single-frequency sub-kHz linewidth Brillouin fiber laser cavity operating at 1 μm, Appl. Opt. 62, 30, 8109–8114.

J. Eur. Opt. Society-Rapid Publ. 2024, 20, 24
© The Author(s), published by EDP Sciences, 2024

https://doi.org/10.1051/jeos/2024022

Available online at: https://jeos.edpsciences.org

EOSAM 2023

Guest editors: Patricia Segonds, Guy Millot and Bertrand Kibler

RESEARCH ARTICLE OPEN 3 ACCESS

Design of an optical system equipped with blue LEDs for the irradiation of *Drosophila melanogaster* cultures

Mónica López-Bautista¹, Jorge Enrique Mejía-Sánchez^{1,*}, Francisco Javier Ornelas-Rodríguez², and Viviana Matilde Mesa-Cornejo¹

Universidad de Guadalajara, Centro Universitario de Los Lagos, Lagos de Moreno, Jalisco C.P. 47460, México

Received 31 January 2024 / Accepted 22 April 2024

Abstract. Drosophila melanogaster, better known as the fruit fly, has become a widely used model organism that has allowed us to understand many biological behaviors, from sleep to neurological diseases, behavioral patterns, reproduction, and the circadian cycle, which coordinates biological rhythms in a 24-hour daily cycle through its main Zeitgerber, light, especially blue light. Therefore, the aim of this work was to build an optical setup with a hexagonal design that allowed a large number of D. melanogaster cultures to be irradiated homogeneously with blue light simultaneously. This array can cover an illuminance range from 0 to approximately 600 lux by applying a current variation from 0 to approximately 1 A. It also has a real-time timer to turn the lights on and off, programmed in a 12:12 LD cycle for 24 h. The optical setup with its unique design can become a very useful tool for developing experiments and understanding paradigms related to blue light at genetic, behavioral and neuronal levels, among others that are still unanswered.

Keywords: Drosophila melanogaster, Optical setup, Circadian cycle, Blue light.

1 Introduction

Light has been fundamental to the evolution of all organisms on Earth and has a profound effect on behavior, physiology and metabolism, which can have a significant impact on the health of mammals, including humans [1]. Light is perceived by a specialized light-sensitive tissue at the back of the eye called retina, which function is to detect light and form images. The retina transmits visual information from the optic nerve to the brain, which can affect both our physical and mental state [2]. Light not only allows us to illuminate the environment for vision, but is also responsible for regulating processes that occur independently of image formation, such as the circadian cycle, which is present in most organisms from cyanobacteria to humans [3, 4]. These rhythms synchronize biological functions such as sleep/wake cycles and hormone levels with the external environment through signals known as zeitgebers, with light being the most important for "photoentrainment" of the rhythm's activity over a period of about 24 h [5].

It should be noted that the disruption of circadian rhythms by light is due to the desynchronization of the

emits a higher intensity in the blue wavelength range, often peaking at 460 nm [8]. Long-term exposure to blue LED light leads to changes in the circadian cycles of humans, ranging from disruption of the cycle to deregulation of their coupled functions, including sleep and mood [9].

Drosophila melanogaster is an excellent model to study how light affects various processes such as hatching, courtship, locomotion, reproduction, etc. It is also often used to study light-influenced circadian rhythms [10]. In humans, prolonged exposure to blue light has been shown to cause sleep disturbances by suppressing the melatonin produc-

tion. Additionally, it can cause visual fatigue and elicit emotional brain responses such as depression and anxiety [11].

internal biological clock with external environmental

conditions and depends on the duration, wavelength and intensity of light [6]. This is common due to living and

working conditions, 24 h a day, 7 days a week [7]. This is

because we live in a globalized and widely digitalized

society, which brings profound and irreversible changes in

our social, domestic and professional environment, leading

to an increasing use of LED technology, applied in various

technological devices, lighting, medical treatments, etc.

Although it gives us as humans independence in daylight,

we are enhancing exposed to light in the blue spectrum as

we spend more time indoors. This is because LED light

² Instituto Politécnico Nacional, Centro de Investigación en Ciencia Aplicada y Tecnología Avanzada, Unidad Querétaro, Querétaro C.P. 76090, México

^{*} Corresponding author: enrique.mejia@academicos.udg.mx

It also shortens the lifespan of *D. melanogaster*, accelerates aging and leads to sleep disturbances, etc. [12].

Although there are some devices for evaluating the effect of blue light in flies, they have several disadvantages such as a limited number of cultures and thus a smaller sample size, as well as a limited range of application. Therefore, the aim of this work was to carry out the optical design of a system for homogeneous irradiation of D. melanogaster cultures with blue LED light. This system allows for the observation of various areas of interest, including strain strain development, longevity, reproduction, courtship to stress response gene expression, brain neurodegeneration, retinal degeneration, antioxidant compound assessment, etc., over an extended period of time and several generations simultaneously. This setup is cost-effective and easy to manipulate. It is programmed in a cycle of 12 light hours and 12 dark hours (12:12 LD) to simulate the alternation of day and night.

2 Materials and methods

2.1 Light source

High-power blue 1W LED with aluminum heat sinks (LED-P1B25-120/41, SiLed®) were used. The dimensions were 7.0 mm \times 4.5 mm \times 5 mm for the encapsulated LED and 18.6 mm \times 19.8 mm \times 15 mm with the aluminum heat sink. The technical sheet indicates that each LED has a minimum luminous flux of 25 and maximum of 45 lm and a threshold voltage of 3.0–3.8 V, with a viewing angle of 120° and a forward current of 350 mA.

The emission spectrum was measured with the Flame Miniature Spectrometer (FLAME-S-XR1, Ocean Insight Inc., Florida, USA). The LED emission spectrum had a wavelength central at 457 nm with a spectral width of $\Delta\lambda$ 45 nm at 25 \pm 1 °C and providing an energy per photon of $4.352\times10^{-19}~\mathrm{J}.$

2.2 Circuit assembly

The HanMatek HM305 variable power supply (HanMatek, China) was used to realize the overall connection of the circuit with a current output of 0–5 A ($\leq 0.2\% \pm 3$ digits) and an output voltage of 0–30 V ($\leq 0.1\% \pm 1$ digit). The LEDs used for the assembly were connected in parallel with a CORDON SPT-1 300 V (20 AWG) cable (Indiana, Ware & Cable, USA) which was connected with the SOL60-100 solder (Electrónica Steren S.A. de C.V., Mexico), with a diameter of 1 mm, a composition of 60/40 tin/lead and a melting point of 183 °C, using the WLC 100 soldering station and a conical ST7 soldering tip (Weller, USA).

2.3 Temperature control

The temperature and humidity are controlled by the laboratory's air conditioning system, then to verify the thermal gradients within the arrangement, two thermohygrometers were used, the USB-502-LCD thermohygrometer (Logicbus, USA) with a measurement range of 0%–100% humidity and a temperature of -35 to +80 °C and an

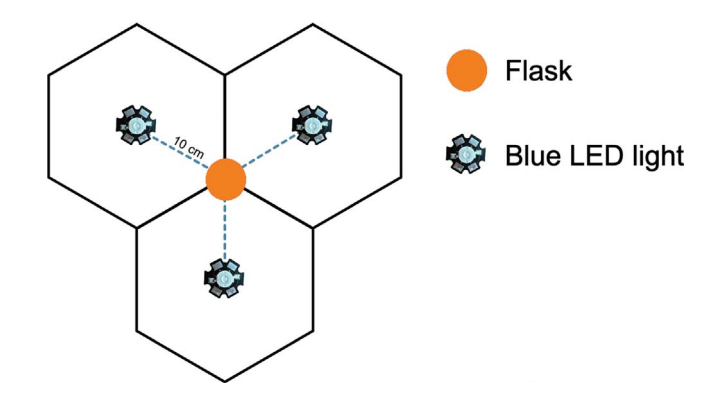


Fig. 1. Location plane of the LED and the flask (at each vertex of the hexagon) separated 10 cm from each other.

accuracy of ± 0.5 °C (± 1.0 °F) and ± 3.0 % relative humidity and a DeltaTrak model 13309 thermohygrometer (DeltaTrak® Inc., USA) with NIST certification. The first one was used to measure variations throughout the day (24 h) allowing for data storage and export.

On the other hand, the second one was used to record the temperature and humidity while the experiment was running.

2.4 Real-time lighting control system

The lights were controlled by an Arduino Uno microcontroller (Arduino, Italy) of 16 MHz in which a real-time lighting control system was implemented to control the on/off operation of the array equipped with blue LED lights operating at a clock rate. The control system was designed to switch the LED power supply in a 12:12 LD cycle. The voltage sources that supply power to the LED assemblies were independent and operate on 120 volts AC. Since the controller of the Arduino Uno board does not have a realtime clock, it was necessary to install the ARD-374 board. which is a Real Time Clock (RTC). This RTC card allowed for programming of the real-time schedule and accurate tracking of the date and time. This type of card contains a backup battery, such as an SR225, which allowed the clock to continue functioning even when the main power source was disconnected.

2.5 Illuminance

The illuminance was measured with the luxmeter (GM-1010, Shenzhen Jumaoyuan Science and Technology Co., Ltd., Shenzhen, China) with an accuracy of $\pm 3\%$ rdg $\pm 0.5\%$ f.s. (<10,000 lux) and $\pm 4\%$ rdg ± 10 dgts. (>10,000 lux), at a surface distance of 10 cm and a sensor height of 5 cm. Five replicates of measurements were taken at each point where a Drosophila culture could be positioned.

2.6 Fly strains and maintenance

The wild strain of *D. melanogaster* (Canton, CS flies) was acquired from the *Drosophila* Stock Center Mexico by the Universidad Nacional Autónoma de México (UNAM). *D. melanogaster* parents were reared at 25 ± 1 °C under

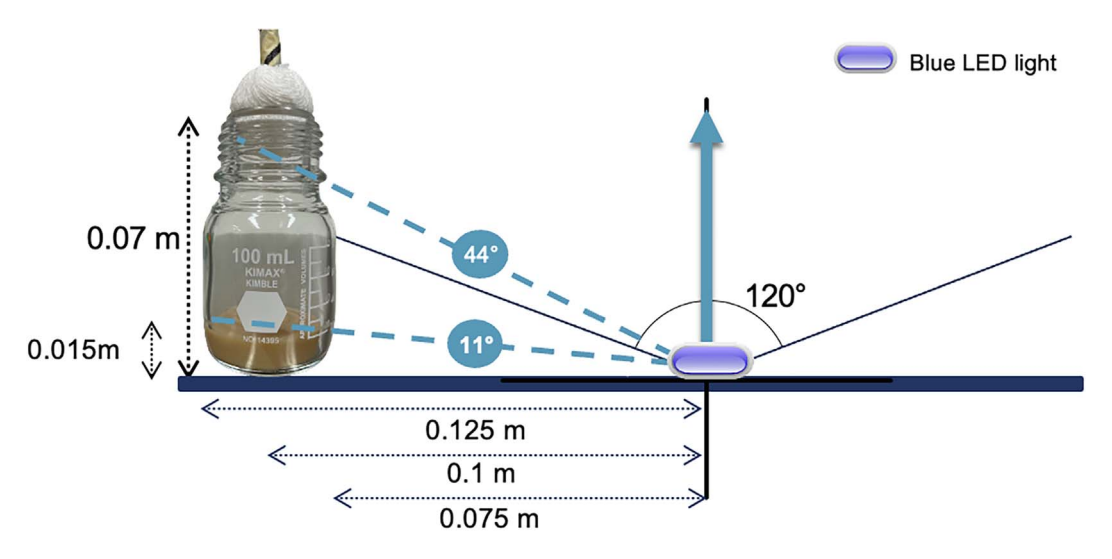


Fig. 2. Distribution of light in relation to the angle of irradiation towards the flask, considering the culture medium, the flies and the cap.

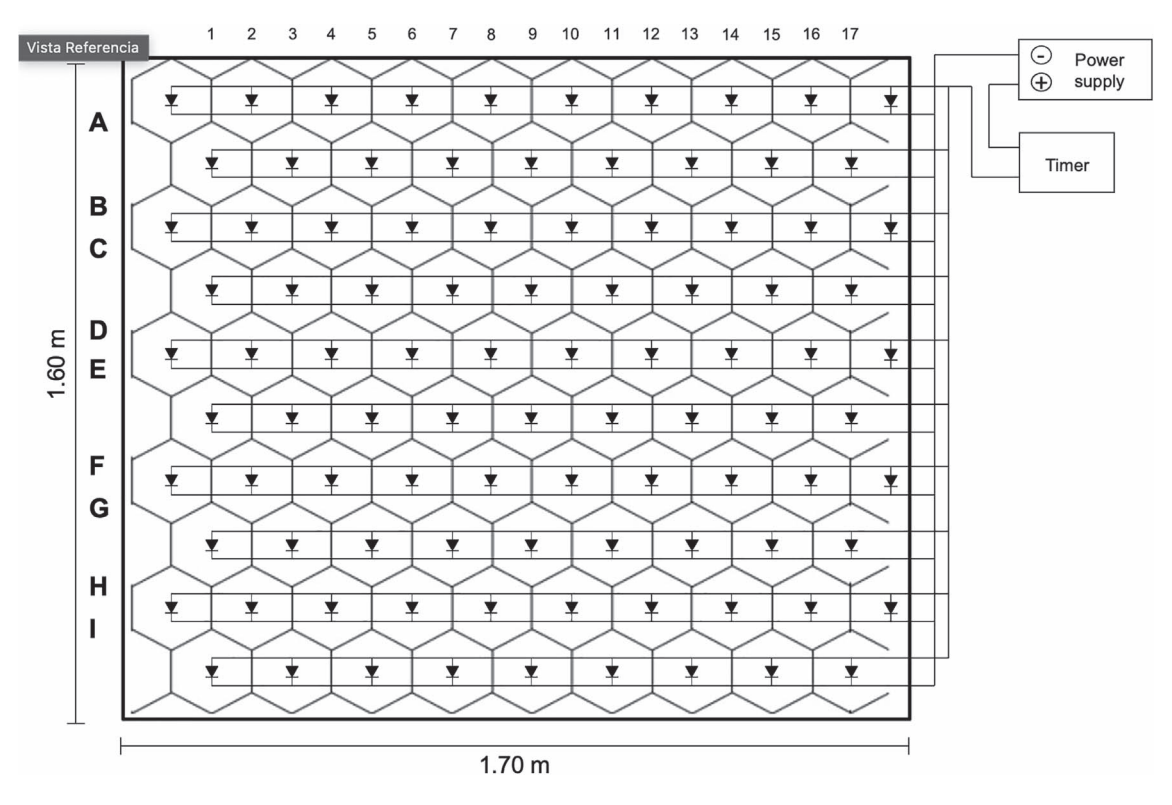


Fig. 3. Electrical diagram of the circuit used to connect 95 blue light LEDs in parallel to a variable power source and consecutively to the timer.

conventional light. Virgin adult Drosophila were separated by sex to avoid copulation and anesthetized with ether. Subsequently, 3 pairs of flies (3 males – 3 females) were paired in a 100 mL borosilicate flask previously filled sterilely with 20 mL of culture medium enriched with yeast. This was carried out in five replicates; flies were mated for 8 days at 25 \pm 1 °C with a humidity of over 40% and an illuminance of ~100 lux in a LD 12:12 cycle. Then, the

parents were sorted out to obtain the offspring, which were kept under the same conditions and separated by sex in different flasks.

2.7 Data analysis

The illuminance data were analyzed with a Shapiro–Wilk test and a QQ-plot using OriginPro statistical software.

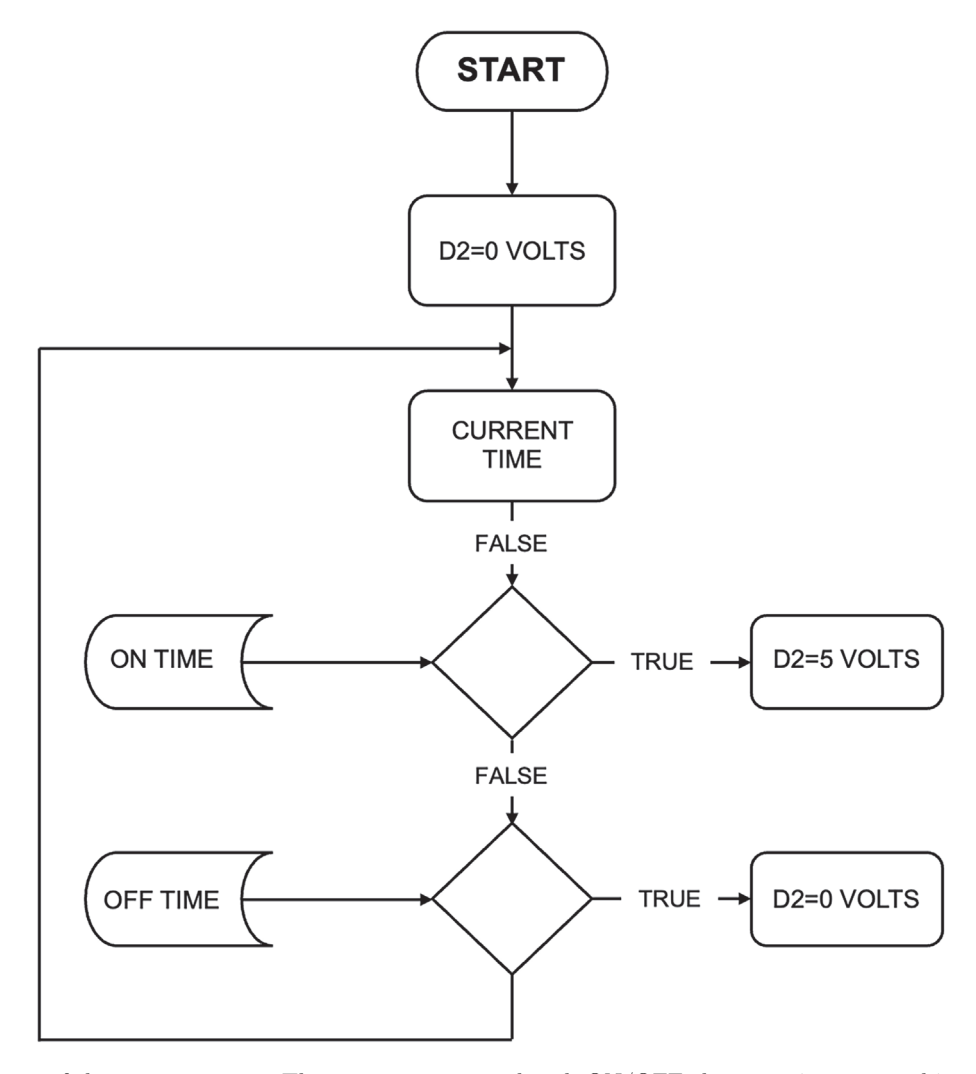


Fig. 4. Flow diagram of the timer program. The timer programmed with ON/OFF change at 7:00 am and 7:00 pm respectively.

The biological assay data were subjected to a two-way analysis of variance (ANOVA) using GraphPrism 8 statistical software.

3 Design and construction of optical assembly

To observe the effects of light on organisms, various devices with light sources, usually of the LED type, have been proposed for the irradiation of *D. melanogaster* [13, 14], one of the drawbacks was to ensure that each organism receives the same amount of light regardless of the number of cultures to be prepared, so a design was initially developed to solve this problem by simple assembly and handling.

A design was developed featuring a hexagonal arrangement within a defined area, with a flask located at each vertex and a blue LED positioned in the center. In this way, each flask receives the illuminance of 3 LEDs around it, at a distance of 10 cm (Fig. 1).

According to the vertical plane of the arrangement, the irradiation angle was 33° , with angles below 11° corresponding to the culture medium and angles above 44° referring to

the cotton plug and unused space. Furthermore, the dimensions of the flask, the culture medium, and their distances from the LED position are shown (Fig. 2).

In order to assemble an optical setup suitable in size for the development and evaluation of D. melanogaster cultures, this design was placed in a specific area inside the laboratory that would allow the layout of the plan according to the previously proposed design. Therefore, the final dimensions of the arrangement were of $1.6~\mathrm{m}\times1.7~\mathrm{m}\times0.2~\mathrm{m}$, which allowed a circuit of 95 LEDs connected in parallel, that were soldered in 10 rows of 10 and 9 LEDs as shown in Figure 3.

Figure 4 shows the operation of the software that controlled the lighting, initially, a 0-volt value was sent to the digital output D2 to ensure that the control started with the light off. Next, the real-time clock (RTC) card was read to obtain the current time (hour and minutes) and this was compared with the programmed time switching on the lighting (7 am). When the real time and programmed switch-on time match, a 5-volt signal was sent through digital output 2, which activated the relay and closed the 3.8 DC-volt circuit to power the lights.

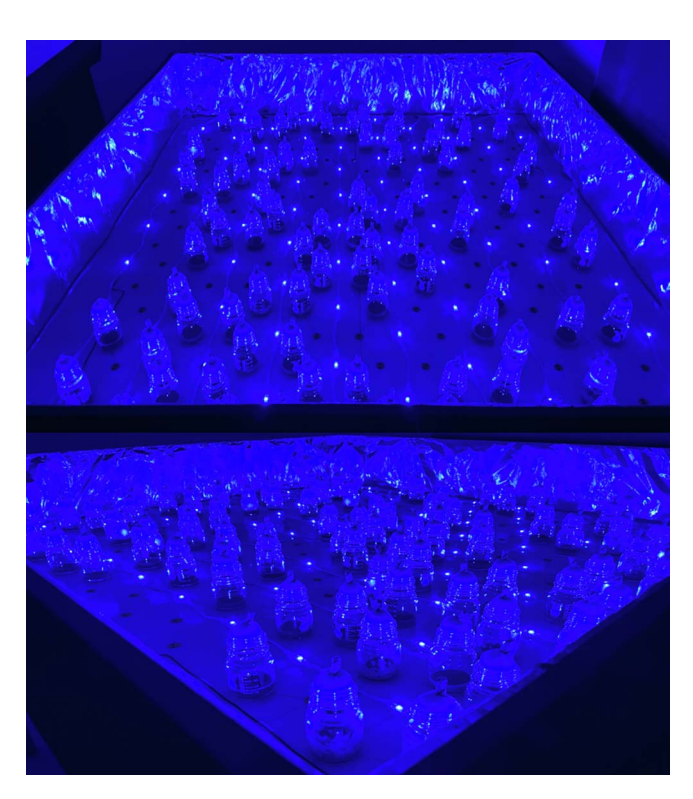


Fig. 5. Prototype of the optical assembly, tested and used for cultures of the development of *Drosophila* flies.

Once the power supply was switched on, it remained active while the software continuously compared the real-time with the programmed switch-off time. When the real-time matched, the scheduled turn-off time, a 0-volt signal was sent through digital output 2, deactivating the relay switch and turning off the 3.8 DC-volt circuit. This cycle was repeated until the real-time matched the programmed switch-on time again.

Additionally, the optical array was protected with walls and ceiling covered internally with aluminum foil to maintain the reflection emitted by the LEDs. This arrangement allowed the manipulation and development of up to 153 Drosophila cultures in 100 mL flasks in an area of 2.72 m² (Fig. 5), which it is suggested can be organized randomly in future experiments. The low-cost blue LEDs were equipped with a useful aluminum heat sink or PCBs (Printed Circuit Boards), which facilitates heat dissipation from the LED to the environment, and helps to maintain the temperature of the LED within safe levels.

4 Characterization of optical system

A characteristic group of insects has been used in chronobiological experiments, from the honeybee (*Apis mellifera*) to the monarch butterfly (*Danaus plexippus*), due to their ease to manipulate and well-defined circadian cycles *D. melanogaster* is the model organism par excellence to understand these processes. Furthermore, the molecular

basis of circadian rhythms is fully characterized in *D. melanogaster*, which, coupled with its fully sequenced genome, represents a significant advantage over other models [15, 16]. When exposing these insects to a stimulus such as light, the source must be quantified, either in the form of measurements such as illuminance or correlated color temperature to directly elucidate their behavior [17].

The illuminance of the light source, the blue LED, was measured in the optical assembly at each point where a culture can be positioned at 190 \pm 4.8 mA. Each flask was illuminated by 3 LEDs according to the proposed hexagonal design. Therefore, the illuminance was indicated by three measurements with the luxmeter, each taken in the normal direction of the light source. The uncertainty in measurements was estimated according to the Guide for the Uncertainty in Measurements (GUM), the relative uncertainty contribution from the instrument (calibration error resolution) was considered as 3%, as reported by the manufacturer for the measurement range and scales used, which is consistent with previous accuracy reports for this metrological class of luxmeters [18]. Additionally, a 1.25% for the reading repeatability. This relative combined standard estimated uncertainty is represented in figure with a coverage factor k=2, ensuring a 95.4% confidence. The data obtained were grouped into 9 classes as shown in Figure 6A. These values were arranged in columns from 1 to 17 and in rows from A to I, where each circle represents a place for a possible culture in the array. Each shade of blue represents the range of illuminance according to an interval of 1.515 lux. In this way, a minimum value of 86.28 ± 2.8 lux (light blue circle at A2) was recorded, while the maximum value was 99.92 ± 3.24 lux (dark blue circle at B12). Overall, the arrangement had an average value of 92.14 ± 2.99 lux. These values correspond to the behavior of a normal distribution, which was verified with the Shapiro-Wilk with p > 0.05 (Figs. 6B and 6C).

This optical arrangement was able to achieve illuminance levels ranging from 0 to 601.12 ± 19.53 lux at a current variation of 0–1.05 A with an uncertainty \pm (2% \pm 10 digits), (Fig. 7). It should be noted that different illuminance levels can be programmed locally via the variable power supply by adjusting the current into the system. The desired illuminance value to test will depend on the objective of the project and the specific design parameters under observation. This flexibility enables a wide range of possibilities, allowing for the analysis of the blue light under various conditions.

On the other hand, the temperature remained stable within the range required by the biological model thanks to the laboratory's air conditioning system. Figure 8A shows that over a period of 24 h, during which the temperature was measured every 10 s with an injected current of 190 ± 4.8 mA, there was only a change of 0.5 °C. Furthermore, to evaluate the change in the temperature caused by illuminance, the current was modified in increments of 0.05 A every 60 min, starting at 0.05 A and ending at 1.05 A with an uncertainty \pm (2% +10 digits), observing a rise 24.5 \pm 0.5 °C to 25 \pm 0.5 °C at 0.25 \pm 0.006 A shown in Figure 8B, after this value, no further temperature changes were detected.

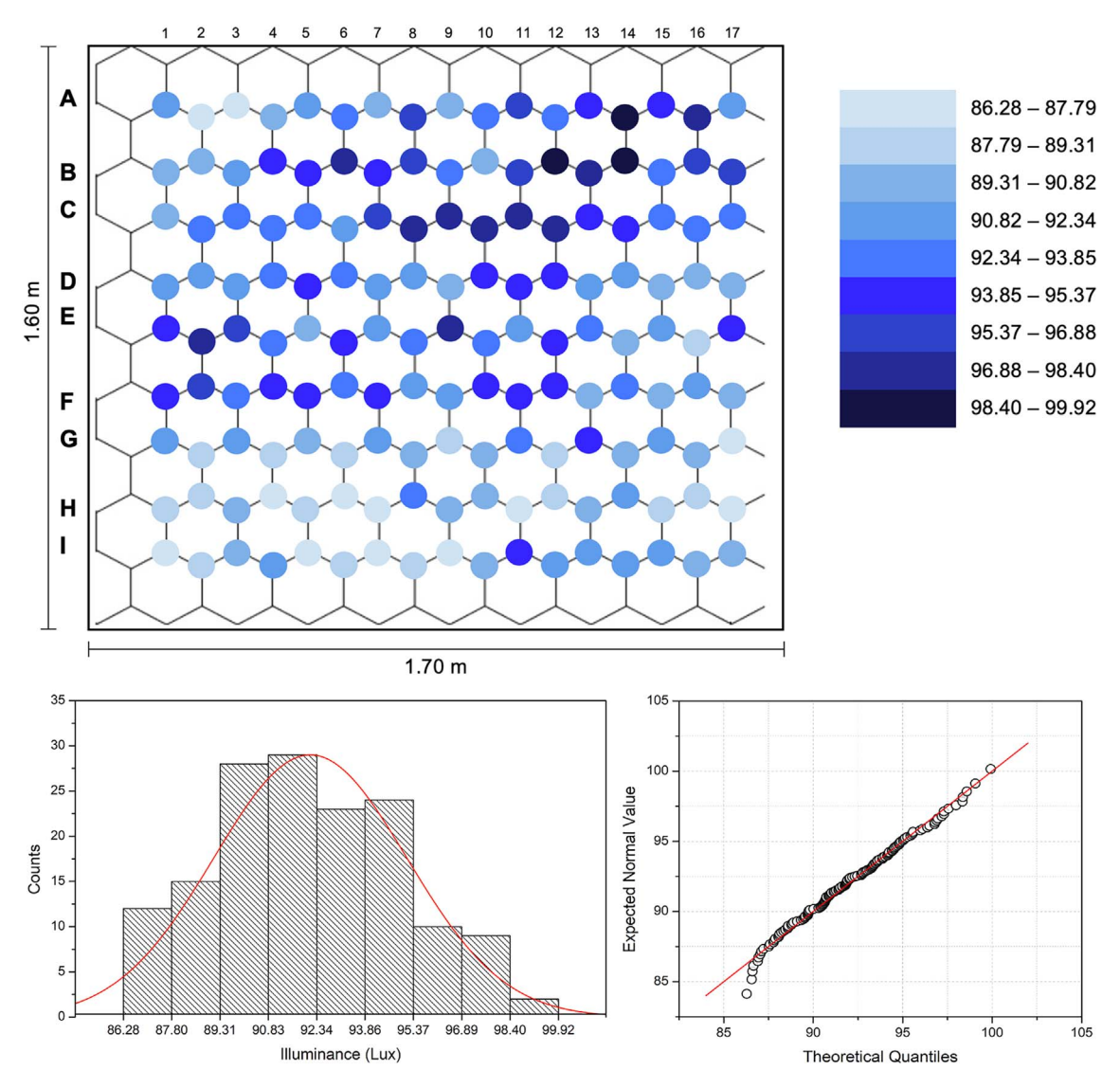


Fig. 6. Representation of the illuminance (uncertainty of 3.25%) in the LED assembly area (A) distribution of the illuminance at the 153 points where each culture flask can be positioned. (B) Histogram of the data grouped into 9 classes. The Shapiro–Wilk test gives a value of p = 0.17754 C. QQ-plot normality with those expected.

5 Biological assay

To verify the non-toxicity of the proposed optical design, an illuminance of ~100 lux was used, which did not register a toxic effect on the development of Drosophila [19] and could be compared with its development under conditions of total darkness (DD). To set the array to ~100 lux, the current in the variable source was manually changed to 205 ± 5.1 mA. Five culture repetitions with three pairs of flies each were exposed to blue light for 8 days, then the parents were discarded. The culture was maintained under the same illuminance and temperature conditions (25 \pm 1 °C) during all stages of metamorphosis until adult flies were obtained and the number of males and females was recorded.

Figure 9 shows the SD of the population averages obtained during the LD/DD periods by sex. For males:

 34.2 ± 8.9 and $33\pm4.94;$ while for females: 38.4 ± 5.17 and $37.2\pm4.60,$ respectively.

It was observed that the number of flies obtained during the LD 12:12 period with the proposed optical design compared to the dark period (DD) did not present a significant difference according to the two-way ANOVA with p=0.669 for LD conditions and p=0.147 by sex.

6 Discussion

The use of *D. melanogaster* as a model organism has been of fundamental importance for the understanding of various biological processes, particularly the circadian cycle that underlies the human being. This cycle is closely linked to temperature and, in general, to light, which serves as the primary driving stimulus due to the presence of rhodopsins

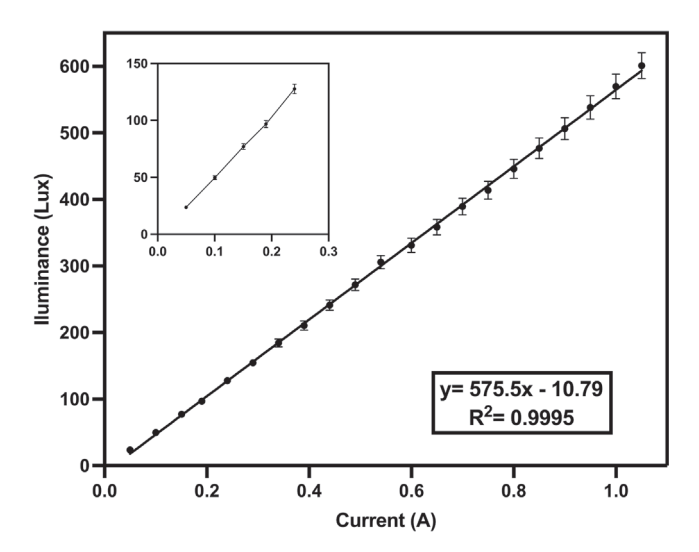


Fig. 7. Measurement of illuminance with respect to the variation of current injected (\pm (2% +10 digits)), into the circuit.

in the visual organs (ocelli and compound eyes) and the Hofbauer-Buchner (HB) eyelets [20]. Since blue LED light is a relatively new light source, its long-term effects on humans are unknow. Therefore, the design of a novel optical setup was proposed as a hexagonal network over a defined area, allowing for the simultaneous and straightforward evaluation of up to 153 Drosophila cultures to understand the effect of blue light on flies. Generally, plastic and/ or glass vials are used for maintenance of D. melanogaster [21, 22] due to their easy handling and low cost. However, limitations arise in the number of offspring compared the proposed configuration, which allowed the monitoring of a large number of cultures, ensuring more precise results in complex biological processes susceptible to being affected by light, such as reproduction, oviposition, sex determination, etc. These processes have not yet been fully understood, unlike studies that were limited by the number of replicates [23, 24]. Additionally, the transgenerational effect of blue light could cause genetic changes that can be passed on to the next generation [25].

The completion of the construction of this arrangement required covering the walls with aluminum foil, which, in addition to being an economical and easily accessible material, also offers a light reflectance of 70%–75% in the blue light range [26]. This reflectance is necessary to ensure the quasi-homogeneous distribution of light in the spaces that are on the sides of the arrangement. While various reflective materials such as mirrors, silver, chrome, and polymers may be highly efficient, they often come with disadvantages such as high cost and difficult handling when applied in the arrangement in question. On the other hand, materials that disperse light, such as softboxes and diffuser paper, aim to soften light but may lead to a loss of light intensity.

Conversely, according to the proposed design and upon completing the construction of the optical setup, the illuminance was found to be quasi-homogeneous, reaching an average value of 92.14 \pm 2.99 lux at 190 \pm 4.8 mA. The variability in the illuminance can be mitigated by randomly placing the cultures at the specified positions. Moreover,

this type of study is often conducted using an incubator equipped with LED lighting [27]. However, a drawback of this approach is the lack guarantee that all cultures receive the same amount of light and the number of replicates may be limited depending on the experiment setup and workspace constraints. One of the disadvantages of using this type of equipment to study the effect of blue light is the low practicality of variating the illuminance, which often requires changing in the type of light installation. However, the optical setup presented has the advantage that the illuminance range, following a linear trend from 0 to 601.12 ± 19.53 lux, can be modified in a direct and simply by adjusting the injected current from 0 to 1.05 A, respectively. It is important to note that in various studies where light has been used as a stimulus, organisms are often exposed to abnormal light intensity or wavelength outside their normal ecological conditions. Similarly, the incubators normally used for the maintenance of *D. melanogaster* are programmed to around 2000 lux for common laboratory experiments, with treatment depending on the exposure time [13]. Although some devices have been developed to assess exposure to LED light in *Drosophila*, they are often limited by space, cost and design, and also focus on studying a single issue, such as retinal degeneration caused by blue light at high illumination [14]. This limitation can result in obtaining an insufficient number of samples for subsequently analysis at the molecular, immunological, physiological and other levels.

In addition to the above, it is known that the developmental cycle of the fruit fly at 25 ± 1 °C is about 10 days, so temperature fluctuations can either slow down and/or accelerate this process [28]. Furthermore, temperature serves as a driving stimulus for circadian cycles, and since D. melanogaster is an ectothermic insect (body temperature varies with ambient temperature) [29], it is important to maintain this parameter as constant as possible. However, studies with *Drosophila* exposed to light are usually carried out with a variation of temperature up to 25 ± 1 °C [24]. In this way, the temperature in the system was set to 25 °C with a small deviation of 0.5 °C to 190 \pm 4.8 mA. In fact, with the change in current from 0.05 to 0.5 A, the temperature varied from 24.5 ± 0.5 °C to 25 ± 0.5 °C. This is due to the fact that the setup is located in a dark room with a stable temperature year-round, allowing the device can operate under the same conditions of temperature, humidity and, especially, luminance, as the light-dark cycle can be easily programmed.

It should be noted that in different modified strains of D. melanogaster, illuminance levels of up to 300 lux were observed without altering the response in terms of reproduction and longevity [30]. For this experiment, the population was obtained from flies maintained in darkness and exposed to blue light at ~100 lux to validate that the proposed design was suitable for evaluating the effect of light on flies. It was expected that there would be no significant differences in both the 12:12 LD and darkness cycle and by sex. The results confirmed that the proposed design is valid and easily reproducible setup. Furthermore, it was reaffirmed that there are no toxic effects on the development of D. melanogaster in terms of reproduction at ~100 lux [19].

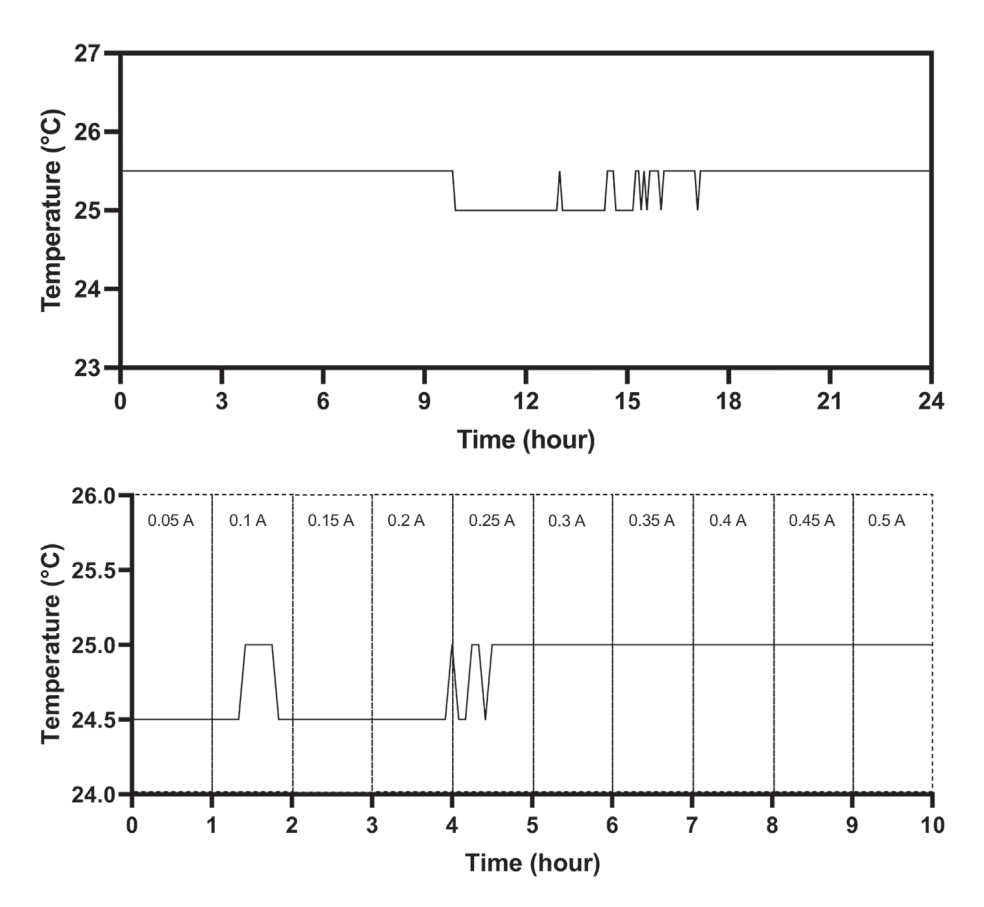


Fig. 8. (A) Temperature measurement throughout 24 h a day at constant current of 190 ± 4.8 mA. (B) Temperature measurement during current variation from 0.05 to 0.5 A (uncertainty of ± 0.5 °C).

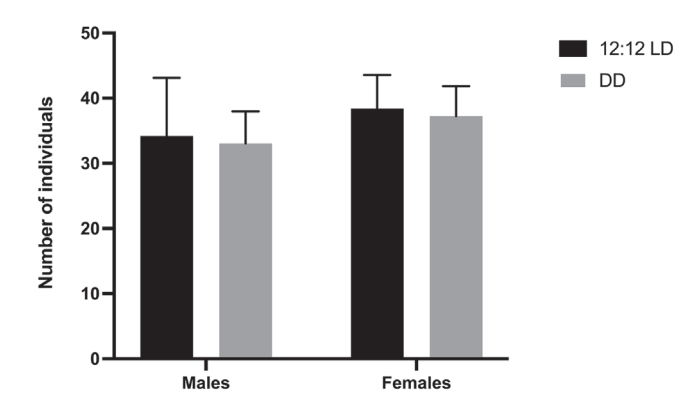


Fig. 9. Effect of blue light on the development of *Drosophila melanogaster* flies. Number of individuals obtained separated into females and males in LD conditions 12:12 h and DD: 24 h - dark conditions at 100 lux.

7 Conclusion

Fruit flies are widely used in laboratory settings to understand various chronobiological processes, where light is employed to observe patterns consistent with the circadian cycle. In particular, exposure to short-wavelength blue light has been linked to proliferation of various problems human

body function, making it an increasingly studied area of interest. Therefore, in this work, a novel optical setup is presented for the development of *D. melanogaster* flies, that allowed the generation of a large number of transgenerational populations with the ability to modulate illumination intensity depending on the experimental design and offered the scientific community the possibility to apply it quickly, easily and inexpensively.

Finally, the optical assembly equipped with LED light represents a tool for studying the effect of blue light on *D. melanogaster* cultures across a wide range of illumination levels. With temperature control facilitated by a real-time system, the light can be switched on and off according to programmed settings. This optical assembly demonstrates quasi-homogeneity in the distribution of illuminance across the work area. Its application extends to various fields of science, engineering and medicine. With its carefully designed alignment, it allows for optimal results as a considerable number of fly cultures can be developed simultaneously, resulting in a high population, according to the conditions required at the experimental level.

Funding

Author Mónica López Bautista to acknowledge the scholarship provided by Consejo Nacional de Humanidades, Ciencia y Tecnología (CONAHCyT, México) for PhD studies 857105.

Conflicts of interest

The authors declare that they have no competing interests to report.

Data availability statement

The data associated with this study is available upon request. Please contact the corresponding author to request access to the data.

Author contribution statement

All authors made significant contributions to this work.

References

- 1 Duffy J.F., Czeisler C.A. (2009) Effect of light on human circadian physiology, Sleep Med Clin. 4, 2, 165–177. https://doi.org/10.1016/j.jsmc.2009.01.004.
- 2 Palczewski K. (2012) Chemistry and biology of vision, J. Biol. Chem. **287**, 3, 1612–1619. https://doi.org/10.1074/jbc. R111.301150.
- 3 LeGates T.A., Fernandez D.C., Hattar S. (2014) Light as a central modulator of circadian rhythms, sleep and affect, Nat. Rev. Neurosci. 15, 7, 443–454. https://doi.org/10.1038/nrn3743.
- 4 Hastings M., Reddy A., Maywood E. (2003) A clockwork web: circadian timing in brain and periphery, in health and disease, *Nat. Rev. Neurosci.* 4, 649–661. https://doi.org/10.1038/nrn1177.
- 5 Grabe S., Mahammadov E., Olmo M.D., Herzel H. (2022) Synergies of multiple zeitgebers tune entrainment, Front. Netw. Physiol. 1, 803011. https://doi.org/10.3389/fnetp.2021.803011.
- 6 Golombek D.A., Rosenstein R.E. (2010) Physiology of circadian entrainment, *Physiol Rev.* 90, 3, 1063–1102. https://doi.org/10.1152/physrev.00009.2009.
- 7 Klerman E.B., Brager A., Carskadon M.A., Depner C.M., Foster R., Goel N., Harrington M., Holloway P.M., Knauert M.P., LeBourgeois M.K., Lipton J., Merrow M., Montagnese S., Ning M., Ray D., Scheer F.A.J.L., Shea S.A., Skene D.J., Spies C., Staels B., St-Onge M.P., Tiedt S., Zee P.C., Burgess H.J. (2022) Keeping an eye on circadian time in clinical research and medicine, Clin Transl Med. 12, 12, e1131. https://doi.org/10.1002/ctm2.1131.
- 8 Behar-Cohen F., Martinsons C., Viénot F., Zissis G., Barlier-Salsi A., Cesarini J.P., Enouf O., Garcia M., Picaud S., Attia D. (2011) Light-emitting diodes (LED) for domestic lighting: any risks for the eye? *Prog. Retin. Eye Res.* **30**, 4, 239–257. https://doi.org/10.1016/j.preteyeres.2011.04.002.
- 9 Hanifin J.P., Lockley S.W., Cecil K., West K., Jablonski M., Warfield B., James M., Ayers M., Byrne B., Gerner E., Pineda C., Rollag M., Brainard G.C. (2018) Randomized trial of polychromatic blue-enriched light for circadian phase shifting, melatonin suppression, and alerting responses, *Physiol. Behav.* 198, 57–66. https://doi.org/10.1016/j.physbeh.2018.10.004.
- 10 Menegazzi P., Yoshii T., Helfrich-Förster C. (2012) Laboratory versus nature: the two sides of the *Drosophila* circadian clock, *J. Biol. Rhythms.* 27, 6, 433–442. https://doi.org/10.1177/0748730412463181.
- 11 Wahl S., Engelhardt M., Schaupp P., Lappe C., Ivanov I.V. (2019) The inner clock-Blue light sets the human rhythm, J.

- *Biophotonics.* **12**, 12, e201900102. https://doi.org/10.1002/jbio.201900102.
- 12 Nash T.R., Chow E.S., Law A.D., Fu S.D., Fuszara E., Bilska A., Bebas P., Kretzschmar D., Giebultowicz J.M. (2019) Daily blue-light exposure shortens lifespan and causes brain neurodegeneration in *Drosophila*, NPJ Aging Mech. Dis. 5, 8. https://doi.org/10.1038/s41514-019-0038-6.
- 13 Ramakrishnan P., Joshi A., Tulasi M., Yadav P. (2023) Monochromatic visible lights modulate the timing of preadult developmental traits in *Drosophila melanogaster*, *Photochem. Photobiol. Sci.* 22, 4, 867–881. https://doi. org/10.1007/s43630-022-00358-1.
- 14 Chen X., Leon-Salas W.D., Zigon T., Ready D.F., Weake V. M. (2017) A programmable optical stimulator for the Drosophila eye, *HardwareX* 2, 13–33. https://doi.org/10.1016/j.ohx.2017.07.001.
- 15 Beer K., Helfrich-Förster C. (2020) Model and non-model insects in chronobiology, Front. Behav. Neurosci. 14, 601676. https://doi.org/10.3389/fnbeh.2020.601676.
- 16 Huang R.C. (2017) The discoveries of molecular mechanisms for the circadian rhythm: The 2017 Nobel prize in physiology or medicine, *Biomed. J.* 41, 1, 5–8. https://doi.org/10.1016/ j.bj.2018.02.003.
- 17 Spitschan M., Stefani O., Blattner P., Gronfier C., Lockley S.W., Lucas R.J. (2019) How to report light exposure in human chronobiology and sleep research experiment, *Clocks Sleep.* 1, 3, 280–289. https://doi.org/10.3390/clockssleep 1030024.
- 18 Rosas E., Estrada-Hernández A. (2016) Effect of photometric detector spectral response quality on white LED spectral mismatch correction factors, *Appl. Opt.* **55**, 5267–5272. https://doi.org/10.1364/AO.55.005267.
- 19 Shen J., Yang P., Luo X., Li H., Xu Y., Shan J., Yang Z., Liang B. (2021) Green light extends *Drosophila* longevity, *Exp. Gerontol.* 147, 111268. https://doi.org/10.1016/j. exger.2021.111268.
- 20 Helfrich-Förster C. (2020) Light input pathways to the circadian clock of insects with an emphasis on the fruit fly *Drosophila melanogaster*, *J. Comp. Physiol. A* **206**, 259–272. https://doi.org/10.1007/s00359-019-01379-5.
- 21 Shibuya K., Onodera S., Hori M. (2018) Toxic wavelength of blue light changes as insects grow, *PLoS One* 13, 6, e0199266. https://doi.org/10.1371/journal.pone.0199266.
- 22 Schlichting M., Menegazzi P., Rosbash M., Helfrich-Förster C. (2019) A distinct visual pathway mediates high-intensity light adaptation of the circadian clock in *Drosophila*, J. Neurosci. 39, 9, 1621–1630. https://doi.org/10.1523/JNEUROSCI.1497-18.2018.
- 23 Liu Z., Zhao Z. (2014) Effects of light interruption on sleep and viability of *Drosophila melanogaster*, *PLoS One* **9**, 8, e105678. https://doi.org/10.1371/journal.pone.0105678.
- 24 Hall H., Ma J., Shekhar S., Leon-Salas W.D., Weake V.M. (2018) Blue light induces a neuroprotective gene expression program in *Drosophila* photoreceptors, *BMC Neurosci.* 19, 1, 43. https://doi.org/10.1186/s12868-018-0443-y.
- 25 Vandegehuchte M.B., Janssen C.R. (2011) Epigenetics and its implications for ecotoxicology, *Ecotoxicology* 20, 3, 607–624. https://doi.org/10.1007/s10646-011-0634-0.
- 26 Echazú R.D., Cadena C.A., Saravia Mathon L.R. (2000) Estudio de materiales reflectivos para concentradores solares, Avances en Energías Renovables y Medio Ambiente 4, 11–16.

- 27 Cho E., Oh J.H., Lee E., Do Y.R., Kim E.Y. (2016) Cycles of circadian illuminance are sufficient to entrain and maintain circadian locomotor rhythms in *Drosophila*, Sci. Rep. 6, 37784. https://doi.org/10.1038/srep37784.
- 28 Fernández-Moreno M.A., Farr C.L., Kaguni L.S., Garesse R. (2007) *Drosophila melanogaster* as a model system to study mitochondrial biology, *Methods Mol. Biol.* **372**, 33–49. https://doi.org/10.1007/978-1-59745-365-3 3.
- 29 Goda T., Hamada F.N. (2019) *Drosophila* temperature preference rhythms: An innovative model to understand
- body temperature rhythm, *Int. J. Mol. Sci.* **20**, 8, 1988. https://doi.org/10.3390/ijms20081988.
- 30 Johnson J.C., Munneke A.S., Richardson H.M., Gendron C.M., Pletcher S.D. (2023) Light modulates *Drosophila* lifespan via perceptual systems independent of circadian rhythms, *Aging (Albany NY)* **15**, 2, 396–420. https://doi.org/10.18632/aging.204472.

J. Eur. Opt. Society-Rapid Publ. 2024, **20**, 25 © The Author(s), published by EDP Sciences, 2024

https://doi.org/10.1051/jeos/2024024 Available online at: https://jeos.edpsciences.org

EOSAM 2023

Guest editors: Patricia Segonds, Guy Millot and Bertrand Kibler

Research Article Open 3 Access

Optical measurement instrument for detection of powdery mildew and grey mould in protected crops

G. Bouquet* D, K. Kaspersen, and K.H. Haugholt

Smart Sensor Systems and Microsystems, SINTEF Digital, Forskningsveien 1, 0373 Oslo, Norway

Received 31 January 2024 / Accepted 2 May 2024

Abstract. This study presents an initiative aimed at developing a real-time optical measurement system for non-contact measurement of airborne fungal spores in protected crops such as strawberries, tomatoes, and cucumbers. The system is based on a customized microscope and an automatic system for trapping fungal spores. It has been tested in the field under real conditions, and image processing algorithms have been developed to identify fungal spores in high-resolution microscope images.

Keywords: Microscope, Fungal spores, Machine vision.

1 Introduction

Ensuring an adequate food supply for the escalating human population is a great challenge. Crop losses and value degradation caused by plant diseases are major constraints to food security globally. Fungicides are important tools in management of plant diseases caused by fungal and oomycete pathogens. Currently, major crop losses are inevitable without the use of fungicides. However, reliance on fungicides is not sustainable since all fungal pathogens tend to develop fungicide resistance [1, 2]. European legislation also restricts pesticide use due to public health concerns and costs associated with pesticide removal from water [3, 4]. In sum, this makes integration and use of new, nonchemical strategies crucial for continued, sustainable food production. Successful management of fungal diseases critically depends on timely treatment. This requires the identification of pathogen type and inoculum concentration in the crop production system. Early detection of spores is a key to enabling rapid and adapted treatment to the plants. This implies that a detection system should be adapted to the detection of low concentrations of spores in air. Various spore-trapping devices are available, but most of them require time-consuming laboratory work for the identification of spores of pathogenic fungi. There have been some attempts at developing semi-automated spore detection systems [5–8], but most of these systems are still immature and not suitable for agricultural field applications. Most of the systems currently described in the literature are based on an off-the-shelf microscope for indoor use, without considerations for online use or field conditions [7]. Commercial

The two major challenges for automated spore detection are 1) developing the right combination of illumination, optics, and sensors to achieve sufficient image quality without losing the required area coverage, depth focus and acquisition speed and 2) training a classifier that can handle different types of spores together with pollen, dust and water droplets at different concentration levels. In a project funded by the Norwegian Research Council, END-IT, we have developed a real-time optical measurement system for detection of spores from grey mould (Botrytis cinerea) and powdery mildew (various species). The system is based on a modified microscope combined with an automatic system for spore trapping and air sampling. The system has been used in field trial and work is on-going on machine vision algorithms for detecting and classifying fungal spores in the presence of pollen, dust and other aerosols.

systems for measuring pollen are available, see for example [9, 10] which makes use of digital holography and fluorescence spectroscopy on particles in flight. The image analysis includes a preprocessing step to remove particles that are not sufficiently round and compact, which essentially means that the particles must be sufficiently spread out to not touch each other. This will remove many fungal spores before the classification starts since spores often stick together in chains or loose clumps. Analyzing particles in flight also requires a long flying path when several detection modalities are to be applied successively, which may add complexity and lead to large instruments. The spore detection system described in [11] also requires the particles to be well separated and it does not include an automatic system for spore trapping. There is thus a need for compact, robust systems adapted for in-field, real-time, and automated detection and classification of spores.

^{*} Corresponding author: gregory.bouquet@sintef.no

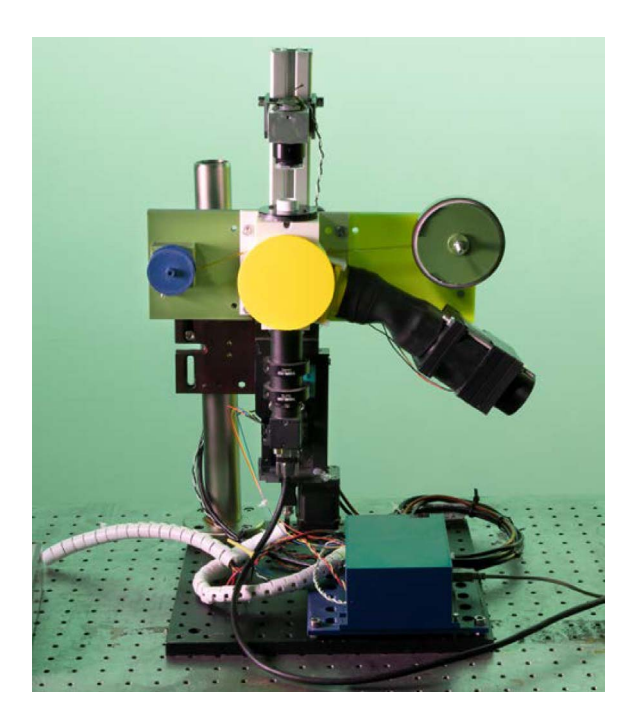


Figure 1. Picture of the automatic sampling and detection system for spores. The total size of the present system is 30 cm by 30 cm by 50 cm. See Figure 2 for a description of the various components.

2 Optical imaging of spores

2.1 Microscope measurement systems

The measurement system is a customized microscope equipped with an automatic system for air sampling and trapping of fungal spores on a transparent tape, see Figures 1 and 2. It consists in a 10X Nikon Achromatic Finite Conjugate Objective, imaging 1 mm² of the tape onto a color CMOS camera (BFS-U3-200S6C-C, Sony IMX183, 20 Megapixels, pixel size 2.4 µm). The microscope is mounted on a motorized linear translation stage for automatic focusing on the spores. A 3D-printed house holds a LED illumination system and a guiding support for the tape. The illumination system is designed to provide images of the spores in transmission (dark imaging) and in scattering (bright imaging), see Figure 2. These two imaging schemes are combined to provide better discrimination of the spores, see Section 3. The spore collection system consists of the tape, an automatic system for moving the tape and an air sampling system, see Figure 2. The tape is made from Kapton@ polyimide. It was chosen based on trial and error with different types of tapes and provided the best compromise in terms of transparency, color, and adhesive properties.

Bright- and dark-field illumination are two illumination schemes that enhance different features in a biological sample [12]. Bright-field microscopy involves illuminating the sample in transmission using typically broad-spectrum light. The contrast in the image results from differential attenuation of light by parts of the sample with distinct

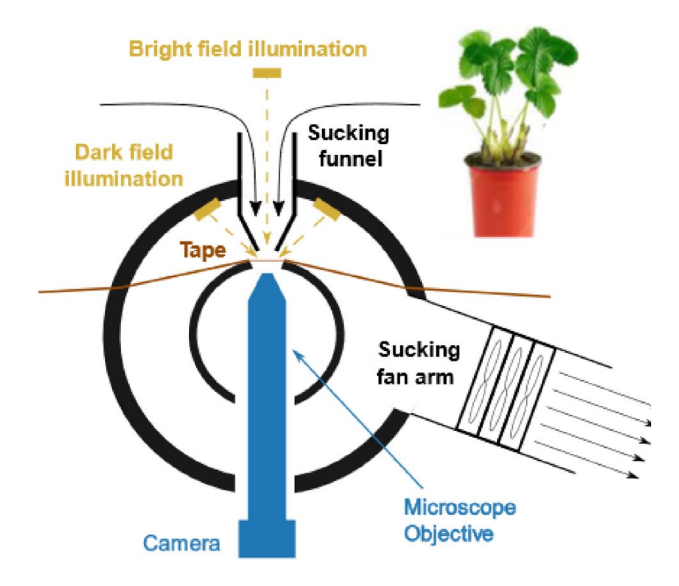


Figure 2. The measurement and sampling system consists of a microscope with $10\times$ magnification, an air sampling system, a tape for trapping the spore, and an illumination system with bright and dark configurations. The air intake at the top is also used to reflect and guide light from the bright field illumination towards the field of view of the microscope. When air is drawn in, small spores (<100 μ m) will follow the air flow and impact the tape at a position corresponding to the FOV of the spectrometer. There the spores are trapped on the adhesive side.

density. This is the simplest form for microscopy with typically high signal-to-noise ratio (SNR). However, for biological samples, which present very small variations in density, the contrast can be poor. Dark-field microscopy, on the other hand, works by excluding the unscattered beam from the image. As a consequence, the field around the specimen is generally dark, while the specimens itself is bright. This allows for enhancing small contrast differences between, e.g., a specimen of interest and the background. However, since the principle is based on making use of scattered light, high SNR is achieved at the cost of long integration time in comparison to bright-light microscopy. In our measurement system, the bright illumination is provided by a white LED (Moonstone 3 W High Brightness 10,000 K LED Light Source), roughly collimated by a lens with a 5 cm focal length.

For the dark-field illumination, a "Dark Field ring" from advanced illumination [13] is utilized in which fifteen white LEDs are accurately positioned in a circular arrangement with a radius of 2.5 cm. The aimed LEDs illuminate the tape at an angle of approximately 45° ensuring circular and symmetrical illumination of the microscope's field of view. The microscope objective focuses light that has been scattered by the samples at a 45-degree angle onto the camera chip.

A typical measuring sequence consists in:

- 1. drawing a fresh part of tape,
- 2. drawing in air,
- 3. focusing the microscope on the tape (see Sect. 2.3),
- 4. acquiring bright and dark images around focus.

The best focus image is then used to train the model or for prediction.

2.2 Optical resolution

To determine the optical resolution of the microscope through the tape, we used a reference object consisting of gold microstructure lanes deposited on silicon. The lane widths are 2.5, 5, 10, and 20 μm and all have a height of 250 nm. The reference object was imaged through the tape, see Figure 3 below for image of the 2.5 μm and 5 μm lane. The optical resolution was determined qualitatively from the images by assuming that when the two sides of the lane cannot be distinguished, the lane cannot be resolved.

In our optical system, this occurs for lanes with width of 2.5 μ m, while the lane with width of 5 μ m can be resolved, see Figure 4. The optical resolution through the tape falls within the range of 2.5–5 μ m.

2.3 Focusing precision

Each time a fresh tape sample is pulled, a slight change in the distance between the tape and the microscope lens occurs. The same happens after drawing in air to collect new spores, attributed to the air pressure on the tape. Consequently, it becomes necessary to refocus the microscope for each of these stages, as commented in Section 2.1.

This is achieved by following the sequence outlined below. Assuming the stepper is positioned at the last found focus point, it is then moved back, for example, 100 full steps from this position, representing approximately 250 μm . Subsequently, the stepper is moved in the opposite direction using a number N of sequences of 32 times 1/32 n d-steps, and images are captured at each new position. Sub-stepping, i.e., using 1/32 n d-steps, is utilized because it was proven experimentally to improve the focusing performance. A focus metric (Brenner algorithm [14]) is computed from each image, to quantify the degree of focusing. The algorithm reads as follows:

Let's S denotes an image with $N \times N$ pixels, where each pixel of S is an integer and its position is indexed by i and j, i.e. S_{ij} . The Brenner algorithm consists of calculating numbers d, dx and dy, defined in equations (1)–(3):

$$d = dx + dy \tag{1}$$

With

$$dx = \sum_{i=0}^{i=N-1} \sum_{j=0}^{j=N-3} (S_{ij+2} - S_{ij})^2.$$
 (2)

$$dy = \sum_{i=0}^{i=N-3} \sum_{j=0}^{j=N-1} (S_{i+2j} - S_{ij})^2.$$
 (3)

Typical focusing curves are shown in Figure 5. The focusing curves present in most cases at least two peaks that we believe correspond to the last layer structures seen in the multilayer structure of the film. In particular, the last peak is the position of the surface of the tape exposed to air and

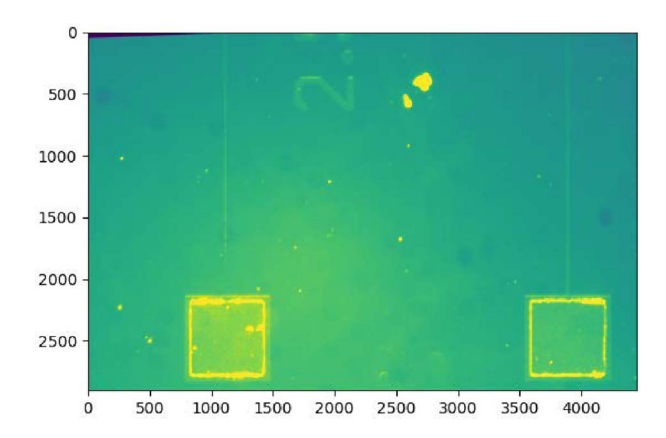


Figure 3. Reference object for measuring optical resolution of the optical system through the tape. See description in the text. The 2.5 μm (left) and 5 μm (right) vertical lanes can be distinguished on the picture. The squares at the bottom are gold pad with 200 $\mu m \times 200~\mu m$ dimensions.

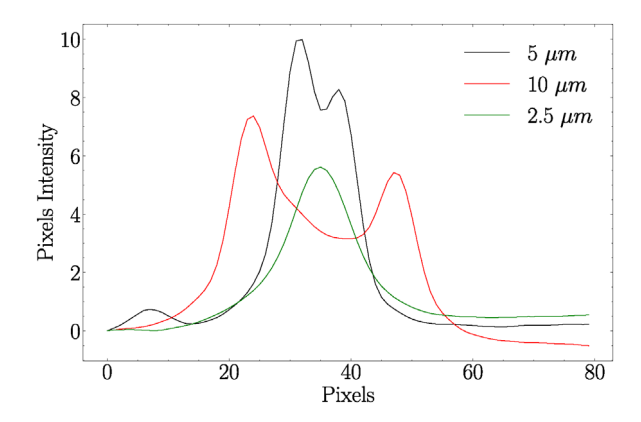


Figure 4. Intensity across the 2.5 μ m, 5 μ m, and 10 μ m lane. Roughly the side of the lane are resolved for the 5 μ m but not for the 2.5 μ m, giving us an optical resolution falling in between 2.5 μ m and 5 μ m.

fungus. When free of dust, fungus or any microscopic objects that can provide strong gradients, the focusing curves may present one to two additional peaks, corresponding to other layer structures, see for example the first two shoulders at ~185 μm and ~208 μm . For final focusing, we choose the last peak and estimate its position with additional precision, using a sub-pixel algorithm. Since we can move the motor with 1/32nd steps, the algorithm is applied with 1/32nd precision from the data acquired with 1 step precision. This is achieved through the following steps:

- 1. Calculate the convolution of the focusing curves with a normal distribution with standard deviation σ . For σ , we choose values between 1.5 and 3.
- 2. In the convolved function y_i , find the maxima and choose the one corresponding to the surface of the tape, i.e., the last one. Denote its position by t_{imax} and its ordinate by y_{imax} .

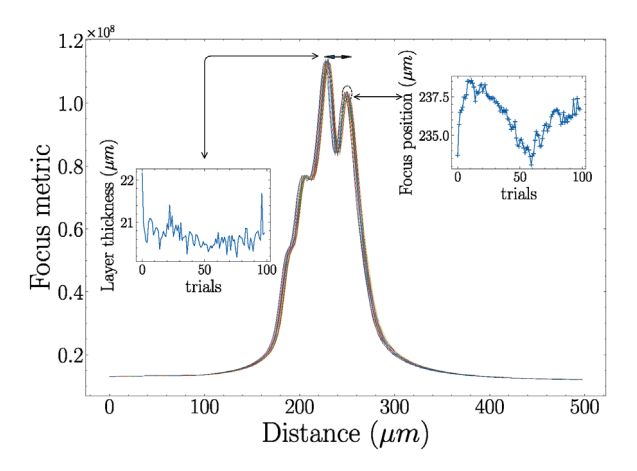


Figure 5. Typical focus curve obtained on a fresh tape. Fresh tape typically comprises four extrema corresponding to what we believe are different layer borders in the tape. The focusing sequence is repeated 100 times and the positions of the two last peaks are calculated with 1/32nd steps precision, see description in the text. The insert, left and right, show the layer thickness and the position of the adhesive side, as calculated for each run.

3. Interpolate the position t_{sub} using a polynomial of order 2 defined in equation (4):

$$t_{\text{sub}} = t_{i \max} + 0.5 \frac{y_{i_{\max}-1} - y_{i_{\max}+1}}{y_{i_{\max}+1} - 2y_{i_{\max}} + y_{i_{\max}-1}},$$
(4)

where $y_{i\max+1}$, $y_{i\max-1}$ are the ordinates of the two nearest point to $(t_{i\max}, y_{i\max})$.

1. In the focusing interval with 1/32nd steps precision, i.e., $t=0,\ 1/32,\ 2/32,\ ...,\ j/32,\ ...,\ M-1$ with $0\leq j\leq 32\ (M-1)$, choose the nearest position to $t_{\rm sub}$.

To test the efficiency of this algorithm, the focusing procedure was repeated 100 times on a fresh tape, devoid of dust and spores. The position of the surface of the tape was calculated using the sub-pixel algorithm above. The evolution of the sub-pixel position for each focusing sequence is shown in the top right insert. The last layer thickness is also evaluated using 1/32nd pixel precision as shown in the middle-left insert. The measured position of the surface presents a long-term variation of roughly 5 μm , over the full measuring sequence. The short-term variation, i.e. from focusing sequence to focusing sequence present smaller variations, typically between 0.1 μm and 1 μm . The Layer thickness is seen to be contained within a 20.5 \pm 0.5 μm range.

After the position of the surface is evaluated, the motor is moved to that position. A new set of M, for example M=5, images around the previously found optimal focus position is acquired, to cope with the variation of the focus positions between the center and the corner. The new set of images around the focus is then used for further image processing and as input to the neural network model.

3 Image processing

3.1 Preprocessing

After the best focused image has been chosen, a composite RGB images is created by replacing the green channel of the bright field image with the mean value of all the color channels of the dark-field (DF) image. This is calculated as:

$$\begin{split} &1. \ RGB_{composite} \left[:; :; : \right] = RGB_{BF} \left[:; :; : \right] \\ &2. \ RGB_{composite} [:; :; Blue] \\ &= \frac{RGB_{DF} [:; :; Red] + RGB_{DF} [:; :; Blue] + RGB_{DF} [:; :; Green]}{3} \end{split}$$

An example of the process is shown in Figure 4 below. Combining the bright and dark images provides better discrimination against the background. It also highlights the living spores since the spherical shape and high-water content of live spores make them function like tiny lenses. Dead spores tend to dry out and therefore do not light up in the same way as live spores.

Examples of images of relevant spores are shown in Figures 6–8. The resolution through the film is good enough to enable distinction between the two types of spores based on their shape and size. We observe that mildew spores sometimes exhibit a crown of small, bright spots in the bright-field illumination. This phenomenon is attributed to the lens-like properties of the oblong mildew structures, with their bodies acting as miniature lenses. The resulting effect of the "mildew lens" and the microscope lens is the formation of an image of the LED mounted on the dark Field ring. This effect is only present in fresh, water filled mildew, as the biological structure of dried-out mildew has collapsed, leading to the disappearance of its lens-like properties.

3.2 Model development

The model is based on the YOLOv5 neural network model [15], commonly used to detect objects in images for a large variety of applications [16–20]. The choice of YOLOv5s as basis for the model development instead of other, larger models, is a compromise between size and performance of the model. We have a relatively limited amount of different features in the images and only a few object classes, so using a larger model would not necessarily give much better results.

In the training of the network, the first layers of the model are kept fixed and only the last layer of the network is retrained with images of powdery mildew and grey mould (acquired in field tests and in the lab). The images are split into three datasets; training, validation and test set. The training and validation sets are using during the training of the model. The test set is used only for reporting of the model results. Since we have a limited amount of spores in the images, the Images containing spores are augmented with flipped versions of the image (flip left-right and flip up-down). Negative images (without spores) are easily available, so they are included without augmentation.

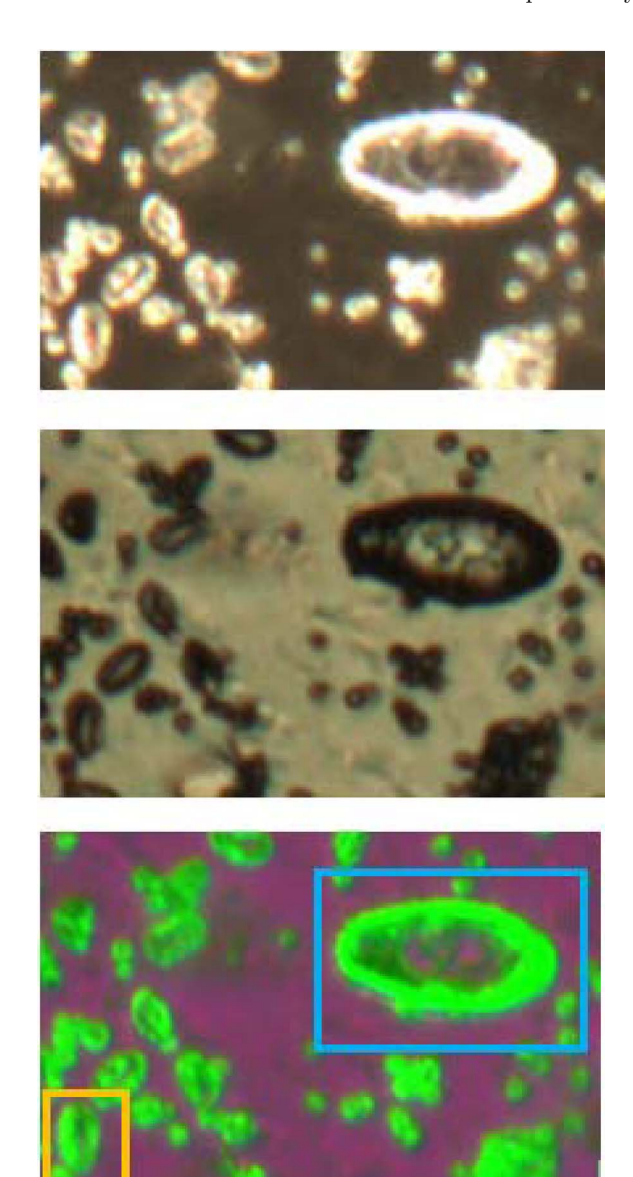


Figure 6. Combination of bright and dark field image into a composite red-green image. We only show a small part of the image to highlight the size difference between spores of powdery mildew (blue box) and grey mould (orange box).

4 Experimental results

Several field tests were conducted during spring and summer 2023 in various greenhouses in the Oslo region in Norway. The measuring system was positioned near the plants and left to collect data during several days (Figure 9). Both greenhouses with healthy plants and greenhouses with disease outbreaks have been investigated.

The model development is still ongoing, but preliminary results indicate that it is possible to detect the relevant spores and separate them from dust and other objects in the images. Current models give mean average precision

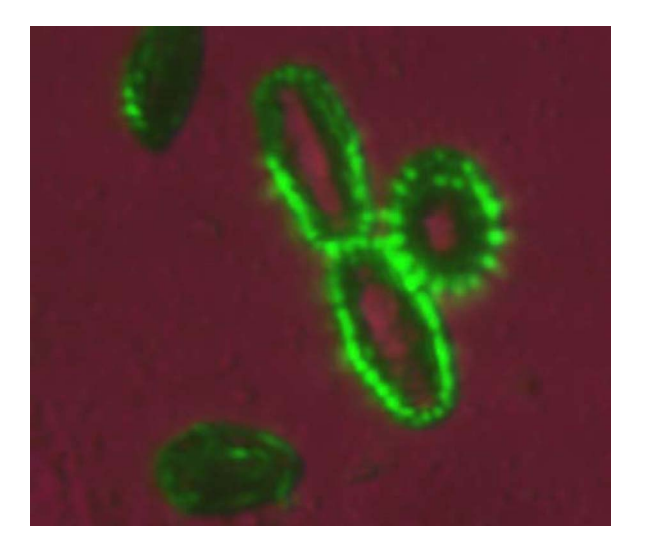


Figure 7. Cucumber powdery mildew. Dark spores are dried out (dead).

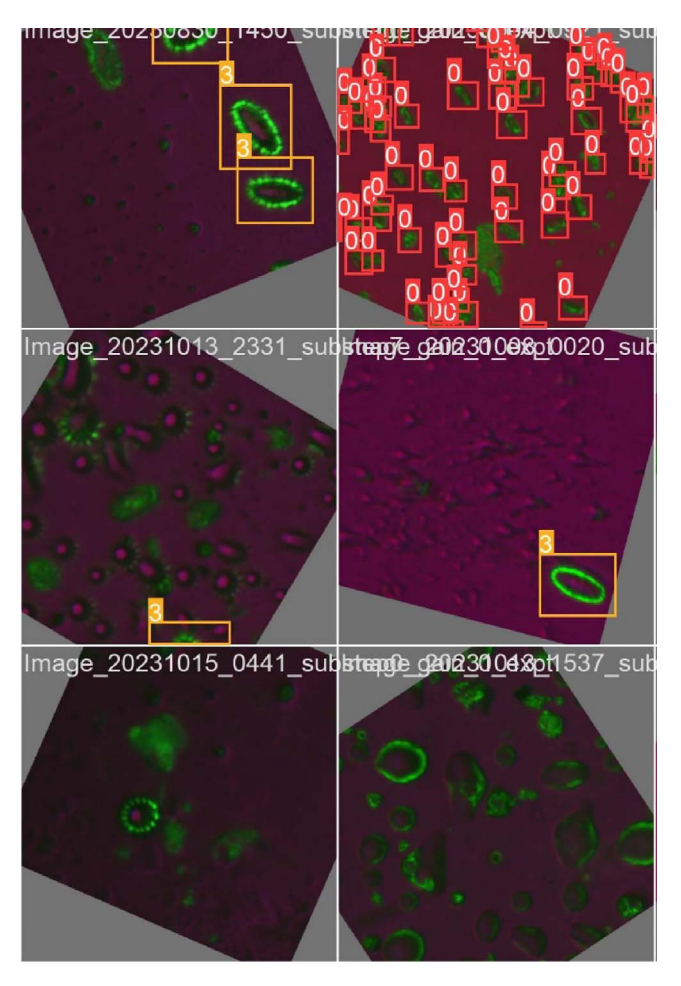


Figure 8. Example of training data that is input to the model development. The spore-like structures in the lower, right image are water droplets.



Figure 9. Measuring system collecting data in a cucumber greenhouse with powdery mildew attack.

Table 1. Classification results for the test set.

	Grey mould	Cucumber powdery mildew
No. of spores	1662	804
Precision	0.71	0.902
Recall	0.946	0.97
mAP50	0.917	0.982
mAP50-95	0.578	0.741

(mAP50) of 0.92 for grey mould and 0.98 for cucumber powdery mildew, see Table 1.

Figure 10 shows examples of classification results for images with spores of grey mould and cucumber powdery mildew. We see that the model is able to correctly detect the powdery mildew even when the image is not perfectly focused. The model also manages to differentiate between the elliptic grey mould spores and circular water droplets.

5 Discussion

The system performs well when it comes to classification accuracy of the spores that are trapped on the tape. However, more experiments are needed to determine which proportion of the spores in the air in a typical greenhouse will effectively make their way to our system. Our system has an air intake that draws air in and an air outtake that



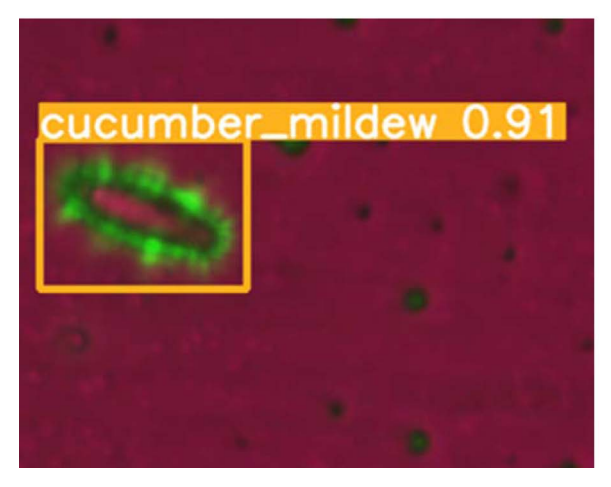


Figure 10. Classification examples for grey mould (top) and cucumber powdery mildew (bottom).

pushes air out. The spores are typically 10–60 um long. Airborne particles with a diameter < 10 µm and a density similar to water are expected to behave passively in relation to air turbulence. In contrast, airborne particles with a diameter of 60 µm will be more influenced by their mass, exhibiting higher inertia against being carried by air flow [21]. Airborne particles with a diameter $< 10 \mu m$ have a falling speed of approximately 0.25 cm/s, settling to the ground in about 11 min from a height of 2 m (average height of a cucumber leaf). Conversely, for a 60 µm particle, the falling speed is around 10.8 cm/s, requiring only 18 s to reach the ground¹. In practical terms, grey mold spores may thus remain suspended in the air for a long time, potentially drifting over long distances in a greenhouse, depending on airflow and turbulence. Mildew spores, which spend a shorter time suspended in the air, will probably be less affected by airflow and drift over much shorter distances. In a large, commercial greenhouse, a large spore "emitted" at one side of the greenhouse might probably not then reach the measuring system before being dried out or before

¹ The gravitational settling velocity for a particle of diameter d and density ρ is $V_s = \rho g d^2 18 \mu$, with g, μ the gravitational acceleration and the air viscosity, see [22].

colliding with infrastructure or another plant. Statistical studies on the concentration of spores in the air are needed to evaluate the full potential of a detection system for, e.g., mildew spores based on air collection.

Another important assumption in our system is that a spore that is drawn in, is a spore trapped on the tape at some position in the FOV. This is a strong assumption which assumes that 1) the spores are not trapped along the side of the funnel on their way to the tape; 2) all the spores that make their way down to the tape will impact the tape and 3) all the spores that impact the tape will adhere to it. We have not made any studies of the number of spores being trapped on the tape versus the number of spores entering the funnel and we do not know the efficiency of our collection system. For example, a more efficient design of the geometry of the collection system might help in directing the spores to the FOV region and avoid collision of the spores with the walls. This should be optimized using e.g. a fluid mechanic simulator, considering the specificity of the spores of interest (size and mass). The geometry of the impact zone might also be further improved by optimizing e.g. the width of the tape, its orientation, and the geometry of the chamber around the tape for maximal impact. Finally, the tape chosen might also be optimized with respect to transparency, and "trapping" efficiency.

The imaging system and detection algorithm operate under the assumption that only a limited number of spore types need to be identified, and that the captured images are not contaminated by very large amounts of dust, pollen, or water droplets. In the greenhouse tests this has so far been a valid assumption. However, for coping with a more generic environment, additional detection modalities and extensive testing are probably needed. For example, fluorescence and multispectral detection could be added as a mean to detect a wider range of spores.

The system we have described currently makes use of a stepper motor to move the microscope. The stepper motor amounts to a large part of the weight and volume of the system and may be replaced by, e.g., a tunable lens [23] to reduce the size and improve the measurement speed.

The effect of the focusing precision and the optical resolution on the model performance has not been extensively evaluated. Testing indicates that the model is relatively robust for poorly focused images of mildew spores, but the results for the much smaller spores of grey mould deteriorate more quickly with inaccurate focus. This will also be the subject of further studies.

There is a very broad corpus of work showing that optical spectroscopy is an interesting tool for the diagnosis of plant diseases. Wavelength ranges such as visible, near-infrared and mid-infrared have been utilized for diagnosis and monitoring of plant diseases in a nondestructive way, see [24, 25] and references therein. Techniques such as Raman, Fourier Transform Infra-Red, and fluorescence spectroscopy, which can provide information about the molecular fingerprint of pathogens, and reflectance spectroscopy have proven effective for early detection and identification of plant pathogens, significantly enhancing disease management capabilities, see [26–28] and references

therein. For the case of mildew, Laser-Induced Fluorescence has been proven to be able to provide presymptomatic detection of powdery mildew on wheat leaves shortly after fungus inoculation [29]. Also, UV-fluorescence spectroscopy has been used for detection of powdery mildew in grapevine [30]. VIS-NIR reflectance spectroscopy was also assessed for the rapid detection of e.g. Botrytis cinerea and Powdery mildew on wine grape [31]. Finally, an interesting approach for indirect detection of strawberry powdery mildew has been achieved in [32] by remotely measuring CO_2 concentration close to the crop, since in infected plants, the ability to absorb CO_2 has been shown to be altered [33].

From this comprehensive but not exhaustive list of works, it is evident that spectral information can add new dimensions to the microscopy detection system discussed in this paper, particularly for detecting powdery mildew and botrytis. Many existing studies that utilize spectroscopy for local inspections close to the leaves rely on bulky and cumbersome equipment. For instance, standard commercial FTIR systems, which are typically expensive and heavy, are often customized for laboratory use and are not well-suited for field applications where large areas need to be monitored in real time. Remote spectral sensing presents a promising solution to overcome these challenges, as it allows for the monitoring of leaves and crops over large areas from a few isolated positions under ideal conditions. The system described in this article bridges the gap between costly, heavy equipment and remote sensing systems by offering a potential for compactness and affordability. It can be deployed to monitor large areas and does not depend on direct leaf inspection, making it relatively unaffected by the initial location or timing of disease development on the crops. As long as spores are present in the air, the suction system stands ready to capture and present them to the imaging system.

6 Conclusions

We have developed a real-time optical measurement system for non-contact measurement of fungal spores in protected crops such as strawberries, tomatoes, and cucumbers. The system combines a collection system of spores and a customized microscope combining bright and dark illumination to detect the spores. The collection of spores is achieved by sampling air and trapping spores on a tape. A YOLOv5 neural network is trained to identify spores of powdery mildew and grey mold. Current models give mean average precision (mAP50) of 0.92 for grey mould and 0.98 for cucumber powdery mildew. The measurement system has been tested in the field under real conditions, in several greenhouses in the Oslo region in Norway. Additional work is needed to estimate the collection rate of the current measurement systems as ground truth for concentration of spores in air is challenging to obtain in the greenhouse. Also, monitoring of additional spores could be achieved by our system by adding detection modalities, e.g. multi spectral imaging and/or fluorescence detection.

Funding

The work presented in this article was conducted as part of the "Environmentally friendly fungal disease management in protected crop production using plant genetic resources and sensor technology" (END-IT) project funded by a grant of the Research Council of Norway under the FFL-JA-Research funds for agriculture and food industry.

Conflicts of interest

The authors declare that they have no competing interests to report.

Data availability statement

Data associated with this article cannot be disclosed due to legal/ethical/other reason.

Author contribution statement

GB, KK and KHH contributed to the conceptualization of the idea. The development of hardware was performed by GB and KHH. The experiments and collection of data were performed by GB and KK. The development of image processing algorithms was performed by KK. GB and KK wrote the manuscript with feedback from KHH. All authors discussed the results and contributed to the final manuscript.

References

- 1 Hahn M. (2014) The rising threat of fungicide resistance in plant pathogenic fungi: Botrytis as a case study, *J. Chem. Biol.* 7, 133–141. https://doi.org/10.1007/s12154-014-0113-1.
- 2 McGrath M.T. (2001) Fungicide resistance in cucurbit powdery mildew: Experiences and challenges. *Plant Dis.* 85, 236–245. https://doi.org/10.1094/PDIS.2001.85.3.236.
- 3 Coelho S. (2009) European pesticide rules promote resistance, researchers warn, *Science* **323**, 450–450. https://doi.org/10.1126/science.323.5913.450.
- 4 Heimbach U., Kral G., Niemann P. (2002) EU regulatory aspects of resistance risk assessment. *Pest Manag. Sci.* **58**, 9, 935–938. https://doi.org/10.1002/ps.538.
- 5 McLaughlin R.P., Mason G.S., Miller A.L., Stipe C.B., Kearns J.D., Prier M.W., Rarick J.D. (2016) Note: A portable laser induced breakdown spectroscopy instrument for rapid sampling and analysis of silicon-containing aerosols. Rev. Sci. Instrum. 87, 5. https://doi.org/10.1063/1.4949506.
- 6 Blank R., Vinayaka P.P., Tahir M.W., Yong J., Vellekoop M.J., Lang W. (2016) Comparison of several optical methods for an automated fungal spore sensor system concept. *IEEE Sensors J.* 16, 5596–5602. https://doi.org/10.1109/JSEN. 2016.2567538.
- 7 Tahir M.W., Zaidi N.A., Blank R., Vinayaka P.P., Vellekoop M.J., Lang W. (2017) Fungus detection through optical sensor system using two different kinds of feature vectors for the classification. *IEEE Sensors J.* 17, 5341–5349. https://doi.org/10.1109/JSEN.2017.2723052.
- 8 Wang Y., Zhang X., Taha M.F., Chen T., Yang N., Zhang J., Mao H. (2023) Detection method of fungal spores based on fingerprint characteristics of diffraction-polarization images. J. Fungi 9, 1131. https://doi.org/10.3390/jof9121131.
- 9 Website of Swisens AS, accessed on 28 May 2024, https://www.swisens.ch/en/swisenspoleno-mars.

- 10 Sauvageat E., Zeder Y., Auderset K., Calpini B., Clot B., Crouzy B., Konzelmann T., Lieberherr G., Tummon F., Vasilatou K. (2020) Real-time pollen monitoring using digital holography. Atmos. Meas. Tech. 13, 1539–1550. https://doi.org/10.5194/amt-13-1539-2020.
- 11 Wang Y., Mao H., Xu G., Zhang X., Zhang Y. (2022) A rapid detection method for fungal spores from greenhouse crops based on CMOS image sensors and diffraction fingerprint feature processing. J. Fungi 8, 4, 374. https://doi.org/10.3390/jof8040374.
- 12 Bradbury S. (1998) Introduction to Light Microscopy, 2nd ed., Bios Scientific Pub Ltd.
- 13 Compact Aimed Dark Field RL2115. Website of Advanced Illumination, accessed on 28 May 2024, https://www.advancedillumination.com/.
- 14 Brenner J.F., Dew B.S., Horton J.B., King J.B., Neirath P. W., Sellers W.D. (1971) An automated microscope for cytologic research. J. Histochem. Cytochem. 24, 100–111.
- 15 Yolov5, Github repository, accessed on 28 May 2024, https://github.com/ultralytics/yolov5.
- 16 Wang H., Zhang S., Zhao S., Wang Q., Li D., Zhao R. (2022) Real-time detection and tracking of fish abnormal behavior based on improved YOLOV5 and SiamRPN++. Comput. Electron. Agric. 192, 106512. https://doi.org/10.1016/ j.compag.2021.106512.
- 17 Jing Y., Ren Y., Liu Y., Wang D., Yu L. (2022) Automatic extraction of damaged houses by earthquake based on improved YOLOv5: A case study in Yangbi. *Remote Sens.* 14, 2, 382. https://doi.org/10.3390/rs14020382.
- 18 Fang Y., Guo X., Chen K., Zhou Z., Ye Q. (2021) Accurate and automated detection of surface knots on sawn timbers using YOLO-V5 model. *BioResources* **16**, 3, 5390–5406. https://doi.org/10.15376/biores.16.3.5390-5406.
- 19 Mathew M., Mahesh T.Y. (2022) Leaf-based disease detection in bell pepper plant using YOLO v5. SIViP 16, 841–847. https://doi.org/10.1007/s11760-021-02024-y.
- 20 Mushtaq F., Ramesh K., Deshmukh S., Ray T., Parimi C., Tandon P., Jha P.K. (2023) Nuts&bolts: YOLO-v5 and image processing based component identification system. Eng. Appl. Artif. Intell. 118, 105665. https://doi.org/ 10.1016/j.engappai.2022.105665.
- 21 Hinds W.C. (1999) Aerosol technology: Properties, behavior, and measurement of airborne particles, John Wiley & Sons.
- 22 Colbeck I., Lazaridis M. (eds) (2014) Aerosol science: Technology and applications, 1st ed., John Wiley & Sons, New York, pp. 89–118.
- 23 Chen L., Ghilardi M., Busfield J.J.C., Carpi F. (2021) Electrically tunable lenses: A review. Front. Robot. AI 8, 678046. https://doi.org/10.3389/frobt.2021.678046.
- 24 Zahir S.A.D.M., Omar A.F., Jamlos M.F., Azmi M.A.M., Muncan J. (2022) A review of visible and near-infrared (Vis-NIR) spectroscopy application in plant stress detection. Sens. Actuators A Phys. 338, 113468.
- 25 Nißler R., Müller A.T., Dohrman F., Kurth L., Li H., Cosio E.G., Flavel B.S., Giraldo J.P., Mithöfer A., Kruss S. (2022) Detection and imaging of the plant pathogen response by near-infrared fluorescent polyphenol sensors. *Angew. Chem. Int. Ed.* 61, e202108373.
- 26 Farber C., Mahnke M., Sanchez L., Kurouski D. (2019) Advanced spectroscopic techniques for plant disease diagnostics. A review. TrAC Trends Anal.l Chem. 118, 43–49. ISSN 0165-9936.

- 27 Kumar R., Pathak S., Prakash H., Priya U., Ghatak A. (2021) Application of spectroscopic techniques in early detection of fungal plant pathogens, in: Kurouski D. (ed), Diagnostics of Plant Diseases. IntechOpen, London, UK.
- 28 Khaled A.Y., Abd Aziz S., Bejo S.K., Nawi N.M., Seman I.A., Onwude D.I. (2018) Early detection of diseases in plant tissue using spectroscopy – applications and limitations. *Appl. Spectrosc. Rev.* 53, 1, 36–64.
- 29 Bürling K., Hunsche M., Noga G. (2012) Presymptomatic detection of powdery mildew infection in winter wheat cultivars by laser-induced fluorescence. Appl. Spectrosc. 66, 12, 1411–1419.
- 30 Bélanger M.C., Roger J.M., Cartolaro P., Viau A.A., Bellon-Maurel V. (2008) Detection of powdery mildew in grapevine

- using remotely sensed UV-induced fluorescence. *Int. J. Remote Sens.* **29**, 6, 1707–1724.
- 31 Beghi R., Giovenzana V., Brancadoro L., Guidetti R. (2017) Rapid evaluation of grape phytosanitary status directly at the check point station entering the winery by using visible/near infrared spectroscopy. *J. Food Eng.* **204**, 46–54.
- 32 H. Pham, Y. Lim, A. Gardi, R.A. Sabatini, Novel Bistatic LIDAR system for early-detection of plant diseases from unmanned aircraft, in: Proceedings of the 31th Congress of the International Council of the Aeronautical Sciences (ICAS 2018), Belo Horizonte, Brazil, 2018.
- 33 Gordon T.R., Duniway J.M. (1982) Effects of powdery mildew infection on the efficiency of CO₂ fixation and light utilization by sugar beet leaves. *Plant Physiol.* 69, 1, 139–142.

J. Eur. Opt. Society-Rapid Publ. 2024, **20**, 27 © The Author(s), published by EDP Sciences, 2024

https://doi.org/10.1051/jeos/2024021 Available online at: https://jeos.edpsciences.org

EOSAM 2023

Guest editors: Patricia Segonds, Guy Millot and Bertrand Kibler

RESEARCH ARTICLE OPEN 3 ACCESS

The role of absorption mechanism on the optimization of processing commercial polymers under high repetition rate femtosecond laser irradiation

Andrés P. Bernabeu^{1,2}, Guillem Nájar^{1,2}, Alberto Ruiz¹, Juan C. Bravo^{1,2}, Manuel G. Ramirez^{1,2}, Sergi Gallego^{1,2}, Andrés Márquez^{1,2}, and Daniel Puerto^{1,2,*}

Received 29 January 2024 / Accepted 17 April 2024

Abstract. The response of three of the most used commercial polymers (poly(vinyl chloride) (PVC), poly (ethylene terephthalate) (PET) and polypropylene (PP)) under irradiation with high repetition rate (1 kHz–1 MHz) femtosecond (450 fs) multi-pulse (N=10–1500) laser at $\lambda=343$ nm, 515 nm (1.40 J/cm² for both former wavelengths) and 1030 nm (1.70 J/cm²) is reported, obtaining a study on how the absorption mechanism influences the processing efficiency for these materials. Tunable ablation depth and diameters are accomplished by modifying repetition rates at a constant fluence and number of pulses. The results highlight the role of absorption mechanism, repetition rate ranges and thermal properties of the materials for benefiting ablation efficiency. Furthermore, the use of high repetition rates improves the laser processing, reducing extended thermal effects and increasing ablation uniformity.

Keywords: Femtosecond laser, Ablation, Polymers, High-frequency, Thermal effects, Absorption mechanism.

1 Introduction

Polymers have become essential materials over the last years. The presence of polymers in an endless number of disciplines, such as technological and medical devices, domestic appliances, food industry or aeronautics [1–3] has been increased because of their notable qualities and their competitive economical cost.

Three of the most commonly used polymers are poly (vinyl chloride) (PVC), poly(ethylene terephthalate) (PET) and polypropylene (PP). PVC is an amorphous polymer, whereas PET and PP are semi-crystalline polymers. These materials can be found in a vast number of ordinary objects [4–6]. Nevertheless, an important application of these polymers is their use in the fabrication of flexible electronical and photonic devices via ultrafast laser techniques [7, 8].

The use of ultrafast laser techniques for manufacturing micro devices has been widely investigated. Several valuable devices have been fabricated, such as microlenses, waveguides, diffractive gratings or microfluidic channels [9–16].

Femtosecond laser sources allow to deliver high intensities on the surface of the materials that produce non-linear absorptions restricted to the irradiated volume [17–20]. This enables to process materials that are transparent to lower light intensities through multiphoton absorption mechanisms. For this reason, ultrashort laser irradiation has become an exceptional tool for tunable material micro-processing [20].

The control of laser parameters is key for achieving a proper processing of the materials. The relation between the irradiation wavelength and the material bandgap becomes crucial because these parameters determinate the dominant absorption mechanism [20]. For higher wavelengths the amount of simultaneously absorbed photons must be greater, reducing the processing efficiency. If the wavelength is such that the photon energy is similar to the material bandgap, better processing results are expected to be obtained.

Another important parameter is the repetition rate. The short processing times demanded by the industry can be achieved with high repetition rate processing. When high repetition rate pulses are irradiated, time between pulses becomes shorter, resulting in shortened processing times and presenting a notable advantage for production purposes [15, 16]. The advantages of high repetition rate processing have been observed in several materials [21, 22], obtaining more uniform ablation and a debris reduction

¹ I.U. Física Aplicada a las Ciencias y las Tecnologías, Universidad de Alicante, 03690 San Vicente del Raspeig, Spain

² Departamento de Física, Ingeniería de Sistemas y Teoría de la Señal, Universidad de Alicante, 03690 San Vicente del Raspeig, Spain

^{*} Corresponding author: dan.puerto@ua.es

in the surroundings of the ablation area. However, a wide range of repetition rate analysis is needed for understanding the impact of repetition rate in ablation efficiency and for controlling the processing outcomes.

We study the effects of processing three polymers with different thermal properties (PVC, PET and PP) using femtosecond laser irradiation for three different wavelengths ($\lambda=343$ nm, 515 nm and 1030 nm) and a wide range of repetition rates (from 10 kHz to 1 MHz), providing a complete study of the processing of these materials under different laser conditions. This investigation highlighted the influence of the dominant absorption mechanism in achieving effective material processing. By adjusting the repetition rates, it was possible to precisely control and vary the ablation depths and diameters of the modifications at the micron level. An explanation for the results can be given by considering the connection between heat diffusion and repetition rate.

2 Experimental

The laser set up includes an NKT aeroPULSE FS50 fiber laser that emits 450 fs laser pulses with an average maximum power of 50 W at the central wavelength of $\lambda = 1030$ nm. Second order ($\lambda = 515$ nm) and third order $(\lambda = 343 \text{ nm})$ harmonics can also be generated through a nonlinear crystal device. Repetition rates can be selected in a range between 500 Hz and 2 MHz for each wavelength. The working fluences are 1.70 J/cm² for $\lambda = 1030$ nm and 1.40 J/cm^2 for $\lambda = 515 \text{ nm}$ and 343 nm. We selected these fluence values based on the single pulse modification threshold for $\lambda = 515$ nm, which is slightly below 1.40 J/cm², according to our fluence tests. This choice ensures that all the emitted pulses are capable of modifying the surface of the materials. Ideally, to assess whether the absorption mechanism significantly influences the process, irradiation at $\lambda = 343$ nm, 515 nm and 1030 nm should occur at identical fluence values. This approach allows that any differences observed in the results for each wavelength to be attributed to the variations in the absorption of the materials at each wavelength. However, $\lambda = 1030$ nm required a higher fluence to induce significant modifications on the surface of the materials. Consequently, the fluence was increased to 1.70 J/cm² for this wavelength.

The system includes a scanner that controls the $X\!-\!Y$ position of the laser beam, allowing to process different geometries on the material samples. The velocity of the scanner can be set between 1 mm/s and 5 m/s. The laser beam is focalized by a f-theta lens leading to 15 μ m, 9 μ m and 7 μ m radii at $1/e^2$ for $\lambda=1030$ nm, 515 nm and 343 nm, respectively. The radii sizes have been determined by the method proposed by Liu et al. [23]. A depiction of the experimental system is presented in Figure 1.

The polymer samples are 300 μ m thick films of PVC, PET and PP. The absorbance spectra of these materials are presented in Figure 2. As it can be seen, the three polymers present an absorption peak for $\lambda \leq 300$ nm. Absorption for $\lambda = 343$ nm is slightly higher than for $\lambda = 515$ nm as seen in Table 1. However, for higher wavelengths absorption is expected to be lower. A simple way for comparing the absorption efficiency for the three

wavelengths is by the estimation of the bandgap. This estimation can be performed from the slope of these peaks. The bandgap value is approximated to the wavelength value at which a straight line with this slope and situated on the top of the peak intersects the abscises axis. The bandgap estimations can be observed in Table 1. Regarding the low absorption of the three materials at the working wavelengths and the high intensities that are provided by an ultrafast laser source, multiphoton absorption is expected to be the dominant absorption mechanism for $\lambda = 1030 \text{ nm}$ and $\lambda = 515 \text{ nm}$ processing. Considering the bandgap energies, the energy of each wavelength can allow us to estimate the number of simultaneous photons that are required to be absorbed. The photon energy for $\lambda = 1030 \text{ nm}$ is 1.20 eV, for $\lambda = 515 \text{ nm}$ is 2.41 eV and for $\lambda = 343$ nm is 3.61 eV. These findings suggest that, across all the three materials, at least 4 photons are needed to be absorbed simultaneously for $\lambda = 1030$ nm, whereas only 2 coincident photons are necessary for $\lambda = 515$ nm. In the case of 343 nm irradiation, it is plausible that twophoton absorption may interplay with linear absorption. This phenomenon could influence the material processing outcomes, as explained in the subsequent sections.

Thermal properties of the three materials have been analysed too (see Supplementary material). Glass transition (T_g) , melting (T_m) , decomposition (T_d) temperatures and heat capacity at T_d are determined from Modulated Differential Scanning Calorimetry (MDSC) and Thermogravimetry (TG). The results are also presented in Table 1.

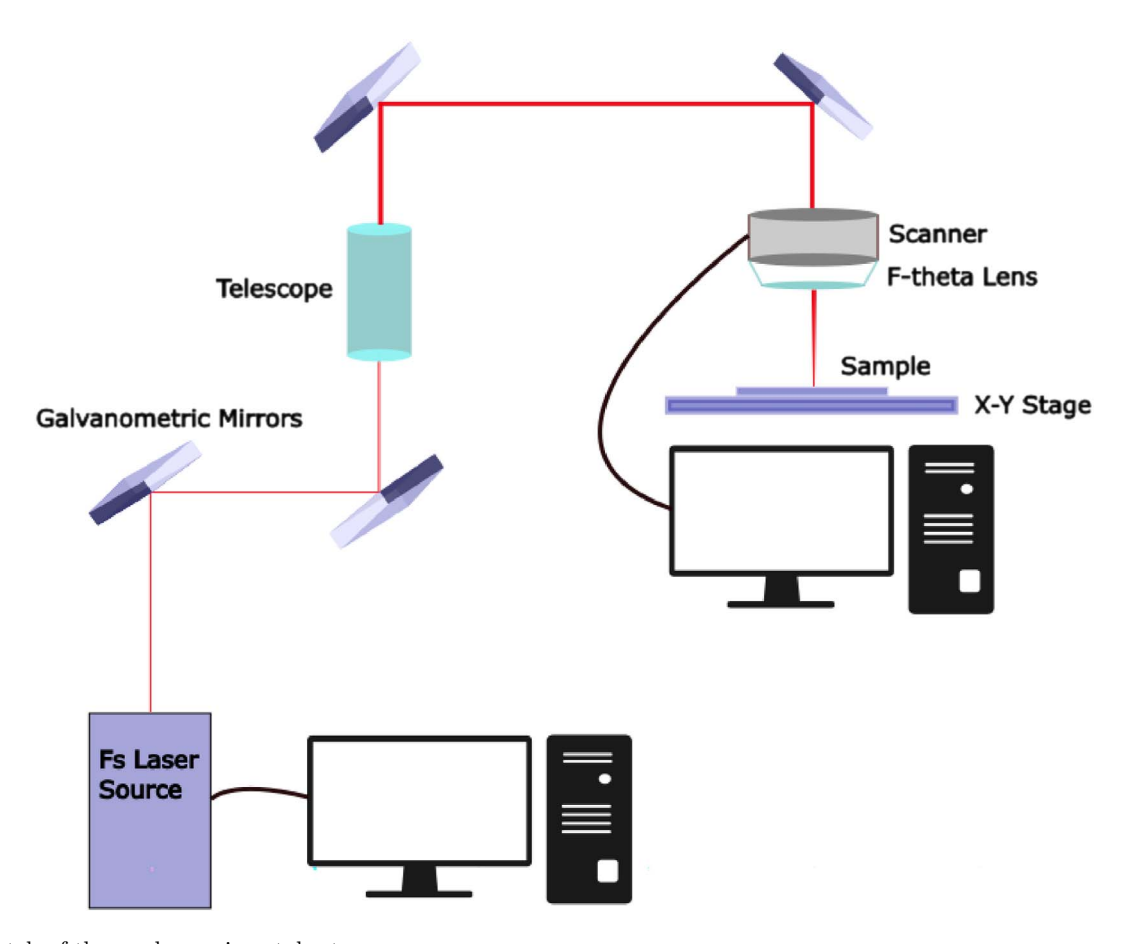
Optical characterization system is composed by an Olympus IX73 microscope with $10\times/0.30$, $20\times/0.45$, $50\times/0.80$ and $100\times/0.90$ MPlanFLN objectives. The ablation depths were measured using this microscope, focusing on the surface of the material and on the deepest region of the induced ablations. The differences between the reading on the micrometric stage on the material surface and on the ablated regions were recorded as the depth measurements. We conducted multiple measurements of the ablation depth for each line to minimize errors. The ablation and modified widths were determined using microscopic images and the micron/pixel calibration that was established.

3 Results and discussion

3.1 Overview

Different series of irradiated lines with different number of pulses per spot-area were processed on the three polymer surfaces at $\lambda=1030$ nm with a fluence of $1.70~\mathrm{J/cm^2}$ and at $\lambda=515$ nm and 343 nm with a fluence of $1.40~\mathrm{J/cm^2}$ for both wavelengths. Each series contains irradiations with different values of repetition rate and scanning velocity. These two parameters were varied in order to obtain a constant number of pulses. Therefore, each sequence consists on lines with the same number of pulses per spot-area, but each line is produced with a different value of repetition rate.

The fact of varying the repetition rate values alters the heat diffusion mechanism. For higher repetition rates, time



 ${\bf Fig.~1.}$ Sketch of the used experimental setup.

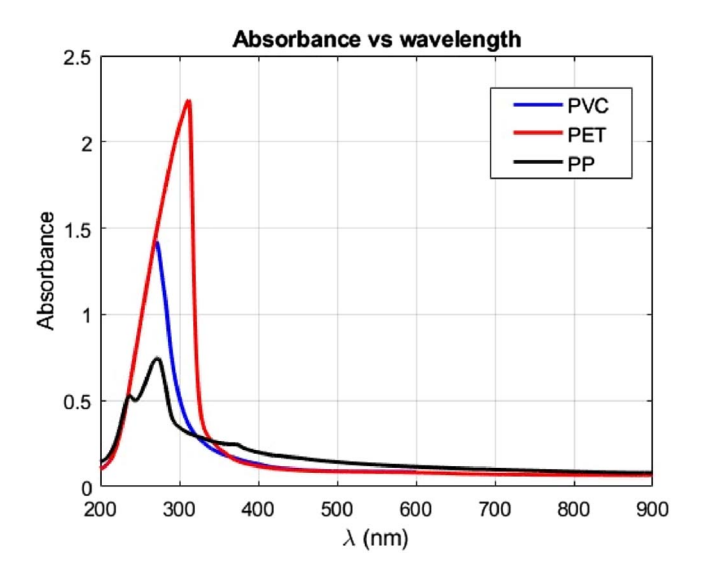


Fig. 2. Absorbance spectra for PVC, PET and PP.

between pulses is reduced, so it is more difficult for the material to spread the induced heat on its surface, leading to higher temperatures that can produce greater changes in the materials. After the last pulse impinges the material, heat diffusion becomes dominant and the high temperatures that have been reached on the irradiated area are able

to enlarge the modified region. Increasing the number of overlapping pulses and the delivered pulse energy also causes a greater increase of the temperature. However, a finer control of the material temperature can be achieved by varying repetition rates while fluence and number of pulses are unchanged.

For this reason, in the following analysis, fluence values and number of pulses are set constant for each repetition rate-varying irradiation series. Consequently, the differences between modified volumes on lines of the same series are attributed to effects related to the thermal characteristics of the materials.

3.2 Results for $\lambda = 1030 \text{ nm}$

Ablation is not the dominant consequence of processing these polymers with $\lambda=1030$ nm irradiations. As it was mentioned above, considering the bandgaps of the materials and the photon energies for this wavelength, at least 4 photons are required to be absorbed at the same time for the three materials for this wavelength. This implies that absorption is less efficient for this wavelength than for $\lambda=515$ nm and 343 nm and, as a consequence, lower temperatures will be reached. This fact is evinced in the following results.

PVC and PET present analogous effects at this wavelength, but at different number of pulses and repetition rate

Table 1. Estimated bandgaps, absorbance for $\lambda =$	343 and for $\lambda = 515$ nm, glass transition temperatures (T_q), melting
temperatures, (T_m) , decomposition temperatures ((T_d) and heat capacity at 25 °C and at T_d for PVC, PET and PP.

Polymer	$\begin{array}{c} {\rm Bandgap} \\ {\rm (eV)} \end{array}$	Absorbance 343 nm	Absorbance 515 nm	T_g (°C)	T_m (°C)	T_d (°C)	C_p at 25 °C (J/kg K)	$C_p ext{ at } T_d \ (ext{J/kg K})$
PVC	3.95	0.216	0.090	72.29	_	225	690	1568
PET	3.80	0.257	0.087	75.55	245.45	349	827	1979
PP	4.00	0.262	0.138	<0	157.96	320	1181	2928

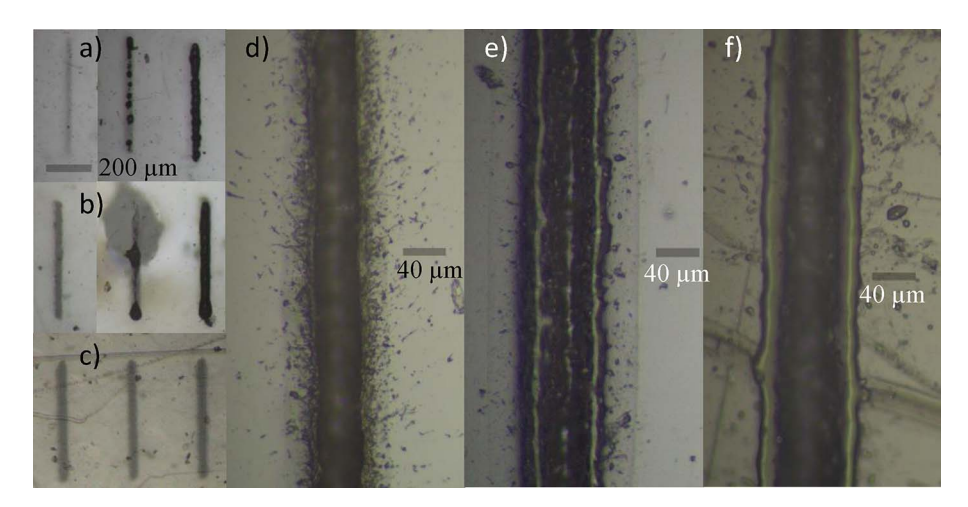


Fig. 3. (a) PVC irradiations at 1030 nm with N=25, 40 and 65 pulses/spot-area from left to right and f=5 kHz. (b) PET irradiations at 1030 nm with N=60 pulses/spot-area and f=2.5 kHz, 110 and 125 pulses/spot-area and f=100 kHz from left to right. (c) PP irradiations at 1030 nm with N=125 pulses/spot-area and f=200, 250 and 300 kHz from left to right. The scale bar shown in (a) is applicable to (b) and (c) too. (d) PVC irradiation at 1030 nm with N=125 pulses and f=1 MHz. (e) PET irradiation at 1030 nm with N=250 pulses and f=100 kHz. (f) PP irradiation at 1030 nm with N=400 pulses/spot-area and f=1 MHz. All the presented irradiations were performed at a fluence value of 1.70 J/cm².

values. For lower number of pulses/spot-area (about 25 for PVC and 60 for PET) only reflectivity changes are observed on the material surface, as seen in the left lines of Figures 3a and 3b. Above these values, thermal effects extended outside the irradiation area emerge. As the number of pulses increases (40–65 for PVC and 80–125 for PET) ablation appears and mixes with those extended thermal effects (see the central lines of Figs. 3a and 3b). Furthermore, burning traces are observable on the surroundings of the irradiated areas, as depicted in Figure 3b. It can be noted that when fluence is lower than the ablative threshold for a certain wavelength, surrounding heat transfer is increased. When ablation is achieved, a greater portion of the transferred energy is used to increase the ablated depth, leading to more restricted area effects. These extended effects are more prevailing for PET than for PVC. For higher number of pulses (65 for PVC and 125 for PET) ablation dominates as it can be noted for the right lines in Figures 3a and 3b. However, for the laser conditions for which ablation is achieved, the uniformity of the lines is quite low and the presence of debris is notable, even for high repetition rate irradiated lines, as seen in Figures 3d and 3e.

The differences between the required number of pulses for ensure ablation between PVC and PET might be explained regarding the heat capacity values at 25 $^{\circ}\mathrm{C}$ and

at T_d that can be seen in Table 1. It can be noted that PET exhibits a slightly greater heat capacities at both temperatures compared to PVC. This suggests that PET requires more energy for elevating its temperature than PVC. This disparity is increased for higher temperatures, as heat capacity differences between both materials are higher at T_d than at 25 °C. As a consequence, this may challenge ablation for PET. The smaller T_d presented by PVC also can benefit ablation compared to PET. The extended thermal effects can be explained by the glass-rubbery phase transitions that suffer PVC and PET when temperature is above 72 °C and 76 °C, respectively (see Tab. 1). These phase changes increase the volume of the material, obtaining thermal effects that are propagated outside the irradiation area. Then, rubbery state resolidifies and causes a change in the refractive index [13, 15, 20, 24, 25], as it is shown in Figure 3d.

On the other hand, PP shows a different behaviour. A higher number of pulses and repetition rate (1000 pulses and 100 kHz or 400 pulses and 1 MHz) is required to ensure a complete ablation. This can be understood regarding the notably higher heat capacity values at 25 °C and, especially, at T_d presented by this material (see Tab. 1). At lower number of pulses (about hundreds of pulses), nonextended reflectivity changes are the main consequences of processing this material, as it is shown in Figure 3c.

The lack of huge external thermal effects (as contrary as in the case of PVC and PET) may be related to the absence of glass-rubbery transition for PP at temperatures above 0 °C. Therefore, PP is already at rubbery state at ambient temperature, and this transition does not occur when the material is processed. Additionally, two homogeneous bleaching regions are discernible on the bordering of the ablation area in Figure 3f. These modifications are attributed to the flow of material that experienced a melting transition. Similar bleaching effects can also be noted on the edges of the ablated lines in PET, as seen in Figure 3e. These modifications are also attributed to the melting transition suffered by PET. The smaller size of bleaching observed in PET correlates with its higher melting temperature (245 °C) compared to PP (158 °C), as presented in Table 1. The lack of these regions for PVC correlates with the absence of melting transition for this material. The homogeneity of the ablation lines processed at high number of pulses and repetition rates is superior to that of PVC and PET, but it remains not entirely satisfactory for PP, as seen

The results of processing these three polymers with 1030 nm laser irradiation indicate that ablation is not achieved across all the studied laser conditions. High number of pulses and repetition rates are required to ensure ablation, especially for PP. Otherwise, only reflectivity changes or non-uniform ablation mixed with thermal effects appear. Even when ablation is accomplished, the resulting lines exhibit low uniformity and homogeneity. Consequently, processing these materials with 1030 nm under these laser conditions represents a less controllable process, obtaining non-optimal outcomes.

3.3 Results for $\lambda = 515$ and 343 nm

The consequences of processing these materials using $\lambda=515$ nm and 343 nm exhibit similarities. Contrary to the $\lambda=1030$ nm case, where ablation induced on the surface of the three polymers is less dominant, ablation is achieved for all the investigated repetition rates and materials for both wavelengths.

This fact aligns with the absorption spectra and bandgaps characteristics of the polymers (see Fig. 2 and Tab. 1). As it was discussed above, two-photon absorption dominates for $\lambda=515$ nm, and appears combined with single photon absorption for $\lambda=343$ nm, contrasting to the four photons that are needed for $\lambda=1030$ nm. Consequently, absorption is more efficient for $\lambda=515$ nm and 343 nm, generating higher temperatures on the material surfaces, that can exceed the decomposition temperature of the materials (T_d , see Tab. 1), enabling ablation. It must be emphasized that ablation has been achieved for a smaller number of pulses and fluence for $\lambda=515$ nm and 343 nm than for $\lambda=1030$ nm, underscoring the influence of the absorption mechanism on the processing efficiency.

However, despite absorbance is higher for $\lambda=343$ nm compared to $\lambda=515$ nm, there are differences in the pulse energy distribution of each wavelength. Specifically, the waist radius for $\lambda=515$ nm is 9 μ m at $1/e^2$, whereas the value for $\lambda=343$ nm is 7 μ m. As a consequence of the lower absorbance for 515 nm for the three materials,

a greater skin depth is expected for this wavelength processing, originating greater optical penetration depths. These facts could affect to the ablation depth and the modification widths, as detailed in this section.

To compare the differences between these wavelengths and materials, ablation depths and modification diameters for 150 pulses/spot-size irradiated lines series were measured across repetition rates ranging from 10 kHz to 1 MHz.

As it can be observed in Figures 4, 5, 6a and 6b, modified areas increase with repetition rate for the repetition rates that are shown in the images. The homogeneity of the processed lines is increased too as repetition rate is risen up. In Figures 4, 5, 6c and 6d 1 MHz irradiated lines are depicted, denoting a notable homogeneity. In contrast to the 1030 nm case (Figs. 3d–3f), the uniformity of the processed lines is remarkably enhanced for 515 nm and 343 nm processing, achieving more favoured outcomes for these two wavelengths.

Figures 4, 5, 6a and 6b also indicate that PVC and PET present greater modified widths and reflectivity changes in the ablation surroundings than PP. PP does not present these reflectivity variations. The two observable bleaching regions on the bordering of the ablation area are also attributed to flowed material, as explained in the previous subsection. In order to clarify the specific modification region, three different parameters are analysed for each material and wavelength: ablation depths, ablation diameters and extended diameters. The ablation depth is characterized as the maximum profundity of the removed volume. The ablation diameter denotes the horizontal width of the darkened ablation region. The extended diameters for PVC and PET are defined as the total reflectivity change widths, while for PP the extended diameters refer to the maximum distance between the external bleaching regions. An illustration of the diameters definitions is given in Figures 4, 5 and 6d.

The presence of reflectivity changes that expand the extended diameters for PVC and PET might be attributed to the phase changes experienced by these materials, as explained in the previous section. The glass transition suffered by PVC and PET at $T_g \sim 75$ °C triggers the enlargement of the modified region and the refractive index variation due to the volume increase during this phase transition. Nevertheless, PP glass transition occurs at temperatures below to 0 °C. As a consequence, this transition will not occur when PP is irradiated. This also explains the larger extended diameters in PVC and PET compared to PP.

PVC and PET also exhibit greater ablation depths than PP. This disparity might also be explained regarding the heat capacity values that can be seen in Table 1, as explained above. The greater PP heat capacities at indicate that this material presents a higher resistance for increasing its temperature compared to PVC and PET, challenging ablation.

Figures 4, 5, 6e and 6f demonstrate that ablation depths and extended and ablation diameters increase with repetition rate, occurring up to approximately 100 kHz for both wavelengths and the three materials. Beyond this range, these three parameters saturate, remaining nearly constant or even decreasing, as seen in the extended diameter for PVC and PET.

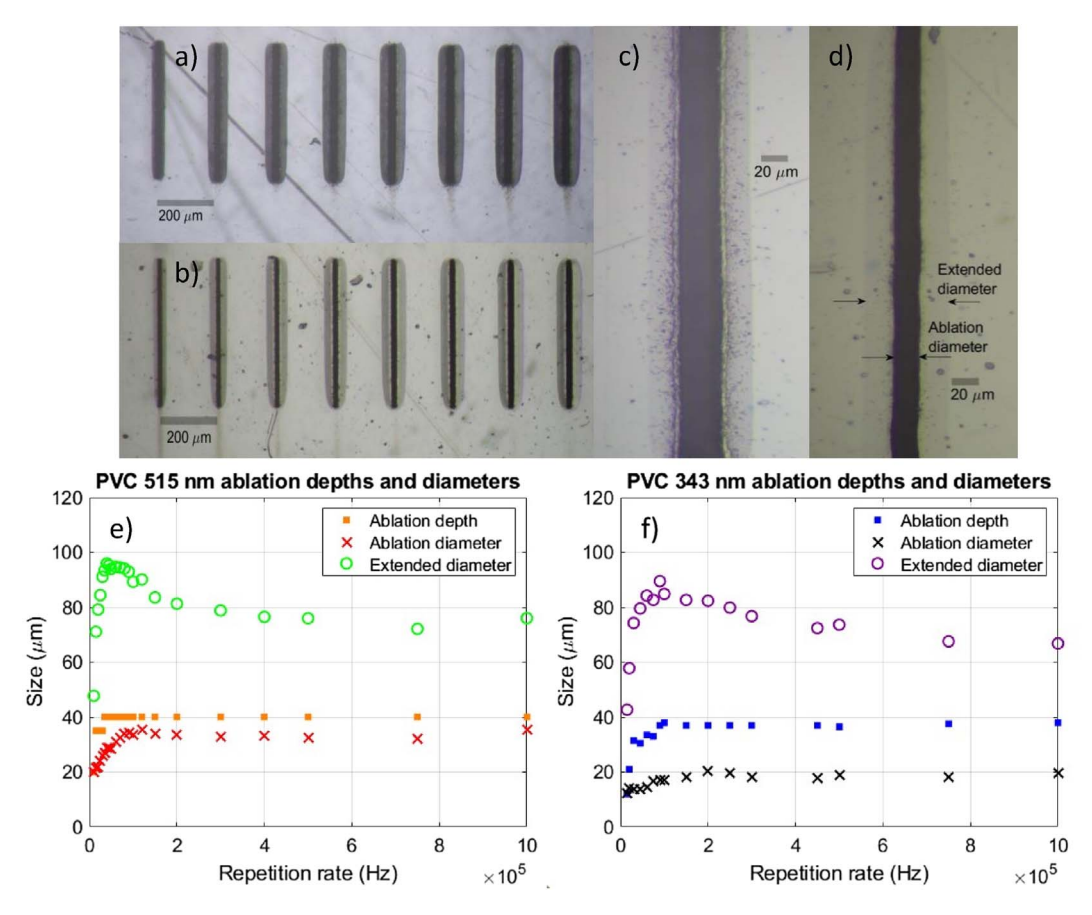


Fig. 4. (a) PVC irradiations at 515 nm with N=150 pulses/spot-area and f=10-45 kHz increasing from left to right. (b) PVC irradiations at 313 nm with N=150 pulses/spot-area and f=15-100 kHz increasing from left to right. (c) PVC 1 MHz irradiation with N=150 pulses/spot-area and 515 nm. (d) PVC 1 MHz irradiation with N=150 pulses/spot-area and 343 nm. (e) PVC measured irradiated lines ablation depth, ablation diameter and extended diameter for N=150/spot-area at 515 nm as functions of repetition rate. (f) PVC measured irradiated lines ablation depth, ablation diameter and extended diameter for N=150/spot-area at 343 nm as functions of repetition rate. All the presented irradiations were performed at a fluence value of 1.40 J/cm².

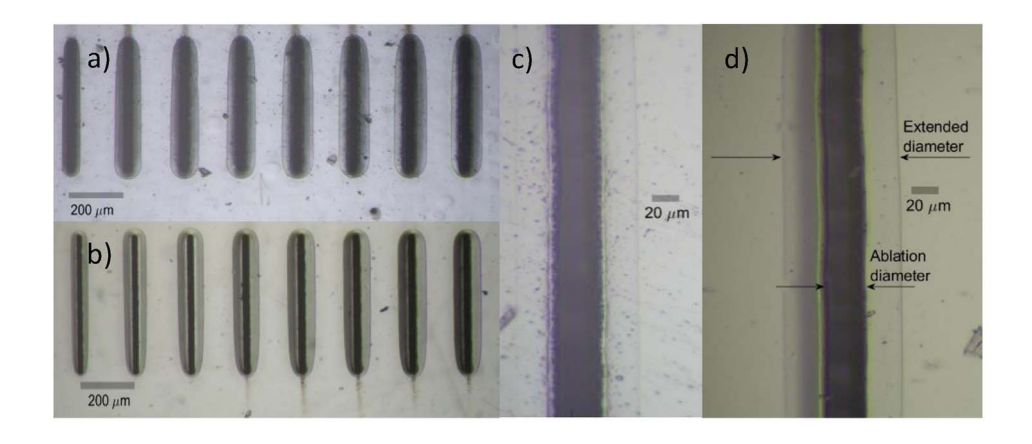
In this sense, two remarkable consequences of processing these materials must be emphasized: Firstly, by varying the repetition rate at a constant fluence and number of pulses a tunable micron-scale depths and modified diameters can be achieved. Furthermore, high repetition rate ablation not only contribute to a higher line uniformity, but also leads to a diminution of extended thermal effects for PVC and PET, enabling more precise processing.

The saturation phenomenon can be understood concerning the thermal diffusivity of the materials and the time between laser pulses. When a pulse impinges the surface of the material, temperature is increased in the irradiated area. At lower repetition rate values (larger time between pulses) materials are able to revert to their pre-pulse temperature, since time between pulses is greater than the diffusion time of the material. However, as repetition rate increases, the reduced time between pulses limits heat diffusion efficiency, leading to cumulative heat effects, that produce a significant rise of the material temperature. The critical repetition rate that supposes the entry into the heat accumulation regimes can be estimated as [13, 20, 26]

$$f_C = \frac{D}{4\omega^2},\tag{1}$$

where D is the thermal diffusivity and ω represents the laser radius at the focal plane. For thermal diffusivities $D \sim 8 \cdot 10^{-8} \ {\rm m^2/s}$ for the three polymers, and $\omega = 7 \ {\rm \mu m}$ for 343 nm irradiations and $\omega = 9 \ {\rm \mu m}$ for 515 nm, the critical repetition rate is $f_C \sim 250\text{--}400$ Hz. Notably, the working repetition rates exceed f_C in all the cases, indicating that all the lines have been irradiated on the heat accumulation regime. Consequently, the increase in ablation depths and diameters with repetition rate can be attributed to the heat accumulation effects that become more relevant as the repetition rate is increased.

Nevertheless, for repetition rates higher than 100 kHz, approximately, no further increments are noted for these three parameters, as illustrated in Figures 4, 5, 6e and 6f. This saturation is attributed to the fact that heat diffusion efficiency is reduced for this range of repetition rates. At these repetition rates, time between pulses becomes so small that temperature of the material remains essentially



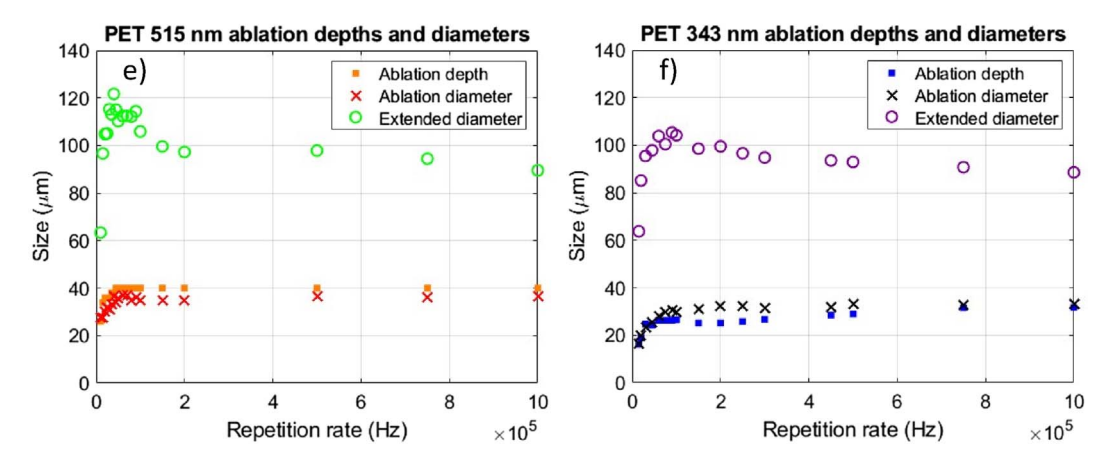


Fig. 5. (a) PET irradiations at 515 nm with N=150 pulses/spot-area and f=10–45 kHz increasing from left to right. (b) PET irradiations at 313 nm with N=150 pulses/spot-area and f=15–100 kHz increasing from left to right. (c) PET 1 MHz irradiation with N=150 pulses/spot-area and 343 nm. (e) PET measured irradiated lines ablation depth, ablation diameter and extended diameter for N=150/spot-area at 515 nm as functions of repetition rate. (f) PET measured irradiated lines ablation depth, ablation depth, ablation diameter and extended diameter for N=150/spot-area at 343 nm as functions of repetition rate. All the presented irradiations were performed at a fluence value of 1.40 J/cm².

constant until the next pulse arrives. As a consequence, material temperatures will not grow significantly if time between pulses is reduced. This occurs when time between pulses becomes considerably smaller than the diffusion time of the material. It must be noted that for 100 kHz, time between pulses $\left(t_{\rm bp} = \frac{1}{f} = 10^{-5}\,\mathrm{s}\right)$ is between 250 and 400 times smaller than the time associated to the critical repetition rate $\left(t_c = \frac{1}{f_c} \sim 2.5 \cdot 10^{-3} - 4 \cdot 10^{-3}\,\mathrm{s}\right)$. This reduction of the time between pulses could enable the saturation effect.

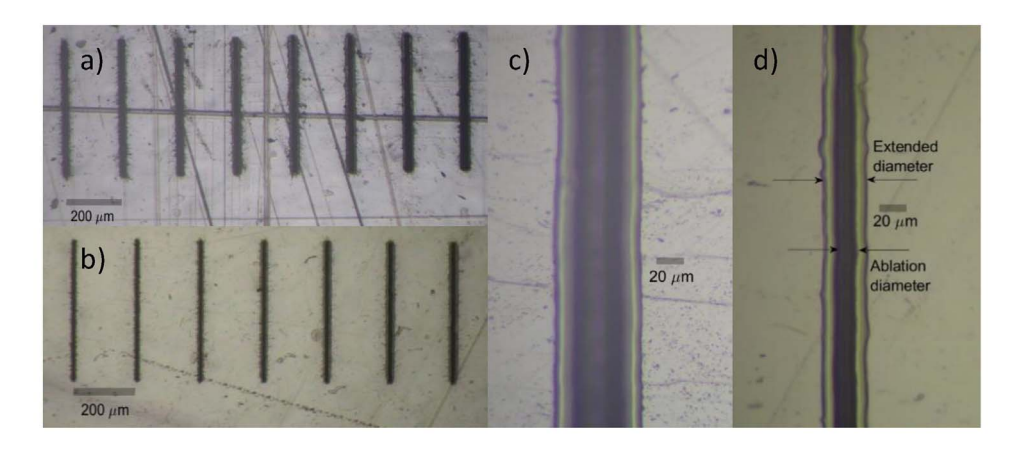
However, this reasoning does not explain the reduction of the external diameter size seen in PVC and PET after reaching a maximum for repetition rates near to 100 kHz (see Figs. 4, 5e and 5f). This phenomenon can be attributed to the way absorbed energy is distributed among different processes. Some part of the absorbed energy is spent for ablating and evaporating the material, another part remains in the vapor as kinetic energy and the residual heat is located in the bulk and the surface of the material, surrounding the ablation volume [27]. Initially, as repetition rate increases, temperatures rise up, increasing the amount of energy available for heat diffusion because a smaller

portion of the absorbed energy is devoted to ablation. Diffusion elevates the temperature on the ablation surroundings and, if temperature becomes greater than T_g the extended diameter will be enlarged. However, at higher repetition rates, temperatures may become sufficient for achieving greater ablation volumes, reducing the available residual energy for heat diffusion [22], resulting in a diminution of the external diameters for both materials.

Considering the ablation diameters saturation repetition rates and the maximum extended diameters repetition rates the transition between the thermal effects dominating regime and the ablation regime can be estimated.

For PVC, the maximum external diameter is originated at 40 kHz for 515 nm and at 90 kHz for 343 nm irradiation. The saturation of the ablation diameters is produced at 70 kHz for 515 nm irradiations and at 90 kHz for 343 nm processing. This indicates that the transition between both regimes is produced between 40 and 70 kHz for 515 nm and about 90 kHz for 343 nm for this polymer.

In the case of PET, the greatest extended diameter is obtained at $30~\rm kHz$ for $515~\rm nm$ and at $60~\rm kHz$ for $343~\rm nm$. Ablation diameters saturate at $60~\rm kHz$ for $515~\rm nm$ and at



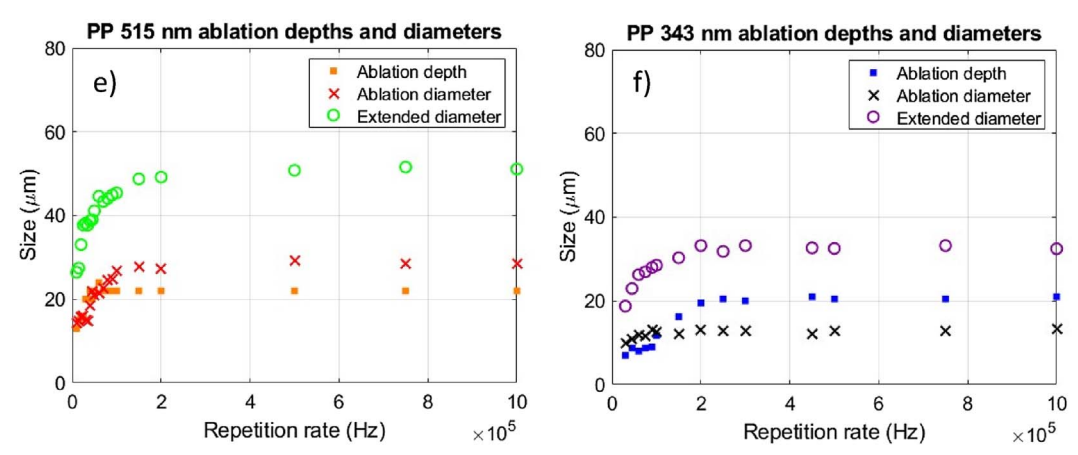


Fig. 6. (a) PP irradiations at 515 nm with N=150 pulses/spot-area and f=10–45 kHz increasing from left to right. (b) PP irradiations at 313 nm with N=150 pulses/spot-area and f=15–100 kHz increasing from left to right. (c) PP 1 MHz irradiation with N=150 pulses/spot-area and 515 nm. (d) PP 1 MHz irradiation with N=150 pulses/spot-area and 343 nm. (e) PP measured irradiated lines ablation depth, ablation diameter and extended diameter for N=150/spot-area at 515 nm as functions of repetition rate. (f) PP measured irradiated lines ablation depth, ablation diameter and extended diameter for N=150/spot-area at 343 nm as functions of repetition rate. All the presented irradiations were performed at a fluence value of 1.40 J/cm².

Table 2. Maximum extended diameter, extended diameter at 1 MHz, ablation diameter at 1 MHz and ablation depth at 1 MHz for PVC, PET and PP at 515 nm and 343 nm irradiation.

Polymer and wavelength	Max. extended diameter	Extended diameter at 1 MHz	Ablation diameter at 1 MHz	Ablation depth at 1 MHz
PVC (515 nm)	96 μm	76 μm	$36~\mu\mathrm{m}$	40 μm
PVC (343 nm)	$90~\mu\mathrm{m}$	$67~\mu\mathrm{m}$	$20~\mu\mathrm{m}$	$38~\mu\mathrm{m}$
PET (515 nm)	$122~\mu\mathrm{m}$	$90~\mu\mathrm{m}$	$37~\mu\mathrm{m}$	$40~\mu\mathrm{m}$
PET (343 nm)	$105~\mu\mathrm{m}$	$89~\mu\mathrm{m}$	$33~\mu\mathrm{m}$	$33~\mu\mathrm{m}$
PP (515 nm)	$51~\mu\mathrm{m}$	$51~\mu\mathrm{m}$	$29~\mu\mathrm{m}$	$22~\mu\mathrm{m}$
PP (343 nm)	$33~\mu\mathrm{m}$	$33~\mu\mathrm{m}$	$13~\mu\mathrm{m}$	$21~\mu\mathrm{m}$

 $75~\rm kHz$ for $343~\rm nm.$ This points that, for this material the transition is produced between 30 kHz and 60 kHz for $515~\rm nm$ and between 60 kHz and $75~\rm kHz$ for $343~\rm nm.$

PP does not exhibit a decrease of the extended diameters for repetition rates greater than 100 kHz. Its extended and ablation diameters reach a maximum at 90 kHz for 515 nm irradiation, remaining constant as the repetition rate is increased. The same behaviour is found for

343 nm, obtaining a saturation for extended and ablation diameters at 150 kHz. This behaviour aligns with the absence of extended thermal effects due to the lack of the glass transition during PP irradiation and confirms that the two bleaching regions are due to deposited material.

Being conscious of the repetition rate ranges where ablation predominates over thermal effects becomes crucial for acquiring control over material processing. A strategic convenient repetition rate can be selected in order to obtain the desired outcome after material irradiation.

There are also differences between both processing wavelengths for the three materials as shown in Table 2. Greater extended and ablation diameters are attained with 515 nm irradiations. The disparities between the maximum extended diameters at 515 nm and 343 nm are significant across the three materials, obtaining significantly greater modification areas at 515 nm. Differences in ablation diameter sizes between 515 nm and 343 nm irradiations at 1 MHz are also notable (1.8 ratio for PVC, 1.1 ratio for PET and 2.2 ratio for PP). Concerning ablation depth, comparable values are obtained for the three materials at both wavelengths: PVC ratio 1.1, PET ratio 1.2 and PP ratio 1. This indicates that greater volumes are ablated with 515 nm compared to 343 nm: 1.9 ratio for PVC, 1.4 ratio for PET and 2.3 ratio for PP.

In terms of the importance of achieving ablations with greater volumes and smaller diameters for acquiring control on the ablation area, it can be noted that, although bigger volumes are removed with 515 nm, the fact that the ablation diameters are smaller for the three materials at 343 nm indicates that sharper ablations can be achieved with 343 nm processing.

These results can be understood considering the differences between the materials absorption and the distinct radius waists at each wavelength. The greater ablation and extended diameters at 515 nm are attributed to the larger radius waists for this wavelength. Nevertheless, the fact that comparable ablation depths are achieved for both wavelengths is a consequence of the higher absorption of the three materials at 343 nm. Thus, generally, lower waist radii and greater absorptions benefit controllable ablation, increasing the processing precision.

4 Conclusions

The behaviour of three commercial polymers has been analysed under three different wavelength ($\lambda = 343 \text{ nm}, 515 \text{ nm}$ and 1030 nm) femtosecond laser irradiation for a wide range of repetition rates. The results point that 1030 nm irradiations are not efficient at our working fluence because for this wavelength, at least 4 photons are demanded to be absorbed at the same time for exceeding the bandgap energy for the three materials. As a consequence, nonuniform ablation, reflectivity changes and undesired extended thermal effects accompanied by burning traces are achieved at this wavelength. Conversely, two photon absorption is the main absorption mechanism for 515 nm and 343 nm processing for the three polymers, leading to a more suitable processing for which ablation is the main outcome. This fact highlights the significance of the dominant absorption mechanism for processing efficiency. For the latter two wavelengths ablation depths and modified diameters are measured, observing an increase of this parameters with repetition rate up to values around 100 kHz, and originating a saturation or even a diminution on the extended diameters for PVC and PET. This indicates that tunable depths and modified areas at the micron

level can be achieved by varying repetition rate at constant fluence and number of pulses. More suitable results are attained at high repetition rates, leading to more uniform lines for all the three materials and reduced extended diameters, particularly for the case of PVC and PET. The saturation effect can be understood considering the relation between the thermal diffusivity of the materials and the time between pulses. The decreasing of the extended diameters for PVC and PET can be explained regarding the distribution of the absorbed energy among ablation processes and heat diffusion. Regarding ablation precision, significant sharper ablations at 343 nm are achieved compared to 515 nm.

Supplementary material

Figure S1: MDSC curves for PVC (a), PET (b) and PP (c). Tg, and Tm are indicated with arrows. Thermogravimetry (TG, in black), derivative thermogravimetric curves (DTG, in blue) and decomposition temperatures (in red) for PVC (d), PET (e) and PP (f).

The supplementary material of this article are available at https://jeos.edpsciences.org/10.1051/jeos/2024021/olm.

Funding

The work was supported by the "Generalitat Valenciana" (IDIFE-DER/2021/014 cofunded by FEDER EU program, project PRO-METEO/2021/006, and INVESTIGO program (INVEST/2022/419) financed by Next Generation EU), "Ministerio de Ciencia e Innovación" of Spain (projects PID2021-123124OB-I00; PID2019-106601RB-I00), by "Universidad de Alicante" (UATALENTO18-10). APB thanks the "Ministerio de Ciencia e Innovación" for the grant (PRE2022-105016).

Conflicts of interest

The authors declare that they have no known competing financial interests or personal relationships that could have appeared to influence the work reported in this paper.

Data availability statement

No data was used for the research described in the article.

Author contribution statement

A.P. Bernabeu: Writing – review & editing, writing – original draft, investigation, data curation. G. Nájar: Investigation, software, data curation. A. Ruiz: Investigation, data curation. J.C. Bravo: Investigation, software. M.G. Ramirez: Methodology, investigation, conceptualization. S. Gallego: Writing – review & editing, writing – original draft, resources, conceptualization, funding acquisition. A. Márquez: Writing – original draft, investigation, conceptualization, funding acquisition. D. Puerto: Writing – review & editing, writing – original draft, supervision, investigation, data curation, conceptualization.

References

- 1 Modjarrad K., Ebnesajjad S. (2014) Handbook of polymer applications in medicine and medical devices, 1st ed, Elsevier, San Diego, CA, USA.
- 2 Ramakrishna S., Mayer J., Wintermantel E., Leong K.W. (2001) Biomedical applications of polymer-composite

- materials: A review, *Compos. Sci. Technol.* **61**, 9, 1189–1224. https://doi.org/10.1016/S0266-3538(00)00241-4.
- 3 Scholz C. (2017) Polymers for biomedicine: Synthesis, characterization, and applications, 1st ed., John Wiley & Sons, Hoboken, NJ, USA.
- 4 Leadbitter J., Day J.A., Ryan J.L. (1997) PVC: Compounds, processing and applications, Rapra Technology Ltd, Shawbury, UK.
- 5 Maddah H.A. (2016) Polypropylene as a promising plastic: A review, Am. J. Polym. Sci. 6, 1, 1–11.
- 6 Carr C.M., Clarke D.J., Dobson A.D.W. (2020) Microbial polyethilene terephthalate hydrolases: Current and future perspectives, Front. Microbiol. 11, 1–23.
- 7 Zacharatos F., Makrygianni M., Geremina R., Biver E., Karnakis D., Leyder S., Puerto D., Delaporte P., Zergioti I. (2016) Laser direct write micro-fabrication of large area electronics on flexible substrates, Appl. Surf. Sci. 374, 117–123. https://doi.org/10.1016/j.apsusc.2015.10.066.
- 8 Sun Y., Rogers J.A. (2007) Inorganic semiconductors for flexible electronics, *Adv. Mater.* **19**, 15, 1897–1916. https://doi.org/10.1002/chin.200739224.
- 9 Xu M., Xue Y., Li J., Zhang L., Lu H., Wang Z. (2023) Large-area and rapid fabrication of a microlens array on flexible substrate for an integral imaging 3D display, ACS Appl. Mater. Interfaces 15, 10219–10227. https://doi.org/10.1021/acsami.2c20519.
- 10 Zheng C., Hu A., Kihm K.D., Ma Q., Li R., Chen T., Duley W.W. (2015) Femtosecond laser fabrication of cavity microball lens (CMBL) inside a PMMA substrate for super-wide angle imaging, Small 11, 25, 3007–3016. https://doi.org/10.1002/smll.201403419.
- 11 Puerto D., Biver E., Alloncle A.-P., Delaporte P. (2016) Single step high-speed printing of continuous silver lines by laser-induced forward transfer, *Appl. Surf. Sci.* **374**, 183–189. https://doi.org/10.1016/j.apsusc.2015.11.017.
- 12 Bollgruen P., Wolfer T., Gleissner U., Mager D., Megnin C., Overmeyer L., Hanemann T., Korvink J.G. (2017) Ink-jet printed optical waveguides, Flex. Print. Electron. 2, 4, 045003. https://doi.org/10.1088/2058-8585/aa8ed6.
- 13 Sola D., Vázquez de Aldana J.R., Artal P. (2020) The role of thermal accumulation on the fabrication of diffraction gratings in ophthalmic PHEMA by ultrashort laser direct writing, *Polymers* 12, 12, 2965. https://doi.org/10.3390/ polym12122965.
- 14 Suriano R., Kuznetsov A., Eaton S.M., Kiyan R., Cerullo G., Osellame R., Chichkov B.N., Levi M., Turri S. (2011) Femtosecond laser ablation of polymeric substrates for the fabrication of microfluidic channels, Appl. Surf. Sci. 257, 14, 6243–6250. https://doi.org/10.1016/j.apsusc.2011.02.053.
- 15 Eaton S.M., Zhang H., Herman P.R., Yoshino F., Shah L., Bovatsek J., Arai A.Y. (2005) Heat accumulation effects in femtosecond laser-written waveguides with variable repetition

- rate, Opt. Exp. 13, 12, 4708–4716. https://doi.org/10.1364/opex.13.004708.
- 16 Eaton S.M., Zhang H., Ling M., Li J., Chen W.-J., Ho S., Herman P.R. (2008) Transition from thermal diffusion to heat accumulation in high repetition rate femtosecond laser writing of buried optical waveguides, *Opt. Exp.* 16, 13, 9443– 9458. https://doi.org/10.1364/oe.16.009443.
- 17 Lenzner M. (1999) Femtosecond laser-induced damage of dielectrics, Int. J. Mod. Phys. B 13, 13, 1559–1578. https://doi.org/10.1142/s0217979299001570.
- 18 Stuart B.C., Feit M.D., Rubenchik A.M., Shore B.W., Perry M.D. (1995) Laser-induced damage in dielectrics with nanosecond to subpicosecond pulses, *Phys. Rev. Lett.* 74, 12, 2248. https://doi.org/10.1103/physrevlett.74.2248.
- 19 Tien A.-C., Backus S., Kapteyn H., Murnane M., Mourou G. (1999) Short-pulse laser damage in transparent materials as a function of pulse duration, *Phys. Rev. Lett.* 82, 19, 3883. https://doi.org/10.1103/physrevlett.82.3883.
- 20 Misawa H., Juodkazis S. (2006) 3D laser microfabrication, Wiley-VCH Verlag, Weinheim, Germany.
- 21 Florian C., Fuentes-Edfuf Y., Skoulas E., Stratakis E., Sanchez-Cortes S., Solis J., Siegel J. (2022) Influence of heat accumulation on morphology debris deposition and wetting of LIPSS on steel upon high repetition rate femtosecond pulses irradiation, *Materials* 15, 17468. https://doi.org/ 10.3390/ma15217468.
- 22 Kerse C., Kalaycıoğlu H., Elahi P., Çetin B., Kesim D.K., Akçaalan Ö., Yavaş S., Aşık M.D., Öktem B., Hoogland H., Holzwarth R., Ilday F.Ö. (2016) Ablation-cooled material removal with ultrafast bursts of pulses, *Nature* 537, 7618, 84–88. https://doi.org/10.1038/nature18619.
- 23 Liu X., Du D., Mourou G. (1997) Laser ablation and micromaching with ultrashort laser pulses, *IEEE J. Quant. Electron.* 33, 10, 1706–1716. https://doi.org/10.1109/3.631270.
- 24 Schaffer C.B., García J.F., Mazur E. (2003) Bulk heating of transparent materials using a high-repetition-rate femtosecond laser, *Appl. Phys. A* **76**, 351–354. https://doi.org/10.1007/s00339-002-1819-4.
- 25 Schaffer C.B., Brodeur A., García J.F., Mazur E. (2001) Micromachining bulk glass by use of femtosecond laser pulses with nanojoule energy, Opt. Lett. 26, 2, 93–95. https://doi. org/10.1364/ol.26.000093.
- 26 Benayas A., Silva W.F., Ródenas A., Jacinto C., Vázquez de Aldana J., Chen F., Tan Y., Thomson R.R., Psaila N.D., Reid D.T., Torchia G.A., Kar A.K., Jaque D. (2011) Ultrafast laser writing of optical waveguides in ceramic Yb:YAG: A study of thermal and non-thermal regimes, Appl. Phys. A 104, 301–309. https://doi.org/10.1007/s00339-010-6135-9.
- 27 Bauer F., Michalowski A., Kiedrowski T., Nolte S. (2015) Heat accumulation in ultra-short pulsed scanning laser ablation of metals, *Opt. Exp.* 23, 2, 1035–1043. https://doi. org/10.1364/OE.23.001035.

J. Eur. Opt. Society-Rapid Publ. 2024, **20**, 29 © The Author(s), published by EDP Sciences, 2024

 $\rm https://doi.org/10.1051/jeos/2024029$

Available online at: https://jeos.edpsciences.org

EOSAM 2023

Guest editors: Patricia Segonds, Guy Millot and Bertrand Kibler

RESEARCH ARTICLE OPEN 3 ACCESS

Manufacturing reflection holographic couplers for see-through applications recorded in photopolymers without prisms: An experimental validation

J.J. Sirvent-Verdú^{1,*}, J.C. Bravo¹, J. Colomina-Martínez¹, G. Nájar¹, C. Neipp^{1,2}, J. Francés^{1,2}, S. Gallego^{1,2}, and A. Beléndez^{1,2}

Received 10 January 2024 / Accepted 13 May 2024

Abstract. In the present work, the viability of a novel recording geometry to produce reflection holographic couplers is analyzed. Recalling the idea of previous works, photopolymers are used as the recording material because they have been proven to be well-suited for the intended see-through application: the capability to provide a virtual image without compromising the information about the surrounding environment. Moreover, holography fundamentals give us the proper background to examine the proposed design, where no prisms or microlenses arrays are used. Aiming to support the analysis, we provide experimental evidence that the produced reflection holographic gratings exhibit the correct properties to work as a coupler, where the sensitivity of the material and its properties are studied and examined.

Keywords: Holography, Photopolymers, See-through, Holographic couplers, Reflection holograms.

1 Introduction

The see-through capability of an Augmented Reality (AR) device defines the purpose of the latter, which is to superimpose a virtual image on the surrounding environment of the user. Aiming for this feature, Holographic Optical Elements (HOEs) are one of the most promising solutions for the incoupler and out-coupler elements, enabling environmental light to interact with the HOE and subsequently producing an image.

Using photopolymers as the recording material has recently been a matter of study within AR [1, 2], thanks to their tuneable capacities, high efficiency, high resolution and low cost. The optical property that undergoes a change under illumination in this kind of recording material is either the refractive index or the absorption coefficient, mainly because of the photopolymerization and diffusion processes that occur during the exposure and thanks to which the optical phase information from an optical element can be stored.

For what follows, the commercial photopolymer Bayfol HX200 from Covestro AG has been used. Among its many studied features [3], the easy processing, long-term stability,

accuracy of grating reproduction and compatibility with standard industrial product-integration process highlight to our purpose. Moreover, as discussed in [4], the non-local diffusion model limits the variety of photopolymers that can be used for reflection holography, where this commercial product has been tested successfully. Particularly, it has been optimized in multiplexing procedures for reflection holograms of diffusing objects [5].

Regarding the core of this work, the majority of the recording holographic geometries, using prisms and microlens arrays, are based on reflection holograms [6], as they provide higher values of the Field of View (FOV), in terms of a wider angular tolerance [7], than the transmission ones and eliminate the stray light that produces ghost images, key factors among many others related to the design of see-through devices.

The use of prisms and index matching oil [8], accounting for the waveguide combiners, permits impinging angles very oblique inside the material inside the material to achieve diffraction angles higher than the critical angle inside the substrate. Even being readily achievable in a laboratory setting, it poses much larger challenges in mass production, mainly because of the need to avoid an air gap, and it is not suitable for any kind of non-contact master-copying automated production method.

¹ Instituto Universitario de Física Aplicada a las Ciencias y las Tecnologías, Universidad de Alicante, Apartado 99, E03080 Alicante, Spain

² Departamento de Física, Ingeniería de Sistemas y Teoría de la Señal, Universidad de Alicante, Apartado 99, E03080 Alicante, Spain

^{*} Corresponding author: jj.sirvent@ua.es

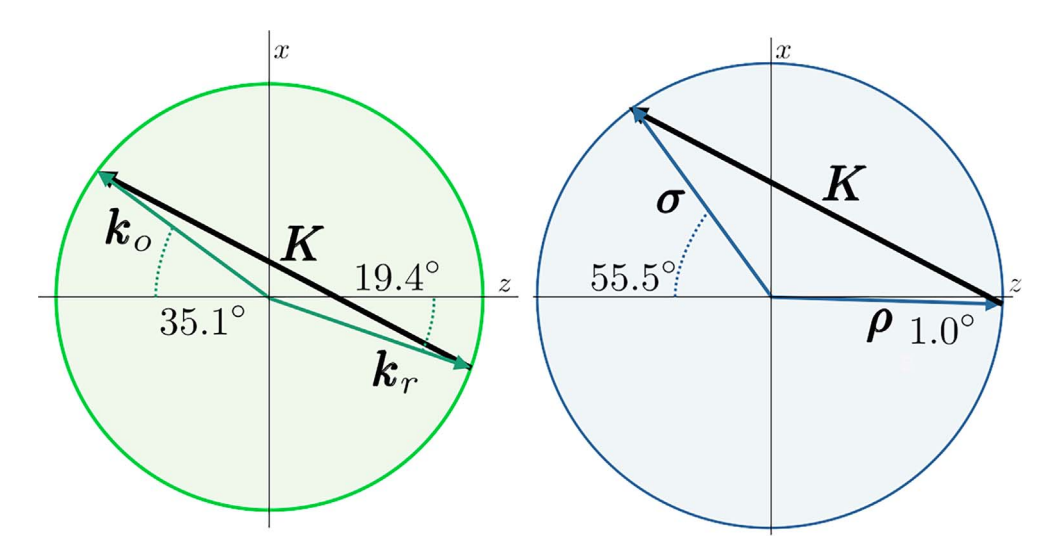


Figure 1. Evald's spheres for the selected geometry, using $\lambda_r = 532$ nm for the recording process and $\lambda_c = 473$ nm as the designed wavelength for the reconstruction stage. The recording structure (green) is built upon the recording angles in the material: 19.4° and 35.1°. The equivalent assembly for the reconstruction step (blue) yields angles of 1.0° and 55.5°. The average refractive index is $n_0 = 1.505$, so the critical angle is $\theta_c = 41.6$ °.

Hence, the novelty of this work lies in presenting an examination of the recording conditions to design the appropriate gratings, extending the fundamentals in previous works [2, 9, 10], using a reflection scheme without the use of prisms, and the experimental evidence about the viability of this approach.

2 Design and theoretical background

Intensity holography can be used to produce the aforementioned HOEs. This technique is built upon the translation of an interference pattern of two waves, known as reference and object waves, into a change in the optical properties of the recording material due to illumination, whose fundamentals are described next.

Focusing the design into the sinusoidal pattern arising from the interference of two plane waves, its main parameters are closely related to the recording geometry, which is depicted in Figure 1. Denoting as \mathbf{k}_o and \mathbf{k}_r the wave vectors of the object and reference beams, the grating is described by its reciprocal lattice vector, \mathbf{K} , as:

$$K = k_o - k_r. \tag{1}$$

Then, the hologram may act as a diffraction grating. In this simplest case, spatial dependence is induced in the refractive index n of the material due to the periodicity of the interference pattern, described as:

$$n(\mathbf{r}) = n_0 + n_1 \cos{(\mathbf{K} \cdot \mathbf{r})},\tag{2}$$

where $n_0 = 1.505$ is the average refractive index of the photopolymer [11], n_1 is the refractive index modulation and r is the position vector of a point in the holographic z - x plane, as in Figure 1.

That being so, with Λ as the grating spacing and φ as the slant angle of the grating vector given by (1), the

Bragg's condition during the reconstruction step yields the angle of incidence θ_B' for which the maximum diffraction occurs, given the reconstruction wavelength λ_c :

$$\cos\left(\theta_{B}^{'}-\varphi\right) = \frac{\lambda_{c}}{2n_{0}\Lambda}.\tag{3}$$

Moreover, following Kogelnik's notation [12], we can establish the angle of the diffracted beam, as its associated wave vector $\boldsymbol{\sigma}$ is related to the transmitted reference reference wave vector $\boldsymbol{\rho}$ and the grating vector within the Bragg condition through:

$$\boldsymbol{\sigma} = \boldsymbol{\rho} - \boldsymbol{K}.\tag{4}$$

Given the detailed relations (1)–(4) between the recording geometry and the grating formation and diffraction properties, we can design a specific geometry with convenient values for the angle of the diffracted beam and the Bragg angle. Then, if we can impose that the former is greater than the critical angle of the substrate, the hologram may work as a holographic coupler [9]. This is why the concrete configuration depicted in Figure 1 has been adopted, using $\lambda_0=532$ nm as the recording wavelength and $\theta_r=30^\circ$ and $\theta_\rho=60^\circ$ as the recording angles in air, which converts to $\theta_r=19.4^\circ$ and $\theta_o'=35.1^\circ$ in the material.

Specifically, using (1), the designed grating has a spatial frequency of $1/\Lambda \sim 5600$ lines/mm and a slant angle of $\varphi = -27.3^{\circ}$. Hence, values obtained from (3) and (4) with $\lambda_c = 473$ nm show that the diffracted beam propagates under the Total Internal Reflection (TIR) principle, as Figure 1 illustrates, when a near-normal incidence beam impinges on the grating.

Using different wavelengths in the recording and reconstruction processes ($\lambda_0 \neq \lambda_c$) permits us to accomplish this condition without using prisms. Noteworthily for this case, the guided wavelength is smaller than the recording wavelength, contrary to the transmission geometries where a wavelength greater than the recording one can be guided.

This can be explained by a general fact: if a grating vector \boldsymbol{K} is recorded with a reference and an object beam and, then, the reconstruction is performed with a greater wavelength, the angle between the reference and diffracted beam becomes also higher. Specifically, if (1) and (4) are combined, then

$$\frac{1}{\lambda_c} \sin \left| \frac{(\widehat{\boldsymbol{\rho}, \boldsymbol{\sigma}})}{2} \right| = \frac{1}{\lambda_o} \sin \left| \frac{(\widehat{\boldsymbol{k_o, k_r}})}{2} \right|. \tag{5}$$

Therefore, to achieve TIR propagation in the reflection schemes, as in Figure 1, we need to reduce this angle as the wave vectors are located at different half z-planes; one in z>0, the other in z<0. For transmission geometries, where both wave vectors share the same region, the angle between them needs to be higher and, hence, the intended operating wavelength needs to be greater than the recording one.

The use of this kind of grating in a waveguide combiner can be straightforwardly assembled if two complementary couplers are placed on the same substrate. Hence, the coupled light from the first one begins to propagate under the TIR, until it reaches the second grating, where it is decoupled, as they both share the same Bragg angle. Moreover, if the multiplexing technique is incorporated into the design, one may build a RGB system.

3 Experimental methods

3.1 Holographic recording setup

Aiming to produce the gratings with the recording geometry described in the preceding section, a two-beam holographic set-up has been used, as represented in Figure 2. The beam from the Excelsior Continuous Wave Laser – 532 nm (Spectra-Physics, Santa Clara, CA, USA) is split into two secondary beams, whose diameter is increased to 1 cm after being spatially filtered and collimated. Also, its ratio can be monitored by the variable beam splitter BC. The mirror M4 ensures the optical path is the same for both arms, that ideally reach the sample with an intensity of ratio of 1:1, inside the material, in order to enhance the fringe's visibility and, thus, the refractive index modulation [13].

In this particular case, we have set that $I_o = 0.7 \text{ mW/cm}^2$ and $I_r = 0.35 \text{ mW/cm}^2$, yielding an average exposure power of 0.5 mW/cm^2 in the interference region, where both beams reach with the same intensity due to the correction with both the area's projection and the Fresnel loss. In a previous work, we have proven that this range of intensities is optimal for different recording schemes [14].

3.2 Characterization of the gratings

In the next section, we will present experimental evidence about the see-through capability of the presented recording geometry. To do so, we need to provide a characterization of the gratings, ensuring that they have the desired properties.

A basic and essential property to study is the transmitted efficiency TE: the ratio of the transmitted intensity from the grating (I_t) and from the cured material where there is no hologram (I_0)

$$TE = I_t/I_0, (6)$$

that can be ultimately converted to the relative diffraction efficiency η in the volume hologram regime through $\eta=1$ – TE. For the following analysis, it is important to note that we work under s-polarization (\perp).

The first aspect to study is the optimal exposure energy that allows the hologram to be fully recorded in the material. As the Bayfol HX 200 has a broad absorption spectrum [15], real-time reconstruction is not possible. In this work, we have recorded samples with different exposure conditions, through the exposure time and the intensity ratio, in order to estimate the sensitivity and the dynamic range of the material. The set-up of Figure 2 enables to study the angular response in the first case, while a spectrophotometer (Jasco 650-V UV-Vis) is used in the second one. The information about the diffraction peaks in the spectral scan is then used to corroborate the grating's geometry quantitatively, instead of the angular information where the grating is less selective [7], but also offers qualitative information about the hologram's performance.

Additionally, for an estimation of the refractive index modulation n_1 from (2) and the optical thickness of the hologram d, Coupled-Wave (CW) theory can be used [12, 16]. Hence, the response of the grating (through its transmitted or diffracted efficiency) can be determined as a function of either the angle of incidence for a reconstruction wavelength λ_c or the wavelength for a fixed angle of incidence θ . Comparing the latter expressions with experimental data of TE as a function of the corresponding variable, n_1 and d are determined.

Lastly, we validate both the Bragg condition near normal incidence, through the playback angle θ_p and the propagation of the diffracted beam through TIR if the intended $\lambda_c=473$ nm is used. In this case, we also use an Excelsior Continuous Wave Laser – 473 nm (Spectra-Physics, Santa Clara, CA, USA) as the laser source.

4 Results and discussion

4.1 Exposure conditions

As stated in Section 3, the optimal exposure range of the photopolymer is studied from the transmission response at Bragg incidence as a function of the exposure conditions. In this sense, the results are shown in Figure 3.

The sensitivity of the material, in this particular scenario, is proven to be about $15~\mathrm{mJ/cm^2}$ according to the mean power exposure during the recording process, which is the threshold to produce an efficient hologram with the presented recording geometry. Also, one may reason that the inherent uncertainty of the measuring process accounts for the repeatability of the same response through different samples, as seen from the higher exposure values in Figure 3.

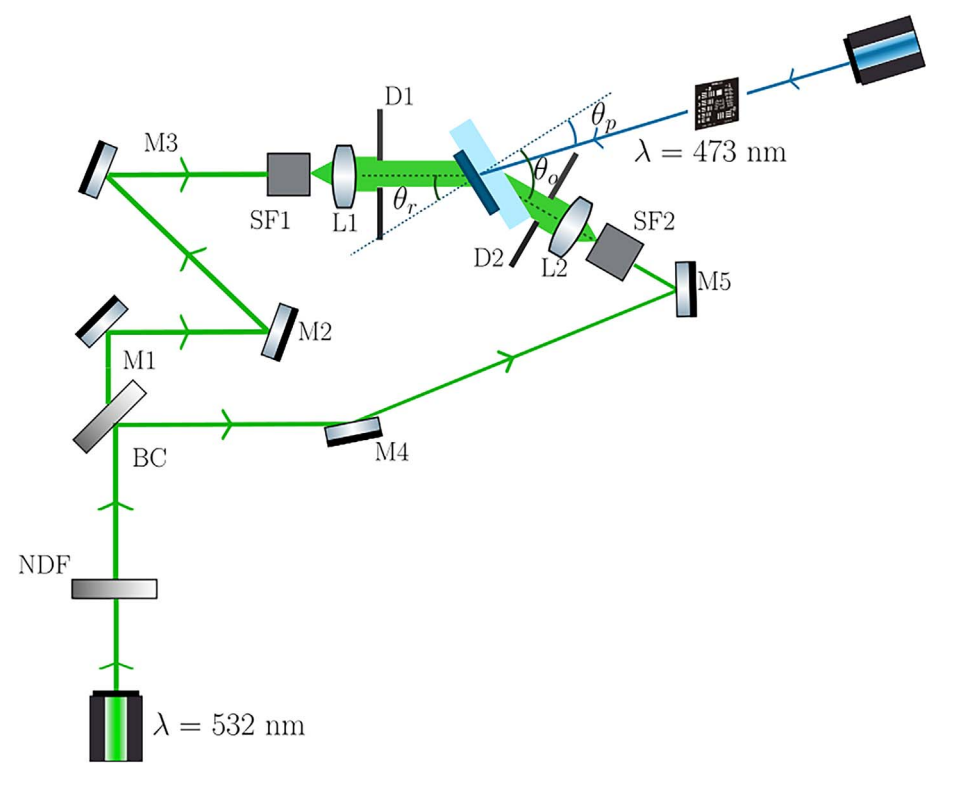


Figure 2. Experimental set-up. M: mirror, NDF: neutral density filter, BC: beam combiner BC: beam combiner, SF: spatial filter, L: lens, D: diaphragm. The photopolymer film is attached to a glass (both depicted in blue) that is placed upon a rotation stage to recombine the beams at the desired angles in the material.

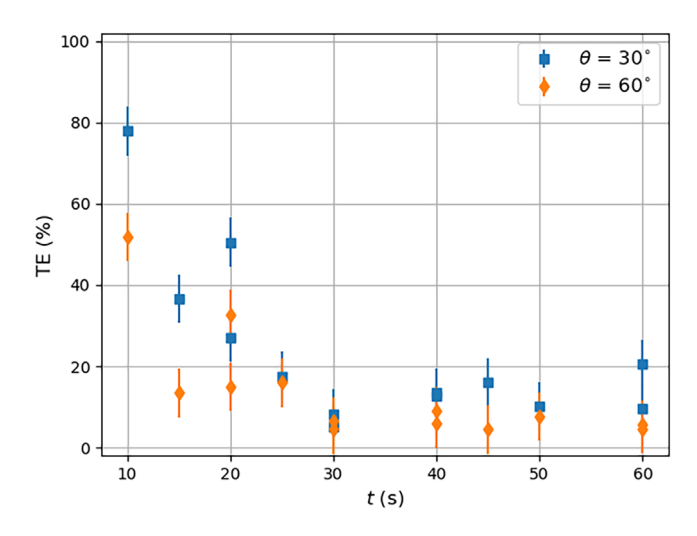


Figure 3. TE of different samples as a function of exposure time t, with intensities of $I_o = 0.7 \text{ mW/cm}^2$ and $I_r = 0.35 \text{ mW/cm}^2$, measured in air, and $\lambda_0 = \lambda_c = 532 \text{ nm}$.

4.2 Angular and spectral selectivity of the gratings

To illustrate the dispersion properties of the designed gratings, we characterize the transmission response of a probe hologram in the saturation regime of Figure 3 through either an angular or a spectral scan. First, experimental data of TE with $\lambda_c = \lambda_0 = 532$ nm is measured as a function of the incident angle, plotted in Figure 4.

Then, experimental data of TE is plotted in Figure 5 as a function of the recording wavelength for a certain angle of incidence θ . Also, an estimation of the refractive index modulation n_1 and the thickness d of the hologram is achieved with the angular scan in Figure 6, where $\lambda_0 \neq \lambda_c = 473$ nm.

At this point, the recording wavelength is used for the reconstruction, so the Bragg condition is fulfilled for incidence at the corresponding recording angles, $+30^{\circ}$ and $+60^{\circ}$, from Figure 1. It is stated earlier that the transmitted intensity from the hologram is compared with the equivalent intensity in the case where no grating is recorded, so TE not being 100% for the complete angular range in Figure 4 indicates that there is an energy trade-off from the 0th-order to the diffracted ones. Both minimum occur at the designed recording angles, which provide the expected response.

As seen in Figure 5, one may recognize the main features of this grating: when impinging with one of the recording angles, the hologram has a diffraction maximum at the corresponding recording wavelength 532 nm. Moreover, at normal incidence, there is a significant peak near 473 nm, whose diffracted counterpart is intended to be guided along the glass substrate.

In detail, for this latter case, there is a 2% discrepancy between the measured and the designed wavelength at normal incidence, that may be explained with a shift in the grating structure: Λ and φ may be directly computed considering the experimental values of both peaks $(\theta_1 = 0^{\circ}, \lambda_1 = 482.0 \text{ nm}), (\theta_2 = 30^{\circ}, \lambda_2 = 532.0 \text{ nm})$ and

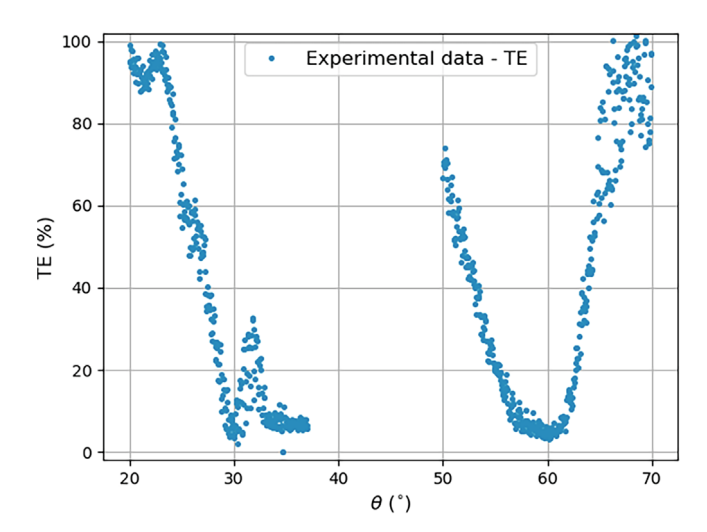


Figure 4. Experimental values of TE as a function of the incident angle in air θ with $\lambda_c = 532$ nm.

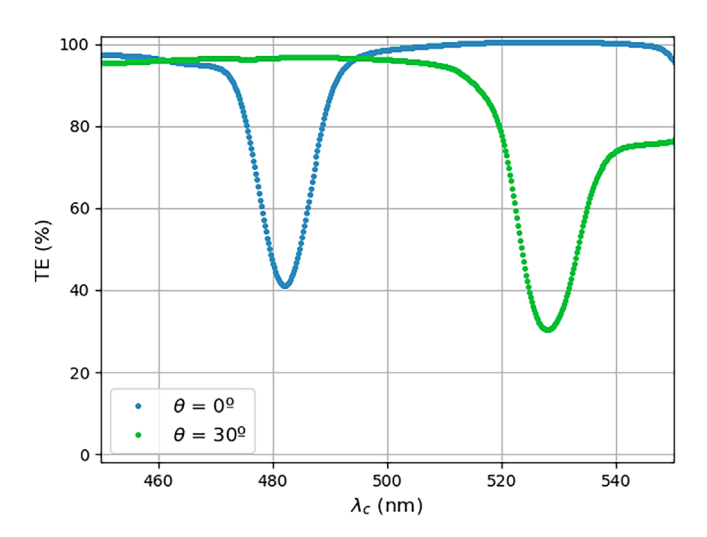


Figure 5. Experimental values of TE as a function of the reconstruction wavelength λ_c with different angles of incidence $\theta = 0^{\circ}$ (blue) and $\theta = 30^{\circ}$ (green).

its uncertainties $\Delta\theta=1^{\circ}, \Delta\lambda=0.2$ nm using (3), thanks to which it holds:

$$\frac{\cos(\theta_1' - \varphi)}{\lambda_1} = \frac{\cos(\theta_2' - \varphi)}{\lambda_2} \tag{7}$$

Then, with (7) and values from Figure 5, it yields a slant angle of $\varphi = -25.8 \pm 1^{\circ}$ and a grating period of $\Lambda = 177.9 \pm 1.3$ nm; or, conversely, a spatial frequency of 5620 ± 40 lines/mm. Recalling the purpose of this work, this HOE exhibits the expected features and the quantitative differences, which may be caused by small deviations during the recording process, are not significant to our cause as it is checked in Section 4.3.

Subsequently, we may proceed with the estimation of the thickness and the refractive index modulation. It is important to note that the whole information about the angular or spectral response is required to do so, while for

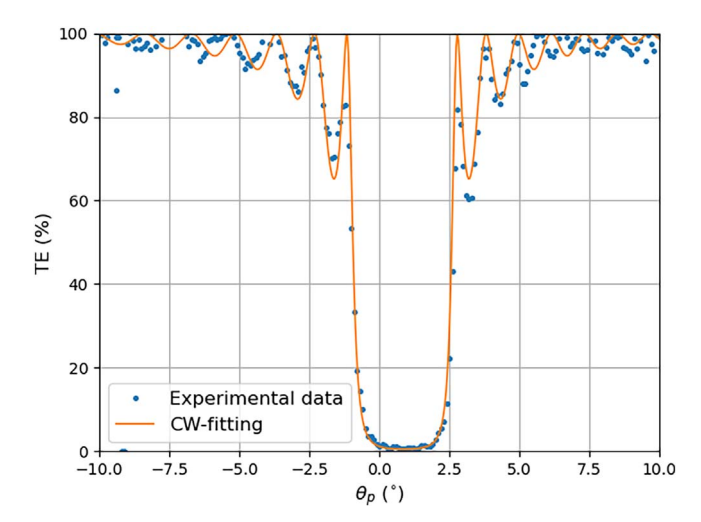


Figure 6. Experimental values of TE (points) as a function of the incident playback angle in air θ_p with $\lambda_c = 473$ nm and the corresponding CW curve (solid).

the calculations with (7) only the peak values are necessary. In this case, the 473 nm-beam in Figure 2 is used, as it provides the intended operating wavelength.

Turning now to the experimental evidence, using $\lambda_c = 473$ nm, best-fitting refractive index modulation of $n_1 = 0.027 \pm 0.002$ and $d = 14.3 \pm 0.1$ µm are obtained, which minimize the RMS between the experimental and the theoretical values, as plotted in Figure 6, where the transmitted efficiency is measured using (6) as a function of the playback angle θ_p .

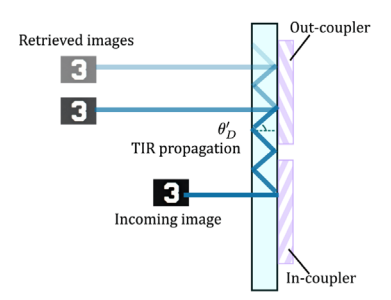
There is a good agreement between the experimental data and the theoretical curve from the CW theory, where the refractive index modulation is consistent with other estimations [5].

It is remarkable that the fitted optical thickness is less than expected for the photopolymer Bayfol HX 200, which is typically 16 μm [11]. This fact may be due to the presence of a subsidiary grating that emerges from the interference between one of the different 2-beam combinations, if accounting for the reflected beams in the recording process, which is also supported by the observation that there is not 100% efficiency between the central lobe and the secondary peaks. These also may explain the transmitted component in the corresponding curve from Figure 5, which can be isolated in this latter case.

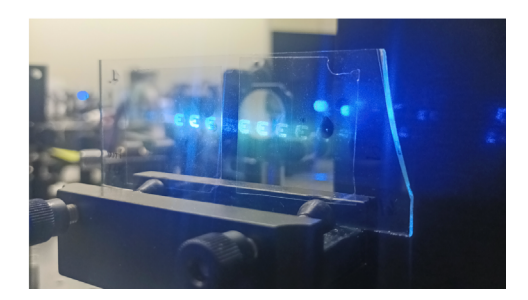
4.3 Experimental validation

As the final step to study the viability of the proposed geometry, we present here Figure 7 in which the sample shows the desired behavior that has just been mentioned: the reconstruction with $\lambda_c=473$ nm yields a diffracted beam that is guided through the glass due to TIR. Indeed, this complete and complement the information in Figures 5 and 6, which also confirmed this near-normal Bragg condition.

Hence, the grating acts as a reflection holographic coupler, whose area is the hologram's size, about 1×1 cm².



(a) Waveguide combiner propagation schematic representation.



(b) Image propagation superimposed on the surrounding environment.

Figure 7. Reflections gratings, recorded with the geometry in Figure 1, acting as in- and out- couplers under blue-light reconstruction.

The whole system, thus, performs as a waveguide combiner, as the schematic in Figure 7a depicts, with see-through capability where an image can be retrieved which do not affect the observer's surrounding environment as in Figure 7b.

5 Conclusions

A new recording geometry has been proposed to produce holographic reflection gratings in photopolymers, devoted to working as couplers in a see-through device. The inspection of the theoretical background has led us to a specific configuration where prisms are not needed, thanks to the ratio of the recording and the reconstruction wavelength being different from unity.

The proper functioning of the designed gratings has been proven and validated in the lab. The sensitivity for the concrete geometry has been found to be around $15 \, \mathrm{mJ/cm^2}$, using Bayfol HX 200 as the photopolymer film, for which the grating vector \boldsymbol{K} has been experimentally obtained using the Bragg wavelength for different angles where only subtle differences have been found. Also, the estimated values for the refractive index modulation and the optical thickness of the material hinted the presence of subsidiary gratings. As these geometries share the Bragg condition partially with each other, the main purpose of the hologram is not affected: we confirmed that the grating has a near-normal incidence Bragg condition if reconstructed with $\lambda_c = 473 \, \mathrm{nm}$ and the corresponding diffracted beam propagates under TIR in the glass substrate.

The presented evidence allows us to look forward to further experimental investigation, either by using a different photopolymer (like the HPDLC, with tuneable capacities after the recording process [17]) or by studying the imaging properties of the system when two complementary gratings are placed in the same glass substrate, with both the in-coupler and the out-coupler as a whole.

Funding

This work was funded by the "Generalitat Valenciana" (Spain) (IDIFEDER/2021/014, cofunded by EU through FEDER Programme; PROMETEO/2021/006 and INVEST/2022/419

financed by Next Generation EU), "Ministerio de Ciencia e Innovación" (Spain) (PID2021-123124OB-I00).

Conflicts of interest

The authors declare that they have no competing interests to report.

Data availability statement

Data associated with this article can be provided through direct contact and under the authors' permission.

Author contribution statement

J.J.S-V. performed the experiments, analysed the data and wrote the paper; J.C.B and J.C-M. implemented the computer code regarding the data analysis; G.N. assisted with the instrumentation and optimized the experiments; C.N. formulated the research goal, wrote, reviewed and edited the paper; J.F validated the overall reproducibility of the results and managed project administration; S.G. formulated and conceptualized the research goal, designed the experiments and wrote the paper; A.B. conceptualized and supervised the research activities and has been responsible of the acquisition of the financial support. Each author has actively contributed to this work and has reviewed and approved the final version of the manuscript.

References

- Kress B.C. (2019) Digital optical technologies, in: Kress B. C., Schelkens P. (eds), *International society for optics and photonics*, SPIE, Vol. 11062, p. 110620J.
- 2 Chakraborty D., Georgiev R., Aspell S., Toal V., Naydenova I., Cody D., et al. (2022) Photonics 9, 936.
- 3 Bruder F.K., Frank J., Hansen S., Lorenz A., Manecke C., Mills J., et al. (2023) Practical holography XXXVII: displays, materials, and applications, in: Blanche P.A.J., Lee S.H. (eds), *International society for optics and photonics*, vol. **12445**, SPIE, p. 1244503.
- 4 Gleeson M.R., Sheridan J.T., Bruder F.K., Rölle T., Berneth H., Weiser M.S., et al. (2011) Opt. Express 19, 26325.
- 5 Vázquez-Martín I., Marín-Sáez J., Gómez-Climente M., Chemisana D., Collados M.V., Atencia J. (2021) Opt. Laser Technol. 143, 107303.

- 6 Xiong J., Yin K., Li K., Wu S.T. (2021) Adv. Photon. Res. ${\bf 2},$ 2000049.
- 7 Blanche P.A. (2014) Field guide to holography, SPIE Press, Bellingham, WA, USA.
- 8 Kaur R., Park J.H., Kumar R. (2024) J. Opt. Soc. Am. A 41, A15
- 9 Fernández R., Bleda S., Gallego S., Neipp C., Márquez A., Tomita Y., et al. (2019) Opt. Express 27, 827.
- 10 Kaur R., Pensia L., Kumar R. (2023) Appl. Opt. 62, 3467.
- 11 Covestro, Bayfol HX200 Datasheet, Covestro AG (2022). https://solutions.covestro.com/-/media/covestro/solution-center/products/datasheets/imported/bayfol/bayfol-hx200_en_86194384-20033146-20033738.pdf?rev=f2fbbfd9c4204f67a

- $921634b8bb66959\&hash{=}11457C8925E83B7209132710495E\\512C.$
- 12 Kogelnik H. (1969) Bell Syst. Tech. J. 48, 2909.
- 13 Neipp C., Gallego S., Ortuño M., Márquez A., Alvarez M.L., Beléndez A., et al. (2003) J. Opt. Soc. Am. B 20, 2052.
- 14 Sirvent-Verdú J.J., Bravo J.C., Colomina-Martínez J., Neipp C., Puerto D., Márquez A., et al. (2023) Heliyon 9, e16646.
- 15 Bruder F.K., Fäcke T., Rölle T. (2017) Polymers 9, 472.
- 16 Gallego S., Ortuño M., Neipp C., Márquez A., Beléndez A., Pascual I., et al. (2005) Opt. Express 13, 1939.
- 17 Gallego S., Puerto D., Morales-Vidal M., Ramirez M.G., Taleb S.I., Hernández A., et al. (2021) Polymers 13, 1858.

J. Eur. Opt. Society-Rapid Publ. 2024, **20**, 34 © The Author(s), published by EDP Sciences, 2024

https://doi.org/10.1051/jeos/2024035

Available online at: https://jeos.edpsciences.org

EOSAM 2023

Guest editors: Patricia Segonds, Guy Millot and Bertrand Kibler

RESEARCH ARTICLE OPEN 3 ACCESS

Design approach for an advanced multi-channel pyrometer for bulk oven processes

Rune Fritzsche*, Clemens F. Kaiser, and Georg Herdrich

Institute of Space Systems, University of Stuttgart, Pfaffenwaldring 29, 70569 Stuttgart, Germany

Received 31 January 2024 / Accepted 22 July 2024

Abstract. Industrial processes such as smelting and sintering require stable and precise temperature control of furnaces. To achieve this, accurate temperature measurements are required. Pyrometry allows for contactless measurement of bulk materials and is particularly suitable for high temperature applications. One of the main influences on the accuracy of pyrometric measurements is the knowledge of the emissivity in the spectral measurement range. To reduce this dependence, two-color pyrometers or multi-color pyrometers can be used. With this in mind, the Institute of Space Systems (IRS) is further developing their existing pyrometer technology by designing an advanced multi-channel pyrometer for bulk oven processes in a joint venture with Stange Elektronik GmbH and New Generation Kilns Grün GmbH. The design approach is explained here and the considered methods of achieving emissivity independent temperature measurements are examined.

Keywords: Pyrometry, Emissivity, Simulation, Multi-color pyrometry, Ceramics, Bulk oven process.

1 Introduction

Industrial bulk oven processes require stable and precise temperature monitoring and control, and thus require accurate temperature measurements. One such process is the hardening of bulk ceramics, primarily kaolinite, in a newly designed kiln, for which the advanced multi-channel pyrometer shall be designed.

The Institute of Space Systems (IRS) at the University of Stuttgart has extensive experience in the field of pyrometry; particularly with the PYREX system which flew onboard the European Space Agency (ESA) mission EXPERT, which was designed to measure the heat flux through a ceramic thermal protection system during atmospheric entry by measuring its backside temperature. [1]

Further developing the IRS pyrometer technology, a new advanced multi-channel pyrometer is designed. The pyrometer shall measure temperatures of kaolinite, in a range of 100–1750 °C where the measurement error shall not exceed 2 K. The surface of the bulk material allows the assumption of diffuse emission and reflection. Six measurement channels shall be used. The measurement frequency shall not be lower than 0.5 Hz. These requirements are reflected in the various design aspects.

Additionaly, the system shall conduct temperature measurements independent of the emissivity of the bulk material. The main target application of the designed

pyrometer is a closed oven system, where a blackbody environment can be assumed because the ambiance is isothermal [2]. Since the goal is to develop a versatile product, a filter system and an algorithm for multi-color pyrometry are part of the pyrometer design. The signal path of each pyrometer channel consists of collimator optics, an optical fiber, a combination of interference filters and a photo diode. Of those components, the filters and diodes have the largest impact on the resulting signal strength and its wavelength dependence. It is decided that the diodes are the same for all channels, while the filters can be interchanged between channels. This interchangeability enables two-color multi-color pyrometry approaches for emissivity independent measurements.

2 Fundamentals

In the following sections, the physical principles used in pyrometry are laid out.

2.1 Thermal radiation

All bodies with non-zero temperatures emit electromagnetic radiation, according to the Stephan-Boltzmann law:

$$\dot{Q} = \sigma \varepsilon A T^4 \tag{1}$$

Q is the radiated power over all wavelengths, σ is the Stephan-Boltzmann constant, e is the emissivity of the radiator, A is its surface and T its temperature [3].

^{*} Corresponding author: $\verb|fritzscher@irs.uni-stuttgart.de|$

The radiated power is non-uniformly distributed over all wavelengths. The spectral distribution of radiation density is described by Planck's radiation law,

$$L_{\lambda} = \varepsilon(\lambda) \frac{2hc^2}{\lambda^5} \frac{1}{e^{hc/\lambda kT} - 1} = \frac{M_{\lambda}}{\pi}, \tag{2}$$

where L_{λ} is the spectral radiance, M_{λ} is the spectral radiant exitance, h is Planck's constant, c is the speed of light, λ is the wavelength and k is the Boltzmann constant [4].

In the context of pyrometry, Planck's radiation law is frequently simplified using the Wien approximation.

The Wien approximation is

$$L_{\lambda} = \varepsilon \frac{2hc^2}{\lambda^5} \frac{1}{e^{hc/\lambda kT} - 1} \approx \varepsilon \frac{2hc^2}{\lambda^5} e^{-hc/\lambda kT}.$$
 (3)

In other publications on multi-color pyrometry like [5–7], the Wien approximation is used to make the emissivity independent temperature determination possible by simplifying the temperature dependence of the spectral radiance in Planck's radiation law. The approximation is feasible in the Wien region $\frac{\hbar c}{\lambda kT}\gg 1.$ Its error is less than 1% if $\lambda T<2898~\mu mK$ [8]. For the given temperatures, that means that the measuring wavelengths would have to be between around 1.4 μm for the high end of the temperature range and 7.8 μm for the low end of the temperature range. Measurements must be taken at high wave lengths though, around 5.0–8.0 μm , as explained in Section 4.1. This means that for high temperatures in the specified measuring range, the Wien approximation would introduce large errors – up to around 41.1% (see Fig. 1) – and thus cannot be used.

2.2 View factor

To measure the radiation emitted by a body, a detector of a finite size must be used. The fraction of the radiation leaving the source that is seen by the detector is indicated by the view factor. The view factor between the radiation source and a pyrometer diode that receives all the radiation that is collected by a collimator is the view factor between two disks on the same axis. It is

$$F_{1-2} = \frac{1}{2R_1^2} \left(1 + R_1^2 + R_2^2 - \sqrt{\left(1 + R_1^2 + R_2^2\right)^2 - 4R_1^2 R_2^2} \right)$$

$$(4)$$

with $R_i = \frac{r_i}{a}$, r_i denoting the radii of the source surface (i=1) and receiving surface (i=2) and a denoting the distance between the two surfaces [9]. For a pyrometer with collimator optics, r_1 is the radius of the measuring point and r_2 is the radius of the collimator aperture.

2.3 Emissivity independent temperature determination

Single-color pyrometers offer highly accurate temperature measurements in clean environments when the emissivity of the investigated object at the measuring wavelength is known. However, in industrial environments contaminants on the surface and in the line of sight, varying surface geometries and emissivities cause significant measurement errors. In contrast, two-color and multi-color pyrometers offer more robust and accurate measurements as the

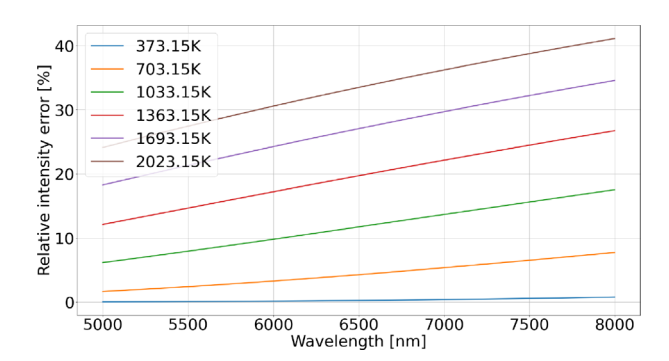


Figure 1. Relative error intruduced by using the Wien approximation in equation (2).

measurement principle mitigates the influence of the stated measurement errors.

2.3.1 Two-color pyrometry

Two-color pyrometers measure the radiation intensity in two narrow wave bands. The ratio of the two signal strengths is then a function of temperature and independent of emissivity, assuming that the emissivity is equal in both wavebands. Since this assumption generally does not hold in practice, the accuracy of two-color pyrometers is too low for the use case at hand [10].

2.3.2 Multi-color pyrometry

Multi-color pyrometers measure the radiation intensity within four or more narrow wave bands. A least-squares technique is used to solve for the unknown emissivity as well as the surface temperature. For this to work, prior knowledge on the functional dependence of the emissivity on the wavelength is required. Typically, the spectral emissivity function is assumed to be continuous and single-valued in the wavelength region in which the measurements are taken. With these assumptions, the spectral function of emissivity can be approximated using an exponential operating on a polynomial or a polynomial [7].

The obtained systems of equations can then be used to determine the surface temperature as explained by Neupane [7].

3 Simulation software

To save on protoyping costs and time that would arise from testing many different combinations of optical components, a simulation software for pyrometers is created at the beginning of the design process. This software, "PyroSim", is implemented using the Python language and the Qt5 graphical user interface library. The software simulates the whole signal path seen in Figure 2. For given temperatures, the software calculates the corresponding voltage signal.

3.1 Structure

A modular approach was chosen for the code. The simplified schematic of the *PyroSim* software structure is shown



Figure 2. Optical signal path per channel.

in Figure 3. Modules for the optical and electrical components as well as a radiation module and a geometry module make up the data model. It is independent of the graphical user interface (GUI). The GUI is connected to the data model via a controller module, which is also connected to a module for saving and loading pyrometer configurations for improved user experience.

Within the data model, the different component types are implemented as independent modules. All optical component modules are supersets of a common base. This makes it easy to add more component types if necessary.

Specific components of the implemented types are saved as text files. Components can easily be added to the software's database by extracting the relevant information from their respective data sheets.

3.2 Logic

The software simulates the signal path from the radiation source to the photo diode as well as the electronic amplification of the photo current. The radiation source is assumed to be a blackbody radiatior. The photocurrent is calculated as

$$I_{ph} = \int_{\lambda} \frac{\mathrm{d}I}{\mathrm{d}\lambda} \mathrm{d}\lambda \tag{5}$$

with

$$\frac{\mathrm{d}I}{\mathrm{d}\lambda} = L_{\lambda} \cdot F_{s-d} \cdot \tau_{\text{fiber}} \cdot \tau_{\text{filters}} \cdot \tau_{\text{lens}} \cdot \tau_{\text{collim}} \cdot R_{\text{diode}}. \tag{6}$$

 L_{λ} denotes the thermal radiation emitted by the radiation source, F_{s-d} denotes the view factor between the source and a diode. $\tau_{\rm fiber}$ is the transmissivity of an optical fiber

$$\tau_{\text{fiber}} = 10^{-\delta(\lambda)l}.\tag{7}$$

where δ is the attenuation of the fiber and l is its length, $\tau_{\rm filters}$ is the transmissivity of a combination of optical filters

$$\tau_{\text{filters}} = \prod_{i} \tau_{\text{filter},i}.$$
 (8)

 $\tau_{\rm lens}$ and $\tau_{\rm collim}$ denote the transmissivities of any lenses in the system and the collimator assembly, respectively. Lastly, $R_{\rm diode}$ is the responsivity function of a given photodiode.

4 Optical design

Based on the *PyroSim* simulation results, as well as optical and physical considerations, the optical configuration was determined. The design considerations for all components seen in Figure 2 are discussed in the following sections.

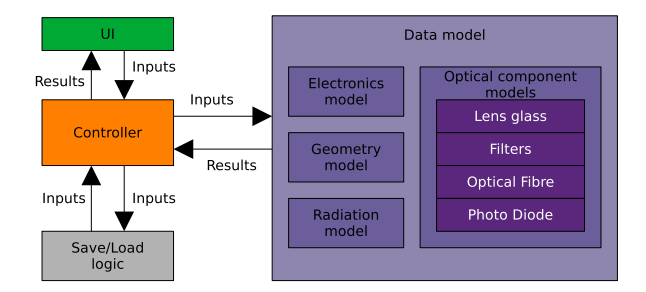


Figure 3. Simplified schematic of the software structure.

4.1 Photo diode

First, a photo diode capable of detecting weak infrared signals was chosen. As is shown in Figure 4, the intensity of a black body radiator at 100 °C is several orders of magnitude lower than that of a black body radiator at 1750 °C, even at the wavelength of maximum radiation intensity at 100 °C. Thus, the sensitive range of the diode is governed by the intensity distribution of a black body at the lowest temperature of the measuring range, 100 °C. A suitable photo diode is the two-stage thermoelectrically cooled Hamamatsu P12691-201G, which is an Indium Arsenide Antimonide detector, as it has a high responsivity across a large part of the relevant wavelength range (around $5.0{-}8.0~\mu m)$ [11]. Its spectral responsivity along with the radiation intensity for a 100 °C blackbody can be seen in Figure 5.

4.2 Optical fiber

The optical fiber needs to have a transmission range that corresponds well to the detection range of the diode. Thus, chalcogenide glass fibers as well as hollow core glass fibers are possible. Since hollow core fibers are susceptible to high bending losses, the IRF-Se-100R by IRflex is chosen [12].

4.3 Optical filters

Optical filters are used to enable a multi-color pyrometry approach. The filters are mounted on a rotating revolver so that each filter can be used for each channel (see Section 5). To achieve the best possible accuracy of emissivity independent temperature determination, six different filters are used, as accuracy increases with the number of wavelength channels [13]. More channels are not possible as explained in Section 7.

The choice of filters is limited to the responsive range of the diode, so roughly $5.0~\mu m$ to $8.0~\mu m$. The oven contains combustion products CO, CO₂ and H₂O, of which only the H₂O absorbs thermal radiation in the relevant wavelength range [14]. The filters are chosen to minimize the absorption by water (see Fig. 6), which is only successful for the three filters at higher wavelengths (Fig. 6). Other factors for the filter choices were the availability and the total transmission of the filters. The chosen filters are listed in Table 1. All filters are manufactured by Northumbria Optical Coatings Ltd. [19].

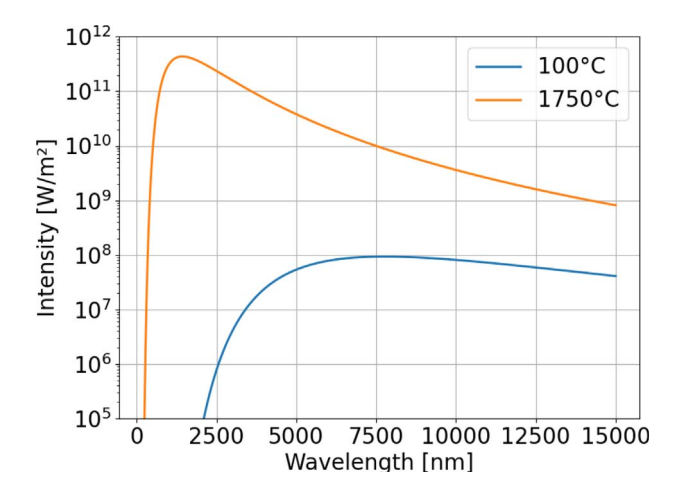


Figure 4. Radiation intensity distribution for the upper and lower temperature limit of the measuring range.

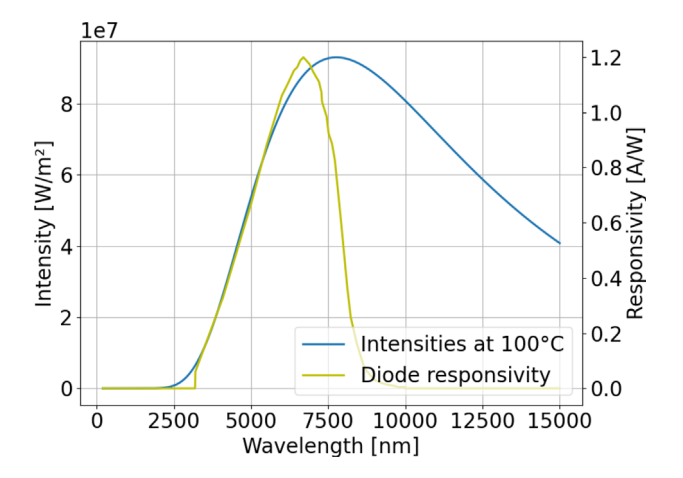


Figure 5. Radiation intensity distribution for the lower temperature limit of the measuring range and diode sensitivity.

4.4 Water vapour

Even though the filters are chosen to minimize the influence of water vapour absorption and emission, it cannot be avoided completely.

Absorption occurs in the air flushed section of the path, that is in the tube described in Section 5.2. It must be taken into account by incorporating the transmission spectrum of water vapour, at the temperature and concentration of the surrounding air, into the signal chain computation, using HITEMP[14] and RADIS [15–18].

Emission occurs in the oven between the tube and the bulk material. In this area, the oven is heated by burning natural gas, which burns at 1937 °C (adiabatic flame temperature) [20]. This flame temperature is assumed to be constant, so the emission spectrum can be calculated and subtracted from the signal before further processing, using HITEMP [14] and RADIS [15–18]. These assumptions regarding water vapour absorption, emission, and constant flame temperature must be validated through comprehensive test measurements to ensure the accuracy of the signal processing approach.

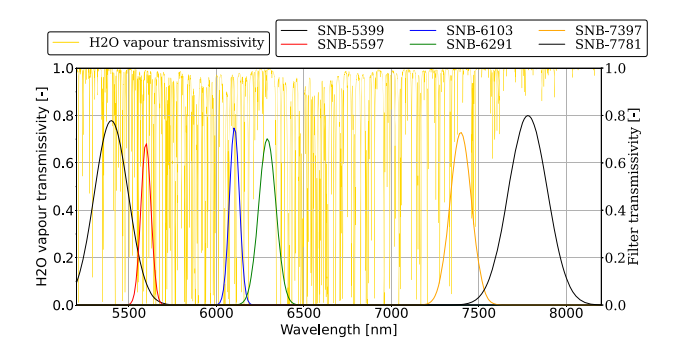


Figure 6. Spectral transmissivties of the filters used and of water vapour at 1 bar and 300 K, HITEMP [14] data visualized using RADIS [15–18].

Table 1. Filter selection for the 6-color-pyrometry.

Filter	CWL [nm]	FWHM [nm]	$\tau_{\rm peak}$ [–]
SNB-5399-000686	5399	228	0.7785
SNB-5597-000429	5597	68	0.8221
SNB-6103-000404	6103	67	0.8451
SNB-6291-001602	6291	115	0.9177
SNB-7397-001521	7397	143	0.8797
SNB-7781-001795	7781	262	0.7997

5 Mechanical design

Mechanically, the pyrometer system has two special features: a filter revolver and sensor heads that are decoupled from the base unit. The general mechanical layout can be seen in Figure 7.

5.1 Filter revolver

The filter revolver is a disk inside the base unit which holds one filter for each of the six measurement channels. The disk is connected to a stepper motor so that the narrow band filters can be interchanged between the six channels. This means that each measurement channel can be used as a six-color pyrometer. Since the required measurement frequency is very low, positioning time is not critical; the six positions can be switched through in less than 0.5 s.

5.2 Sensor heads

The sensor heads consist of a collimator which focuses light into an optical fiber which is connected to the base unit. This ensures that the base unit is far away from the heat source. Furthermore, it allows for high flexibility in terms of sensor placement. The sensor heads are placed on special viewports in the oven walls wherever temperature measurements are required. These ports consist of a tube that leads through the insulating layers (see Fig. 8), which is threaded outside the oven so that the sensor heads can be screwed on. The tube, whose dimensions are yet to be determined, limits the size of the measuring area. The measuring area

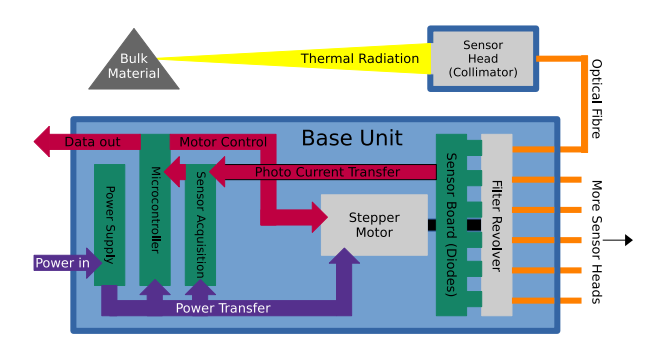


Figure 7. Schematic of the pyrometer system design.

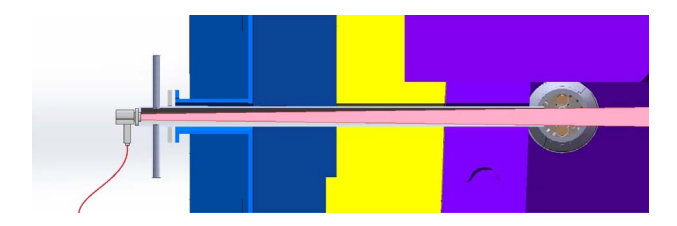


Figure 8. Conceptual drawing of the sensor head placement in the oven wall with the cone of vision of the sensor head in red.

otherwise depends on the collimator's beam divergence. Since spacial accuracy is not a requirement, no further measures to limit the measuring area were taken. Between the tube and the sensor head, there are ports for air flushing, minimizing the heating of the sensor heads and preventing dust buildup on optical components.

6 Electronic design

The electronic design is required to provide data aguisition and stepper motor control as well as data processing. For these tasks, Stange Elektronik GmbH has designed four printed circuit boards inside the base unit: A sensor board, a sensor acquisition board, a micro controller board and a power supply board (see Fig. 7). The sensor board houses the photo diodes. On the sensor acquisition board, the photo current of the diodes is converted into a voltage using transimpedant amplifiers. Depending on the photo current, different amplification circuits can be selected for each channel using relays. The micro controller board houses an ATSAMD51N19A-AU micro controller. The controller controls the stepper motor and calculates the target temperature from the measurement voltages for each channel. Lastly, the power supply boards provides power to all other boards as well as the stepper motor.

7 Emissivity independent temperature determination

Emissivity independent temperature determination can be achieved using multi-color pyrometry approaches, as explained in Section 2.3. These approaches are made possible via the optical, mechanical and electronic design discussed so far.

The requirements and prior design decisions lead to a six-color approach: More wave bands tend to produce more accurate temperature measurements as seen in [13], but several limitations lead to just six channels being feasible. Firstly, the requirements state that the six measurement channels of the pyrometer shall measure simultaneously. This means that, given the mechanical design and the filter revolver assembly, the number of wave bands must be a multiple of the number of measurement channels. For 12 or more wave bands, it is not possible, with the available sources for narrow band pass filters, to find a filter configuration without substantial overlap between the channels.

7.1 Application on ceramics

The emissivity of ceramics is dependent on the temperature of the surface and the wavelength at which the radiation is measured [21]. Here, the temperature dependence can be ignored, as the temperature is assumed to be constant during a multi-color measurement cycle, since the observed bulk oven processes are slow moving. Thus, only the wavelength dependence has to be considered.

7.2 Method

There are multiple methods of determining the temperature from the radiation intensity measurements in the different wavelength bands. The relevant methods are linear least-squares fitting and a non-linear least-squares fitting as described by Neupane et al. [7]. Here, the output signals (voltages) from the six wave bands are used to determine the photocurrent of the diode. From those photocurrents, the spectral radiance at the center wavelength of each channel is obtained from equation (6). Since the Wien approximation is not applicable, a nonlinear least squares approach has to be taken to obtain the measured temperature: the linear least-squares method as described by Neupane et al. [7] requires the simplifications that the Wien approximation makes possible. The objective function to optimize for is

$$\mathcal{X}^2 = \sum_{i=1}^6 \left(L_{\lambda_j, \text{meas}} - L_{\lambda_j, \text{guess}} \right)^2, \tag{9}$$

where λ_j is the center wavelength of each wave band, $L_{\lambda,\text{meas}}$ is the spectral radiance derived from the measurements and $L_{\lambda,\text{guess}}$ is the guessed spectral radiance. $L_{\lambda,\text{meas}}$ is obtained from the measurement voltage using

$$L_{\lambda_{j},\text{meas}} = \frac{U_{\text{meas}}}{\lambda_{j} R_{\text{meas}} F_{s-d} \tau_{\text{fiber}} \tau_{\text{filters}} \tau_{\text{lens}} \tau_{\text{collim}} R_{\text{diode}}}, \quad (10)$$

where $U_{\rm meas}$ is the voltage signal and $R_{\rm meas}$ is the measuring resistance. This calculation is error prone due to uncertainties in the view factor, as the distance between the sensor head and the measured object changes during the oven process. Since this error is not wavelength dependent though, it only scales the emissivities that the

method described here yields, but doe not change the temperature.

 $L_{\lambda, \mathrm{guess}}$ is obtained using equation (2) with a third degree polynomial, with four coefficients a_0-a_3 describing the spectral emissivity distribution. The least squares minimization was accomplished using the Nelder-Mead algorithm as implemented in the lmfit Python library [22], and imposing bounds of $0.8 < \varepsilon < 1$, which are taken from the known emissivity values of kaolinite [23]. The parameters for the optimization are the four coefficients of the emissivity polynomial as well as the measured temperature. More information on this method of temperature determination can be found in [7].

7.2.1 Problems

The method described above can be used for temperature (and emissivity) determination with better accuracy than simply assuming black body radiation in a closed, potentially isothermal environment. When simulated input values calculated with the emissivity distribution of kaolinite [23] are used, which represents a best case scenario neglecting noise and other error sources, several problems for the implementation in the final product present themselves. First, this simulated best case accuracy is still too high for the requirement of 2 K, in fact, absolute error values go up to 90 K. As seen in Figure 9, the higher the temperature gets, the more the estimated temperature oscillates. Algorithms other than Nelder-Mead oscillate a lot less, but their error is considerably higher. The emissivity estimations produced by the Nelder-Mead algorithm (see Fig. 10) are almost perfectly straight, first order polynomials, even though the parameters of the least squares minimization allow for third order polynomials. More investigation to obtain better fits is necessary here. Secondly, the narrow wave band filters are not sufficiently narrow to assume monochromaticity, a multi-band pyrometry approach must be chosen (where L_{meas} and L_{guess} in equation (9) are substituted by

$$\int_{\lambda_{J}}^{\lambda_{J'}} L(\lambda, T) \mathrm{d}\lambda \tag{11}$$

[24]). With this approach, no least-squares fit that is better than assuming a constant emissivity of unity could be achieved. Further investigation is necessary to improve the accuracy using the multi-band approach.

Lastly, the computing time of the temperture determination algorithm is high, taking a few seconds per temperature determination on consumer hardware, which is obviously not acceptable given the desired measuring frequency of 0.5 Hz. Expected performance on the microcontroller in the finished product would be much worse.

8 System test and calibration

The pyrometer system has to be tested during the design process, and calibrated before it can be used for temperature determination. For both tasks, the same test setup is used. It consists of a radiation source, a reference thermometer and the pyrometer prototype.

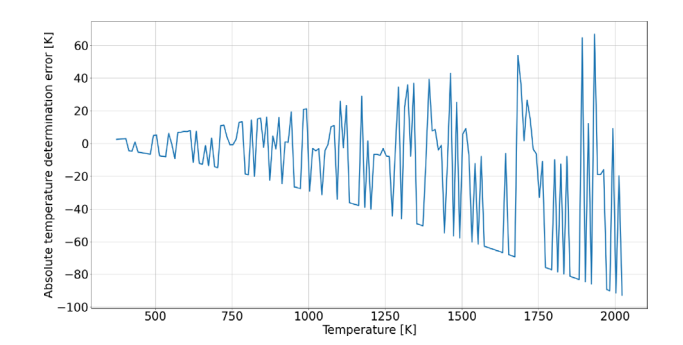


Figure 9. Temperature estimation error.

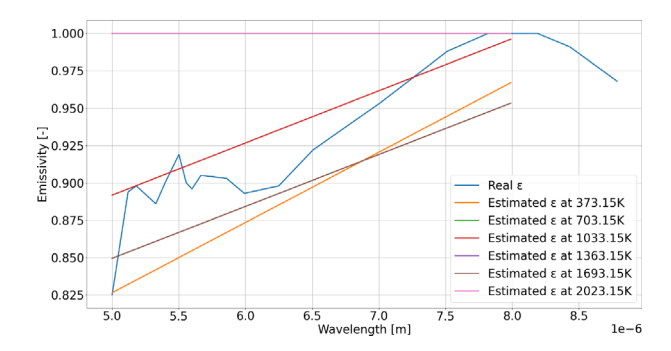


Figure 10. Comparison of estimated emissivity functions and real emissivity of kaolinite [23].

8.1 Radiation source

The radiation source is a cavity radiator that was built at the IRS. It approximates a black body radiator with an effective emissivity $\epsilon_{\rm BB}>0.99$ [2]. It can operate at temperatures up to 2400 °C. Below around 700 °C, the temperature of the radiation source can not be kept stable by the control system.

8.2 Reference thermometer

The reference thermometer is a linear pyrometer, LP3, developed by KE Technology GmbH. In the range between 950 °C and 2400 °C, the measurement error is, for a 95% confidence interval, ± 2.1 K as per the last calibration in 2023.

8.3 Validation of the simulation software

For testing and validation of the simulation software, the radiator is set to six different temperatures within the measuring range of both the LP3 and the prototype pyrometer. An early prototype, using an FD1000W photodiode [25], a Thorlabs RC08SMA-P01 collimator [26], a Thorlabs FG200LCC fiber [27], a 6 mm thick barium flouride lens and no filters was tested and compared against simulation results obtained with the PyroSim software.

Measurements were recorded using a LeCroy Wave Surfer 434 oscilloscope [28]. The comparison shows a good agreement between the simulated and measured data (see Fig. 11). The maximum relative error of this dataset is

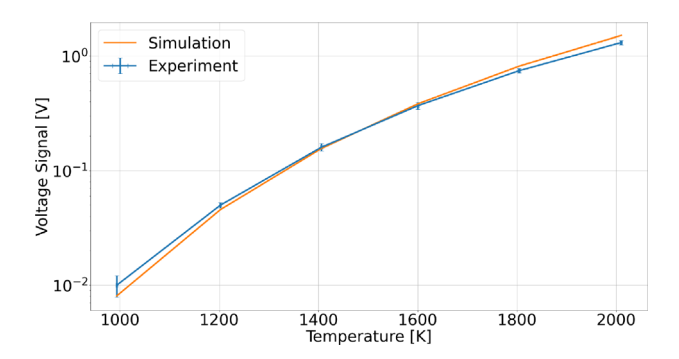


Figure 11. Temperature-signal-relation comparison between experiment and simulation.

19.3%, its average relative error is 9.69%. Error sources are the uncertainty of the reference pyrometer, the uncertainty of the oscilloscope and diode degradation. It is worth noting that, due to the instability of the radiator temperature below 700 °C as well as the responsivity of the prototype's diode in shorter wavelengths, no relevant measurements were obtained in the range of 100–700 °C. A new testbed and prototype will be created in the future to validate the simulation software throughout the whole measuring range of the pyrometer system.

9 Conclusion

A pyrometer system is designed as a versatile measuring instrument for the temperature control of industrial bulk oven processes. It features six channels with sensor heads that are decoupled from the base unit which houses the photodiodes. In the design process, a simulation tool is created which can be used for spectral sensitivity studies with different optical components. The expansion of the instruments capabilities to include emissivity independent temperature determination is examined by investigating multi-color pyrometry with regard to the application on ceramics. The requirements on the pyrometer system can not be fulfilled, as the algorithm for the emissivity independent temperature determination is still inaccurate. Further optimization of the fitting algorithm is necessary in the future in order to minimize the measurement error. Additionally, the accuracy must be verified in a controlled laboratory environment and tested in the industrial environment of the planned use case.

Acknowledgments

We would like to thank Stange Elektronik GmbH for their help in the electronic design of the pyrometer system. We also want to thank New Generation Kilns Grün GmbH for providing insight into bulk oven processes.

Funding

This research was funded by the "Zentrales Innovations programm Mittelstand (ZIM)" by the German government, specifically the "Bundesministerium für Wirtschaft und Klimaschutz" under grant number KK5034904SY1.

Conflicts of interest

The authors declare that they have no competing interests to report.

Data availability statement

Numerical data created using *PyroSim* is available. Data that was experimentally obtained during the verification of the software is available as well.

Author contribution statement

R. Fritzsche wrote the article with contributions from C. Kaiser, who supervised the writing. R. Fritzsche and C. Kaiser carried out experiments and testing with the black body simulator. R. Fritzsche programmed the simulation software, using an earlier prototype of a *PyroSim*-like tool developed by G. Herdrich, and implemented the least squares optimization algorithm. The conceptualization, funding acquisition and project administration was done by G. Herdrich.

References

- 1 Herdrich G., Lein S., Preci A., Steinbeck A., Fasoulas S., Auweter-Kurtz M. (2012) The flight of EXPERT: assessment of nonequilibrium effects with the IRS payloads PYREX. Available at https://arc.aiaa.org/doi/pdf/10.2514/6.2011-3625
- 2 Bauer G., Bischoff K. (1971) Evaluation of the emissivity of a cavity source by reflection measurements, Appl. Opt. 10, 2639–2643.
- 3 Stephan P. (2013) B1 Wärme und verschiedene Arten der Wärmeübertragung, in: VDI-Wärmeatlas. VDI-Buch, Springer Vieweg, Berlin, Heidelberg, pp. 19–22, ISBN 978-3-642-19981-3, https://doi.org/10.1007/978-3-642-19981-3 3.
- 4 Kabelac S., Vortmeyer D. (2013) K1 Strahlung technis cher Oberflächen, in: *VDI-Wärmeatlas. VDI-Buch*, Springer Vieweg, Berlin, Heidelberg, pp. 1083–1096, ISBN 978-3-642-19981-3, https://doi.org/10.1007/978-3-642-19981-3 68.
- 5 Magunov A.N. (2009) Spectral pyrometry (review), Instrum. Exp. Tech. 52, 451–472.
- 6 Mekhrengin M., Meshkovskii I., Tashkinov V., Guryev V., Sukhinets A., Smirnov D. (2019) Multispectral pyrometer for high temperature measurements inside combustion chamber of gas turbine engines, *Measurement* 139, 355–360.
- 7 Neupane S., Jatana G.S., Lutz T.P., Partridge W.P. Jr. (2022) Development of a multi-spectral pyrometry sensor for high-speed transient surface-temperature measurements in combustion-relevant harsh environments, *Sensors (Basel)* 23, 1, 105.
- 8 Madruga F.J., Fernandez D.A.F., Lopez-Higuera J.M. (2004) Error estimation in a fiber-optic dual waveband ratio pyrometer, *IEEE Sensors J.* 4, 3, 288–293.
- 9 Vortmeyer D., Kabelac S. (2013) K2 Sichtfaktoren, in: VDI Wärmeatlas. VDI-Buch, Springer Vieweg, Berlin, Heidelberg, p. 1097–1114, ISBN 978-3-642 19981-3, https://doi.org/10.1007/978-3-642-19981-3 69.
- 10 Morris A.S., Langari R. (2012) Chapter 14 Temperature measurement, in: *Measurement and Instrumentation*, Butterworth-Heinemann, Boston, pp. 347–396, ISBN 978-0-12-381960-4, https://www.sciencedirect.com/science/article/pii/B9780123819604000140.

- 11 Hamamatsu (2023) P12691-201G photodiode data sheet. Available at https://www.hamamatsu.com/content/dam/hamamatsu-photonics/sites/documents/99_SALES_ LIBRARY/ssd/p12691-201g kird1136e.pdf.
- 12 IRflex (2024) IRF-Se-100 optical fiber data sheet. Available at https://irflex.com/products/irf-se-series/.
- 13 Cassady L., Choueiri E. (2003) High accuracy multicolor pyrometry for high temperature surfaces. Available at https://alfven.princeton.edu/publications/pdf/cassadyiepc-2003-079.pdf.
- 14 Rothman I., Gordon R., Barber H., Dothe R., Gamache A., Goldman V., Perevalov S., Tashkun J., Tennyson J. (2010) HITEMP, the high-temperature molecular spectroscopic database, J. Quant. Spectrosc. Radiat. Transf. 111, 2139– 2150. XVIth Symposium on High Resolution Molecular Spectroscopy (HighRus-2009).
- 15 Pannier E., Laux C.O. (2019) RADIS: A nonequilibrium lineby-line radiative code for CO₂ and HITRAN-like database species, J. Quant. Spectrosc. Radiat. Transf. 222–223, 12– 25
- 16 van den Bekerom D., Pannier E. (2021) A discrete integral transform for rapid spectral synthesis, J. Quant. Spectrosc. Radiat. Transf. 261, 107476.
- 17 Gamache R.R., Vispoel B., Rey M., Nikitin A., Tyuterev V., Egorov O., Gordon I.E., Boudon V. (2021) Total internal partition sums for the HITRAN2020 database, *J. Quant. Spectrosc. Radiat. Transf.* 271, 107713.
- 18 Kochanov R.V., Gordon I.E., Rothman L.S., Wcisło P., Hill C., Wilzewski J.S. (2016) HITRAN application programming interface (HAPI): a comprehensive approach to working with spectroscopic data, J. Quant. Spectrosc. Radiat. Transf. 177, 15–30.

- 19 Northumbria Optical Coatings Ltd. (2024) Filter catalogue. Available at https://www.noc-ltd.com/catalogue.
- 20 Guarco J., Langstine B., Turner M. (2021) Practical considerations for firing hydrogen versus natural gas. Available at https://cea.org.uk/wp-content/uploads/2021/06/Zeeco-Hydrogen-Article.pdf.
- 21 Azzali N., Meucci M., Di Rosa D., Mercatelli L., Silvestroni L., Sciti D., Sani E. (2021) Spectral emittance of ceramics for high temperature solar receivers, Solar Energy 222, 74–83.
- 22 M. Newville, T. Stensitzki, D.B. Allen, A. Ingargiola (2015) LMFIT: non-linear least-square minimization and curvefitting for python (0.8.0), Zenodo. https://doi.org/10.5281/ zenodo.11813.
- 23 Bishop J.L., Lane M.D., Dyar M.D., Brown A.J. (2008) Reflectance and emission spectroscopy study of four groups ofphyllosilicates: smectites, kaolinite-serpentines, chlorites and micas, Clay Minerals 43, 35–54.
- 24 Araŭjo A. (2017) Multi-spectral pyrometry a review, *Meas. Sci. Technol.* **28**, 082002.
- 25 Laser components (2024) FD1000W photodiode data sheet. Available at https://www.lasercomponents.com/fileadmin/user_upload/home/Datasheets/fermionics/fd1000w.pdf.
- 26 Thorlabs (2024) RC08SMA-P01 collimator data sheet. Available at https://www.thorlabs.com/thorproduct.cfm?-partnumber=RC08SMA-P01.
- 27 Thorlabs (2024) Thorlabs FG200LCC optical fiber data sheet. Available at https://www.thorlabs.com/drawings/ced53982697fa6e9-4F485F70-9E46-714D-D173431648BFE8A8/FG200LCC-SpecSheet.pdf.
- 28 LeCroy Corporation (2006) Wavesurfer specifications. Available at https://www.valuetronics.com/media/vti/datasheets/ LeCroy%20WaveSurfer%20400%20Series.pdf.



The European Optical Society is a non-profit society, and an umbrella organization for all national optical societies around Europe. Our members extend from Europe to all over the world.

Our mission is to foster collaboration among individuals and organizations interested in optics, optoelectronics, and related fields. We strive to advance research, facilitate its practical applications, and promote the industrial potential of optics. To achieve this, we organize international conferences, workshops, training sessions, exhibitions, and other events. Additionally, we maintain strong connections with like-minded societies and organizations worldwide.

By joining EOS, you become part of a vibrant and expanding community dedicated to optics and photonics. With over 4,000 members—including societal, corporate, individual, associate, and student categories—we welcome both individuals and institutions.

EOS membership includes various benefits. You can explore the benefits and advantages here:

https://www.europeanoptics.org/pages/members/join-us/benefits.html

EDSAM

The European Optical Society Annual Meeting, EOSAM, is a major international scientific conference and exhibition covering all aspects of optics and photonics.

EOSAM covers all aspects of optics and photonics within several topical meetings and sessions. It is attended annually by around 500 top researchers, key leaders, students, and industry experts from over 30 different countries all over the world.

EOSAM is a great platform for presenting the most recent research results, connecting and catching up, as well as bridging the gap between research, education, and industry.

Each year EOSAM moves into different optics and photonics hubs better serving the local communities and at each time creating a unique EOSAM experience for the attendees. EOSAM has been organized since 2006 in France, Scotland, Germany, the Netherlands, Italy, and Portugal.



9 -13 September 2024 Naples, Italy

EOSAM 2024 TOPICAL ISSUE: PUBLISH AN EXTENDED PAPER

EOSAM 2024 took place in Naples, Italy, on 9–13 September 2024.

Participants can still submit extended articles based on their conference presentations to the <u>EOSAM 2024 Topical Issue</u> of the Journal of the European Optical Society-Rapid Publications (JEOS-RP).

The submission deadline is January 31, 2025.



JEOS-RP published by EDP Sciences in cooperation with:













24 - 28 August 2025 Delft, The Netherlands

European Optical Society Annual Meeting

EOSAM 2025: ABSTRACT SUBMISSION IS OPEN

Abstract submission for <u>EOSAM 2025</u> is officially open! See the wide range of topics to submit to, and be part of Europe's major optics and photonics gathering. Submissions are accepted for oral and poster presentations, for all topics.



Why Publish in JEOS-RP?

- Rigorous peer review
- Strict ethical policies following the COPE code of conduct (<u>read more</u>)
- Rapid publication: median time from submission to first publication \approx 73 days (calculated over 2023)
- Impact factor: 1.9
- Very fair publication fees with no page charges and further discounts for EOS members
- Open-access Creative Commons licence (CC BY)
- Author services: performant search engine, article metrics, bookmarking, online submission, and peer review portal...
- Reader services: free e-mail alerts and RSS Feeds, CrossRef®, and DOI
- Large visibility of the published papers through indexation in main databases

Editor-in-Chief: Silvia Soria

Co-editors: Riad Haidar, Gerd Leuchs, Sergei Turitsyn

